Development of a Hybrid desalination process with hydrate-based desalination and multistage flash

PhD Thesis

Pranav Thoutam

A thesis submitted in partial fulfilment of the requirements of the Teesside University for the degree of Doctor of Philosophy
July, 2021

Supervisors
Dr. Sina Rezaei Gomari
Dr. Faizan Ahmad
Prof. Meez Islam

ACKNOWLEDGEMENT

The one who created quantum fluctuations that called for big bang, the one who generated four fundamental forces during quantum inflation and expansion that govern the functioning of every micro and macroparticle of the universe, the one who narrated the generation of conscience out of nothing, the one who has been generating legions of ground shattering scientific discoveries through us by residing in every element of the universe as Vishnu, is the one whom constantly praise. I thank him for my fundamental existence, for facilitating me with the most admirable parents, for my conscience, and for making me a part of his grandiose narration. I thank the two most ineffably spectacular people that gave me birth, raised me, sustained me, encouraged me, dedicated their entire lives for me, sacrificed their every whim and wish to make my dreams come true and finally made me truly understand the meanings of "Maatrudevobhava" and "Pitrudevobhava". No language in this world could be successful enough to even start defining them as my parents. Additionally, my grandmother Andal Manthena and my aunt and Sri Krishna Manthena had contributed immensely into developing myself into a person who I am right now. I dedicate my thesis to all these four people.

I would like to thank those exemplary teachers that entered my life bearing torches when I was lost in dark, walked with me, and showed the way to enlightenment. They have not just fulfilled their professional requirements, but inspired me into experiencing the joy of knowing, inspired my curiosity into asking questions, created a controlled environment that taught me not only the lessons of academia, but also the life, ethics and responsibilities. They have showed me the potential purpose of my existence. I am eternally indebted to them – "Aachaaryadevobhava".

I sincerely thank Dr. Sina for numerous reasons. After my post-graduation, I had no other plans but to pursue PhD, upon the topic that I was profoundly zealous into materializing. Those days were the darkest of my life and I thank Dr. Sina for accepting my project when I needed it the

most. During these four years, I might have been an inadequate researcher but Dr. Sina has never been anything less than a complete guide. He fulfilled every requirement of this project even by pushing his boundaries to manifest it into a productive study. There might have been a few moments in these four years where I lost my motivation, but Dr. Sina has been downright perseverant with absolutely no pauses. Without him, this project would not have even existed and I thank him from the bottom of my heart. I also sincerely thank Dr. Faizan Ahmad and Prof. Meez Islam for their invaluable contribution to this project. Their inputs have always been highly insightful and pragmatic.

I thank Prof. Antonin Chapoy and the research team at Heriot-watt university hydrate lab for facilitating me with their laboratory facilities to conduct the experimental analysis that was cardinal for this study. I specially thank Dr. Chapoy for not only guiding me through the experiments and reviewing my papers but also teaching me the fundamentals regarding various technical aspect of hydrate formation phenomenon. I also thank my colleagues at the university and the most magnificent friends for understanding me, motivating me and being there for me.

CONTENTS

LIST OF FIGURES

LIST OF TABLES

.

NOMENCLATURE

A	Heat transfer area, m^2
a_a, b_a	Debye-Huckel parameters specific to ion 'a'
A_{DH}, B_{DH}	Debye-Huckel constants
a_m, b_m	Attraction, repulsion parameters for Peng-Robinson Equation of State (equation 5.1)
B	Brine flowrate, kg/s
B_{DH}	Temperature dependent Debye-Huckel constant
c	Shape factor
C0	Nucleation site concentration in the aqueous phase, m^{-3}
Cb	Ion concentration in the bulk stream, kg/m^3
Ci	Ion concentration at the liquid-solid boundary layer, kg/m^3
Cs	Saturation concentration, kg/m^3
D	Diffusion coefficient, m^2/s
D_i	Distillate flowrate, kg/s
Dh	Hydraulic diameter of the tube, m
di	Inner diameter of the condenser tube, m
do	Outer diameter of the condenser tube, m
f_e^*	Frequency of attachment at the point of hydrate equilibrium, (molecule/s)
fi	Fugacity of the gas 'i', MPa
fi,gas	Fugacity of the gas under the operational conditions, MPa
fi,H	Fugacity of the hydrate under the hydrate equilibrium conditions, MPa
G	Growth constant, m/s

G_{ex}	Excessive free energy of the dissolved gas and the free water combined (kJ/m^3)
H_i	Henry law's constant for the guest gas 'i', MPa. m^3/mol
h_{in}	Inside heat transfer coefficient, $W/m^2.K$
h_{out}	Outside heat transfer coefficient, $W/m^2.K$
I	Ionic strength, mol/m^3
J	Rate of nucleation, molecule/s
K_{nuc}	The constant factor for the induction time, s
k_D	coefficient of mass transfer, $m^4/s.kg$
Kgas, mgas	The empirical attributes of the hydrate forming gas for the equation 2.3
kij	Binary interaction parameter used in Peng-Robinson EOS
k_r	Reaction rate constant, $m^4/s.kg$
k_{rem}	Removal rate constant, $m^3/s.kg$
K_{sp}	Solubility product, mol^2/kg^2
ktube	Thermal conductivity of the tube, kW/m.K
LMTD	Log mean temperature difference, ^oC
MCR	Recirculated coolant mass flowrate, kg/s
m_d	Progressive deposition rate, $kg/s.m^2$
M_f	Intake seawater, kg/s
m_f	Net scale deposition, $kg/s.m^2$
m_i	Molality of the dissolved gas, mol/kg
M_{i0}	Concentration of the dissolved gas under the conditions of hydrate equilibrium, molecule/m^3
M_R	Flowrates of recycled brine, kg/s
m_r	Mass removal rate, $kg/s.m^2$

n^*	Number of building units when the system exhibited the work done W^*
n_w	Number of water molecules in the hydrate building unit
P	Operational pressure, MPa
Pe	Equilibrium hydrate formation pressure at the given operational temperature, MPa
PPump	Power consumed by the pump, kW
Q	volumetric flow rate of gas, m^3/s
R	gas constant, J/mol.K
R_c and	Critical radius of the hydrate nucleus, m
Re	Reynolds number (equation 6.43)
r_{fi}	heat transfer resistances on the inside of the condenser tube, $m^2.^oC/kW$
r_{fo}	heat transfer resistances on the out sides of the condenser tube, $m^2.^oC/kW$
Sc	Schmidt number
T_{di}	Temperature of vapour after passing through the demisters, K
T_f	Temperature of the coolant, K
t_{ind}	Induction time, s
T_r	Temperatures of the guest gas, K
Ts	Surface temperature inside the tubes, K
T_V	Temperature of vapour, K
U	Overall heat transfer coefficient, $kW/m^2.^oC$
v	Friction velocity, m/s
Vel	Velocity of the coolant stream flowing inside the condenser tubes, m/s
$V_{excess,t}$	Excess volume created by the formation of hydrate, m^3
V_h	Volume of the hydrate building unit, m^3

V_r	Reduced volume, m^3
$V_{T,t}$	Total volume of gas supplied into the hydrate reactor at any time t, m^3
V_w	Volume of a water molecule, m^3
V_w	Molar volume of water, m^3/mol
v_wC	Mole fraction
W	Total work done for the formation of nucleus successfully, J
W*	Maximum work-done by the system to form a successful hydrate nucleus, J
X	Salt concentration (g/kg)
x_i	Mole fraction of dissolved gas in liquid
yi	Mole fraction of the guest gas
Z	Compressibility factor
z	Zeldovich factor
Z_a	Ionic charge on the ion 'a'
α	Volume fraction of the hydrate with respect to the rectors volume
β	Mass transfer coefficient reaction, m/s
μ_i^l	Chemical potential of the gas 'i' in the liquid, kJ/mol
μ_i^v	Chemical potential of the gas 'i' in the vapour, kJ/mol
$\emptyset_i$	Coefficient of fugacity of the gas 'i'
Δμ	Chemical potential difference, kJ/mol
μH	Chemical potential of the hydrate, J/m^3
μ_w	Chemical potential of water, J/m^3
υ_w	Viscosity of water, kg/m.s
ρf	Density, kg/m^3
ρh	Density of hydrate, kg/m^3

ρ_w	Density of water, kg/m^3
σ_f	Shear strengths of the fouling layer, N/m^2
τ_f	Surface shear stress, N/m^2
φ	Heterogeneity factor
σ	Superficial energy (J/m^2)

ABSTRACT

MSF (Multi-stage flash) desalination process faces two main challenges that made industrialists choose to RO (Reverse Osmosis) process over MSF: Corrosion and fouling; and carbon emission. As it was seen from the literature, the scale formation occurring in the condenser tubes could reduce the heat transfer rates by 80%, drastically affecting the total performance and production ratios of the column. On the other hand, ever since the Paris agreement, the restriction upon the total industrial carbon emission have been becoming complicated annually. Even though, hydrate formation had the capacity in addressing both the issues, challenges like stochasticity associated with hydrate nucleation and lower hydrate formation kinetics discouraged the process from industrial application as an independent plant. Hence, the current project proposed the usage of hydrate formation phenomenon to improve the performance of Multi-stage flash (MSF). The study focussed on analysing the practicability of HBD (Hydrate Based Desalination) -MSF hybrid and HBCC (Hydrate Based Carbon Capture)-MSF hybrid as an industrial application.

Addressing the stochasticity of hydrate nucleation, the evaluation of stochasticity was studied under various operational conditions by using the theoretical mathematical model proposed by Kashchiev and Firoozabadi. In addition to this analysis, a theoretical induction time equation was derived and validated based on the experimental analysis. The optimum pressure and temperature conditions to conduct hydrate formation experiments for desalination applications were derived based on this induction time analysis. Hydrate formation experiments in the presence of saline water and impure guest gas were conducted under various influencing factors such as kinetic additives and physical interventions. The study concluded that the energy invested upon stirring was unnecessary as the initial hydrate formation was higher in case of quiescent conditions.

Addressing the carbon capture through HBCC, tertiary amines were added to the mixture of Tetrahydrofuran (THF) + Sodium dodecyl sulphate (SDS) + Distilled water, which was aimed at separating CO_2 from post-combustion gas capture mixture. A set of experiments were conducted under various amines and their concentrations of amine along with various pressure conditions. It was observed that the carbon selectivity was higher at operational pressures and in the presence of TIPA. When evaluated the practicability of HBCC-MSF hybrid, from the perspectives of both water usage and the carbon emission during hydrate formation, an optimistic version of HBCC was observed to be effective to be used for carbon capture. Finally, for the analysis of HBD-MSF practicability of industrial application, mathematical models were created addressing MSF-OT (Once Through) and MSF-BR (Brine Recycle) in SIMULINK. Even though, the introduction of HBD precursor to MSF was seemed to be improving the performance of MSF, the overall practicability of MSF-HBD was observed to be less due to the slower hydrate formation kinetics. Hence, it was concluded that the combination of HBD-MSF for hybrid could be viable only when the higher input water requirements of HBD are addressed.

LIST OF PUBLICATIONS

Thoutam, P., Rezaei Gomari, S., Ahmad, F. and Islam, M., 2019. Comparative Analysis of Hydrate Nucleation for Methane and Carbon Dioxide. *Molecules*, *24*(6), p.1055.

Thoutam, P., Rezaei Gomari, S., Chapoy, A., Ahmad, F. and Islam, M., 2019. Study on CO2 Hydrate Formation Kinetics in Saline Water in the Presence of Low Concentrations of CH4. *ACS omega*, *4*(19), pp.18210-18218.

Thoutam, P., Gomari, S.R., Chapoy, A., Ahmad, F., Islam, M. and Ahmed, I., 2021. Enhancement of CO 2 capture through hydrate formation: the effect of tetrahydrofuran (THF) and tertiary amine solutions. *International Journal of Environmental Science and Technology*, pp.1-14.

Thoutam, P., Rezaei Gomari, S., Ahmad, F. and Islam, M., Addressing the challenges of MSF through hydrate precursor. Desalination (to be submitted).

Chapter 1

Introduction

1.1. Multistage flash: Current status and challenges

By the end of 2002, 36.5% of installed Brackish and Seawater desalination plants were of Multistage Flash (MSF) while 47.2% were accounted for Reverse Osmosis (RO). When considered specifically Seawater desalination plants, the percentage will become 61.6% of MSF and 26.7% of RO (IDA, 2004 and Khawaji *et al*., 2008). Khawaji further explained that according to international desalination inventory 15, the world's desalination capacity increased up to 40 million cubic meter per day with an annual growth of 12% having dominated by MSF among plants producing over 5,000m^3/day. According to Global Water Intelligence (2004), the MSF plant named Al-Jubail in Saudi Arabia was the largest plant with a capacity of 815,120m^3/day while the largest contemporary Seawater Reverse Osmosis (SWRO) plant being Ashkelon, Israel with a capacity of 273,972m^3/day (GWI, 2004; Kronenberg *et al*., 2004).

The global desalinated water share of MSF used to be 78% in 1999, which has been plummeted down to 36.5% by 2002, while reverse osmosis has been in a huge surge from 10% in 1999 to 47.2% in 2002. This is because of the factors such as low carbon emission and low freshwater production costs (Bruggen *et al*., 2002; Khawaji *et al*., 2004; Elimelech *et al*., 2011). Bruggen *et al*. (2002) further explained that the average cost of water purification through RO is much lower with a range of USD 0.5 - 0.7/m^3 than MSF with a range of USD 0.9 - 1.4/ m^3 of freshwater production.

However, the cost of RO may escalate up to USD 0.99/m^3 when considered seawater (Mezher *et al*., 2011). Despite of lower operational costs, the membrane technology has not achieved long term cost effectiveness for seawater desalination due to the susceptibility towards fouling through corrosive components, impurities and pH (Ostuni *et al*., 2001 and Elimelech *et al*., 2011). According to the current status, SWRO is only capable of separating 99 to 99.6% of salts depending on the inlet water quality, while MSF can produce water with 99.99% purity (Corry *et al*., 2008; Elimelech *et al*., 2011; Yousuf *et al*. 2014). Despite of low carbon emission through SWRO, the membrane fabrication has not yet been sustainable for commercial membrane production due to the nondegradable solvents used for Cellulose membranes or high carbon emission in composite membrane fabrication (Perez *et al*., 2016).

Despite having high desalinating capacities and wide application in high water stressed gulf area for its reliability and easy control, MSF has its own drawbacks such as vulnerability towards corrosion, scale formation and low energy efficiency or high carbon emission as explained. An MSF plant with a specific heat consumption 60 kWh/m^3, performance ratio 10, electrical energy consumption rate 3 kWh/m^3 will have a specific CO_2 emission ranging from 9.29 to 18.03 kg/m^3 depending upon the load. The similar RO plant with a specific energy consumption 5 kWh/m^3 will have CO_2 emission in between 2.77 to 4.91 kg/m^3 (Afgan *et al*., 2002). With this rate an MSF plant as huge as Al-Jubail will have a carbon emission up to 14.7 million kg/day, which can considerably contribute to global warming.

1.2. Hydrate based desalination.

An induction of Gas-Hydrate precursor could be able to offer a potential solution for all the aforementioned issues of MSF. Gas-hydrates are also termed Clathrates, which has been derived from a Greek word Khlatron (Barrier). Clathrates are crystalline compounds formed by water molecules at low temperature and high-pressure conditions in the presence of

hydrocarbons. A phase diagram showing the stable conditions for CO_2 - hydrate has been given in the figure 1.1 (Voronov, et al., 2016). Physically gaseous hydrocarbons are trapped in hydrate cavities formed by three-dimensional assembly of water molecules connected by hydrogen bonds. Chemically these clathrate structures are free of salt and hence formation of clathrates represents Desalination phenomenon, which is also called Hydrate Based Desalination (HBD) (Chatti *et al*., 2004). Due to high volume of gas capturing ability, with 175:1 volume ratio of Gas CO_2 at Standard temperature and pressure to hydrated CO_2 and relatively low-pressure requirement for CO_2 hydrate formation, gas-hydrate process with CO_2 as guest gas can be a desirable option for Hydrate Based CO_2 Capture (HBCC) from either pre-combustion or post-combustion gases (Dashti *et al*., 2015 Sloan *et al*., 1998).

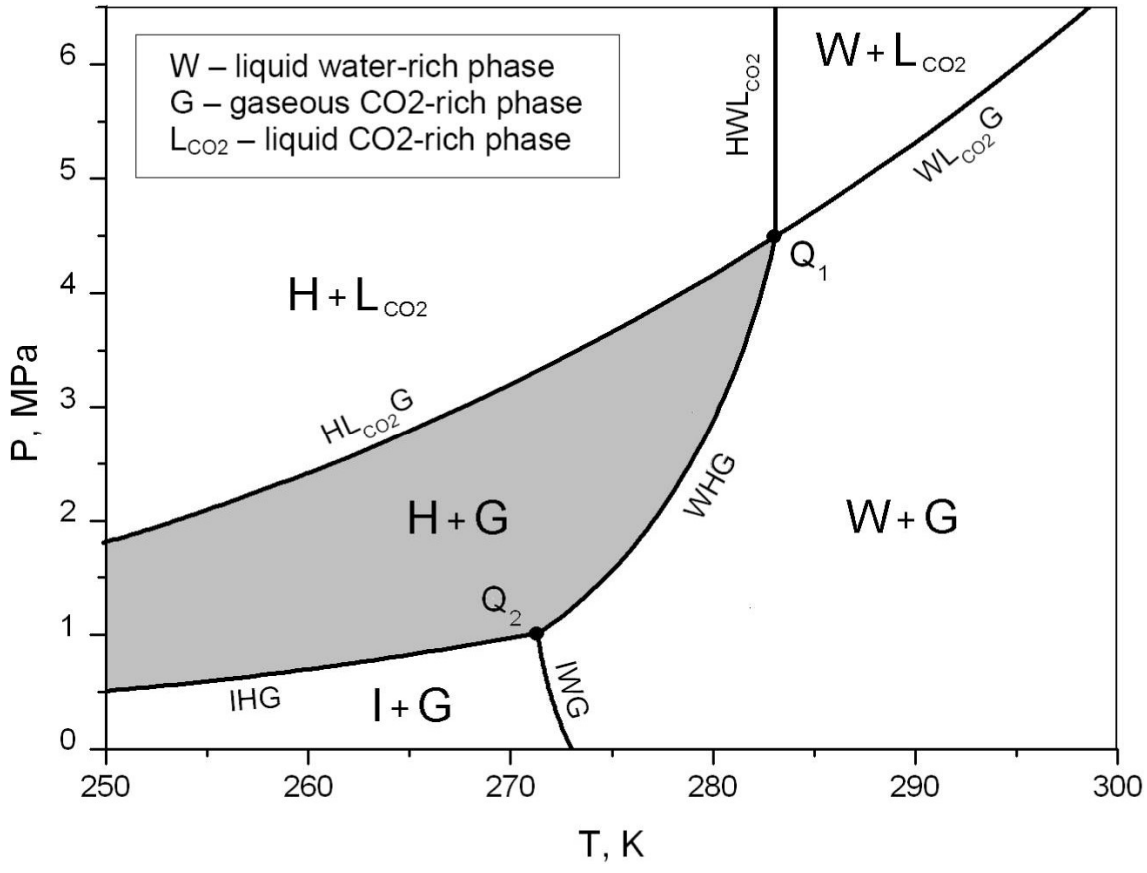

Figure 1.1. Phase-envelop of CO_2-hydrate (Voronov, et al., 2016)

According to Youssef *et al*. (2014) hydrate-based desalination can reach out to a desalination capacity of 99% of salt removal with the freshwater production cost as low as USD0.63/m^3. Under current status, HBD alone may not be able to produce potable water and hence can be used for pre-treatment in a hybrid desalination plants. With an efficient capture of CO_2 and a fair desalination capacity, combining with HBD can be a potential solution to address the issues of MSF.

1.3. Problem statement, Aims and Objectives.

1.3.1. Problem statement

As explained so far, despite MSF being the most reliable and simple desalination process, its operation consists of various challenges in terms of susceptibility to fouling in the condenser tubes and the carbon emission. Various chemical solutions addressing the problem of scale formation were already addressed through acid treatment and anti-scalant introduction into the feed water. However, these solutions pose various issues starting from the requirement of high precision in injecting the amount of these chemicals into the feed water, triggering corrosion and causing eutrophication issues. Even with the green anti-scalant substances, there have been considerable incoherence amongst the efficiency observations published by various authors, which seeks further study upon their efficiency. Even though there have been various industrial scale attempts in improving the total productivity and flexibility of existing MSF desalination systems in the combination of MED and RO, they have not addressed the issues such as scale formation and CO_2 emission. Even after the deployment of pre-treatment methods using NF and FO, to reduce the scale formation in MSF desalination columns, it still did not solve the issue as FO and NF were themselves vulnerable to scale formation. In addition, these processes did not address CO_2 emissions, requiring an additional capturing mechanism, complicating the entire plant functioning.

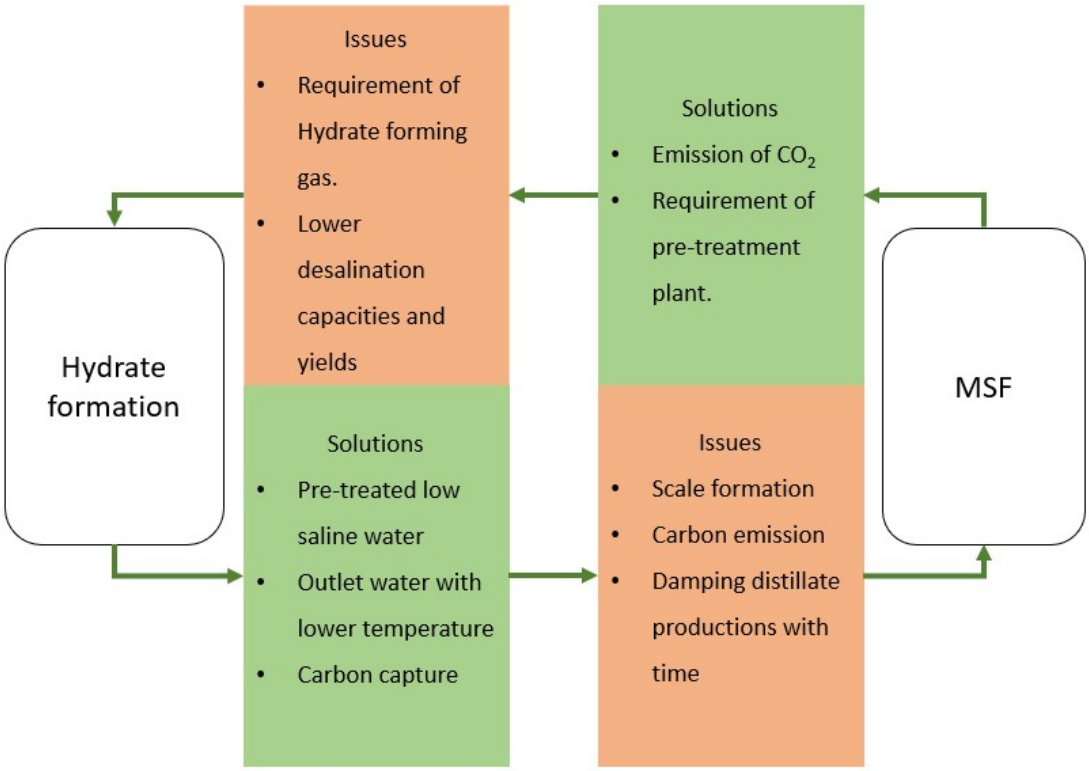

Figure 1.2. The two major components of this study: MSF and Hydrate formation, their issues and the solutions offered from each other.

.

Hence, the current study proposes hydrate formation precursor for desalination and another hydrate forming mechanism to capture CO_2 to understand how the phenomenon of hydrate formation could be used to address the issues associated with MSF. For an extremely limited industrial application of HBD due to various issues associated with the process as well as the fundamental understandings of hydrate formation phenomenon, the current study did not consider economic analysis of the hybrid system. The study mainly focused upon examining the mechanism of hydrate formation under various chemical and physical conditions to understand the product (hydrate) quality and generation kinetics towards the application of water pre-treatment as well as carbon capture. Thereafter using these results, the overall performance of HBD-MSF hybrid system was analysed from the perspective of carbon emission, scale formation and fresh-water productivity. The mutual dependency of Hydrate

formation and MSF have been shown in the figure 1.2. The HBCC-MSF design configuration has been shown in the figure 1.3. The two hybrid desalination designs, for which the practicability has been investigated through this study were shown in the figure 1.4.

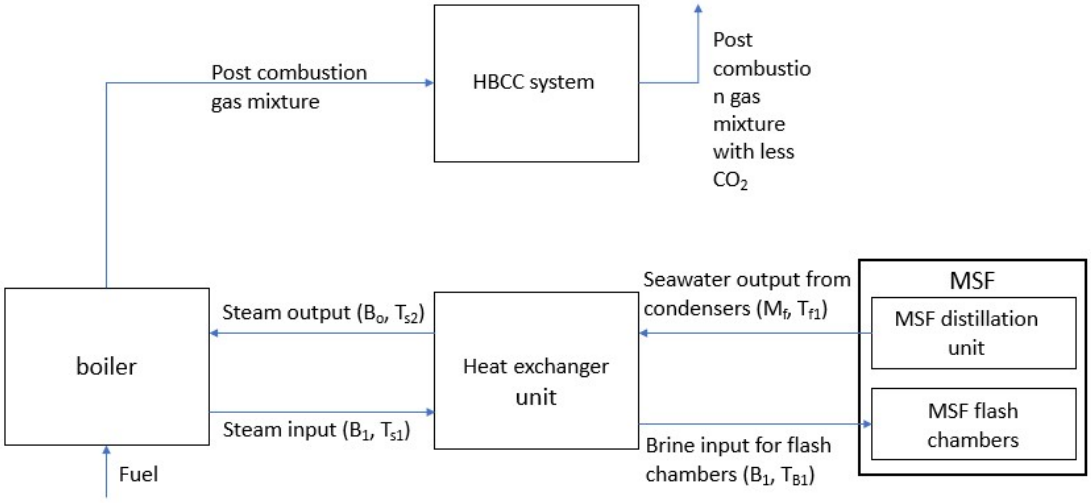

Figure 1.3. *The configuration of HBCC-MSF system*

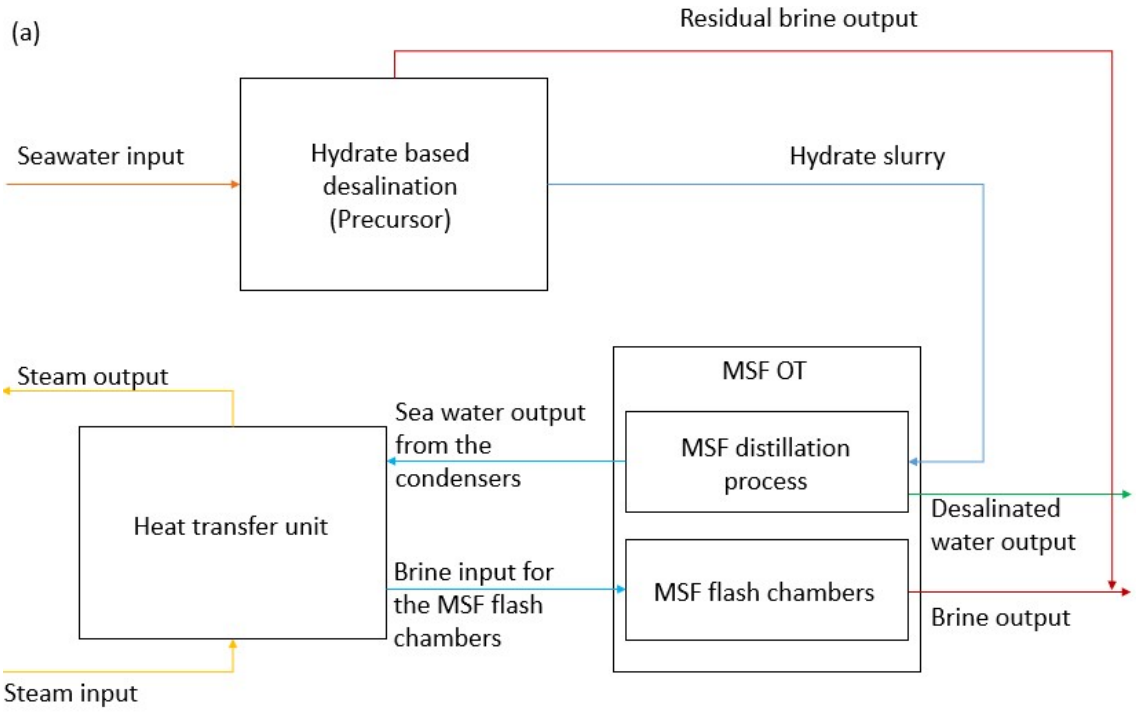

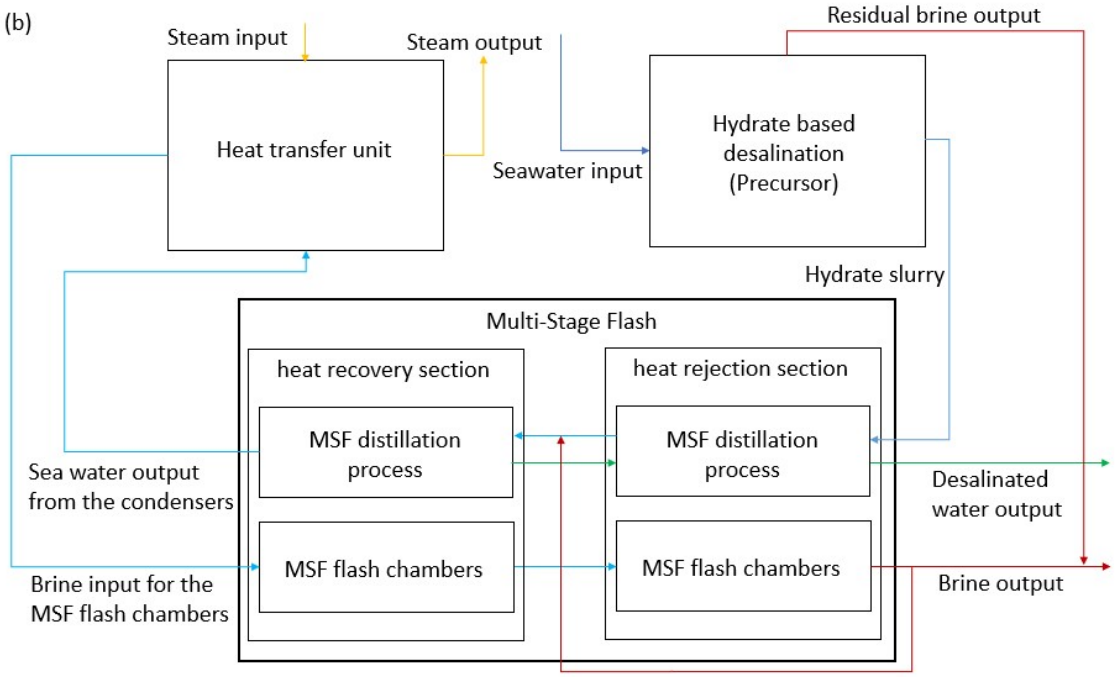

Figure 1.4. Hybrid of HBD and MSF with OT (a) and BR (b) configurations

1.4.2. Aim

To examine the efficiency of hydrate formation precursor in enhancing the overall performance and ensure low-carbon emission of MSF.

1.4.3. Objectives

- To design a mathematical model upon hydrate nucleation to calculate various governing parameters of nucleation such as the rate of nucleation and hydrate volume fraction and also to derive hydrate induction time equation combining various models proposed on nucleation.
- To analyse hydrate nucleation from the existing model to understand the causes and consequences of the delays behind hydrate formation. This understanding could be used to choose the most suitable operational conditions for hydrate formation experiments.
- To experimentally analyse the kinetics, total yield, and the product salinity of hydrate formation under various operational conditions suitable to generate pre-treated water for MSF desalination.

- To analyse the kinetics and the yield of hydrate formation, the extent of gas consumption into hydrate to understand the efficiency of CO_2 capture by hydrate formation, whereby understanding the carbon reduction from MSF effluence contributed by hydrate formation process.
- To design a dynamic MSF desalination process to understand the effects of $CaCO_3$ scale formation in the condenser tubes.
- To design and analyse a hybrid desalination system combining HBD and MSF to assess the performance of MSF from the perspectives of performance ratio and production ratio with and without the hydrate precursor as well as overall practicability of the hybrid.

1.4. Contribution to knowledge

While designing a compatible hydrate-based desalination and carbon capture system addressing the issues of MSF, the study required to understand the optimal chemical and physical conditions to perform hydrate formation process that would ensure an optimum performance of the hybrids. From the perspective of hydrate-based desalination (HBD), the compatibility was from the perspective of water quality, hydrate formation kinetics and yield. From the perspective of hydrate-based carbon capture (HBCC), this compatibility was checked in terms of the system's ability to separate CO_2. During the process of establishing the most compatible physical and chemical operational conditions for the HBD and HBCC, alongside evaluating the practicability HBCC-MSF and HBD-MSF systems, the study has been successful in achieving the following.

The study utilised a comparative analysis amongst various cases created by changing the calculating methods for parameters such as gas fugacity and dissolved gas concentration to evaluate the sensitivity of Kashchiev and Firoozabadi's model for calculating hydrate

nucleation rate and induction time. The study also served to understand under what conditions the sensitivity was less and the most favourable operational conditions for hydrate nucleation. Under what pressure and temperature conditions, the deviation amongst the resulting values of nucleation parameters calculated from various models were deviating the least?

The experimental analysis without thermodynamic additives evaluated the effect of gaseous impurities and the electrolytes in discouraging the hydrate formation. They have also been utilised to understand how physical and thermodynamic barriers affect the hydrate formation kinetics with time and how various surfactants with different carbon chain lengths could help in improving the kinetics. At the end of every experiment, the residual water was subjected to conductivity tests to examine the salt removal capacity of hydrate formation process.

A second set of experiments were conducted in the presence of THF as the thermodynamic additive in the presence of tertiary amines to evaluate the carbon capture efficiency of hydrate formation process from the post-combustion gas mixture. These experiments elucidated on how thermodynamic additives could suppress the requirement of higher operational pressure conditions to form hydrates in the presence of gaseous CO_2 at low concentrations. This analysis also resulted in an understanding of how two commercial tertiary amines could improve the selective separation of CO_2 from the post-combustion gas mixture. This segment of hydrate formation demonstrated the capacity of hydrate formation under the selected chemical and physical conditions in separating CO_2 and its practicability for the industrial application focussed on thermal desalination process.

The final stage of the study developed a configuration consisting of Both Hydrate Based Desalination (HBD) and Multi-Stage Flash (MSF) to evaluate the practicability of the combination from the perspective of overall performance ratio and production ratio. As a part of this segment, Calcite and Aragonite scale formation with and without pre-treatment of HBD.

This concluded the study with the comments on how the suppression in scale formation induced by the pre-treatment of seawater through HBD improve the performance of MSF and also the drawbacks of using HBD from the perspective of overall production ratio.

1.5. Structure of the thesis

Following this chapter, the thesis has been divided into six chapters.

Chapter 2 presents the critical evaluation of various hybrid desalination systems, their structures and their respective efficiencies along with drawbacks in addressing the issues faced by MSF through a comparative literature analysis. The chapter also offers an understanding of various mathematical modelling developed to predict different aspects of hydrate formation under a wide range of operational conditions. An extensive critical evaluation of various promotors, physical interventions and inhibiting conditions has been presented to evaluate the techniques that have been employed to improve the overall kinetics of hydrate formation. This information combined with the research gaps were used to develop methodology to design a hybrid MSF-hydrate desalination system that could efficiently address the scale formation and carbon emission from MSF.

In the chapter 3, a sensitivity analysis of theoretical mathematical model for nucleation proposed by Kashchiev and Firoozabadi (2000, 2002a, 2002b, 2003), could be found. This sensitivity analysis would be based on the parameters such as the extent of gas consumption and the fugacity of the guest gas for a wide range of operational conditions. This analysis gives an understanding of how these parameters could affect the accuracy of the nucleation models proposed by Kashchiev and Firoozabadi and under what operational conditions this accuracy is more affected. Based on the principles of Kashchiev and Firoozabadi (2002b) and Sloan and Koh (2007), a theoretical induction time is proposed, which is validated through experimental

observations. This induction time is used to find out the optimum operational conditions to carry out the hydrate-based desalination experiments.

Chapter 4 offers the experimental analysis of hydrate formation and its sensitivities towards various chemical and physical conditions such as impurities, promoters and physical interventions. This sensitivity is calculated in terms of the volumetric gas consumption, which directly indicates the hydrate formation, where a comparative analysis amongst various considered systems is done. Along with the sensitivity, the effect of physical and thermodynamic barriers is analysed during the hydrate formation experiments to understand their effects on the total yield of hydrate formation. In addition, the desalination capacity of the hydrate formation process is measured through water activity measurements.

Chapter 5 offers the experimental analysis of hydrate formation aimed at selective separation of CO_2 from the post combustion gas mixture ($85\%N_2+15\%CO_2$). The chapter discusses various opportunities proposed in the literature to separate CO_2 through hydrate formation and their respective separation efficiencies. Following this, to improve the carbon selectivity, tertiary amines are added to the system, where the overall gas consumption is observed and compared with the quiescent systems to check if amines are discouraging/encouraging the hydrate formation. The residual gases from the hydrate systems are collected after the experiments, subjected to gas chromatography and the carbon concentrations are compared to check the effect of amines over the selectivity of CO_2 into hydrates.

Chapter 6 offers a mathematical evaluation of the HBD-MSF hybrid using SIMULINK in terms of the performance ratio and production ratio of MSF-OT, MSF-BR and HBD-MSFOT and HBD-MSFBR systems. For this the total scale deposition and the reduction of heat transfer coefficient are calculated using water salinity data gathered from the experimental analysis mentioned in the chapter 4.

Chapter 7 offers overall conclusions of the thesis comparing the research gaps and the research contributions of the current thesis. In addition, it also offers the potential research areas into which the current study could be extrapolated.

1.6. Summary

In this chapter subjects like global water stress, requirement of economic yet efficient water desalination processes, various challenges with MSF desalination processes, and the studies that tried to address these issues were discussed. From the existing studies, it was observed that the contemporary industry solutions towards addressing the scale formation as well as carbon capture from the MSF desalination processes were inadequate to provide sustainability towards both the plant and the environment. As much as the existing MSF/RO or MSF/MEA desalination systems did not address the issues of MSF, the pre-treatment by FO or NF were failed to effectively address those issues. Even the chemical methods to suppress the scale formation were either with the questionable efficiency or unsustainable towards the environment. Amongst of all, the major gap that was found in the literature was the development of a single process to address both the issues of MSF desalination process. Hence, the study aimed at developing a more scale resilient desalination process for pre-treatment of seawater before injecting into MSF while developing the same phenomenon to capture CO_2. After the discussion of various aspects of the challenged faced by MSF, the chapter concluded with the proposal of developing HBD-MSF hybrid process for desalination and HBSS-MSF hybrid process for carbon capture.

Chapter 2

Literature review on Hydrate formation

2.1. Introduction

For being simple to operate and highly compatible towards larger scale fresh-water production, MSF has been the most chosen thermal water desalination process in the world. MSF desalination plants produce approximately 94% of the total fresh water from thermal desalination plants in the world, while 53% of the total freshwater production in MENA (Middle East and Northern Africa) is occurring through it (Al-Mutaz, 2020). However, MSF as a process is highly vulnerable to scale formation thus leading to high maintenance costs and high carbon emissions leading to high carbon tax (Liu, et al., 2015; Al-Mutaz, 2020). According to Liu et al., (2015), an MSF desalination plant producing approximately five million cubic meter water per day in produces approximately 14000 tons of CO_2 per day. On the other hand, the scale formation due to the precipitation of the prevalent salts in the seawater causing resistance towards heat transfer in the distillers leading to high operational costs to the desalination industries towards the maintenance (Al-Anezi & Hilal, 2006). There have been numerous solutions proposed addressing either of the issues, which are elaborated in the section 2.2.

2.1.1. Carbon capture

The high dependency of global energy demand on fossil fuel on the one hand and the high cost of carbon capture technologies on the other have necessitated additional research effort and resources to develop effective low-cost CCS technologies (Gibbins & Chalmers, 2008). In fact, the high cost of these technologies is hindering their widespread implementation (Anderson & Newell, 2004; Gibbins & Chalmers, 2008). Various techniques addressing carbon capture, storage and CO_2 utilization have been reported in the literature (Anderson & Newell, 2004;

Gibbins & Chalmers, 2008; Markewitz, et al., 2012; Leung, et al., 2014). Before employing a CCS technique, it is necessary to understand the fuel and the combustion technology employed by the industry involved along with its carbon emissions. Three main types of carbon capture combustion methods are found in the literature: post-combustion, pre-combustion and oxyfuel techniques. In comparing these methods, Gibbins and Chalmers (2008) and Leung et al. (2014) have stated that the capital and electricity costs of post-combustion were lowest for gas-fired systems, whereas for coal-fired systems pre-combustion gas capture costs were cheapest. However, the world's dependence on coal is declining (Rutledge, 2011). According to the Energy Information Administration (2019), coal production in the U.S. decreased by 9% in 2019, and it was forecast to decrease further by 7%. The present study therefore focuses upon post-combustion gas capture.

Most carbon capture technologies focus on absorption, while less attention has been paid to adsorption and membrane technologies (Bhown & Freeman, 2011). This might be attributed to the wide usage of absorption techniques around the world for carbon capture and gas sweetening. Among the absorption technologies available, chemical absorption is considered to be a mature process due to its use for decades in industrial gas processing (Yu, et al., 2012). In addition, these technologies are also known for their retrofitting capabilities. Due to their higher carbon loading from the formation of less strong carbamates, sterically hindered amines such as alkanolamines have been introduced into the solvent solutions (Sartori & Savage, 1983; Sartori, et al., 1987; Bougie & Iliuta, 2012). For high- equilibrium carbon loading capacity (1.0 mol of CO_2 per mol of amine) and with lower regeneration energy requirements, compared to monoamines and diamines, tertiary amines are a good choice for inclusion in absorption mixtures. This is further evidenced by the usage of blended amines, including tertiary amines and others, in the absorption solution in order to enhance carbon loading (Hagewiesche, et al., 1995; Mandal, et al., 2001; Kim, et al., 2016). Despite low reaction kinetics, it has also been

observed that the carbon loading per mole of tertiary amines is higher at lower temperatures (Rho, et al., 1997; Tong, et al., 2013). This is attributed to the low solubility of CO_2 under high temperature conditions (Daneshvar, et al., 2004).

Triisopropanolamine (TIPA) and Triethanolamine (TEA) were amongst the most researched tertiary alkanolamines addressing carbon capture and storage through absorption. Rayder et al (2012) through his comparative analysis provided CO_2 absorption data of in the presence of TEA and TIPA (Henni, et al., 2012). According to this study, the 30wt% of TEA solution required considerably higher pressure to capture comparative amounts of CO_2 with 10% of TIPA solution. A similar observation was made when compared two studies done by Chauhan et al. (2003) and Chung et al (2010) who have done carbon loading experimental studies in the presence of TIPA and TEA respectively (Chauhan, et al., 2003; Chung, et al., 2010). At 313K and 36.27 KPa pressure, in the presence of 2mol/l of TEA the carbon loading was obtained to be 0.345 mol of CO_2/mol of amine. Under the similar conditions, the similar carbon loading was observed in the studies of Chauhan et al. (2003) with the introduction of 1.5 mol/l of TIPA instead of 2 mol/l of TEA. On the other side, the efficient carbon capture technology should also provide effective amine regeneration capabilities as well, in which TEA was observed to be more efficient (Baltar, et al., 2020). Overall, the absorption process for carbon capture is energy-intensive, especially the stripping stage which requires high temperature (120^{o}C) and low-pressure conditions (Sartori & Savage, 1983). Hence, there has been keen research interest in alternative gas capture technologies such as chemical looping, electro-chemical pumping and hydrate-based gas separation (Sabil & Partoon, 2018). However, the current study investigates the effectiveness of hydrate formation in capturing CO_2 emitted from the thermal desalination process, amines were added to improve the selectivity into the aqueous-hydrate phase. For the application of carbon capture through hydrate formation, it is important to

investigate if the amines either encourage or discourage hydrate formation in the solutions, which has been investigated in the presence of TEA and TIPA.

2.1.2. Scale formation

Scale formation through the precipitation of salts from the saline water under heightened temperatures is a universal issue for all the major desalination processes around the globe. Especially in thermal desalination processes such as MSF and Multi-effect desalination (MED), operating at higher temperatures, this issue was even higher. Amongst all the parts of these desalination systems, the condenser tubes have been regarded to be most vulnerable to failure through the issues such as corrosion and scale formation. Approximately 80% of the outages occurring in these desalination processes were due to the failure of condenser systems, where 90% of them occur in the condenser tubes. Hence, condenser failure in thermal desalination processes is by default considered as the tube failure (El Din & Mohammed, 1998; El-Dahshan, 2001). Depending upon the pH requirement of scale formation, the scales are often classified as alkaline and non-alkaline scales. When the pH of the system increases, the bicarbonates in the system would convert into carbonate, causing carbonate supersaturation resulting in alkaline scale formation (Glade & Al-Rawajfeh, 2008). Hence, controlling the scale formation would be important to suppress alkaline scale formation. The trigger behind the formation of alkaline scale is the lower solubilities of salts as well as accelerated decomposition of bicarbonates under heightened solution temperatures. The most common composition of alkaline scale consists of $CaCO_3$ and $Mg(OH)_2$. Calcium Carbonate based scale formation has been understood to be the most common type of scale that occurs at temperatures as low as 45^{o}C, whereas Magnesium hydroxide based scale formation occurs at temperatures above 75^{o}C which is most common for the MSF desalination systems operate at top brine temperatures above 108^{o}C (El Din & Mohammed, 1989; El Din & Mohammed, 1994; El Din, et al., 2005).

Amongst the non-alkaline scales, $CaSO_4$ scale has been found to be the most common one. Similar to $Mg(OH)_2$, $CaSO_4$ would require temperatures as high as 75^oC to form. As explained by Al-Sofi (1999), the precipitation of $CaSO_4$ in any form in MSF plants was observed to have occurred only when the plant is operated at TBT more than 120^oC. Unlike alkaline scales, $CaSO_4$ would be the result of reaction of the pre-existing components in the saline water and independent of pH of the solution (Al-Sofi, 1999; Shams El Din, et al., 2005; Wildebrand, et al., 2007). In fact, as stated by Shams El Din et al (2005), for an MSF system operated with a TBT (Top brine Temperature) 112^oC, the first three stages were completely covered with $Mg(OH)_2$ scale while the later stage were dominated by $CaSO_4$, with an increasing quantities of $CaCO_3$ with stages. As the current study has been focussed on how pre-treated water from hydrate-based desalination process could improve the Multi-stage flash, the system was considered to be operating at temperatures lower than 90^oC top brine temperature and hence, only $CaCO_3$ scale formation was considered. However, in order to give an overall idea, the basic mechanism of $Mg(OH)_2$ as well as $CaSO_4$ were also superficially explained.

The crystallization of $CaCO_3$ could occur in three different forms: Aragonite, Calcite and Vaterite, where Aragonite is the most expected to form in water with higher salinity such as seawater (Zhong & Mucci, 1989). Researchers understood that the rate of scale formation would be dependent upon the concentration of bicarbonates (salt) in water, TBT and the partial pressure of CO_2, while other researchers believed that the scales could also form under low temperature conditions without the presence of CO_2 (Mubarak, 1998). Scale formation is a profoundly complex phenomenon, that has been explained by means of mass transfer, heat transfer and chemical reactions, while considering the physico-chemical properties of the scale material, water and the operational conditions of the process. As explained by Kazi, the scale formation undergoes the following stages (Kazi, 2012): transportation, Initiation, attachment, removal and aging.

- The transportation phase consists of the diffusion of scale forming substrate from the bulk water to the scale forming surface (or the solid-liquid boundary). This phase is dependent upon the particle size and the velocity of the stream.
- Initiation phase consists of a heterogeneous nucleation at the scale forming surface where the scale formation has not yet been spontaneous. However, the formation of nucleus would trigger a continuous scale growth
- This is the phase where the transported scale formation species would be accumulated and attached at the scale forming surface. This please is dependent upon the attributes of the surface such as roughness, elasticity and density.
- The removal phase occurs when the velocity of the liquid is high causing high shear forces that would eventually disengage the accumulated scale forming substrate to disengage from the surface into the stream.
- After a certain age, the scale deposited on the surface would break into parts, which is called aging.

Preventing scale formation completely is impossible (Alsadaie, 2017). Addressing the problem of scale formation, various chemical and physical solutions were under application as well as examination. In order to prevent alkaline scale formation, acids such as H_2SO_4 are added. In addition, various commercial anti-scalants that are derived from condensed polyelectrolytes, polyphosphates and organophosphonatesare also widely used industrially (Hamed & Al-Otaibi, 2010).

The chemical prevention of scale formation techniques is often adjoined with challenges such as improper dosage, unsustainability, and instability. When induced with improper amounts of antiscalant, the salt can agglomerate around the molecular chain of the additive making the prevention process ineffective. The effectiveness of antiscalant are highly dependent upon pH, temperature and pressure conditions as well (Dyer & Graham, 2002). Under the conditions of

water with high ionic charge density, the anionic charge density of the antiscalant would be reduced, diminishing the effectiveness of the additive (Hasson, 1999). Under the unsuitable pressure and temperature conditions or in the presence of impurities such as iron and aluminium, the antiscalant molecules could become unstable causing degradation of the substance (Amjad & Zuhl, 2007). Moreover, there have been numerous studies mentioned the environmental challenges of anti-scalant substances related to the questionable biodegradability. Especially, these challenges emerge due to the concentration of phosphonates in the brine water during its disposal (Boels, et al., 2012; Pervov, et al., 2015; Chen, et al., 2017; Shi, et al., 2017).

Hence, there have been numerous alternatives proposed as well as in use such as mechanical cleaning including both offline (brushing) and online (balls) or by water flushing or hosing or controlled mechanical vibrations (Steinhagen, et al., 1993; Al-Ahmad & Aleem, 1994; Song, et al., 2010; Pogiatzis, et al., 2012). However, these cleaning methods are labour intensive (Müller-Steinhagen, et al., 2011).

As this study proposes gas hydrate formation as a solution for both the challenges posed by MSF desalination columns, the current chapter elaborates the theory, detective and predictive mechanisms, current status and future prospects of gas hydrate process for the application of desalination and carbon capture along with the other solutions proposed for the betterment of MSF desalination plants.

2.2. MSF hybrid designs

The most commonly available hybrid systems contained the combination of MSF and Reverse osmosis processes together. The main aim of operating MSF and RO together was to improve the efficiency of RO as well as to decrease the water production costs. There have been numerous desalination plants installed in Saudi Arabia and UAE with the combination of MSF

and RO together where they work in parallel and entirely independent from each other. In these hybrid systems MSF and RO share a common water and power intake while their outputs will be merged at the end (Hamed, 2005). In 1989 Saudi Arabia's SWCC (saline Water Conversion Corporation) first introduced the concept of hybrid desalination in the combination of MSF/RO where the SWRO (Sea Water Reverse Osmosis) plant was coupled with dual purpose MSF/power plants. Initially, the plant was combined with SWRO with a capacity of 12.5 MIGD fresh water production, while, in 1994, a second phase of SWRO with a capacity of 12.5 MIGD was added. Combining these capacities with MSF desalination column, the total water production capacity of the hybrid plant has reached 80 MIGD freshwater (Al-Badawi, et al., 1995) Due to the increased water demand in Madina and Yanbu the existing MSF desalination plants of capacity 40 MIGD were integrated with a SWRO plant of capacity 28.16, for which a single stage SWRO was selected (Nada, et al., 1995). The first ever pre planned MSF desalination plant was built in Fujairah, UAE with a combination of MSF having 62.5 MIGD capacity and SWRO with 37.5 MIGD capacity. Generally, in winter the power demand drops by 40% limiting the need of operating an entire MSF section which could be used for cleaning and maintenance related purposes. For most of these cases, the hybrid concept was planned and executed aiming for a constant water supply throughout the year as well as to lower the annual energy consumption. Amongst the latest developments of MSF accompanied hybrid desalination plants Fujairah 1 Independent Water and Power Plant Expansion can be discussed. The expanded plant was designed to produce an extra 30 MIGD freshwater where the total production would be 100 MIGD. Out of the total freshwater produced 37.5 MIGD was contributed by RO while the rest 62.5 MIGD water would be produced by MSF (Nishia, et al., 2020). According Awerbuch et al. (1989) the following points served as main reasons behind the establishment of MSF/RO hybrid desalination systems:

1. The cost of freshwater production from MSF/RO hybrid has been lower than either of the desalination columns.
2. RO counterpart in MSF/RO hybrid takes relatively less sea water intake compared to an independent RO plant.
3. The blending of produced waters from RO and MSF could be able to produce water with a desirable quality. However, as MSF is known to produce water with more than portable standards the water quality from RO is generally manipulated.
4. Instead of using multiple RO processes together an MSF/RO hybrid desalination could use a single stage RO process. In addition, the membrane life could also be improved.
5. The total power consumption could be optimised by using the electric power production from MSF plant to run RO plant.
6. The addition of RO produced water with the water MSF could reduce the temperature of MSF reduced water.

Supporting these arguments there have been numerous studies conducted, where a considerable amount of improvement in the functionality of individual desalination columns has been achieved in the hybrid desalination column. As reported by Hamed (2005) when used the reject sea water from MSF as feed for the RO process, the overall productivity of RO was observed to have increased. Supporting this statement, it was observed that a one degree rise in feed water temperature would result in three degree rise in the total freshwater production from RO. As per the observations of (El-Sayed, et al., 1998) an improvement of approximately 45% was observed in the final freshwater production from RO when the temperature of feed water raised from 15°C to 33°CFrom the perspective of power consumption a total reduction of 42% in the power consumption was observed for MSF/RO hybrid system compared to either of the individual systems. Amongst the studies done upon MSF/RO hybrid desalination plants with one of them being the pre-treatment process for the other one, the study done by Cardona et al.

(2002) can be discussed. They proposed a model where the seawater-reject from RO would be fed to the MSF desalination system, aiming at improving the overall water productivity of the system. In another study done by Mishra et al. (1999) an improvement of overall water productivity for the combination of MSF/RO was observed. They have proposed a model where the blow down brine water from MSF would be fed into the RO process. Despite having higher salt concentrations in the feed water, its higher temperature was observed to have compensated the productivity issues of RO.

An extensive economic analysis of MSF/RO hybrid desalination by considering multiple configurations of the plant was done by Helal et al. (2003). They claimed a model consisting of RO having the feed from the mixture of seawater and brine water rejects of MSF to be comparatively more economical with the water production cost 13% less than the independent RO process. In their further study they have examined the water cost from the perspective of MSF desalination system (Helal, et al., 2004). They have proposed seven models with the major differentiating factor being the blow down water intake of the individual desalination processes in the hybrid. They proposed to improve MSF desalination system by utilizing the membrane reject water from RO process into the heat recovery section of MSF which decreased the total water cost production by 17 to 24%.

Even Though, these studies have analysed various configurations of MSF/RO hybrid desalination columns from the perspective of water production economy they have failed to address the major issues associated with MSF desalination process: Lower performance ratio (the ratio of product water mass flow rate with the flow rate of steam in the brine heater) of MSF associated with fouling issues and Carbon emission. There have been a few studies upon the combination of Thermal-Thermal hybrid desalination columns involving MSF and MED (Multi effect Desalination).

From the economic analysis conducted by Nayfey et al. (2005), the hybrid of MED/MSF resulted in 9% less water production costs of MED while 31% water production costs of MSF. The simulation studies conducted by Zac and Mitsos (2014) involved the combination of MSF and MED with alternative vapor routing which resulted in higher performance ratio of the hybrid desalination system. However, this study did not address the issue of fouling in the condensed tubes. Hassan et al. (1997) addressed the issue of scale formation and proposed the concept of pre-treatment using nanofiltration process (NF). Through NF they have observed 37.3% reduction of total TDS (Total Dissolved Solids). In the studies conducted by Hamed et al. (2005), the combination of NF/MSF assured low Ca^{+2}, SO_4^{-2} concentration in the brine assuring no $CaSO_4$ scale formation even at higher top brine temperatures (TBT). They further analysed that this increase in top brine temperature from 100°C to 130°C improved the water production by 48%.

Another study by Al-Rawajfeh (2012) observed the formation of $CaSO_4$ precipitation in MSF desalination columns under various TBT conditions in the presence of NF. They have concluded that the TBT could reach to a value of 145°C with 50% of feed pre-treatment by NF whereas this value could reach to 175°C with 100% feed pre-treatment before $CaSO_4$ precipitation occurs. When used FO process with the 40% recovery ratio whereas the product of FO would be used to dilute the coolant water flowing into the heat recovery section of MSF assured no $CaSO_4$ scale formation until the TBT upto 135°C (Darwish, et al., 2016).

The efficiency of Tri hybrid water desalination plant from the perspective of water recovery by suppressing $CaSO_4$ scale formation was studied by Hamed et al. (2009). They proposed a design where the product of NF is fed to RO while the product of Ro is fed to the feed of MSF heat rejection section. They have observed that the MSF could be operated upto 130°C of TBT without forming any $CaSO_4$ scale. As these hybrids were focussed upon MSF desalination

columns operating at high TBT conditions, they have focussed on the types of scales MSF was the most vulnerable to ($CaSO_4$). This made them ignore the other types of scale formations such as $CaCO_3$ and $Mg(OH)_2$, which were the most common types of scales under lower TBT conditions (Alsadaie and Mujtaba, 2017). Even Though, this study was focussed on CO_2 release from MSF condensers its main focus was upon the heat transfer efficiency, whereby he has not covered the CO_2 release during the brine heating process. From the perspective of $CaCO_3$ scale formation Altaee et al. (2013) examine the efficiency of Forward Osmosis (FO) process in lowering the scale thickness. A 47% reduction in scale thickness was found in their studies when used 32% of FO recovery.

Addressing the CO_2 release from MSF distillers Al-Rawajfeh (2016) associated NF to MSF desalination. Where he has observed 100% decrease in CO_2 release in the MSF-OT (Once Through) and MSF-BR (Brine Recycle) condensers as well as the heat transfer resistance was decreased by 100%. There have been numerous other studies found in the literature involving either NF or FO pre-treatment processes to improve the performance of MSF desalination process which yielded similar results (Barba et al., 1982; Hassan, et al., 1999; Hilal et al., 2004; Llenas et al., 2013; Ayoub et al., 2014; Roy et l., 2017; Abdelkader et al., 2018).

However, as per numerous studies, neither NF nor FO processes were resilient towards scale formation as these processes use membranes and the temperatures these processes were operated on would allow scale formation (Lee et al., 1999; Lee and Lee, 2000; Lin et al., 2006; Xu et al., 2010; Gwak and Hong, 2017; Choy et al., 2018; Kim et al., 2018). Hence, for the application of both CO_2 capture as well as scale formation hydrate formation was proposed in this study, which is more resilient towards scale formation.

2.3. Chemical scale inhibitors

Generally, two types of chemicals have been used in different distillers to curb the issues related to scale formation (Ghani & Al-Deffeeri, 2010):

- Supporting the depletion of carbonate ions in seawater by using acid (generally H_2SO_4), which is known with the name acid treatment.
- By using ant agglomerating agents, where the undissolved substances are encouraged to rather suspend in the stream than precipitating onto the heat-transfer surface. It is generally called treatment through chemical additives.
- The combination of the two where the carbonates are partially dissociated and the undissolved solids would suspend in the water stream, which is called hybrid treatment method.

During the acid treatment process, Sulphuric acid is added to the water flow into the MSF condensers, where the acid is added up to the concentrations of 120ppm. For H_2SO_4 being an extensively a corrosive material, the addition of it would require highest attention so that its quantity would not exceed the requirement (Elliot, 1969). After the addition of adequate quantities of H_2SO_4, the resultant water would have a pH of 7.5. Especially these anti-agglomerating agents which would suppress the homogeneous nucleation for the scale formations that were highly used for commercial purposes are polyphosphates or triphosphates, lignin sulphonic acid derivatives and antifoaming agents. Polyphosphates suppress the deposition of the unsaturated $CaCO_3$ particles onto the heat transfer surface when added with concentrations 1-2ppm (Elliot, 1969). Generally, the lignin derivatives are surface active agents that are anionic in nature which would support the scaling particles to be dispersed throughout the flowing stream. One of the most common challenges found in using the polyphosphate based anti-scaling substance is the thermal degradation when the plant is operated at a temperature of above 100^oC, where the degradation would be doubled upon the rise of every

6ºC temperature. The issue would affect the entire functioning of MSF by forming less polymerised material, when occurred and the solution could be expensive (Suslick, 1998). In addition, there have been many other anti-scalants were introduced to the desalination industry addressing the scaling issues such as Organophosphates, ATMP, HEDP, PBTC and Organo electrolytes. Amongst these, the current market has been dominated by Organophosphates (MarketsandMarkets, 2020). At the same time, for being non-biodegradable, the phosphorous based anti-scaling substances could cause eutrophication issues, where the usage of these chemicals have been regulated and the permissible levels of usage have been persistently decreasing annually (Hasson, et al., 2011; Feiner, et al., 2015). As suggested by Popov et al., (2016) amongst all green anti-scalants, PMA (Polymaleates), PASP (Polyasparates), PESA (Polyepoxysuccinates) along with other copolymers with PA, such as PAAS (Poly Acrylic acid), PASP (Poly aspartic acid sodium salt), have been claimed to have more industrial prospects. Even though, there have been numerous comparative analysis over these green inhibitors, due to the conflicting results over the order of their efficacies, their industrial applications have not been industrialised (Ali, et al., 2015; Wang, et al., 2015; Wang, et al., 2015.; Zhao, et al., 2016). The conflicts might have been caused by various contradicting experimental conditions by taking brines of different chemical compositions (Popov, et al., 2016). This requires an extensive analysis over the efficacies of these green anti-scalants under a wide range of operational conditions with various chemical compositions of brine.

2.4. Gas hydrates

Gas hydrates are ice-like crystalline compounds that are both triggered by as well as trap the dissolved gas molecules which are chemically influenced by the water-gas inter-molecular van der Waal's forces of attraction, into their cages. Hydrates are generally formed under high pressure and low temperature conditions. They have been first discovered by Sir Humphry Davy and remained a scientific curiosity for the laboratory analysis for decades until they were

found to be the culprits of plug formation in the under-sea natural gas pipelines (Hammerschmidt, 1934). Due to the industrial revolution led by fossil fuels, the issues related to plug formation carried the research into discovering various methods to depress hydrate formation in the pipelines through establishing methods for the calculation of hydrate-water phase equilibrium under various thermodynamic conditions. These methods included the efficiency analysis of various hydrate inhibitors as well as the insulation of undersea natural gas pipelines using phase-change materials (Anderson & Prausnitz, 1986; Sloan, et al., 1998; Ballard & Sloan, 2002; Sa, et al., 2013; Parsazadeh & Duan, 2016).

Even though, gas hydrates were studied from the perspective of flow assurance in the oil and gas industry, currently the formation is regarded as the potential solution for various global challenges. Apart from desalination and carbon capture, the hydrate formation as a process possesses of potential for various industrial applications such as natural gas and hydrogen storage and transportation, flow assurance, district and data centre cooling and the separation of temperature sensitive hydrate forming liquids (Hand, et al., 1974; Chatti, et al., 2005; Eslamimanesh, et al., 2012; Babu, et al., 2015; Yin, et al., 2018). It was mentioned in the studies conducted by Javanmardi and Moshfeghian (2003), corrosion in water desalination plants is directly proportional to temperature, which gave an advantage to the desalination processes with operational temperatures low such as hydrate formation and hence attracted major research attention (Javanmardi & Moshfeghian, 2003). As the current study mainly focusses upon the gas hydrate formation for the application of carbon capture and desalination, the articles related to these purposes were highlighted in this chapter.

Numerous studies have been cited in literature addressing carbon capture from various gaseous mixtures produced from combustion, pre-combustion as well as polluted ores through hydrate formation (Hand, et al., 1974; Gayet, et al., 2005; Li, et al., 2010; Li, et al., 2011; Kolev, 2011; Kumar, et al., 2013; Fosbøl, 2017; Li, et al., 2017). From various studies, with an operational

cost of $8.75 per ton of captured CO_2, hydrate-based gas separation has been proven to be very economical when compared to both absorption and membrane ultra-filtration with operational costs $30-$60 and $50-$78 respectively (Li, et al., 2011; Li, et al., 2017).

From the perspective of desalination, gas-based hydrate formation could be considered under freeze desalination technique where the desalinated water can be recovered from a series of steps such as gas hydrate formation, washing of hydrates and the dissociation. Hydrate formation comes with an advantage of being operated under less corrosive temperature conditions while a disadvantage of requiring high operational pressure. If involved either pre-combustion or post-combustion gas mixture to form hydrate formation in the saline water, the process could lead to both desalination as well as carbon capture, however, high compressions are needed (Babu, et al., 2018). Various articles provided salt removal efficiencies ranging from 60-80% in the first stage, while further improvement in the salt removal efficiencies were observed up to 97% (Park, et al., 2011; Kang, et al., 2014). Numerous studies as well as review studies mentioned the results and analysis of hydrate formation in the presence of different guest gases (Max & Pellenbarg, 1999; Aliev, et al., 2008; Park, et al., 2011; Kang, et al., 2014; Babu, et al., 2018), kinetic as well as thermodynamic additives (Zhong & Rogers, 2000; Torré, et al., 2011; Roosta, et al., 2013; Xu & Li, 2014; Babu, et al., 2015) and physical interventions such as stirring, porous media, nano-particles, hydrogels, dry water and dry gels (Seo, et al., 2005; Carter, et al., 2009; Linga, et al., 2009; Pasieka, et al., 2013). However, most of these studies aimed at desalination work with a single gas as hydrate former.

Towards the development of a combinatorial process to simultaneously capture CO_2 as well desalination, Babu et al. (2018), in their study discussed the timelines and pilot plants of hydrate formation by sending CO_2 to the seabed where CO_2 would be captured as hydrate without the requirement of excess compression. However, the transportation of CO_2 to the seabed was found to be expensive (Lee, et al., 2016; Babu, et al., 2018). Addressing the

requirements of high pressure, SF6 and HFC-forming hydrates were cited to be used in studies without requiring higher operational pressures. However, their low availability in nature as well as industrial gaseous emissions make limit their preference for hydrate-based desalination. Additionally, HFCs and CFCs were proven to be environmentally unsustainable as well as harmful and hence encouraging their production in the name of desalination process would result in various environmental concerns (de Chazournes, 1998; Lee, et al., 2016). Through their review on the experimental apparatus design for hydrate formation for various purposes, Linga and Clarke (2016) expressed their concern over the cost of stirring, separation of hydrate from the porous media (Linga & Clarke, 2016).

Despite the proof of concept for these applications was demonstrated by the hydrate formation, its industrial application has still been highly restricted because of technological issues associated with it (Duc, et al., 2007; Li, et al., 2010; Nohra, et al., 2012; Fosbøl, 2017). These technological challenges were sparse amongst the factors such as the higher sensitivity of hydrate formation towards the thermodynamic conditions such as pressure and temperature, low yields of resultant hydrates, and also the requirement of higher driving forces contributing to less economy of the process. In order to address these issues, the mechanism of hydrate formation was supposed to be understood both the thermodynamics as well as the kinetics (Englezos, 1993; Sloan, 2003; Sloan, 2005; Khurana, et al., 2019). However, researchers starting from Ribeiro Jr and Lage (2008) to Khurana et al (2019) pointed out the requirement of the efficient models to understand the initiation as well as the progress of hydrate formation. Generally, the hydrate formation as a process is generally dealt in two stages: nucleation and crystal growth (Ribeiro Jr & Lage, 2008).

2.4.1. Nucleation

As explained by Ribeiro Jr and Lage (2008), hydrate formation is the process of phase change where the supersaturation initiates the process as shown in the equation 2.1.

$$G + n_w H_2O \rightleftharpoons G.n_w H_2O \quad 2.1$$

Prior to hydrate formation, the hydrate forming gas has to be dissolved into water under the hydrate forming conditions making itself available to trigger the phase change.

2.4.2. Classical nucleation theory

The entire process of hydrate nucleation mechanisms was first founded by utilising the pre-existing Classical Nucleation Theory. The theory was initially proposed to explain the mechanism of liquid condensation and later modified for the application into the fields such as crystallization (Volmer & Weber, 1926; Becker & Dö ring, 1935). According to the theory, for the hydrate formation to take place, the Helmholtz free energy of the dissolved gas should be higher to the Helmholtz free energy of the hydrate. The entire process could be hindered by the resistance provided by the formation of an interface, which is also termed as the superficial energy as shown in the equation 2.2. This is due to the molecules at the interface exhibit higher free energy than both the liquid as well as the hydrate phases. The hydrate formation process would only become spontaneous under the conditions where the total Gibb's free energy change of the hydrate formation process would become zero.

$$\Delta G_H = (H_G - H_H) + \Delta G_{int} \quad 2.2$$

The Gibbs free energy change of the hydrate formation is dependent upon the volume of the cluster which would be the cube of the radius, while the resistance is positively influenced by the surface area, which would be directed by the square of the radius (Sear, 2007). At the initiation of the hydrate formation, the volume factor of the hydrate cluster would be overshadowed by the surface area counterparts. This would cause the formed hydrate clusters

to dissociate due to the greater resistance provided by the molecules in the cluster's surface. However, under the provision of sufficient driving force, which would be more than the driving force to maintain hydrate-water equilibrium conditions, the phase shift would occur towards the higher hydrate fractions in the system. As the hydrate forms, with the size of the hydrate crystals, the volume factor of the hydrate would increase, dominating the resistance provided by the surface area term after the size of the crystal reaching a specific radius value, which is called the critical radius. At the critical radius, the Gibb's free energy change of the hydrate formation process would become zero under the given operating conditions. Under the conditions where the radius of the hydrate crystal is higher than the critical radius, the hydrate formation process is spontaneous. Even though, numerous hydrate formation mechanisms were proposed based on the classical nucleation theory, treating hydrate formation merely as a chemical process has its own drawbacks (Vysniauskas & Bishnoi, 1983; Sloan, 2003a). Those drawbacks could be surfaced while calculating excess free energy and the critical radius and also, the consideration of hydrate formation as a macroscopic process could lead to errors in determining the exact hydrate structures (Thompson, et al., 1984; Khurana, et al., 2017).

2.4.3. Nucleation site

In a system having no impurities in the liquid suspension, the hydrate formation, hypothetically occurs in the liquid bulk, which is called homogeneous nucleation. However, in the presence of any surface, this nucleation would occur along the surface and is called Heterogeneous nucleation. In the presence of a surface, the work required for the formation of hydrate in creating a new surface would be decreased, making the hydrate formation process spontaneous under lower driving force conditions. In the presence of a surface to form the hydrates, a lower critical radius size was observed. The value of critical radius is governed by the contact angle between the hydrate and the surface it occurs (Kashchiev & Firoozabadi, 2002a; Kashchiev & Firoozabadi, 2002b).

The occurrence and propagation of hydrate nucleation would also be governed by the solubility of the hydrate forming gas. There used to be an assumption that the gas that is relatively low soluble initiates hydrate nucleation at the has-liquid-wall interface while the gas that has higher solubility would initiate hydrate formation along the reactor walls. To validate these statements, Long and Sloan (1996) conducted hydrate formation experiments in the presence of CO_2 and CH_4 in a 1cc cell under the quiescent conditions. Contrary to the premise, the nucleation of both the gases were observed to be occurring at the gas-liquid interface at the wall. The same observation was consolidated by Takeya et al (2000), who observed the nucleation through a high-speed video camera. Even though the hydrate nucleation occurred at the gas-liquid interface at the wall irrespective of the solubility of the hydrate forming gas, the propagation of the hydrate was along the gas-liquid interface for the low soluble gas, while it was along the wall for the higher soluble gas (Long & Sloan, 1996; Takeya, et al., 2000).

The same observations were made for various gases such as ethane, propane, dichlorofluoroethane and their combinations in water and SDS solutions and observed the same (Lin, et al., 2004; Li, et al., 2005; Gayet, et al., 2005; Lee, et al., 2005; Hussain, et al., 2006). However, in the presence of stirring, the hydrate nucleation of ethane and methane were observed to have occurred everywhere in the reactor (Englezos, et al., 1987). Nevertheless, it was later explained that the hydrate clusters that were observed suspended in the bulk were originally nucleated at the gas-liquid interface and dispersed within the liquid due to the stirring (Sloan Jr, 2007).

2.4.4. Induction time

Induction time as a term has numerous interpretations. Even though, they all have focussed upon the time gap between the system reaching hydrate operational conditions and the observable hydrate formation, while measuring the induction times from various perspectives and various detection techniques the definition of induction time changes accordingly.

Theoretically, induction time is the time taken for the hydrate nucleation to become spontaneous. From the modelling perspective, induction time could either be the time taken for the first hydrate nucleus to achieve the critical radius for the given operational conditions (Ribeiro Jr & Lage, 2008) or for the system to achieve a particular hydrate volume fraction (Kashchiev & Firoozabadi, 2003). From the experimental perspective, the term could be either the time taken for the system to exhibit an exponential gas consumption in an isobaric system or exponential pressure reduction in an isochoric system (Thoutam, et al., 2019). It can also be the time at which the system experiences a temperature rise due to the exponential hydrate formation (Thoutam, et al., 2019; Chen, et al., 2020) or the time at which the intensity of projected light through the hydrate forming liquid starts to reduce (Parent & Bishnoi, 1996; Wilson & Haymet, 2010) or the viscosity of the liquid starts to increase (Zheng, et al., 2017).

Amongst the earlier studies that first discovered the foundation of induction time, one has to mention the study of noble gas hydrate formation conducted by Barrer and Ruzicka (1962). They have observed that the experiment did not result in hydrate formation despite providing adequate conditions for hydrate equilibrium. The similar observation was mentioned in the studies of Maini and Bishnoi (1981), who experimented on methane hydrate formation (Barrer & Ruzicka, 1962; Maini & Bishnoi, 1981).

However, the induction time was first discovered by Barrer and Edge (1967), where they observed a time gap of one hour for the crypton hydrate to form from the ice (Barrer & Edge, 1967). The similar observation was done by Falabella (1975), who observed a similar induction time for the hydrates of the gas mixture methane and crypton (Falabella, 1975). Ever since the discovery of induction time as a concept it has been the focus of debate for many researchers starting from its existence, causes till its measurement. Various proposals were made such as structural oscillation theory proposed by Sloan and Fleyfel (1991) where the induction time was resulted by the oscillation in between two structures of hydrate under the influence of two

gases in the considered gas mixture (Sloan & Fleyfel, 1991). They also continued to verify their observations by producing zero induction time for the cyclopentane hydrate formation. However, their theory was proven wrong by Skoveborgh et. al., (1993), who measured the induction times for the hydrate systems having pure gas mixtures of methane and ethane in a stirred tank reactor (Skovborg, et al., 1993). They continued by explaining the driving forces provided by thermodynamic factors such as pressure and temperature as well as physical factors such as stirring speed are important for a system to demonstrate a particular induction time value alongside the chemical composition of the system.

Along with the aforementioned factors, researchers also discovered that the thermal history of water would also play an important role in the system's choice of induction time value. The research done by Vysniauskas and Bisnoy (1983) resulted in a lower induction time value for dissociated hydrate and also dissociated ice when compared to the hydrate formation in the tap water. They explained that the ordered and rigid microstructures of water in dissociated water and ice serve as templates for the hydrate formation making the process easier and faster (Vysniauskas & Bishnoi, 1983). This has been termed as the memory effect of water. The similar observations were done by Giavarini et. al., (2003), who produced propane hydrates from melting ice as well as liquid water (Giavarini, et al., 2003). However, they observed no change in the kinetics of hydrate growth (Vysniauskas & Bishnoi, 1983; Linga, et al., 2007; Parent & Bishnoi, 1996). Following research numerous other authors acknowledged the influence of water thermal history upon hydrate nucleation (Schroeter, et al., 1983; Monfort & Nzihou, 1993; Moudrakovski, et al., 2001; Link, et al., 2003; Servio & Englezos, 2003; Lee, et al., 2005a; Lee, et al., 2005b; Lee & Englezos, 2006; Oshima, et al., 2010; Ripmeester & Alavi, 2016)(7-19). Contrary to the hypothesis of memory effect Buchanan et. al., (2005) through his neutron diffraction experiments found that the structure of water exhibits no difference before methane hydrate formation and after its decomposition (Buchanan, et al., 2005). Supporting

their conclusions Wilson and Haymet (2010) observed no significant difference in the induction times in their repetitive THF hydrate formation and dissociation experiments through the cycles of super cooling and heating. They also suggested that the induction times for stochastic irrespective of the thermal history of the water. Along with these disputes the major dispute has been associated with the stochastic nature of hydrate nucleation. In determining the induction time, one of the earliest attempts to determine the induction time was done by Natarajan et. al., (1994), they proposed an equation to determine the induction times of carbon dioxide, ethane and methane in a stirred tank reactor (Natarajan, et al., 1994). Their time of nucleation was dependent upon the fugacity of the gas and hydrates along with the parameters addressing the nature of gas and the equation is mentioned in equation 2.3.

$$t_{ind} = K_{gas}\left(\frac{f_{i,gas}(T_{op},P_{op})}{f_{i,H}(T_{op},P_{eq})} - 1\right)^{-m_{gas}} \quad 2.3$$

Where t_{ind} is the induction time, $f_{i,gas}$ is the fugacity of the gas under the operational conditions and $f_{i,H}$ is the fugacity of the hydrate under the hydrate equilibrium conditions while K_{gas} and m_{gas} are the attributes of the hydrate forming gas and are empirical quantities. Even though equation 2.3 was able to represent the experimental data, under the conditions where the driving force hydrate nucleation was low equation 2.3 was observed to be deviating profoundly. Similar observation was made by numerous authors which propelled them to the conclusion that the hydrate nucleation is stochastic, especially under the conditions of low driving force (Servio & Englezos, 2003; Lee, et al., 2005b; Lee, et al., 2007; Mali, et al., 2018). The driving force of the nucleation was taken as shown in the equation 2.4.

$$Driving\ force\ = \left(\frac{f_{i,g}}{f_{i,H}} - 1\right) \quad 2.4$$

Although the apparent driving force of the hydrate formation was taken to be based on the fugacity, as the fugacity is highly dependent upon the operational pressure, the physical

interpretation of the equation 2.4 could be addressed by the difference of operational pressure and the hydrate equilibrium pressure. Apart from the consideration of fugacity as the driving force of hydrate nucleation, numerous authors considered the temperature difference between the operational conditions and the hydrate-water equilibrium conditions as their driving force (Knox, et al., 1961; Pangborn & Barduhn, 1970; Ganji, et al., 2006).

A year before the proposal of induction time for the hydrate nucleation by Natarajan et. al., (1994) by means of their driving force based on fugacity another author came up with the concept of driving force based on the chemical potential of the system. In 1993, Skovborg et. al. proposed their driving force to be chemical potential difference between water and the liquid and the hydrate under the given operational pressure and temperature conditions. They continued their research by comparing the driving force with the experimentally obtained values of induction time and concluded that the observed induction times were large under low driving forces (< -80 J/mol).

Transforming the calculation of driving force to a more generic approach Sloan (1998) proposed his driving force to be based on the Gibb's free energy change of hydrate formation in the system. Although the fundamental expression was proposed by Sloan (1998), it was Kashchiev and Firoozabadi (2002a) that expanded the equation through an extensive thermodynamic analysis. According to Kashchiev and Firoozabadi (2002a) the supersaturation (driving force) of the system is given by the difference between the chemical potential of the individual phase prior to hydrate formation (water and gas) and the chemical potential of the resultant hydrate. And the corresponding equation was shown in Equation 2.5.

$$\Delta\mu = \mu_{Gs} + n_w\mu_w - \mu_H \qquad 2.5$$

Where $\Delta\mu$ is the chemical potential difference (driving force), n_w is the number of water molecules participated in the nucleus formation, μ_w is the chemical potential of water and μ_H

is the chemical potential of the hydrate. Along with the driving force, Kashchiev (2000) proposed the work done by the system during the formation of hydrate as the energy barrier, which was presented as the equation 2.6 (Kashchiev, 2000).

$$W(n) = -n\Delta\mu + G_{ex} \quad 2.6$$

Where the excessive free energy of the dissolved gas and the free water combined was represented by G_{ex}. The workdone would reach to its maximum value under the formation of a successful hydrate nucleus which was represented by W* and the number of building units when the system exhibited the workdone W* is represented by n*. The equations to calculate W* and n* are represented by 2.7 and 2.8.

$$W^* = 4C^3{v_h}^2{\sigma_{ef}}^3/27\Delta\mu^2 \quad 2.7$$

$$n^* = 8C^3{v_h}^2{\sigma_{ef}}^3/27\Delta\mu^3 \quad 2.8$$

By taking the chemical potential of gas as a function of reference chemical potential, activity and the concentration the chemical potential of the gas has been expanded and used in the equation 2.5 to produce the equation 2.6.

$$\Delta\mu = {\mu^R}_{Gs} + kTln(\gamma v_w C) + n_w\mu_w - \mu_H \quad 2.10$$

Where v_wC is the mole fraction and ${\mu^R}_G$represents the reference chemical potential of the dissolved gas. Generally, the chemical potential of the gas in the gas phase should be equal to the chemical potential of the gas dissolved in the liquid phase. By substituting the reference chemical potential of the gas by the chemical potential of the gas in the gas phase in the equation 2.11 along with a few adjustments, the supersaturation could be transformed into the equation 2.11.

$$\Delta\mu = {\mu^R}_{GG} + kTln(\chi v_w C) + n_w\mu_w - \mu_H \quad 2.11$$

After the application of isothermal conditions into the equation 2.11 along with a few adjustments, the potential difference of the system could be transformed into the equation 2.12 which is shown as follows.

$$\Delta\mu = kT\ln\left[\frac{\emptyset_P P}{\emptyset_{P_e} P_e}\right] + \Delta v_{eq}(P - P_{eq}) \quad 2.12$$

Where $$\Delta v_{eq} = (n_w v_w - v_H)\Big|_{P_{eq},T} \quad 2.13$$

By considering n_w to be independent of temperature, by incorporating hydrate dissociation per building unit along with the application of Taylor's expansion, under Isobaric conditions, the chemical potential difference equation would be transformed into the equation 2.14.

$$\Delta\mu = \Delta s_H^d \Big|_{T_{eq},P}(T_{eq} - T) \quad 2.14$$

Generally, the hydrate formation experiments are either carried out in isochoric or isobaric conditions, whereas the temperature is kept constant in either of them (Linga & Clarke, 2017). However, considering the exothermic nature of the hydrate formation, it would be more appropriate to acknowledge the temperature fluctuations during the hydrate growth stage with respect to the kinetics of hydrate formation in the system (Liu, et al., 2011). The equations 2.12 and 2.13 were used in this study to calculate various parameters of nucleation such as rate (equation 3.16), induction time (equation 3,24) and the hydrate volume fraction (equation 3.26).

As an extension to their work on nucleation model, using the supersaturation equations proposed in their previous studies (equation 2.12 and 2.13), Kashchiev and Firoozabadi proposed various equations to calculate the induction times of the methane hydrate formations systems (Kashchiev & Firoozabadi, 2003). The following equations (equation 2.15, 2.16, 2.17) represent the inductions times under various physical conditions.

For Instantaneous nucleation

$$t_{nuc} = K_{nuc}[e^{\left(\frac{\Delta\mu}{kT}\right)} - 1]^{-1} \quad 2.15$$

For Isothermal progressive nucleation

$$t_{nuc} = K_{nuc}e^{\frac{-\Delta\mu}{kT}}(1 - e^{\frac{-\Delta\mu}{kT}})^{\frac{-3m}{(1+3m)}}e^{\left(\frac{-W}{(1+3m)kT}\right)} \quad 2.16$$

For Isobaric progressive nucleation

$$t_{nuc} = K_{nuc}e^{\frac{-\Delta s_e \Delta T}{kT}}(1 - e^{\frac{-\Delta s_e \Delta T}{kT}})^{\frac{-3m}{(1+3m)}}e^{\left(\frac{-W}{(1+3m)kT}\left(\frac{\Delta\mu}{\Delta s_e \Delta T}\right)^2\right)} \quad 2.17$$

Where m is the exponent in the power law equation of crystal growth, while K is the kinetic constant which is defined as follows for volume and surface polynuclear mechanisms.

Homogeneous Nucleation

$$K_{nuc} = \left[\frac{(1+3m)\alpha_d}{bQ^{3m}A}\right]^{\frac{1}{1+3m}} \quad 2.18$$

Heterogeneous nucleation

$$K_{nuc} = \left[\frac{(1+3m)\alpha_d V_s}{bA_s Q^{3m} A}\right]^{\frac{1}{1+3m}} \quad 2.19$$

Ribeiro and Lage (2008), in their review of the current status and future directions of hydrate formation, they have expressed their concern of some parameters of hydrate nucleation being empirical. Especially, the hydrate volume fraction of the system at the induction time was not mentioned in their study. This is because, the authors considered their induction time to be perceived by the temporal evolution of the light intensity passed through the hydrate forming solution under the operational conditions, which was based on the experiments conducted by Natarajan (Natarajan, 1993; Natarajan, et al., 1994). However, the main drawback was not mentioning the hydrate volume fraction at the induction time, which was proven to be variable with varying operational pressure and temperature conditions. If considered the induction time

proposed by Kashchiev and Firoozabadi (2003), one would calculate the time taken for the system to attain a certain hydrate volume fraction, which might not represent the actual induction time of the system. Hence, the induction time was derived in this study, which was explained in the chapter 3.

Additionally, as Kashchiev and Firoozabadi's model is highly dependent upon the available dissolved gas and the gas fugacity in the aqueous system, they have chosen rather obsolete techniques to calculate these parameters. In their study, they used Henry's and Peng-Robinson (PR) models to calculate the extent of gas dissolution as well as gas fugacity respectively (Robinson, et al., 1985; Kashchiev & Firoozabadi, 2002a). However, numerous studies were evolved successively proposing methodologies to accurately measure the gas dissolution and fugacity under a wide range of operational conditions (Henry, 1803; Raoult, 1887; Michels, 1936; Wiebe & Gaddy, 1939; Blanco C & Smith, 1978; King, et al., 1992). When compared the generic studies with the gas specific models, the accuracy was estimated to be higher in the gas specific models. The fugacity and gas dissolution correlations were semi-empirical and fitted in such a way that they were able to accurately measure the system properties for a wide range of operational conditions (Duan, et al., 1992; Duan & Sun, 2003; Duan & Mao, 2006a; Duan, et al., 2006b). However, to understand how these gas specific and generic models would influence the dissolution and fugacity by influencing their respective internal parameters, they had to be applied into the Kashchiev and Firoozabadi nucleation model under a wide range of operational conditions representing both hydrate favourable and unfavourable conditions.

2.5. Role of chemical promotors

2.5.1. Kinetic additives

Experimentally, Induction time was observed to be influenced (reduced) by various physical, thermodynamic as well as chemical factors. Thermodynamic factors could directly influence the driving force of hydrate formation by either increasing the pressure or decreasing the

temperature. The increase in the reactor volume was observed to have reduced the variability of induction time (McCallum, et al., 2007). In order to influence the system in resulting either higher hydrate formation kinetics or yields, various researchers utilised a variety of chemical components, which are majorly identified as either kinetic additives or thermodynamic additives. Kinetic additives do not influence the required operational conditions such as temperature and pressure of the system, but improve the kinetics of the system whereas, thermodynamic additives influence hydrate equilibrium conditions.

Surfactants have been widely used in the literature as kinetic additives to improve the kinetics of hydrate formation under the considered operational conditions. Surfactants are amphiphilic compounds consisting of a hydrophilic head and a hydrophobic tail and are mainly used to decrease the interfacial tension at various surfaces. Based on the charge of hydrophilic end of the surfactant, they are classified into three major groups namely cationic, anionic and non-ionic surfactants. For having dual centres present in their molecular structure, surfactants contribute to various effects at gas-liquid, solid-liquid and liquid-hydrate interfaces (Khurana, et al., 2017). In 2007, various surfactants with respect to the carbon chain length and their effect over the hydrate formation kinetics were observed by Daimaru et al. According to them, the hydrate formation kinetics were inversely related to the length of the carbon chain (Daimaru, et al., 2007). Kumar et al (2015) compiled hydrate nucleation and the growth data of various hydrates in the presence of a wide range of surfactants (Kumar, et al., 2015). The similar observation was made by numerous other authors making SDS the most effective as well as well-researched surfactant for the suppression of hydrate induction time (Han, et al., 2002; Link, et al., 2003; Zhang, et al., 2007; Yoslim, et al., 2010; Kang & Lee, 2010; Zhong & Rogers, 2000) (Zhang, et al., 2007; Yoslim, et al., 2010).

When it comes to the mechanism of surfactant influence over the hydrate nucleation, Kalogerakis et al. (1993) observed a considerable reduction in liquid side mass transfer

coefficient, supporting the diffusion of dissolved gas into the hydrate nucleation sites. They further observed that the anionic surfactants were significantly effective for the use of hydrate promotion than non-ionic surfactants (Kalogerakis, et al., 1993). Karaaslan and Parlaktuna (2000) considered anionic, cationic and non-ionic surfactants as kinetic promotors for the formation of natural gas hydrates, where they observed that anionic surfactants were effective in reducing the induction time in all the concentrations whereas cationic surfactants were effective in only lower concentrations (Karaaslan & Parlaktuna, 2000). When considered the CO_2 hydrate nucleation, anionic surfactants, especially SDS was proven to be more effective in both suppressing the induction time as well as improving the hydrate formation kinetics, which was followed by non-ionic surfactants (Tween 80) and then cationic surfactants (DTAC) (Kumar, et al., 2013). Even amongst the anionic surfactants such as STS and SHS, SDS was observed to be considerably more effective in reducing the induction time (Okutani, et al., 2008).

According to Yoshim et al., (2010) the addition of SDS (240-1000PPM) could increase the gas uptake up to 14 times to the quiescent conditions, in the system containing a gas mixture of propane and methane. When the system contained SDS with a concentration of 645 and 2200PPM, the drop in the system's pressure, which represents the yield of hydrate formation was observed to be at its maximum. The have further observed that the presence of SDS would change the morphology of the hydrate present at the gas-liquid interface from impervious to porous so that the gas dissolution process would not be obstructed by the hydrate at the has-liquid interface.

2.5.2. Thermodynamic additives

One of the major concerns with the hydrate formation in the presence of less hydrate forming gases is that the requirement of profoundly high-pressure conditions. It would make the hydrate formation for gas separation, especially carbon capture from the post combustion (15-

20% CO_2 + 80 - 85% (N_2+O_2+H_2)) and the precomputation gas mixture (40% CO_2 + 60% H_2), formation of hydrates in the presence of the gases such as CH_4, H_2, N_2, O_2 and noble gases. other. The addition of thermodynamic additives would reduce the induction time by changing the entire hydrate formation mechanism of the system. According to Reibero and Lage (2008), thermodynamic additives or the semi-clathrates would form the hydrates and occupy the larger cages while the dissolved gases occupy the smaller cages. The absence of the dissolved gas provides the liquid phase with the required capillary forces so that the gases would be absorbed into the liquid phase and then the hydrates (Ribeiro Jr & Lage, 2008). Unlike the kinetic additives, thermodynamic additives are generally used to either reduce the required pressure conditions for hydrate formation or to separate an easy hydrate forming gas under reduced pressure conditions (Dashti, 2015). Since the current study deals with the CO_2 capture, the effect of thermodynamic additives in capturing CO_2 have been discussed in this section.

Various thermodynamic additives have been used to promote hydrate formation as well as to reduce the induction time such as Tetrahydrofuran (THF), Tetra-n-butyl ammonium bromide (TBAB), Propane, Cyclopentane. Amongst these promoters, THF has been widely used for its efficiency (Dashti, 2015). To estimate the effect of THF, Tang et al (2013) experimented upon CO_2 gas separation from N_2 from the gas composition of 59mol% CO_2 and 41mol% of N_2 in an isochoric stirred tank reactor system in the presence of SDS. They observed that the presence of THF has greatly improved the hydrate formation by reducing the induction time as well as improving the gas loading into the liquid. The gas loading into the liquid was significantly high when taken 3mol% of THF while the minimum requirement of THF was observed to be 1mol% THF to observe the difference (Tang, et al., 2013).

Park et al. (2013) studied the effect of THF concentration in curbing the CO_2 from the pre-combustion gas mixture of 60%H_2 and 40% CO_2 in a stirred tank reactor. They varied THF concentrations from 1mol% till 10mol% to check the gas-liquid equilibrium pressure and the

stability of the hydrate and observed that the reduction in operational pressure did not occur beyond 5.6mol% THF concentration. However, at 5.6mol%, the hydrate equilibrium pressure was reduced from 8MPa to 0.5MPa (Park, et al., 2013). For a post combustion gas mixture, at 273.7K, the equilibrium hydrate pressure was observed to have reduced from 7.7MPa to 0.35MPa when conducted the hydrate formation experiments in a semi-batch stirred tank reactor with 1mol% THF and water system. When induced the gas mixture of 16.9mol% CO_2 + 83.1mol% N_2, at 8.5MPa and 273.7K, the induction time varied in between 5min to 10min (Linga, 2007). For a similar gas concentration, Linga et al, (2008), experimented upon CO_2 hydrate formation in the presence of 1mol% THF, where they observed an operational pressure reduction from 7.5MPa to 2.5MPa for the possible hydrate formation and the recovered CO_2 purity to be as high as 94%, which was also observed by Park et al. (2013) (Linga, et al., 2008; Park, et al., 2013).

However, in order to produce the hydrate with high purity, more than one cycle of hydrate formation might be required. According to Adeyemo et al (2010), the number of cycles required to produce CO_2 of purity 98% from the feed gas mixture of 17% CO_2 purity would be three cycles (Adeyemo, et al., 2010). There have been numerous other researchers that validated the efficiency of THF in supporting the hydrate formation with the feed mixture of low carbon concentrations by reducing the required operational pressure as well as induction time (Kang & Lee, 2000; Kang, et al., 2001; Lee, et al., 2010; Daraboina, et al., 2013; Yang, et al., 2017; Cai, et al., 2018; Xie, et al., 2019).

Due to its impacts at lower molar concentrations, Tetra-n-butyl ammonium bromide (TBAB) has also attracted the research attention in recent times. When attempted to separate CO_2 from the post combustion gas mixture (15% CO_2, 85% N_2), through hydrate formation in a stirred tank reactor, Balendria et al (2012) observed the reduction in equilibrium pressure of hydrate with the increase in TBAB concentration in the liquid (Belandria, et al., 2012a). The same

authors further observed that the hydrate equilibrium conditions were reduced from 10.1MPa at 275.2K to 1.57 MPa at 285.7K with the addition of 30wt% TBAB for the same post combustion gas mixture (Belandria, et al., 2012b). Similar reductions in gas hydrate equilibriums were detected by numerous other authors (Duc, 2007; Li, et al., 2010; Mohammadi, et al., 2013). For the carbon capture from the pre-combustion gas mixture (40% CO_2 and 60% H_2), Babu et al (2014) carried out hydrate formation experiments in the stirred tank vessel varying the TBAB concentrations from 0.1mol% to 3.0mol% and observed that the hydrate formation was supported by the low concentrations of TBAB while the addition of TBAB over 0.3mol% resulted in longer induction times (Babu, et al., 2014). Through their studies upon CO_2 recovery from the mixture of CO_2 and H_2, Kim et al (2011), concluded that the optimal concentration of TBAB to be 1mol% where the CO_2 recovery was observed to be 24% with the induction time of 25.53min whereas the induction time was reduced to 0.17 hour in the presence of 3mol% THF, which was in contrast with the observations made in Babu et al (2014) (Kim, et al., 2011). To check the extent of recovery of the CO_2 from the pre-combustion gas mixture through hydrate formation in the presence of 5wt% and 10wt% of TBAB, experiments were conducted by Gholinedzhad et al (2011). According to their observations, to achieve CO_2 purity with over 96% from 40%, a cycle of two hydrate formations in the presence of 10wt% of TBAB was required (Gholinezhad, et al., 2011).

Along with THF and TBAB, another sect of the researchers validated the efficiency of hydrate promoting characteristics of cyclopentane. Li et al (2012) observed an induction time as low as 15s for hydrate formation when used the pre-combustion gas mixture in the presence of 5vol% of cyclopentane (Li, et al., 2012). The similar observation was made by Zhang and Lee

(2008), where the induction time of CO_2 hydrate formation was less than 0.2hous and the entire process was completed within two hours (Zhang & Lee, 2009). However, at 3.06MPa, pure CO_2 does not require any thermodynamic additive to form hydrates with observable kinetics (Thoutam, et al., 2019). With the addition of 1.5vol%, the equilibrium pressure of hydrate formation in the presence of pre-combustion gas mixture has reduced from 5.3MPa to 1.3MPa. In addition, it took two hydrate formation cycles to produce high purity CO_2 (98%) from the feed composition of 40% CO_2 (Zhang, et al., 2009). However, there was no much experimentation was done with cyclopentane in hydrate formation having post-combustion gas mixture as feed (Dashti, 2015). Even though, propane gas a capacity of promoting hydrate formation by reducing hydrate equilibrium pressure, unlike the aforementioned thermodynamic promoters, propane is the gaseous additive (Kumar, et al., 2006; Babu, et al., 2013). Hence may not be economical to be used for the carbon capture process. THF and TBAB, propane forms sII hydrates at approximately 0.4MPa pressure and 275K temperature (Hendriks, et al., 1996; Giavarini, et al., 2003). Supporting their observations, the studies of Kumar et al (2009) showed that the addition of 2.5mol% of propane to the system reduced the required pressure for the system by 49% (Kumar, et al., 2009). In their study of hydrogen separation from the pre-combustion gas mixture of CO_2+H_2, using 2.5mol% of propane, Kumar et al (2009) observed that 57% of the hydrate large cages were occupied by CO_2. Even though, most of the studies observed sII type of CO_2 hydrate formation in the presence of propane, later it was understood that the probability of sII hydrate formation was inversely proportional to the concentration of CO_2 in the feed (Babu, et al., 2013). There have been a few studies were found that examined the efficiency of other thermodynamic additives such as $TBANO_3$, TBPB (Li, et al., 2012). Even though, thermodynamic additives could improve the extent of hydrate formation by lowering the hydrate equilibrium pressure and the induction times, the carbon loading of hydrates in the presence of these additives were found to be not

as much as the extent of hydrate formation as compared to the quiescent systems. This may restrict the applicability if hydrate formation in the presence of thermodynamic additives from the carbon capture applications. When induced the thermodynamic additive into the hydrate forming solutions, the additive would be in competition with the gas in occupying the cages, as well as, not all the cages are filled with the gas when accelerated hydrate formation was observed in the presence of thermodynamic additives (Kang & Lee, 2000; Kumar, et al., 2009; Dashti, 2015). Hence, as an attempt to improve the gas absorption into the liquid as well as to promote the selective separation of the gases during the hydrate formation tertiary amines were added to the liquid phase in this study which will be discussed in chapter 5. As the thermodynamic additives participate in the hydrate formation, the resultant hydrate contains the substrate, which requires another distillation process for their elimination from the dissociated hydrate to produce fresh water. Hence, for the experiments conducted for desalination, to keep the cost of desalination process low, thermodynamic additives were excluded.

2.5.3. Physical interventions

During the hydrate formation, the system develops various resistances that restrict any further hydrate formation. Generally, the resistances are provided by the following reasons:

- Superficial energy requirement to form a new phase
- Localized nucleation
- Temperature raise with an extensive hydrate formation
- Resistance provided by the hydrate formed along the gas-liquid interface

Most of the physical interventions were introduced into the hydrate formation systems to suppress the effects of these resistances and hence to improve the induction times as well as the yield of hydrate formation (Linga & Clarke, 2017). Most of the hydrate formation experiments mentioned in this chapter generally utilised stirred tank reactors in order to ensure

adequate dispersion of hydrate nuclei in the system that were formed at the gas liquid interface. Due to the presence of nuclei throughout the system, stirring creates an opportunity for the hydrate to achieve higher yields. However, there was a very little study done on the comparative quantitative analysis to measure the extent to which stirring improves hydrate yield compared to the quiescent conditions (Linga & Clarke, 2017). One of the major drawbacks of stirring were found to be the plunge in the rate of temporal gas uptake due to the difficulty in stirring in the presence of hydrate in the system, contributing to the reduction of final hydrate yield as well as excess energy consumption (Linga, et al., 2009; Linga, et al., 2012).

Addressing these issues, various researchers came up with different physical interventions such as porous media, nano particles and foams. Silica gel and silica sands were the most popular physical interventions that was studied for their efficiency in increasing the hydrate formation yield as well as their ready availability for cheaper prices (Seo, et al., 2005; Adeyemo, et al., 2010; Kang & Lee, 2010; Kang & Lee, 2010a; Kang, et al., 2013; Kumar, et al., 2013; Babu, et al., 2013a; Babu, et al., 2013b). From the perspective of hydrate formation kinetics, Seo et al (2005), through their NMR micro-imaging observed that the dispersed water in the pores of silicagel was ready to react with the dissolved gas to form hydrates. They added an 85% water to hydrate conversion was occurred within one hour of the experiment. The same observation was reported in the experimental analysis of hydrate formation conducted by Adeyemo et al. (2010), in the presence of CO_2/N_2 and CO_2/H_2 gas mixtures when added THF to the system. However, in the absence of THF the gas uptake was reduced to one tenth of the value produced in the presence of 1mol% of THF. They further added that the silica gel efficiency was higher when chosen the particles with larger pores. However, silica sand produced higher water-hydrate conversions when compared to silica gel (Babu, et al., 2013a; Babu, et al., 2013b).

In addition to the porous media, studies were also conducted over the effect of nano particles over the kinetics and the yield of hydrate formation (Chari, et al., 2013; Chari, et al., 2013a; Prasad & Sowjanya, 2014; Chari, et al., 2015; Prasad & Chari, 2015; Prasad, 2015). Unlike the porous media contained with silica gel, the silica nano particles were introduced into water along with stirring. According to Chary et al (2013), the conversions of water to hydrate in the presence of 1:8 and 1:4 (particles to water) ratios of silica nanoparticles were observed to be approximately 40% and 80%, where as this value was approximately 2.5% in the quiescent system. Apart from these physical interventions, studies were found on the effects of foams and polymers in order to absorb the heat of hydrate formation and thus to improve the hydrate yield (Su, et al., 2008; Su, et al., 2009; Yang, et al., 2011; Fan, et al., 2012; Nambiar, et al., 2015).

However, the usage of porous media poses challenges such as the difficulty in hydrate recovery as well as the lower volumetric capacity. In other words, when the hydrate formation was aimed at desalination, the hydrate needs to be recovered and separated from the silica gel and silica sand particles. When used the nano particles, this separation process would be even difficult. Moreover, due to the elevated viscosity of the water in the presence of nanoparticles, the energy consumption for stirring would be higher. On the other side, due to the extra volume occupied by the silica particles, for the same amount of hydrate in the quiescent and stirred systems, the requirement of reactor volume would be higher. When used the foams, the systems gravimetric efficiency would be low (Linga, 2017). Hence, in the current study, only stirring was used as the required physical intervention (chapter 4 and 5).

2.6. Methodology

2.6.1. Working principle of Multistage flash

An MSF desalination process consists of multiple elements connected in series called stages. These stages consist of various co-current and counter streams consisting of brine, vapour and the coolant. The MSF desalination process has been classified mainly into two configurations: MSF-OT (Once through) and MSF-BR (Brine recycle). In both the models, seawater enters the MSF at the condenser tube at the last stage, which counter flows with respect to the flashing brine amongst the stages.

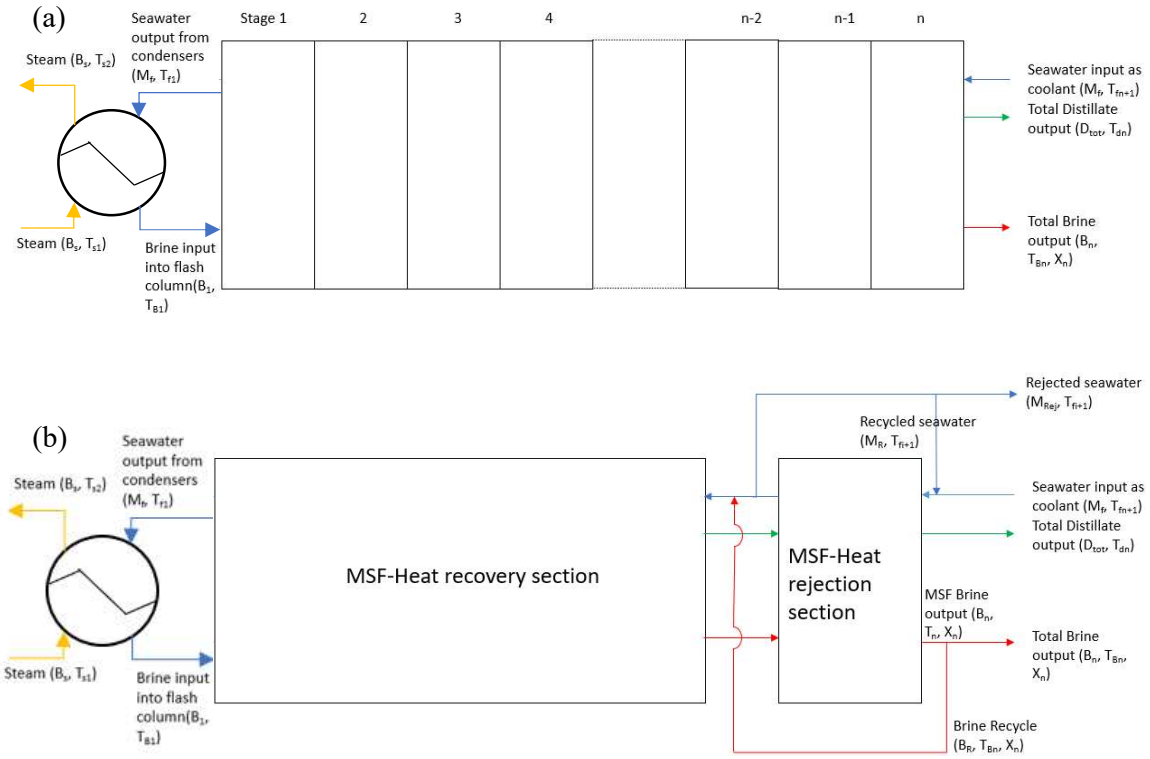

Figure 2.1. The illustrations of the working process of MSF-OT (top) and MSF-BR (bottom) desalination processes.

This seawater acts as the coolant to the flashed vapour at various stages and condense them into distillate stream, which also flows counter currently with respect to the seawater. As the seawater flows through the condenser tubes, the released energy of vapours while they condense would heat up the seawater. The seawater exiting at the first stage would have the

maximum temperature, which then sent to the brine heater. The brine heater consists of superheated steam being sent at low pressure conditions, which heats up the seawater to the saturation temperature and sent into the flash chamber of the first stage. All these stages would operate with a damping pressure gradient where the pressure decreases as the stage number increases. When the heater seawater enters into the flash chamber which operates at comparatively lower pressure conditions, it becomes superheated and flashes.

The flashing vapours will condense by losing its heat to the seawater flowing in the condenser tubes and makes the distillate stream. The remaining brine water enters the next stage, which operates at a lower pressure, becomes superheated again, resulting in flashed vapour. This vapour would further condense by exchanging heat with the coolant water flowing in the condenser tubes. The brine with high salinity exiting the last stage would be disposed in the MSF-OT. In case of MSF-BR, a fraction of the exiting brine would be recirculated into the condenser tubes of the heat recover section, while the same amount of the coolant water exiting the heat rejection section would be separated from the stream and a fraction of it would be recirculated into the last stage of the heat rejection section along with the seawater input (Kalogirou, 2014). The illustrations of MSF-OT and MSF-BR have been given in the figure 1.1.

2.6.2. Addressing the problem statement and research objectives

As mentioned in the chapter 1, the main aim of this study is to improve the performance of MSF desalination process from the aspects of low carbon emissions and the scale formation. In order to analyse them, two parameters were considered in this study: performance ration and production ratio, where performance ratio is the ratio of freshwater production rate (in kg/s) from the system and the rate of steam supplied to the brine heater (kg/s). The production ratio is the ratio between the rate of freshwater production from the system (in kg/s) and the rate of seawater input to the system (kg/s). These values will be calculated with and without

the induction of hydrate formation process in two configurations designed for MSF desalination, where the design 1 represents MSF-OT (Once Through), while the design 2 represents MSF-BR (Brine Recycle) model. From the perspective of Carbon capture, the results were analysed with respect to the concentration of CO_2 in the final gaseous effluence after treating the gaseous waste from the power generator for MSF brine heater through hydrate-based carbon capture system (HBCC).

Even though, the main focus was held on improving the performance of MSF desalination process, due to various discrepancies associated with the fundamental understanding of hydrate as a phenomenon, major portion of the study focuses upon understanding various aspects of hydrate formation starting from nucleation till hydrate yield. Despite the popular convention of choosing the operational conditions from the hydrate-water equilibrium conditions, for this study, it was very important to make sure the hydrate induction times were low with the choice of the most compatible operational conditions to make sure a constant supply of pre-treated water to MSF. Hence, the initial study was focussed upon modelling of hydrate nucleation process through ASPEN Custom modeller software, to understand the kinetics of nucleation and also to derive the induction time equation. As it is shown in the figure 2.2, the derivation of optimum pressure and temperature conditions by understanding the sensitivities of Kashchiev and Firoozabadi (2002a, b) equations towards hydrate forming gas concentration and the fugacity at various operational conditions. The gas concentration and fugacity were calculated through various theoretical and empirical equations and the results were distributed in six different cases. This distribution has been explained in the section 3.2.1. Using these parameters, nucleation parameters such as rate, induction time, volume fraction of nuclei were calculated in all these cases. A case wise comparison has been made to check their deviation from the base case through which analysis was done emphasizing the pressure and temperature conditions at which the deviations were higher.

Hydrate formation experiments were conducted to find out the most accurate case amongst the considered by comparing the calculated and the experimentally observed induction times. The induction time values from the most accurate case were analysed to calculate the optimum pressure and temperature conditions to conduct hydrate formation experiments for hydrate-based desalination process. Further explanation regarding the model configurations, its respective outcomes and conclusions were given in the chapter 3.

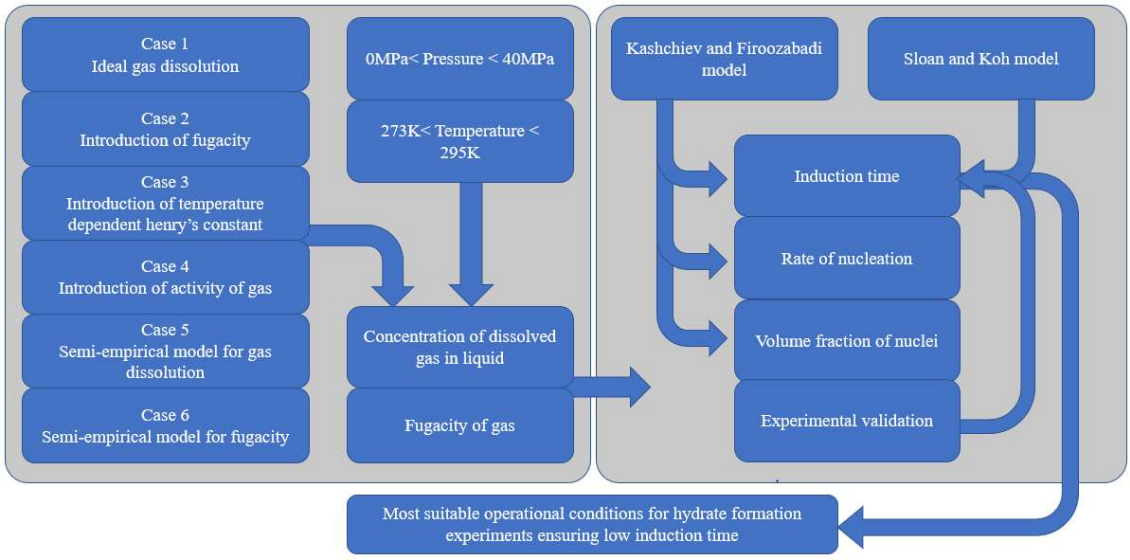

Figure 2.2. Methodology of deriving the most compatible operational conditions for experimental analysis through mathematical modelling.

As the hydrate formation was focussed upon carbon capturing and desalination, in order to keep the possible future prospects of linking these two processes together open, the hydrate-based desalination considered CO_2 hydrate formation. Through this consideration, the high concentrated CO_2 gas mixtures from the system of HBCC processes could be used for the hydrate formation in the HBD processes. While preparing the liquid solutions to be used for hydrate formation for the application of desalination, the main focus was held upon the suitability of produced hydrate to be used for the purpose of pre-treated water for MSF desalination so that it would produce water with potable standards. Hence, no thermodynamic additives were added. This was because, thermodynamic additives tend to participate in the

hydrate formation process, whereby their removal through an additional removal process would be required in order to produce potable water. Moreover, most of the thermodynamic additives were toxic to consume as well as their presence in the MSF blowdown stream would pose environmental concerns. As shown in the figure 2.3, the hydrate formation experiments were conducted under various chemical compositions such as the addition of salts, CH_4 to understand the effects of impurities upon the kinetics of hydrate formation and then the addition of promoters such as surfactant (kinetic additive) and the stirring were introduced to the system. The final outputs in terms of over gas consumption into the system addressing to the extent of hydrate formation yield, amongst all these systems were compared to analyse the effects of the impurities and the promoters. In addition to this comparative analysis, the hydrate formation profiles were analysed to understand how physical barriers and thermodynamic barriers could affect the hydrate formation kinetics with time. The final hydrate was collected and dissociated to subject the resultant aqueous solution to the activity tests to measure the salt concentration and also the desalination ability of hydrate formation in various systems that were considered.

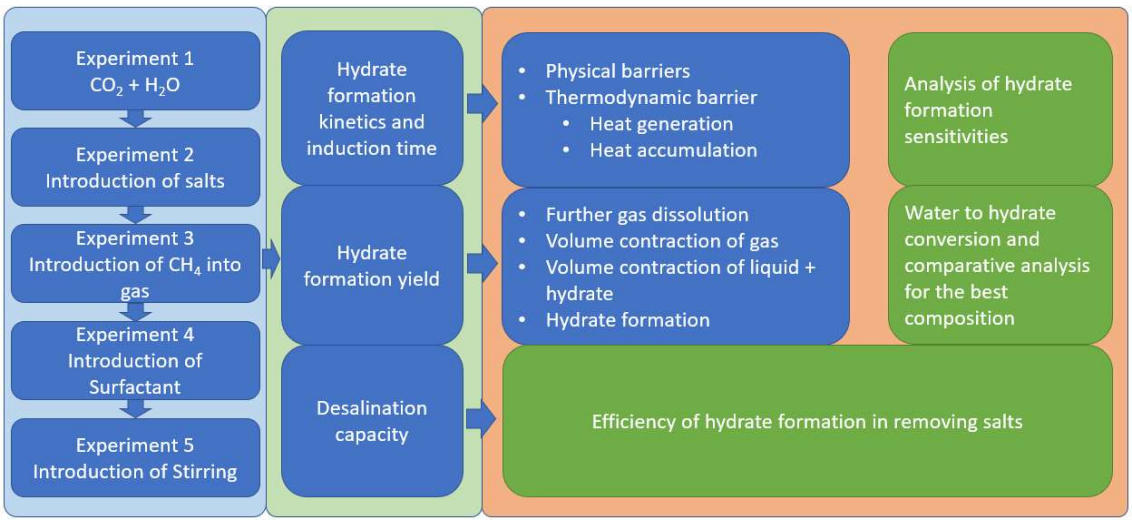

Figure 2.3. Methodology of deriving the most compatible chemical formulations for the hydrate-based water desalination through experimental analysis.

Further explanation upon the process methodology, chemical and physical configurations of the hydrate formation systems for desalination as well as the relevant conclusions were explained in the section 4.2.

While preparing the chemical solutions for hydrate-based carbon capture, the main focus was held on the kinetics of hydrate formation process. As the post-combustion gas solution consists of only 12-18% CO_2, the system needs higher driving forces in terms of elevated operational pressures, causing elevation in the process cost. Hence, as shown in the figure 2.4, while preparing the liquid solutions for the application of gas capture, thermodynamic additives such as THF were used, so that the required operational pressure could be reduced.

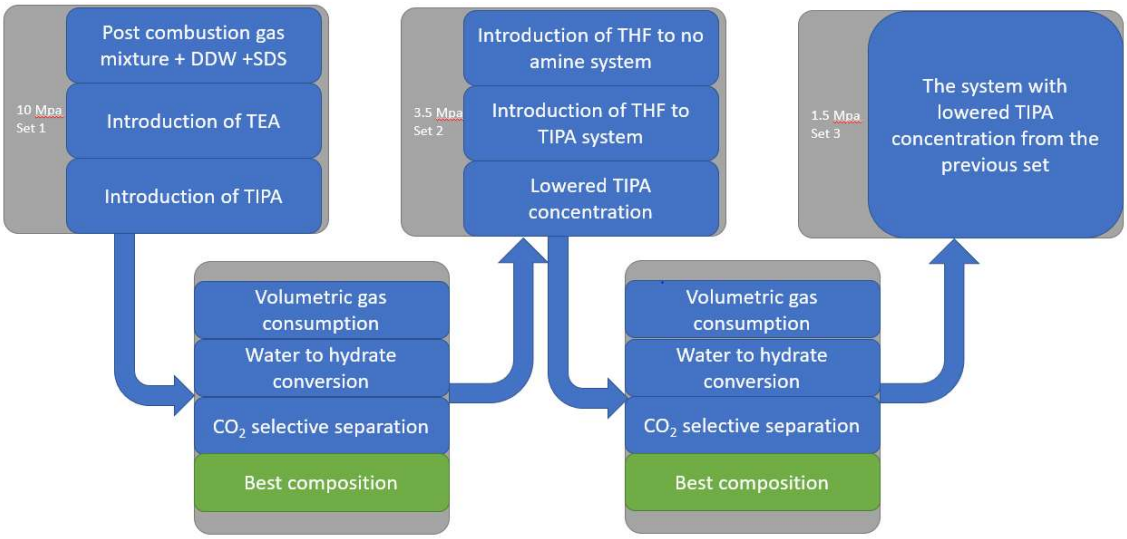

Figure 2.4. Methodology of deriving the most compatible chemical formulations for the hydrate-based carbon capture (HBCC) through experimental analysis.

In order to improve the CO_2 selectivity into the hydrate from the feed gas mixture, tertiary alkanolamines were added. The efficiency of hydrate formation process over the capture of CO_2 was analysed from the perspective of the final CO_2 concentration in the effluent gas from the HBCC system used for the experimentation. As the study was aimed at improving MSF from the perspective of lowering carbon emissions, the analysis of effluent gas from the HBCC for the concentration of CO_2 to calculate the reduction in CO_2 concentration before and after

the treatment through hydrate formation should be adequate. Further explanation upon the process methodology, chemical and physical configurations of the hydrate formation systems for carbon capture as well as the relevant conclusions were explained in the sections 5.1, 5.2 and 5.3.

The chapter 6 was focussed on developing a model for MSF operated at low TBT conditions to eliminate $Mg(OH)_2$ and $CaSO_4$ scale formations, while being able to calculate $CaCO_3$ scale deposition and its consequences upon the total freshwater output. Two MSF configurations were considered with one representing MSF-OT while the second one representing MSF-BR model. Various parameters starting from the overall rate of scale deposition, overall mass deposition, fouling heat transfer coefficient, total heat transfer coefficient, overall freshwater production rate, performance ratio and the production ratio were calculated and presented on the timeline. Along with the rate of change calculations, studies representing the effect of temperature and the salinity over the scale formation were also observed and discussed in this study. Thereafter, the contribution of HBD to the suppression of overall scale formation, lowered temporal decline of the total heat transfer coefficient and lowered temporal declines of the performance ratio and the production ratio were calculated and presented on the conclusive note. Combining all the information provided by the figures 2.2, 2.3 and 2.4 has been presented in the figure 2.5, which would represent the overall methodology of this study. A further process description for the figure 2.5 could be found in the sections 3.1, 4.1, 5.1 and 6.1.

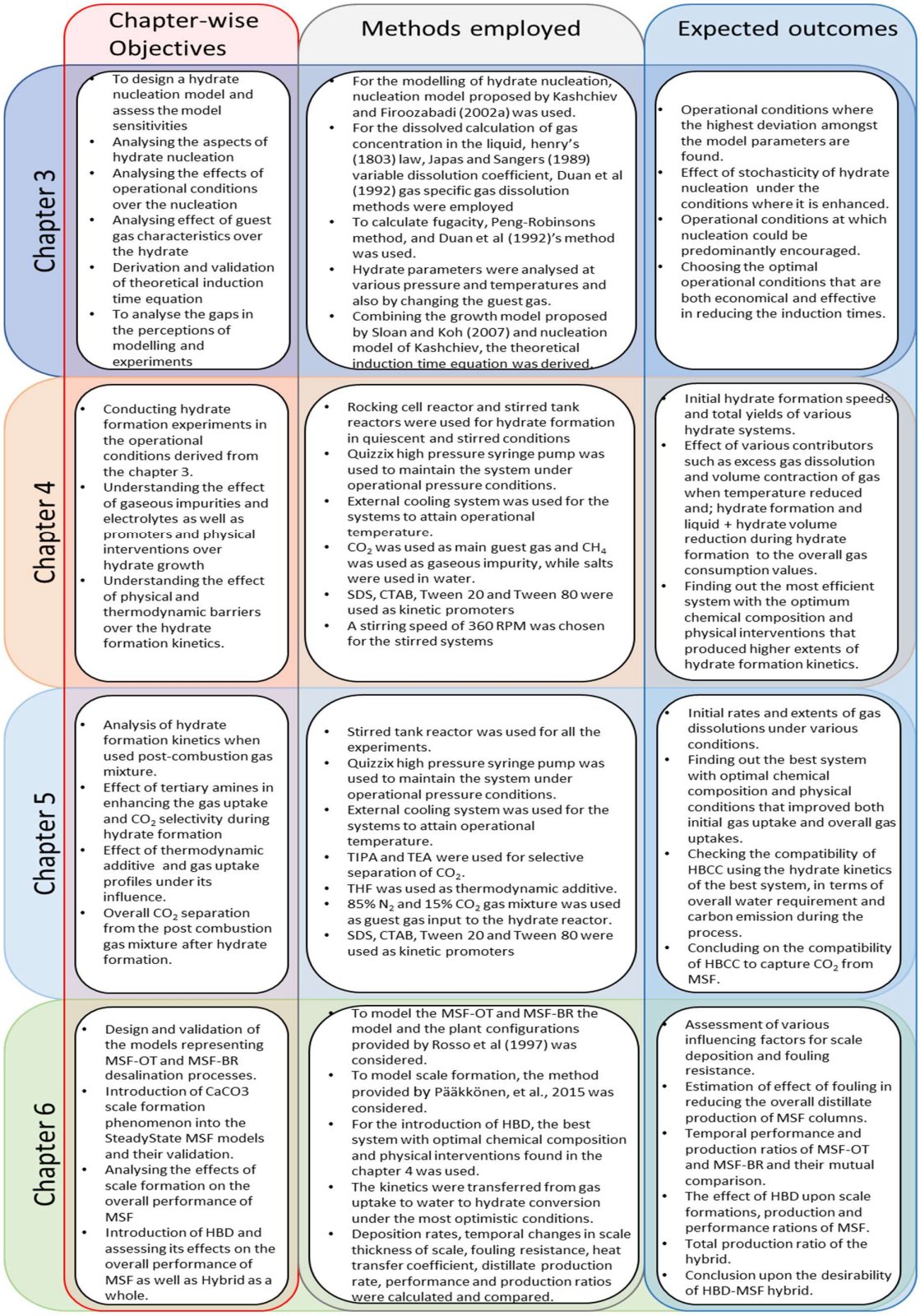

Figure 2.5. Synopsis of the overall methodology of this project.

2.7. Experimental Set Up and Data Acquisition

The hydrate formation experiments were conducted under both isothermal and isobaric conditions where the detection of hydrate formation was done by volumetric gas consumption (gas loading). These experiments were conducted in either a rocking cell jacketed type reactor for quiescent system or in a stirred tank jacketed type reactor. The inner volume of the jacketed rocking cell was 377 ml where the rig was capable of 180^{o} pneumatic rocking. The rocking was used during the gas resolution process. The rig was capable of an operational temperature ranging 303.15K-323.15K with a maximum operable pressure of 70 MPa. The coolant was circulated through a jacket of the rig from a cryostat to maintain the system under operational temperature conditions. The cryostat was capable of an accuracy range 0.05K. The rig was insulated with polystyrene board around it along with the plastic foam covering the connecting pipeline to reduce any heat transfer with the surroundings.

In order to monitor the temperature in the jacket during the hydrate formation a platinum resistance thermometer with an accuracy of ±0.05K was positioned in it. The pressure measurement was done using a Quartzdyne Pressure Transducer which is capable of measuring pressure with an accuracy of ±0.03MPa. The PC was connected through an RS 232 Serial port where the pressure and temperature data were recorded. The schematic diagram of the experimental setup as well as the jacketed type rocking cell reactor are given in figure 2.6(b). Pressure and temperature transducers and the temperature controller as well as the probe were connected to the reactor. To maintain the reactor under desirable pressure conditions a Quizix high pressure syringe pump (Q6000-10K model) was attached to the reactor thorough a gas supply cell. Pressure and temperature transducers, the pump and temperature controller as well as the probe were connected to the data acquisition system.

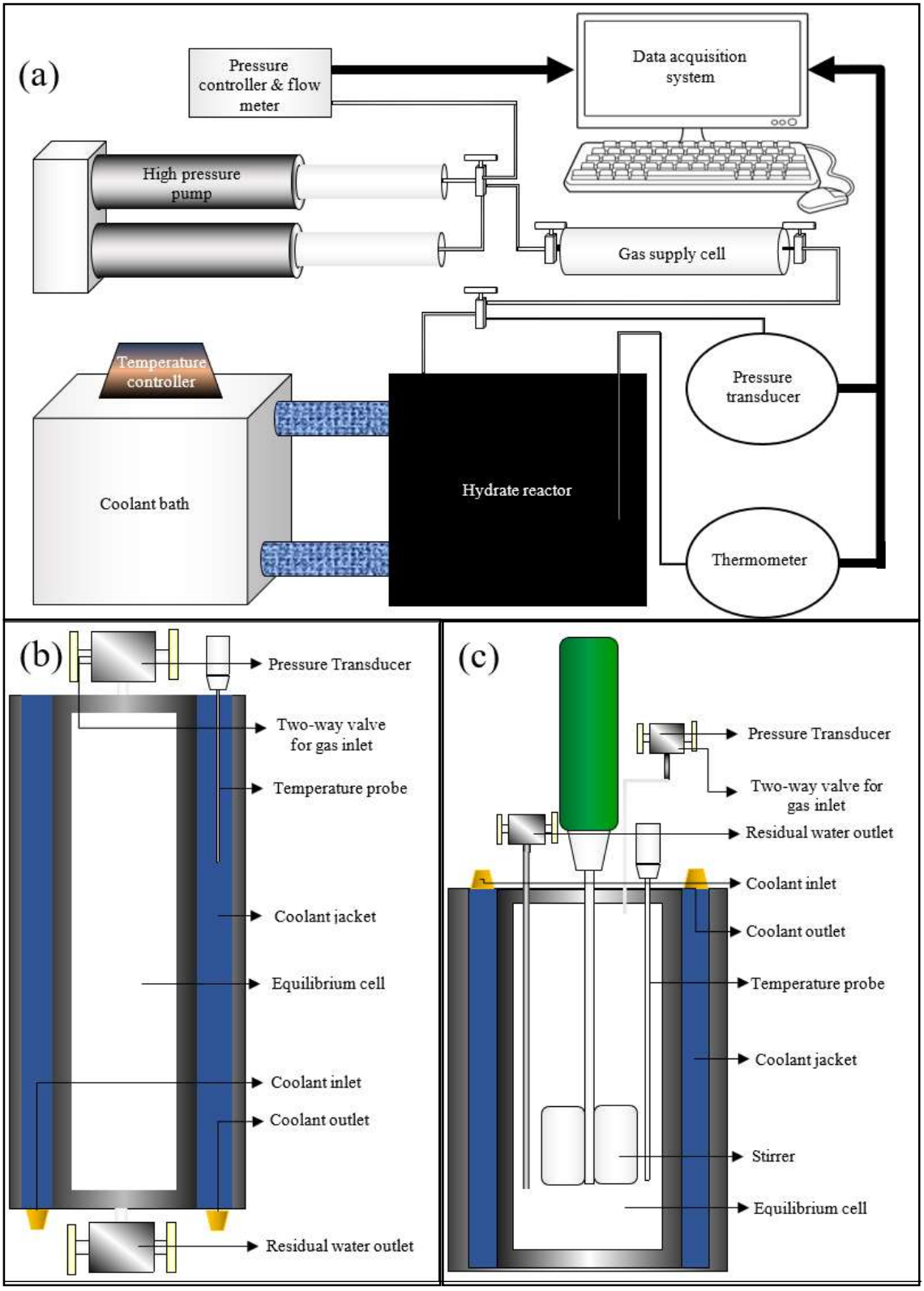

Figure 2.6. Configurations of Experimental set-up: (a) Overall experimental set-up; (b) rocking cell reactor

2.8. Summary

In the pursuit of proposing an efficient precursor to address the challenges faced by MSF desalination column, hydrate formation process has been proposed along with its compatibility in addressing those issues were discussed in the chapter 1. This chapter, however, provided an extensive literature review over the phenomenon of hydrate formation, its challenges and process improvement techniques. Starting from the ambiguity in understanding the fundamental phenomenon of hydrate formation till the requirement of high pressure, profound sensitivity of the process towards impurities as well as operational conditions and low hydrate yields were understood to be the challenges in hydrate formation process. Major ambiguity was associated with the phenomenon of hydrate nucleation, where there has been a schism with researchers having two opposing opinions over the predictability of hydrate nucleation. However, to some extent, under the higher driving force conditions, it was observed that this unpredictability has been considerably lower as the system experiences considerably negligible induction times. In addition, the improvement of hydrate yield and kinetics through the introduction of various physical and chemical additives were explained in this chapter. This review has been utilised to design overall methodology of the study as well as to design the model components to deduce the desirable knowledge over the hydrate nucleation process. In addition, this knowledge has been useful in selecting an appropriate chemical composition for the hydrate formation systems for the applications like desalination and carbon capture.

Chapter 3

Hydrate nucleation: Mathematical modelling

3.1. Introduction

For offering potential solutions to various fields such as acid gas capture, gas selective separation and storage, water desalination, gas/energy transportation, hydrate formation attracted immense attention from the researchers. However, mathematical stochasticity into the nucleation and crystal growth restricted along with the profound sensitivities of hydrate formation towards its physical and chemical conditions have limited its industrial application (Ribeiro & Lage, 2008; Linga & Clarke, 2016). There have been numerous mathematical models proposed to predict hydrate formation in terms of both nucleation as well as crystal growth. However, for the parameters used in these models were not presumptive, these values were deduced from the experimental observations, which questioned their self-sufficiency and their applicability in the conditions outside the experimental conditions (Ribeiro & Lage, 2008).

As mentioned in the chapter 2, starting from the pressure and temperature conditions used for homogeneous hydrate formation, its unpredictability would be contributed by various parameters such as the surface energy, solubility, fugacity, activity of the additives, and their involvement in the hydrate formation. All these parameters would contribute to the induction time, yield and the structure of hydrates. In order to suffice the aim of the current study, a choice has to be made over the operational conditions depending upon the predictability and practicability of these conditions towards hydrate formation. This choice has been made using

a modified version of the theoretical model proposed and developed by Kashchiev and Firoozabadi (2000, 2002a, 2002b, 2003). The main outcomes of this model were verified through the experimentation. The model being theoretical, allows its user to explore wide ranges of pressure and temperature conditions without having to use the parameters that are derived from the experimentation. However, it is important to examine under what conditions the model deviates the most as well as which parameters influence the outcomes profoundly, which requires a thorough examination over the model under a range of experimental conditions. This examination has to occur at various stages of hydrate formation: dissolution, nucleation and crystal growth. The study mainly focuses on the yield of hydrate formation and the time taken, the current chapter focusses mainly upon the dissolution, rate of nucleation as well as induction time. Even though, each stage has been examined individually, the study also considered their mutual dependency. Hence, it is impossible to evaluate hydrate nucleation without evaluating the gas dissolution into the system. In addition, without evaluating the hydrate nucleation, it is impossible to evaluate the hydrate growth accurately.

The Henry's model used for calculating gas concentration and fugacity in Kashchiev and Firoozabadi model were replaced with relatively more accurate sei-empirical models as mentioned in the chapter 2. were This application would also be helpful to derive the deviations amongst the final outputs when used different models, and check under what conditions the deviations are acceptable, which could eventually calibrate the main Kashchiev and Firoozabadi's model. As the study has been focussed upon CO_2 capture, CO_2 has been taken as the main hydrate forming gas in the study, for the comparative analysis, a relatively less hydrate forming gas such as methane was considered. In order to execute this comparative analysis, six cases were considered. While the first case being the most basic one with the usage of ideal gas equation for the fugacity while sixth case used the gas specific model for both the extent of gas dissolution and fugacity, whereas the second case was the reproduction of the

Kashchiev and Firoozabadi's nucleation model. By using these models, various nucleation parameters were evaluated such as rate of nucleation, induction time and the hydrate volume fraction. Each case was viewed from two stances: isothermal and isobaric. The isothermal condition represents the repetition of the same hydrate formation process under the constant temperature at various pressure conditions. The similar analogy was applied to the isobaric stance.

In addition to the calibration of Kashchiev and Firoozabadi's nucleation model, the study also addressed the disambiguation persisted in the definition and the detection of induction time. Theoretically, the concept of hydrate formation is understood as the time where the process of nucleation becomes spontaneous (Sloan Jr & Koh, 2007). However, the in Kashchiev and Firoozabadi's model, the term was defined as the time at which the concentration of nuclii in the system reaches to a certain point. This was detected by the reduction in the intensity of transmitted light through the aqueous system of the hydrate reactor. The disambiguation was not just limited to the Kashchiev and Firoozabadi's model but also various studies used different techniques such as the raise of gas volume intake in the isobaric hydrate formation experiments or the plunge of pressure in the isochoric hydrate formation experiments and temperature fluctuations (Anklam & Firoozabadi, 2004; Sloan Jr & Koh, 2007; Kazemeini, et al., 2012). These detection techniques have been useful in observing the induction times experimentally. Hence, this study considered the need of deriving an equation towards theoretically evaluating the induction time for various hydrate formation systems based on the Kashchiev and Firoozabadi's model as well as the equation for hydrate volume fraction. The derivation of theoretical induction time could be used as a bridge in between the theoretical hydrate formation phenomenon and the practical observations. This induction time values have been used in the chapter 6 to understand the final rates of hydrate formation.

3.2. Methodology

Hydrate nucleation parameters such as rate of nucleation, extent of crystal growth, induction time and hydrate volume fractions have been focussed on this chapter. It studies the influences of the concentration of dissolved hydrate forming gas and its physical properties like fugacity have been examined under various hydrate forming operational conditions. A quiescent system consisting of pure guest gases (CO_2 or CH_4) was considered excluding any physical interventions such as stirring or porous media and chemical additives such as kinetic and thermodynamic additives. Methane was taken for the comparative analysis because its been widely studied in the modelling for the purpose of energy storage and transportation through hydrate formation. In addition, methane is comparatively a high hydrate forming gas than other abundant gases such as N_2, H_2, or O_2 under relatively lower pressure conditions. For the achievement of a reliable comparison between CH_4 and CO_2 hydrate nucleation, the hydrate physical properties were kept same for both the hydrates. However, the superficial energy barrier as well as the volume of hydrate building unit for CO_2 have been taken lower than the value that was taken for CH_4 in the study of Kashchiev and Firoozabadi (2002a): $14 mj/m^2$ and $0.151 nm^3$ (Anderson, et al., 2003).

For the calculation of dissolved gas concentration, along with the Henry's model representing a generic approach as considered by Kashchiev and Firoozabadi (2002a, b and 2003), Duan's model representing a gas specific semi-empirical model was also considered (Duan, et al., 1992; Duan & Sun, 2003; Duan & Mao, 2006a; Duan, et al., 2006b). Even though, there have been a few models proposed to calculate the gas dissolution in the presence of hydrates, they have been excluded as the study focusses merely on hydrate nucleation and not during the hydrate growth (Bergeron & Servio, 2009; Hashemi, et al., 2006; Lang & F., 2016). The application of these cases has been progressively made case wise, which was distributed amongst six cases.

3.2.1. Cases

For the ease of analysing the influence of each evaluation method in calculating the nucleation parameters, inclusion/change of each evaluation method has been considered as a new case. Thus, a total number of six cases were created to discuss the sensitivity of these parameters.

The study made the following assumptions while some of them were adapted from the Kashchiev and Firoozabadi (2002a)'s nucleation model:

- The entire hydrate formation process is triggered by the primary nucleation where further nucleation processes would become indistinguishable.
- The water becomes saturated with the dissolved guest gas under the operational conditions before the occurrence of progressive primary nucleation.
- The dissolved guest gas is distributed evenly throughout the aqueous solution.
- The temperature fluctuations are negligible during the hydrate nucleation.
- Similar to the distributed dissolved gas in the aqueous phase, the nucleation also occurs evenly throughout it.
- The dissolution occurs through the undisturbed diffusion of the guest gas into the liquid while the occurrence of nucleation.
- The nucleation is homogeneous, which is not hindered either by the heterogeneous nucleation occurring at the gas-liquid interface.

3.2.1.1. Case 1

The dissolution of gas into the aqueous phase in this case considered the ideal gas characteristics. Imbibing them characteristics, the basic Henry's law was used to calculate the dissolved gas into the aqueous phase (Henry, 1803). The concentration of dissolved gas into the aqueous phase was calculated as follows:

$$X_i = H_i P \quad (3.1)$$

Where X_i is the mole fraction of dissolved gas in liquid, H_i is Henry law's constant for the guest gas 'i' and P is the operational pressure. In this study, H_{CO2} has been taken as $3.3x10^{-4}$ while H_{CH4} was considered to be $1.4x10^{-5}$ (Sander & R., 2015). As the gas was taken incompressible, the fugacity of the guest gas has been omitted from this case.

3. 2.1.2. Case 2

This is the case where the compressibility of the guest gas was introduced into the study. The coefficient of fugacity ($\emptyset_i$) values were calculated using Peng-Robinson (PR) equation of state. The extent of gas dissolution was calculated from the following equation:

$$X_i = \emptyset_i H_i P \quad (3.2)$$

As the equation 3.2 was the one that was considered in the nucleation model proposed by Kashchiev and Firoozabadi (2002a, b and 2003), this case has been considered to be the base case for the comparative analysis to calculate the deviations. The rates of nucleation calculated from this case has been compared with the values produced by Kashchiev and Firoozabadi (2002b) to validate the approach of this study.

3. 2.1.3. Case 3

The temperature dependence of the gas dissolution into the aqueous phase has been in this phase. As seen from the experimental observations of Japas and Sengers (1989), the gas dissolution into both the aqueous and non-aqueous solutions followed a parabolic profile where the extent of gas dissolution reaches to a maximum point before plunging down (Japas & Sengers, 1989). Harvey (1996) attributed it to the dimensionless Henry's law constant while producing its temperature dependent equation (Harvey, 1996). This temperature dependent Henry's constant (k_H) has been used in this case to calculate both CO_2 and CH_4 gas dissolutions, which is as shown in the equation 3.3:

$$\ln(k_H) = \ln(p_l^s) + \frac{A_H}{T_r} + \frac{B_H}{T_r}(1 - T_r)^{0.355} + \frac{C_H}{T_r^{0.41}} e^{(1-T_r)} \quad 3.3$$

Table 3.1. Henry's constant (k_H) parameters to be substituted in equation 3 (Anderson, et al., 2003).

	A_H	B_H	C_H
CO_2	-9.4234	4.0087	10.3199
CH_4	-11.0094	48362	12.5220

Where the saturation pressure of water was p_l^s , reduced temperature was T_r and the parameters of the correlations were A_H, B_H and C_H as shown in the table 3.1. Equation 3.3 was substituted in the equation 3.4 to calculate the concentration of dissolved gas into the aqueous phase.

$$X_i = \frac{\emptyset_i P}{k_H} \quad 3.4$$

3. 2.1.4. Case 4

The electromagnetic forces of interactions among the ions in the aqueous phase have been represented by the activity coefficient (γ_i). Generally, the activity coefficient for both CO_2 and CH_4 are taken to be unity when the accurate results were not needed, especially at higher temperature conditions. On the contrary to this assumption, Diamond and Akinfiev (2003) have observed the values to be deviating from one at the lower temperature conditions. Despite this observation, according to the authors the consideration of unity for the activity coefficient could still be practicable when the gas concentration in the liquid is considerably low. As the main focus of this chapter is to understand what conditions could potentially create deviation from the values produced by Kashchiev and Firoozabadi's nucleation model, the activity coefficient, in this case, was considered to be a non-unity number. Equation 3.5 shows the equation used in this case to calculate the mole fraction of dissolved gas concentration including the activity coefficient of the ions in the aqueous phase:

$$X_i = \frac{\emptyset_i P}{k_H \gamma_i} \quad 3.5$$

Measurement of activity coefficient through various correlations was proposed in various studies under the given operational conditions (Renon & Prausnitz, 1968; Vera, et al., 1977; Anderson, et al., 2003; Islam & Carlson, 2012). Nevertheless, for methane, these activity coefficients were not available and hence these equations were derived from the gas dissolution model proposed by Duan el at (1992). The ability of any system to provide molecules into its surrounding was taken as the chemical potential of the system. Duan et al (1992) utilised the equation 3.6 and 3.7 to calculate the chemical potential of both the vapour and liquid phases while proposing their equation of state for the system consisting of H_2O-CO_2-CH_4.

$$\mu_i^v = \mu_i^{v0} + RT\, lnf_i \quad 3.6$$

$$\mu_i^l = \mu_i^{l0} + RT\, lna_i \quad 3.7$$

The chemical potential of the guest gas 'i' under the defined operational conditions in dissolved and vapour states were represented by the terms μ_i^l and μ_i^v, while the initial chemical potentials of the gas 'i' in the dissolved and vapour states were represented by μ_i^{l0} and μ_i^{v0}. R, f_i and a_i were the gas constant, fugacity and activities of the gas 'i'. Considering the equal chemical potential for every component in all the phases within the system, the equation 3.6 and 3.7 were equated, which resulted in the equation 3.8.

$$\gamma_i = \frac{\emptyset_i P}{m_i} e^{\left(\frac{\mu_i^{l0} - \mu_i^{v0}}{RT}\right)} \quad 3.8$$

The molality of the dissolved gas was represented by m_i. Since the solution considered in this case was the ideal solution, μ_i^{l0} represents the chemical potential of the ideal liquid where as

μ_i^{v0} referred the ideal gas. As the study required only the difference of the chemical potentials of the gas in liquid and vapour phases, μ_i^{v0} was set to zero (Denbigh, 1981).

$$\gamma_i = \frac{\emptyset_i P}{m_i} e^{\left(\frac{\mu_i^{l0}}{RT}\right)} \quad 3.9$$

The molality term mentioned in the equation 3.9 was calculated from the Duan's model for gas dissolution, while the activity coefficient was calculated from the equation 3.9. This activity coefficient was substituted in the equation 3.5 to calculate the dissolved gas mole fraction in the aqueous phase.

3. 2.1.5. Case 5

The gas specific gas dissolution model was introduced in this case. A semi-empirical model proposed by Duan et al (2006a and b) was considered in this case to calculate the amount gas dissolved into the aqueous phase under the considered operational conditions in CO_2 and CH_4 systems respectively. Duan proposed gas dissolution model based on the specific particle interaction theory by combining it with Duan et al (1992) equation of state. Equation 3.10 was used to calculate the concentration of gas in the pure water system:

$$\ln(m_i) = \ln(y_i \emptyset_i P) - \frac{\mu_i^{l0}}{RT} \quad 3.10$$

The mole fraction of the guest gas in the gas phase was represented by y_i. Assuming relatively negligible water concentration in the vapour phase, the term y_i was set to 1. Similar to the case 4, the coefficient of fugacity mentioned in the equation 10 was calculated from Duan et al (1992, 2006a) model.

3. 2.1.6. Case 6

Contrasting the previous cases, case 6 has been mainly focussed upon the fugacity of the guest gas. In all the cases, to calculate the fugacity of the gases, for the measurement of nucleation

parameters PR model was used, adapting the methodology of Kashchiev and Firoozabadi (2002a, b, 2003).

Table 3.2. Parameters of equations 3.11 and 3.12 (Duan *et al*., 1992 for CH_4 and 2006a for CO_2)

		CO_2	CH_4
	1	2	
C_1	1.0	$-7.1734882 \times 10^{-1}$	$8.72553928 \times 10^{-2}$
C_2	4.7586835×10^{-3}	1.5985379×10^{-4}	$-7.52599476 \times 10^{-1}$
C_3	$-3.3569963 \times 10^{-6}$	$-4.9286471 \times 10^{-7}$	$3.75419887 \times 10^{-1}$
C_4	0.0	0.0	$1.07291342 \times 10^{-2}$
C_5	-1.3179396	0.0	$5.49626360 \times 10^{-3}$
C_6	$-3.8389101 \times 10^{-6}$	$-2.7855285 \times 10^{-7}$	$-1.84772802 \times 10^{-2}$
C_7	0.0	1.1877015×10^{-9}	$3.18993183 \times 10^{-4}$
C_8	2.2815104×10^{-3}	0.0	$2.11079375 \times 10^{-4}$
C_9	0.0	0.0	$2.01682801 \times 10^{-5}$
C_{10}	0.0	0.0	$-1.65606189 \times 10^{-5}$
C_{11}	0.0	0.0	$1.19614546 \times 10^{-4}$
C_{12}	0.0	-96.539512	$-1.08087289 \times 10^{-4}$
C_{13}	0.0	4.4774938×10^{-1}	$4.48262295 \times 10^{-2}$
C_{14}	0.0	101.81078	$7.53970000 \times 10^{-1}$
C_{15}	0.0	5.3783879×10^{-6}	$7.71670000 \times 10^{-2}$

1: $P < P_b$ (P_b is the bubble point pressure of CO2); 2: $P > P_b$

However, for this case, the fugacity coefficient, substituted in the driving force term was taken from the correlations proposed by Duan et al (1992, 2006a and b). The equations 3.11 and 3.12 represent the coefficient of fugacity terms as proposed by Duan model.

$$\emptyset_{CO_2} = C_1 + \left(C_2 + C_3T + \frac{C_4}{T} + \frac{C_5}{(T-150)}\right)P + \left(C_6 + C_7T + \frac{C_8}{T}\right)P^2 + \left(C_9 + C_{10}T + \frac{C_{11}}{T}\right) lnP + \frac{\left(C_{12}+\frac{C_{13}}{T}\right)}{P} + \frac{C_{14}}{T} + C_{15}T^2 \quad 3.11$$

$$ln\emptyset_{CH_4} = Z - 1 - lnZ + \frac{\left(C_1+\frac{C_2}{T_r^2}+\frac{C_3}{T_r^3}\right)}{V_r} + \frac{\left(C_4+\frac{C_5}{T_r^2}+\frac{C_6}{T_r^3}\right)}{2{V_r}^2} + \frac{\left(C_7+\frac{C_8}{T_r^2}+\frac{C_9}{T_r^3}\right)}{4{V_r}^4} + \frac{\left(C_{10}+\frac{C_{11}}{T_r^2}+\frac{C_{12}}{T_r^3}\right)}{5{V_r}^5} + \frac{C_{13}}{2C_{15}}\left(C_{14} + 1 - \left(C_{14} + 1 + \frac{C_{15}}{V_r^2}\right)e^{\left(-\frac{C_{15}}{V_r^2}\right)}\right) \quad 3.12$$

Where Z, V_r, T_r were compressibility factor, reduced volume and the temperatures of the guest gas respectively. The correlation parameter values of c_i have been shown in the table 3.2. Additionally, for the ease of analysis certain terms have been defined, modifications were done to the existing correlations of Kashchiev and Firoozabadi's nucleation model along with the derivations of new equations. In addition to these cases, certain terms were defined to ease the description in the analysis, a few modifications were made to the correlations proposed by Kashchiev and Firoozabadi (2002a, 2002b, 2003), and several equations were derived from the existing correlations, which are explained in sections 3.2.1, 3.2.5 and 3.2.6.

3.2.2. Isothermal and isobaric processes

Generally, the terms Isothermal and Isobaric are seen from two different stances when mentioned in any literature: 1. The conditions under which the process has been taken place or 2. The considered conditions, under which the non-isothermal/non-isobaric set of experiments were analysed. In this study, the hydrate formation phenomenon was considered to be both isothermal and isobaric. This means, the hydrate formation experiences absolutely no fluctuations from the pre-set temperature and pressure conditions. However, these terms were

used to explain on what basis the different hydrate formation processes were linked. In addition, these terms were used to understand how process variables behaved when the isothermal-isobaric hydrate formation process occurs along the varying temperature and varying pressure conditions. Hence, the isothermal process represents a comparative analysis of the hydrate nucleation parameters for the collection of hydrate formations that occurred under the same temperature conditions with varying pressure. Isobaric process represents the comparative analysis of nucleation parameters for the collection of hydrate formations occurred under the same pressure and varying temperature conditions. As it is mentioned in the chapter 2, the hydrate formation process had been an exothermic process, which confirms the temperature fluctuations during the hydrate formations. However, the main focus in this chapter being the primary hydrate nucleation and not the growth, the assumption of constant temperature during the nucleation could be practicable.

3.2.3. Deviation

Hydrate nucleation parameters were calculated under a range of temperature and pressure conditions. Typically for isothermal process of analysis these values were calculated at a temperature reference point of 273.2K, while the pressure reference point was taken to be 30MPa for the isobaric process of analysis. As mentioned in the section 3.2.1, for each operational temperature and pressure, various nucleation parameters were deduced considering different dissolution and fugacity models. The isotherms and isobars of nucleation parameter values deduced from each case were plotted against operational pressure and temperatures respectively. In addition to these plots, the deviations of the nucleation parameter values derived from all the cases from the base case (case2) were plotted. These deviations have been derived from the equation 3.13.

$$\Delta = \left(\frac{\Lambda_j - \Lambda_2}{\Lambda_2}\right) \qquad 3.13$$

Where the deviation was represented by Δ while the nucleation parameter derived from the case j was represented by Λ_j.

3.2.4. Rate of nucleation by Kashchiev

The rates of nucleation were calculated by the nucleation model proposed by Kashchiev and Firoozabadi (2002b). However, the equation was slightly modified in order to serve the constraints of the current study. The rate of primary nucleation proposed by Kashchiev and Firoozabadi has been mentioned as the equation 3.14:

$$J = z f_e^* C_0 e^{\frac{\Delta\mu}{kT}} e^{\frac{-W}{kT}} \quad 3.14$$

where J is the rate of nucleation (molecule/s); fe* is the frequency of attachment at the point of hydrate equilibrium, z is the Zeldovich factor, C_0 represents the nucleation site concentration in the aqueous phase, $\Delta\mu$ represents the super-saturation, w was the total work done for the formation of nucleus successfully. Kashchiev and Firoozabadi (2002a and b) mentioned the correlations for these parameters were provided. The following equation 3.15 represents the frequency of molecular/nucleus attachment at the point of equilibrium.

$$f_e^* = \varepsilon(4\pi c)^{\frac{1}{2}} v_h^{\frac{1}{3}} D M_{i0} n^{*\frac{1}{3}} \quad 3.15$$

where ε, c and v_h represents the sticking coefficient, shape factor and the volume of the hydrate building unit. D and n* were the gas diffusivity with the aqueous system to the primary nucleation sites and the number of building units required for a stable nucleus. The following equation 16 was derived by substituting the equation 3.15 in 3.14:

$$J = z\left(\varepsilon(4\pi c)^{\frac{1}{2}} v_h^{\frac{1}{3}} D M_{i0} n^{*\frac{1}{3}}\right) C_0 e^{\frac{\Delta\mu}{kT}} e^{\frac{-W}{kT}} \quad 3.16$$

The term M_{i0}, as shown in the equation 15 represents the concentration of the dissolved gas under the conditions of hydrate equilibrium. The term $e^{\frac{\Delta\mu}{kT}}$ represents the extrapolation to the

hydrate formation conditions from the equilibrium conditions such as operational pressure and temperatures. In the Kashchiev and Firoozabadi's nucleation model, M_{i0} was calculated from Henry's law at the hydrate equilibrium temperature and pressure conditions and extrapolated to the operational conditions by the exponential term. In this study, the product of M_{i0} and the exponential term was considered and represented as M_i. This term Mi was considered to be the dissolved gas concentration under the operational conditions. This consideration transformed the equation 3.14 into 3.17:

$$J = z\left(\varepsilon(4\pi c)^{\frac{1}{2}} v_h^{\frac{1}{3}} D M_i n^{*\frac{1}{3}}\right) C_0 e^{\frac{-W}{kT}} \qquad 3.17$$

In order to validate the equation 3.17, the isotherms of rates of primary nucleation values were generated using the equation 3.14 and 3.17 within the limitations of the case 2 and their respective deviations were plotted against the operational pressure conditions in the figure 3.1. As it is seen in the figure 3.1, the deviations in between the values generated by the equation 3.14 and 3.17 were negligible, validating the applicability of the equation into this study.

According to Kashchiev and Firoozabadi (2002a) the work done for the critical hydrate nucleus is provided in the equation 3.18:

$$W = \frac{8c^3 v_h^2 \sigma_{ef}^3}{27\,\Delta\mu^2} \qquad 3.18$$

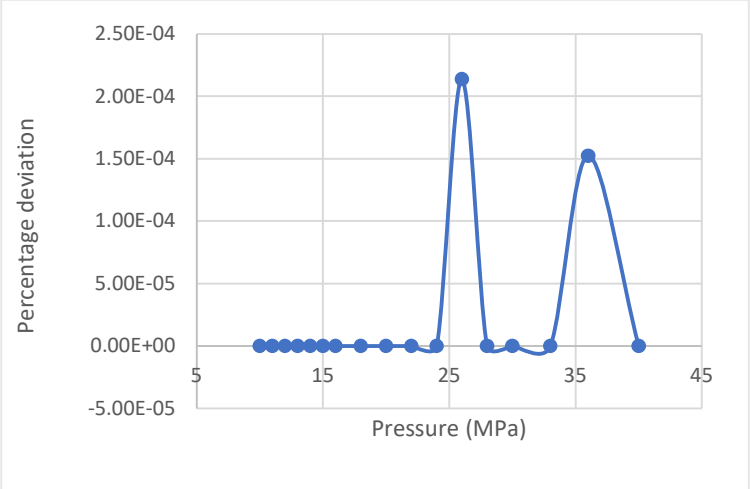

Figure 3.1. The deviation of the nucleation rates calculated from the equation 17th of the current study from the equation proposed by Kashchiev and Firoozabadi (2002a)

From equations 3.17 and 3.18, the following observation was made:

$$J \propto e^{\left(-\frac{1}{\Delta\mu^2}\right)}$$

According to Kashchiev and Firoozabadi (2002a), the driving force was represented by the parameter Δμ and addressed by the term super-saturation. The exponential relationship between the hydrate nucleation rate and the supersaturation expressed the profound sensitivity of the primary nucleation rate with the driving force. The supersaturation was calculated from the equation 3.19:

$$\Delta\mu = kT \ln\left(\frac{\emptyset P}{\emptyset_e P_e}\right) + (n_w v_w - v_h)(P - P_e) \qquad 3.19$$

where $\emptyset_e$ was the coefficient of fugacity and P_e was the equilibrium hydrate formation pressure at the operational temperature conditions, while V_w and n_w were the volume of a water molecule and the number of water molecules in the hydrate building unit respectively.

3.2.5. Induction time derivation

As explained in the section 3.1, the induction time as a concept had numerous definitions and measurement techniques, which led to various discrepancies amongst the researchers in the practicability of induction time calculations (Kashchiev & Firoozabadi, 2003; Sloan Jr & Koh,

2007; Ribeiro & Lage, 2008). Even the definition of Kashchiev and Firoozabadi (2003) was not sufficient enough to provide an absolute value for the induction time. Hence, this study attempted to derive the theoretical induction time values based on the definition provided by Sloan and Koh (1998). According to them, the induction time is the elapsed time before which the hydrate formation becomes spontaneous, and the hydrate formation becomes spontaneous when the crystal size crosses the critical radius by overcoming the superficial energy resistance.

As part of the theoretical induction time derivation, the equation for the extent of progressive growth of the hydrate crystal proposed by Kashchiev and Firoozabadi (2003) was considered. This progressive growth of primary nucleation crystal was equated with the critical radius equation proposed by Sloand and Koh (1998) as shown in the equation 3.20.

$$r(t) = (Gt)^m \tag{3.20}$$

where G was the growth constant where the m value was equal to 0.5 for growth occurred by the undisturbed diffusion of dissolved gas during the progressive growth of spherical hydrate crystals. G was calculated by using the equation 3.21:

$$G = 2\varepsilon v h D M_i (e^{(\frac{\Delta\mu}{kT})} - 1) \tag{3.21}$$

$$R_c = \frac{2\sigma}{(\Delta g)} \tag{3.22}$$

where R_c and Δg were the critical radius of the hydrate nucleus and Gibbs free energy per unit volume of the formed hydrate respectively. According to Sloan and Koh (1998), the Gibbs free energy could be calculated by using the equation 3.23:

$$-\Delta g = \frac{kT}{v_h} \ln\left(\frac{\emptyset P}{\emptyset_e P_e}\right) + \frac{n_w v_w (P - P_e)}{v_h} \tag{3.23}$$

Finally, by combining the equations 3.20-3.23, the derivation of theoretical induction time (t_{ind}) equation was done, which is given by the equation 3.24:

$$t_{ind} = \frac{\sigma^2}{2\varepsilon v_h \mathrm{D}(M_i - M_{i0})(\Delta g)^2} \quad 3.24$$

Where the surface energy (σ) would be lesser than the effective surface energy σ_{eff} which could be calculated from the equation 3.25. Θ is the contact angle between water and the solid surface of the vessel.

$$\sigma = \frac{\sigma_{eff}}{(0.25(2+cos\ )(1-cos\Theta)^2)^{\frac{1}{3}}} \quad 3.25$$

This equation 3.25 has been used in the section 3.4.3 to validate the induction times calculated from the considered cases.

3.2.6. Hydrate volume fraction at the theoretical induction time

As explained in the section 3.1 Kashchiev and Firoozabadi (2003)'s definition of induction time followed an experimental perspective. According to them, the induction time was the time taken by the system to produce the hydrate occupying a certain volume fraction of the total the reactor's volume. The induction time calculation method proposed by Kashchiev and Firoozabadi was represented by the equation 3.25. An exemplary value of 0.01 was taken addressing the hydrate volume fraction with respect to the reactors volume to eb substituted in the equation 3.25.

$$t_{ind}^{K} = \left(\frac{3\alpha v_w(1+3m)}{4\pi z f_e^*(2\varepsilon v_h D C_e)^{3m}}\right)^{\left(\frac{1}{1+3m}\right)} \left(e^{\left(\frac{-\Delta\mu}{kT}\right)}\left(1 - e^{\left(\frac{-\Delta\mu}{kT}\right)}\right)^{\left(\frac{-3m}{1+3m}\right)}\right)\left(e^{\left(\frac{W}{(1+3m)kT}\right)}\right) \quad 3.25$$

where the volume fraction of the hydrate with respect to the rectors volume was represented by α. The hydrate volume fractions were calculated to check the validity of the assumption of taking hydrate volume fraction to be a certain volume for the confirmation of induction time under the considered operational conditions.

Equation 3.26 was produced by equating equations 3.24 and 3.25, along with a few adjustments to suit the cases as explained in the section 3.2.4.

$$\alpha = \left(\frac{4\pi z\ e^{*}\left(2\varepsilon v_h D C_e (M_i - M_{i0})\right)^{3m}}{3v_w(1+3m)}\right)\left(t_{ind} e^{\left(\frac{-W}{(1+3m)kT}\right)}\right)^{(1+3m)} \qquad 3.26$$

3.3. Experimental setup

There have been a few techniques proposed and carried out to detect the local nucleation processes. However, these processes were not efficient enough to detect the global primary nucleation that occurs in the macro systems. This is due to the unpredictability associated with discovery of the nucleation sites in the macro hydrate reactors. Even though, detection and physically observing primary nucleation process, the progressive nucleation could be perceived through induction time. Hence, through this study, an attempt has been made to detect the induction times experimentally to validate the theoretical induction time equation (equation 3.24) proposed in this study.

Before conducting the hydrate, formation experiments, the reactor was cleaned and removed of pre-existing gases through vacuuming. Thereafter, the guest gas was sent into the reactor under the hydrate operational pressure conditions for the process of gas dissolution. The temperature was maintained at a considerably high value (287.15K), to ensure no hydrate formation during this process. The gas supply data was collected and observed for its asymptotic value. Once the solution became saturated with the dissolved gas into the aqueous phase, the system temperature was set to the hydrate formation temperature (274.15K) to encourage the hydrate formation as well as the time was set to zero. For CO_2 and CH_4 hydrate formations, the operational pressures 3.5 MPa and 12 MPa were chosen. The system was observed for exponential gas uptakes as well as the temperature fluctuations to detect the induction times.

3.4. Results and discussions

3.4.1. Dissolved gas concentration in aqueous medium

As this study bases the nucleation model proposed by Kashchiev and Firoozabadi, their definition of gas dissolution was considered in this study (Kashchiev and Firoozabadi, 2002b). Instead of conventional terms for measuring concentration such as molarity, molarity or mole fractions, their study considered number of molecules of gas per unit volume of water. The values of guest gas concentrations in aqueous phase were converted into molecules per unit volume of water in all the six cases to fit to the models.

By comparing the gas concentration isotherms and isobars from the figures 3.2 and 3.4, it was clearly seen that the extent of gas dissolution of CO_2 would be ten times higher than CH_4. It further implicates that the availability of CO_2 for hydrate formation in the aqueous phase would be ten times higher than the availability of CH_4. The deviations of aqueous phase gas concentration isotherms and isobars of other cases from case 2 were shown in the figures 3.3 and 3.4. As seen in these figures, apart from the case one, which depicts the ideal gas and solution conditions, none of the other cases showed the exponential deviations with either pressure or temperature. The profiles of rest of the cases showed deviations that were either asymptotic or decreasing in nature, while showing significantly less magnitude from the case 1. However, the deviations of isotherms from the cases 5 and 6 were shown the tendencies of negative values in the case of methane at higher temperature conditions. Apart from these exceptions, in all the cases, the deviation values of both isotherms and isobars resulted in positive values. Except from the case 1, the rest of the cases were resulted in higher deviations at lower pressure and higher temperature values. In addition, these deviations were found to be higher for CO_2 rather CH_4. Considering all these observations, it was understood that the modelling requires higher precision for less hydrate formation conditions such as higher temperature, lower pressure and CH_4 so as to calculate gas dissolution values accurately.

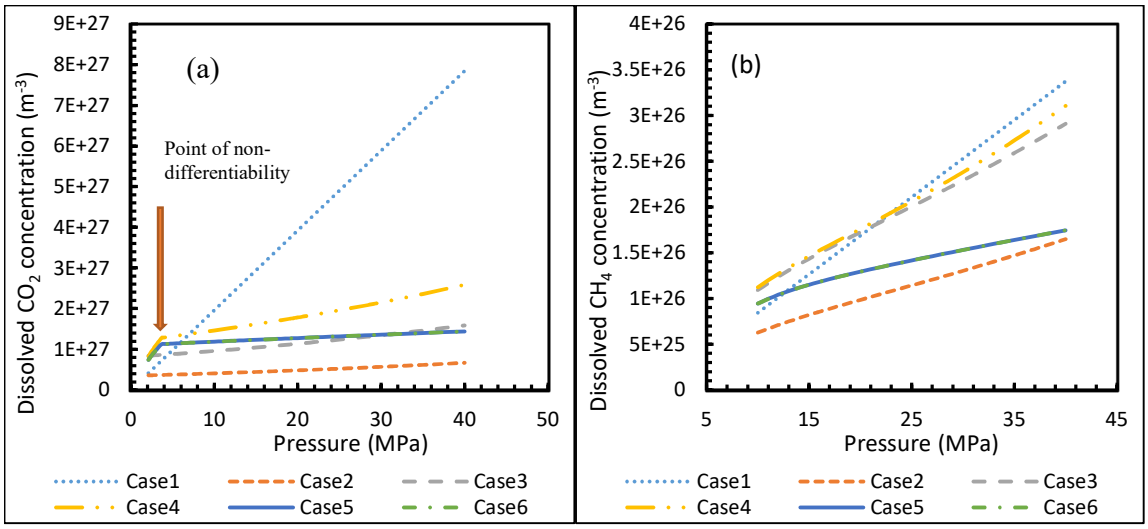

Figure 3.2. Dissolved gas concentration profiles for CO_2 (a) and CH_4 (b) under isothermal conditions into water at an operational temperature of 273. Points of non-differentiability were absent in the first three cases, while they appeared from the case 4. The values profiles of 5 and 6 have been overlapped with each other

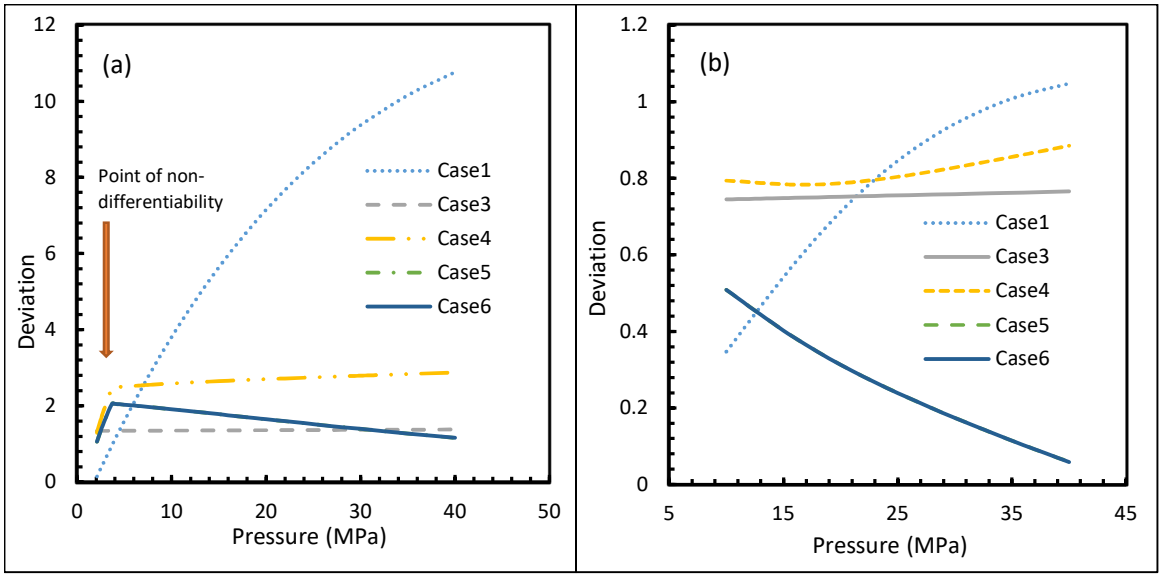

Figure 3.3. The case-wise deviation profiles of gas concentration from the base case 2 for the gases CO_2 (a) and CH_4 (b) under the isothermal conditions with the system being operated at 273.2K. These profiles highlight the points of non-differentiability more than the profiles shown in the figure 3.3. The case 1 addressing the idea gas scenario showed an exponential deviation with respect to pressure from the base case 2.

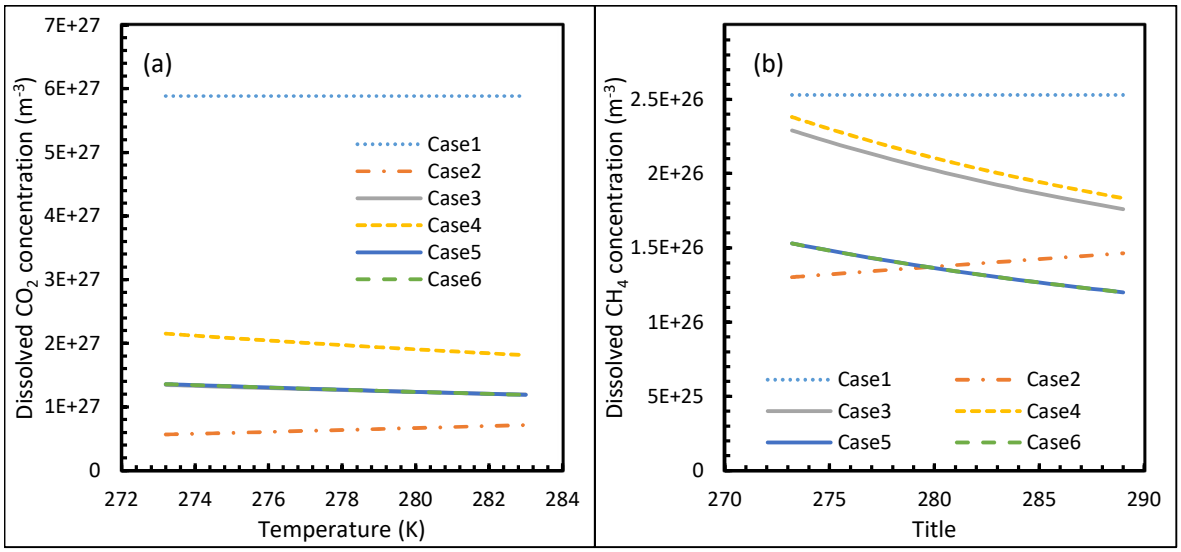

Figure 3.4. Dissolved gas concentration profiles for CO2 (a) and CH4 (b) under isobaric conditions into water at an operational pressure 30MPa. Due to the lack of temperature variable parameter in the case 1, the ideal case (Case 1) showed no change in its profile. Similar to figure 3.3, the values of case 5 overlapped with case 6.

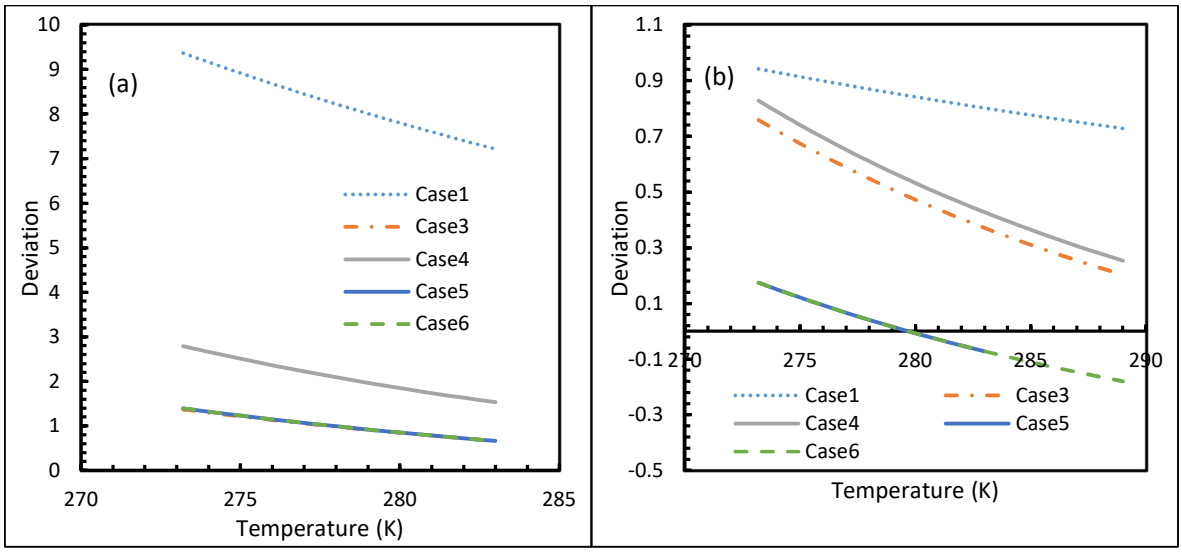

Figure 3.5. The case-wise deviation profiles of gas concentration from the base case 2 for the gases CO_2 (a) and CH_4 (b) under the isobaric conditions with the system being operated at 30MPa. These deviations from case 2, however, reduced as the temperature increased. The deviations were profoundly higher in case of CO_2 guest gas.

From the figures 3.2 and 3.3, except for the cases 1 and 2, a point of non-differentiability was observed in the case of CO_2. A point of non-differentiability is the point on a profile, where more than a single tangent is possible. Typically, this point would be situated at the intersection of two continuous curves.

This point of non-differentiability was observed at 3.5MPa pressure on the isotherms of CO_2 concentration in aqueous phase, which according to Duan et al (2002) was the bubble point pressure of CO_2. An extensive explanation over the effect of bubble point pressure on the nucleation parameters was explained in the section 3.4.2. The dissolved gas concentrations of the cases 5 and 6 were similar to each other while the case 4 showed an overall positive deviation in the case of CO_2. For CH_4, nevertheless, these values obtained in case 5 and 6 were comparable to that of case 2. The anomaly observed in case 4 were contributed by the assumptions made with respect to the chemical potential. These gas concentration in the aqueous phase profiles as well as their respective deviation profiles were used in the further analysis of nucleation parameters so as to understand the influence gas availability in the hydrate formation medium (aqueous phase) on the nucleation process.

3.4.2. Rate of Nucleation

As observed from the section 3.4.1, the availability of CO_2 in the aqueous phase was considerably higher to CH_4. Analogous to this statement, CO_2 hydrate nucleation was observed to be considerably faster than CH_4. CO_2 hydrate nucleation was observed to have instigated at the pressure as low as 2.1MPa at 273.2K, where the nucleation rates touched $10 m^{-3} s^{-1}$, while CH_4 hydrate formation was initialized at pressures as high as 11MPa and was comparable to the observations made by Kashchiev and Firoozabadi (2002b). Under the isobaric conditions, CO_2 nucleation showed an earlier depletion at lower temperatures than CH_4 nucleation, except for the case 6, which can be seen in the figure 3.10.

As seen from the equation 17, the rate of nucleation is linearly proportional to the concentration of dissolved guest gas. Thus, the case wise deviation profiles of CO_2 and CH_4 hydrate nucleation rates matched the gas concentration profile deviations except for the case 6, which has been seen in the figures 3.7 and 3.10. However, the nucleation rate deviations observed in the case 6 were profoundly higher, which refers to an intense sensitivity of nucleation rates towards the driving force as explained in the section 3.1. As the governing factor of the driving force was the fugacity of the guest gas value, it could be understood that the rates of nucleation were highly sensitive to the fugacity values. For example, the rates of nucleation for CO_2 at 5MPa and 273.2K was calculated to be $3.28x10^{28}$ $m^{-3}s^{-1}$ for case 6, whereas the value was $9.98x10^{12}$ $m^{-3}s^{-1}$ in case of case 2 as shown in the figure 3.7a. The hydrate nucleation rates have been deviated excessively at lower pressure conditions and then decreased as the pressure increased further. These deviations increased with the increase in temperature (figure3.6 and figure 3.9). Hence, it could be concluded that the deviations were lower at hydrate favourable operational conditions and vice versa. However, the hydrate nucleation profiles of CO_2 have deviated more from case 2 than CH_4.

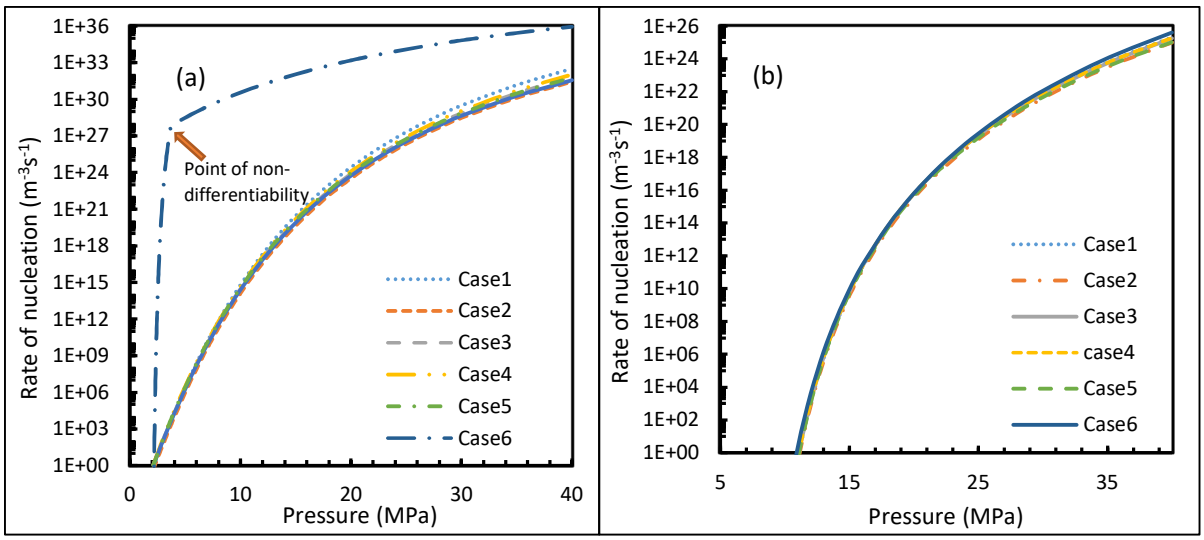

Figure 3.6. The nucleation rate profiles for CO_2 (a) and CH_4 (b), under isothermal conditions with operational temperature 273.2K. High nucleation rates of CO_2 has been shown in these profiles when compared to CH_4 as guest gas. Contrasting the profiles shown in the gas dissolution (figure 3.2), the point of non-differentiability was seen only in the case 6.

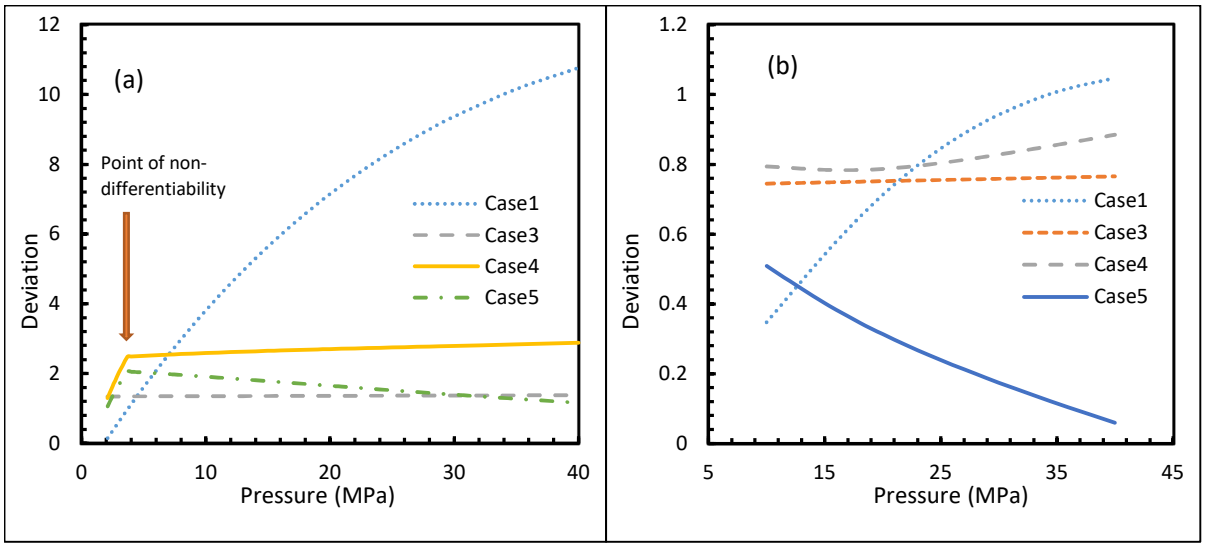

Figure 3.7. The case-wise deviations of CO_2 (a) and CH_4 (b) nucleation rates of cases 1-5 under isothermal conditions with the reference temperature 273.2K. These profiles followed the same structure of the profiles resulted in the figure 3.3 (deviations of dissolved gas concentrations)

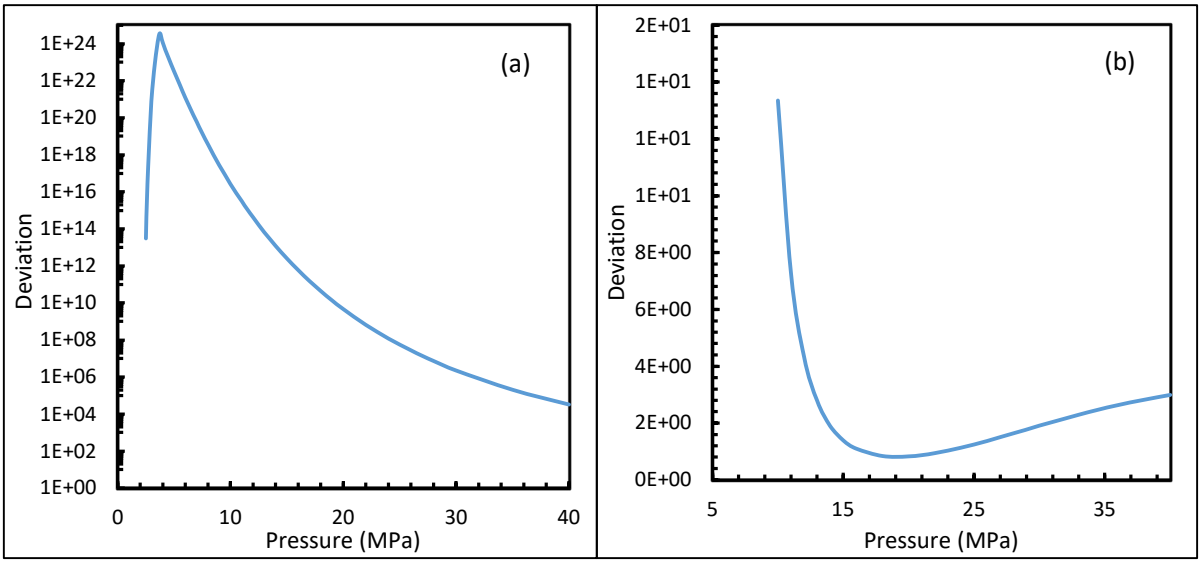

Figure 3.8. The deviations of CO_2 (a) and CH_4 (b) nucleation rates of the case 6 under isothermal conditions with operational temperature 273.2K from case 2. The profiles generally showed asymptotic curves where the deviations yielded to a particular value under high pressure conditions. Higher deviations were observed in case of CO_2 when compared to CH_4. For CH_4, either at lower pressure conditions or hydrate unfavourable conditions, high deviations were observed.

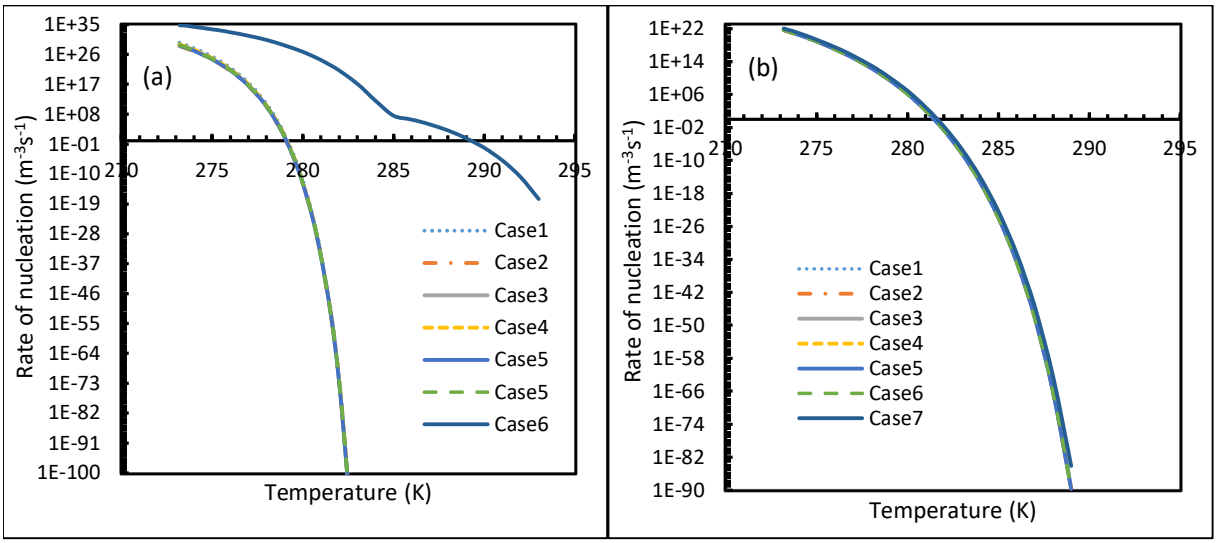

Figure 3.9. The isobaric nucleation rate profiles of CO_2 (a) and CH_4 (b), at a reference operational pressure of 30MPa. The profiles of all the cases except for the case 6 clearly show earlier depletions in CO_2 nucleation rates at relatively lower operational temperatures as compared to CH_4, In addition, similar to the figure 7, the point of non-differentiability is seen only in case 6.

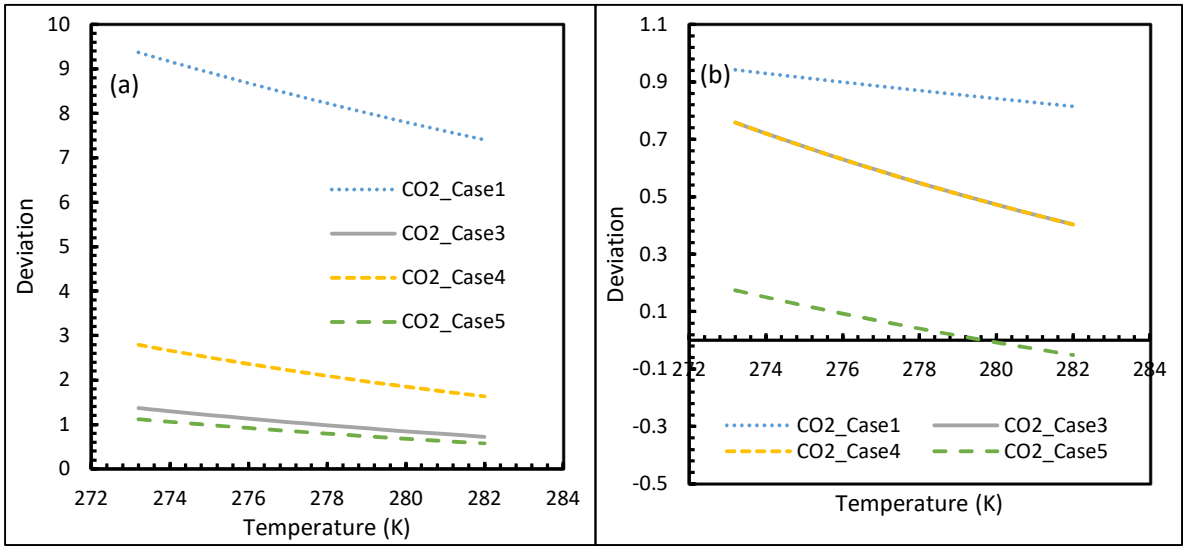

Figure 3.10. The case-wise deviations of CO_2 (a) and CH_4 (b) nucleation rates of cases 1-5 under isobaric conditions with the reference pressure 30MPa from case 2. The profiles have been resulted similar to the profiles shown in dissolved concentration.

Despite noticing the similar profiles of deviations in both the isotherm and isobars of hydrate nucleation rates and the gas concentrations, the point of non-differentiability was found only in the case 6 of nucleation rate profiles. This reflects upon the negligible influence of the gas

concentration in the liquid over the qualitative behaviour of the hydrate nucleation process as much as the guest gas fugacity. It has been observed that the CO_2 and CH_4 would differ from each other in terms of their phase behaviour under the considered operational conditions. As the compressibility of CH_4 was negligible in these conditions, CH_4 was understood to be a near ideal gas while CO_2 was understood to be a real gas.

To explain it further, the figure 3.12 could be taken as reference. As it is shown in the figure, the compressibility factors of the guest gases CH_4 and CO_2 were plotted against operational pressures. To be specific, under the given operational conditions, CO_2 can change its phase from gas to liquid and vice versa, while CH_4 cannot. Hence, CH_4 was observed to be a super-critical fluid and hence no point of non-differentiability was found in case of CH_4 as it was seen in case of CO_2.

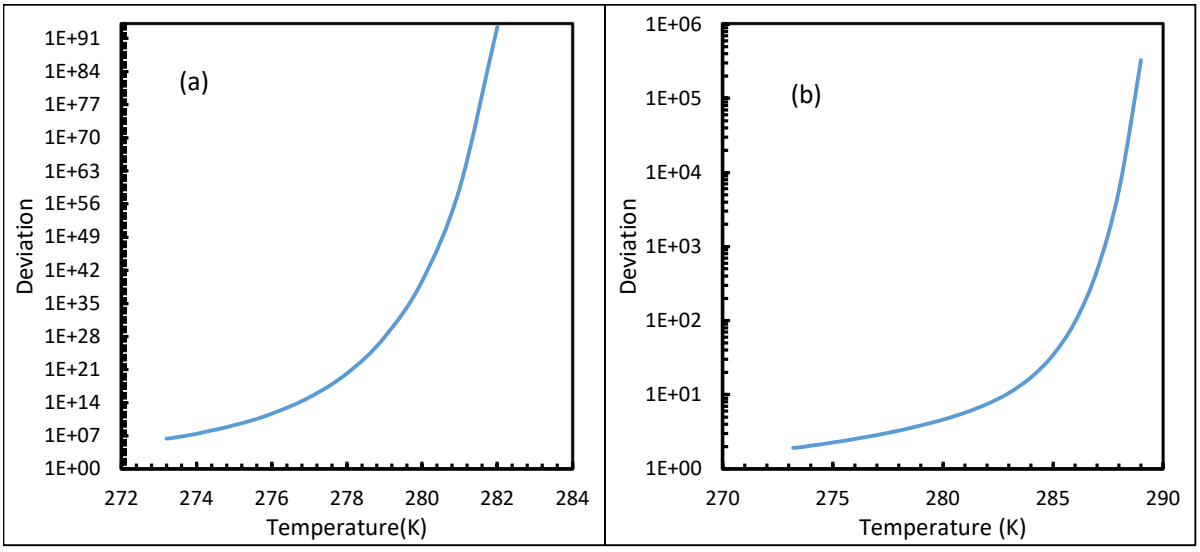

Figure 3.11. The deviations of CO_2 (a) and CH_4 (b) nucleation rates of the case 6 under isobaric conditions with operational temperature 30MPa, from case 2. Contrary to the rest of the cases, less deviations at lower temperatures (hydrate unfavourable conditions) were observed in both the gases. Relatively CO_2 nucleation rate showed profound deviation from case 2.

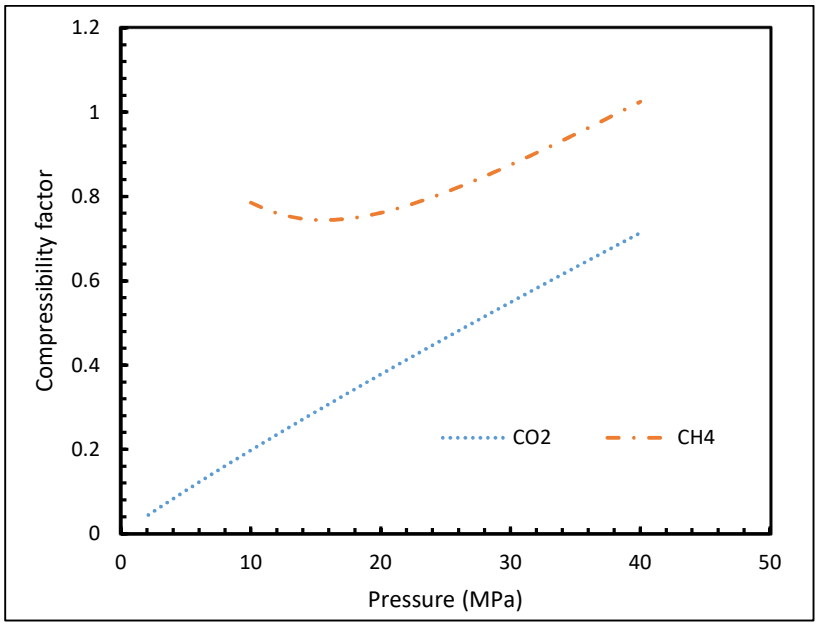

Figure 3.12. Compressibility factors of CH_4 and CO_2 under the considered operational conditions.

Most of the conventional models calculating the gas dissolution into liquids comprised of empirical formulations, where the internal parameters were adjusted so that the final result would implicate the nearest practical value under the operational conditions. Contrasting the profiles of the rest of the cases, case 6 produced the nucleation rates with a point of non-differentiability in its isotherms, which explains the profound sensitivity of the Kashchiev and Firoozabadi's model towards the nature of the gas in terms of its fugacity. To understand how the fugacity of the gases were changing with pressure, the isotherms of fugacity calculated from PR and Duan models were plotted against pressure and temperature respectively in the figure 3.13 and 3.14. Similar to the rates of nucleation a point of non-differentiability was found in the isotherms of CO_2 fugacity. However, in the isotherms of CH_4 fugacity it was absent, which explains the smooth profiles of nucleation rates in case of CH_4. Nevertheless, a considerable deviation of case 6 from case was observed at higher pressure conditions.

The point of non-differentiability was not just limited to isothermal analysis as it was also observed in isobaric analysis as well. The point of non-differentiability caused higher CO_2 hydrate nucleation rates at higher temperatures in case 6 than the rest of the cases. Generally, at higher temperatures, such as the temperatures over 285K, CO_2 hydrate nucleation rates plunged to lower values than CH_4 nucleation rates. However, for case 6, the rate of nucleation values at 30MPa and 285K were derived to be 3.67×10^{7} $m^{-3}s^{-1}$, while for CH_4, this value was derived to be 4.25×10^{-23} $m^{-3}s^{-1}$. The values for CO_2 hydrate nucleation rates for the rest of the cases were found to be less than 10^{-100} $m^{-3}s^{-1}$. Contrasting the isothermal observations, here the point of non-differentiability was not explained from the profiles of fugacity. It was observed to be the point at which the bubble point pressure crosses over the hydrate equilibrium pressure as shown in the figure 3.14. In order to produce more practicable values of gas dissolution into water, Duan et al. (2003), proposed various sets of fugacity correlations depending upon operational temperature conditions. The crossover of bubble point pressure with equilibrium pressure with operational temperature triggered the change of fugacity correlation which influenced the supersaturation ($\Delta\mu$) value. As explained in the section 3.1, the hydrate nucleation rates were highly sensitive towards supersaturation values. The change in supersaturation profiles resulted in the higher rates of CO_2 nucleation at higher temperatures. According to Chapoy et al (2014), the hydrate-water equilibrium pressure for CO_2 hydrates experiences an exponential growth at higher temperature conditions when considered the equilibrium pressure of CH_4 hydrates. These observations were further supported by the experimental studies of Daraboina et al., (2014) and Aresta et al., (2016). From these observations, it can be understood that the higher nucleation rates of CO_2 hydrates at higher temperatures derived from the case 6 were greatly deviated from the practical observations. Hence, it could be concluded that the fugacity values produced by the semi-empirical formulations of Duan's model has failed to produce practicable values, despite contributing to

the model in producing accurate values of CO_2 dissolution for a wide ranges of temperature and pressure conditions.

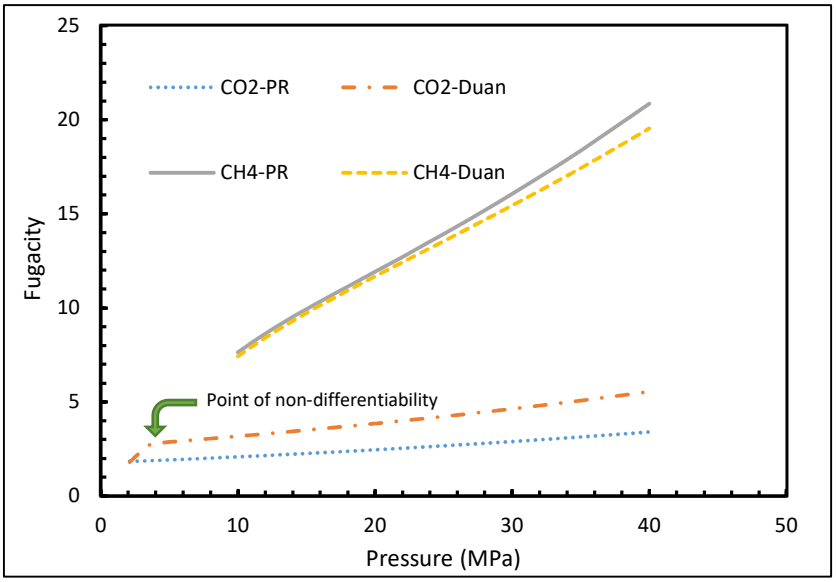

Figure 3.13. Comparison of fugacity calculated from PR and Duan models for CO_2 and CH_4

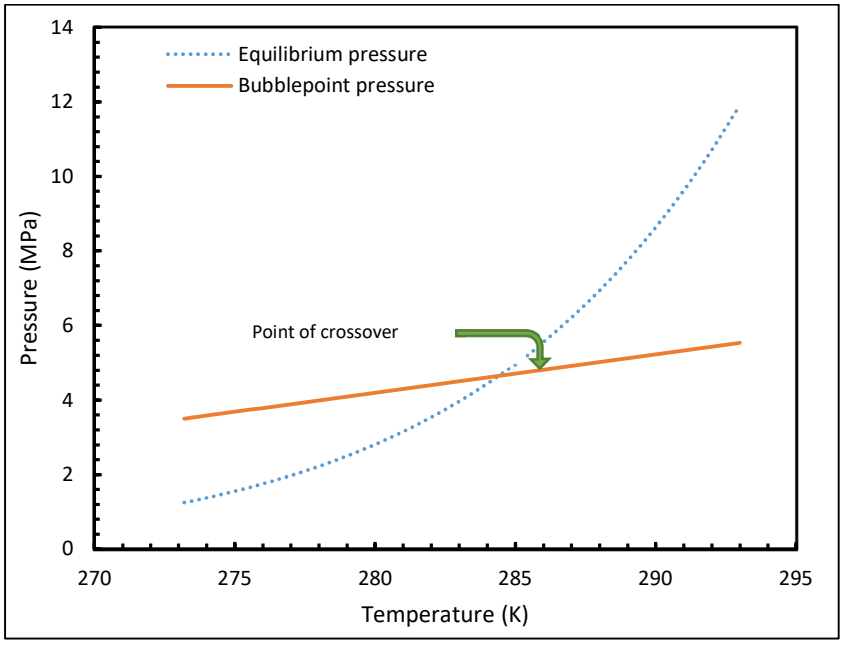

Figure 3.14. Bubble point pressure and equilibrium pressure profiles of CO_2 under the considered operational temperatures. The point of crossover at 285K has been clearly seen in this figure.

3.4.3. Induction time validation and sensitivity

The induction times of both CO_2 and CH_4 hydrates were calculated by using the equation 3.24 and analysed through isothermal and isobaric conditions. Due to the assumptions involved in the current study, especially because of the assumption that considers progressive nucleation, the practicability of the equation 3.24 might be limited. This study derived various induction times values of both CO_2 and CH_4 hydrate formations under a wide range of temperature and pressure conditions to understand under what conditions they are experiencing higher extents of case-wise deviations. It also enabled the study to calibrate the equations through a cross-comparison of derived induction time values with the experimental observations. The enormous difference between the speeds of nucleation for both CO_2 and CH_4 could be observed from the figures 3.15 and 3.17. The rapidity of CO_2 hydrate formation was clearly depicted by the figure 3.15, while suggesting longer induction times for CH_4 hydrate formations.

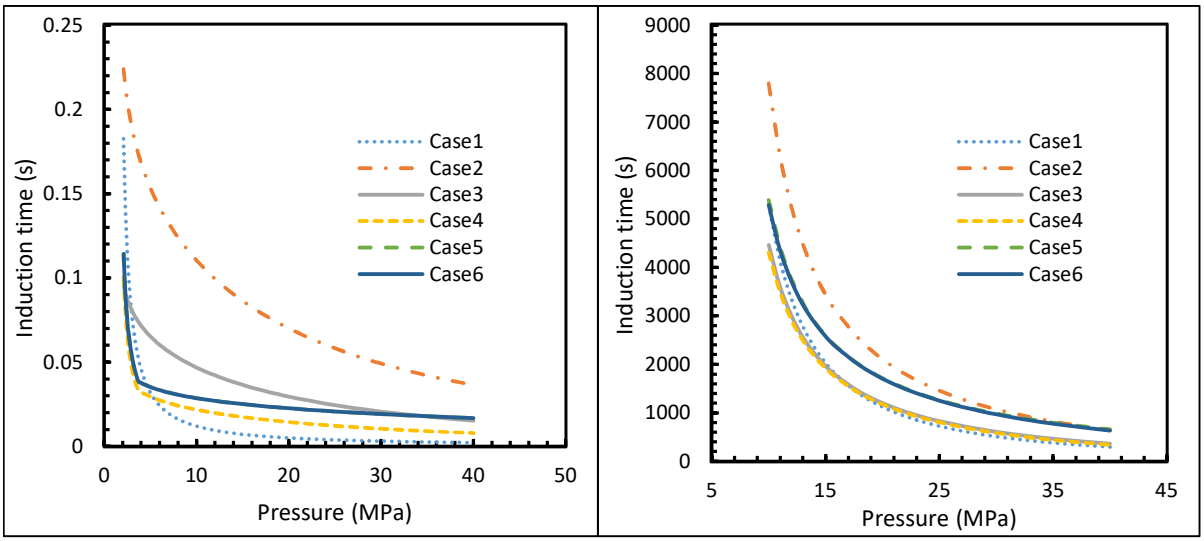

Figure 3.15. Theoretical CO_2 (a) and CH_4 (a) hydrate induction time profiles, under isothermal conditions with reference temperature 273.2K. Through these asymptotic profiles relative rapidity of CO_2 nucleation can be clearly seen, which has been seen in the values of CO_2 hydrate theoretical induction time. The point of non-differentiability has been observed in CO_2 induction time profiles, which was similar to the concentration of CO_2 profiles shown in Figure 3.3a.

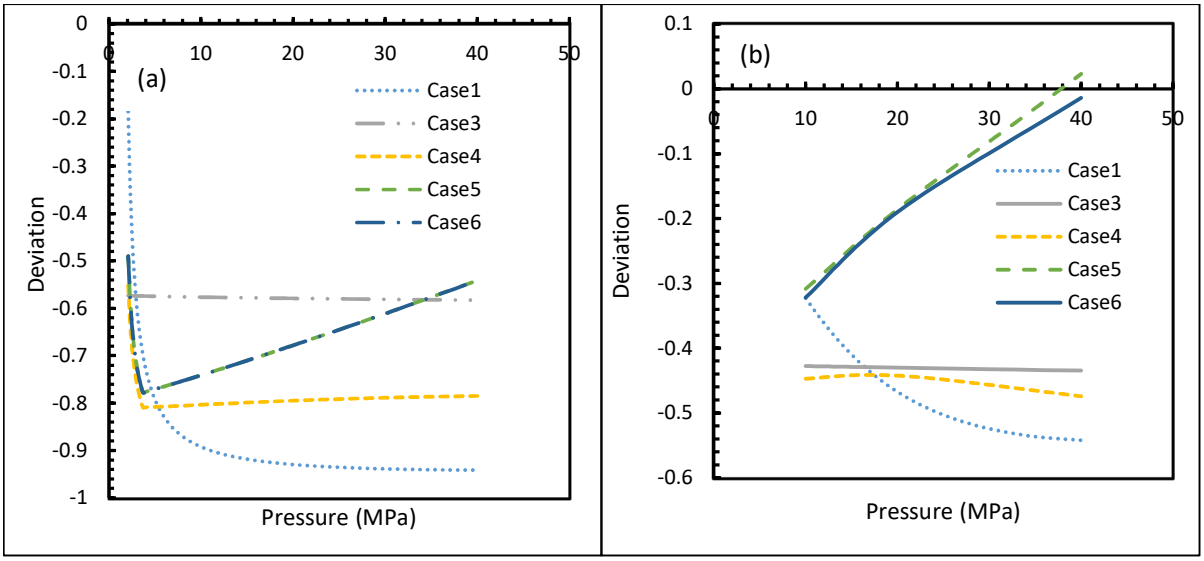

Figure 3.16. The case-wise deviations of CO_2 and CH_4 hydrate theoretical induction times under isothermal conditions with operational temperature 273.2K, from case 2. The shapes of these [profiles were similar to the deviation's profiles of hydrate nucleation when they were inverted with respect to X-axis. Cases 4, 5 and 6 showed the point of non-differentiability for CO_2 denoting the phase changing tendencies of the gas. In addition, in the profiles of cases 5 and 6, a tendency of shifting into positive deviation has been observed.

As it was shown in the figures 3.16 and 3.18, the case wise deviations of the induction time profiles were not as divergent as nucleation rate profiles. This might be because of the lack of exponentiality associated with the lack of exponentiality in the equation 3.24. Contradictory to the rates of nucleation values, the point of non-differentiability was found in the cases 4 -6. It means, unlike the rate of nucleation profiles, the induction time profiles were able to express the phase change behaviours of CO_2 gas in the cases 4 and 5 as well. After 3.2MPa, for the cases 1 and 2 showed steeper profiles compared to the cases 5 and 6. It implies the difficulty of hydrate formation with CO_2 in liquid state. This difficulty was further confirmed from the figure 3.16 where the deviation profiles turned from negative values to the positive values with pressure.

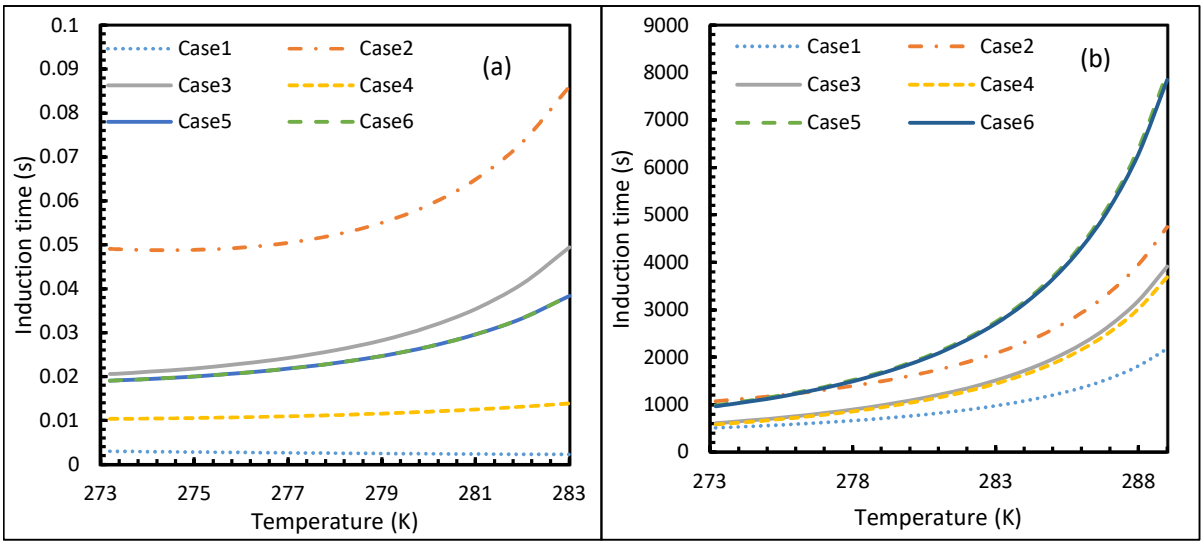

Figure 3.17. CO_2 (a) and CH_4 (b) hydrate theoretical induction time profiles, under isobaric conditions with operational pressure 30MPa. Even though, the nucleation rates were depleted at lower temperatures increase of CO_2, the theoretical induction times were observed to be considerably lower when compared to CH_4.

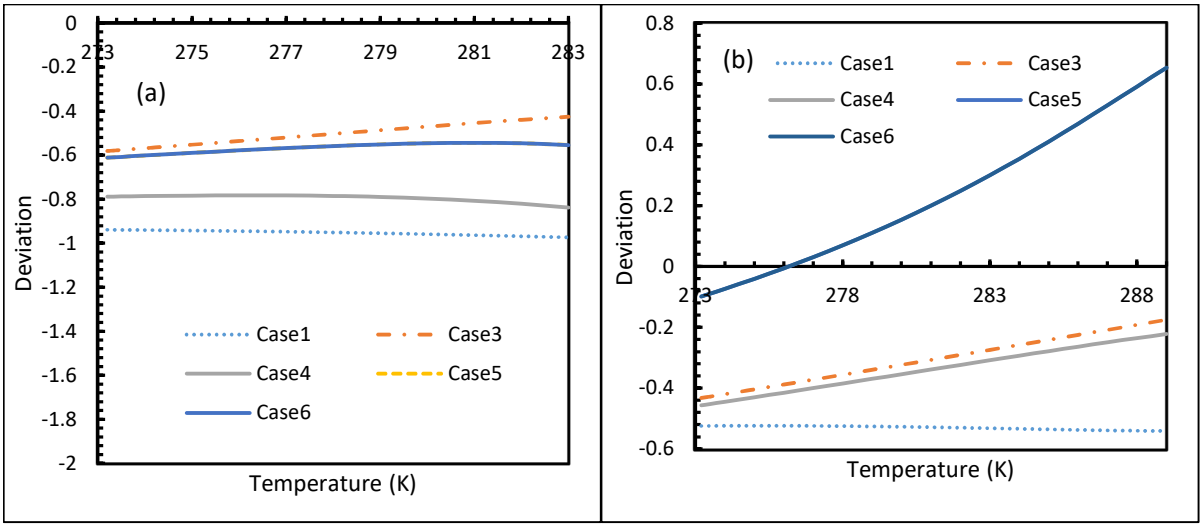

Figure 3.18. The case-wise deviations of CO_2 (a) and CH_4 (b) hydrate theoretical induction times under isobaric conditions with operational pressure 30MPa, from the case 2. These profiles were analogous to figure 3.17, from the perspective of their similarity to their respective nucleation profiles. The cases 4, to 6 showed the point of non-differentiability referring the phase-change behaviour of CO_2. Even though, the deviations showed tendencies to shift from negative values to positive values, the actual shift was only seen in case of CH_4 after 277 K in the case 6.

For the numerical quantitative analysis of theoretical induction times, the values of CO_2 induction time were found to be 0.029s, whereas it was 5200s for CH_4 at 10MPa and 273.2K. Under the operational conditions of 30MPa and 285K, CO_2 induction times were measured to be 0.051s, while this value was calculated to be 3600s for CH_4. As explained in the section 3.1, there have been numerous ways in detecting/observing the induction times practically. However, for the theoretical calculation of induction time, the universal definition and the method is yet to be developed. Amongst all the definitions available, the most practicable definition could be the point on time scale where the hydrate growth would become spontaneous under the given operational conditions.

Even after achieving the steady state, the speed of hydrate growth does not need to be with higher kinetics as the kinetics are governed by the factors such as operational pressure, temperature, guest gas attributes, chemical composition of both the liquid and gaseous states and the available physical interventions. The speed of hydrate growth could potentially make the difference in the obtained values of induction times from one detection technique to another technique. For example, Kashchiev and Firoozabadi (2003) considered the volume fraction of the hydrate as the determining criteria to detect the induction time. They suggested the temporal evolution of the intensity of light passed through the hydrate reactor as the detection technique. According to them, the time at which the hydrate volume fraction reaches a certain value was considered as the induction time. However, when compared to the time at which the hydrate growth becomes spontaneous, the induction time considered by Kashchiev and Firoozabadi could either be an earlier point or the later point on time depending upon the speed of hydrate growth which would be dependent upon the hydrate formation conditions.

Hence, the induction time would be profoundly subjective towards the perception or the interpretation of the researcher. The resultant error would be even intensified when the study focuses upon the hydrate formation under the less hydrate formation conditions such as low

pressure, high temperature or in the presence of less hydrate forming guest gas. Thus, even though the nucleation model proposed by Kashchiev and Firoozabadi was used as the base of this study, their induction time was not considered. However, their correlation for progressive hydrate growth was taken into consideration to derive the equation 3.24, which has been used to calculate the induction time.

As shown in the figures 3.16 and 3.18, similar to the deviations of dissolved gas concentrations in the aqueous phase, the deviations of the CO_2 hydrate induction times showed either asymptotic or decremental profiles with pressure or increasing profiles with temperature with less magnitude apart from the case 1. Nevertheless, the isobars of methane induction time profiles derived from the cases 5 and 6 were seen to be progressed positively from the case 2 with temperature. Hence, it could be concluded that the correlations of induction time and the correlations of its internal parameters require more accuracy at high temperature and low-pressure conditions, while for CH_4, these observations were only restricted to low pressure conditions.

In addition to the calibration of theoretical induction time equation (equation 3.24) under a wide range of pressure and temperature conditions, its experimental practicability was validated through a set of hydrate forming experiments. Two experiments were conducted under the operational pressure conditions of 3.5 MPa and 12 MPa at 274.15K for CO_2 and CH_4 as guest gas respectively. Since this study was mainly focussed upon the hydrate formation phenomenon under the quiescent conditions, no chemical additives or physical interventions were considered for the experiments.

After the gas dissolution into the reactor at higher temperature and operational pressure, when the temperature was set to the experimental temperature, an immediate gas consumption was observed. There could be four contributing factors for this gas consumption:

1. Gas contraction at lower temperature
2. Excess gas dissolution into water at lower temperature
3. Hydrate formation.
4. Volume contractions of the aqueous+hydrate phase with the progression of hydrate formation

In order to detect the induction times, the volumetric contributions of gas consumptions by all these factors were calculated. From the experimental perspective, the time taken for the system to show the initial step change in the volumetric gas consumption after the temperature drop was considered to be the induction time. As observed by various researchers, for having less superficial energy barrier as well as the highest rate of cooling, hydrate nucleation is always initiated at the gas-liquid-wall interface (Ribeiro & Lage, 2008).

The experimental volumetric gas consumptions in case of both CO_2 and CH_4 hydrate formations were presented in the figure 3.19. Despite the primary nucleation was suggested to be heterogeneous, in accordance with the calculated induction times from the equation 3.24, a profound difference was found in the observed induction times of CO_2 and CH_4 experimental induction times. As suggested by the exponential profile of gas consumptions with time as shown in the figure 3.19b, the gas consumption contributed by the factors 1 and 2 were indistinguishable from 3 and 4. Nevertheless, the induction time of CH_4 was observed at 1700s (figure 3.19a). Thereafter, the surface energy of water with stainless steel surface was calculated by substituting the experimental induction times in the equation 3.24. The surface energy value was used to calculate the contact angle of water with stainless steel. This contact angle was used to validate the practicability of the equation 3.24.

Table 3.3. Contact angles calculated from the considered cases

S.No	Cases	Contact angle	Percentage deviation
1	Case 1	74.06135	11.87515
2	Case 2	59.81841	-9.63987
3	Case 3	77.2854	16.74532
4	Case 4	78.60491	18.73853
5	Case 5	68.69664	3.771358
6	Case 6	69.15816	4.468515

As it was seen in the literature, the contact angle of the water with the wall was dependent upon the roughness of the surface of the vessel the water was contained in as well as the material composition (Prajitno, et al., 2016). Typically, the contact angle of water with stainless steel would be in between 60^o-80^o when used a smooth surface (Kalin & Polajnar, 2014). According to Kalin and Polajnar (2014), the contact angle between water and the stainless steel would be 66.2^o when taken the smooth wall surface. The contact angles of water and the stainless-steel surface were calculated using six cases as well as their respective deviations from the literature value and listed in the table 3. As seen from the table, cases 5 and 6 resulted in relatively least errors with the percentage deviation less than 5%. Validating the accuracy of the cases 5 and 6 for the considered operational pressure and temperature conditions.

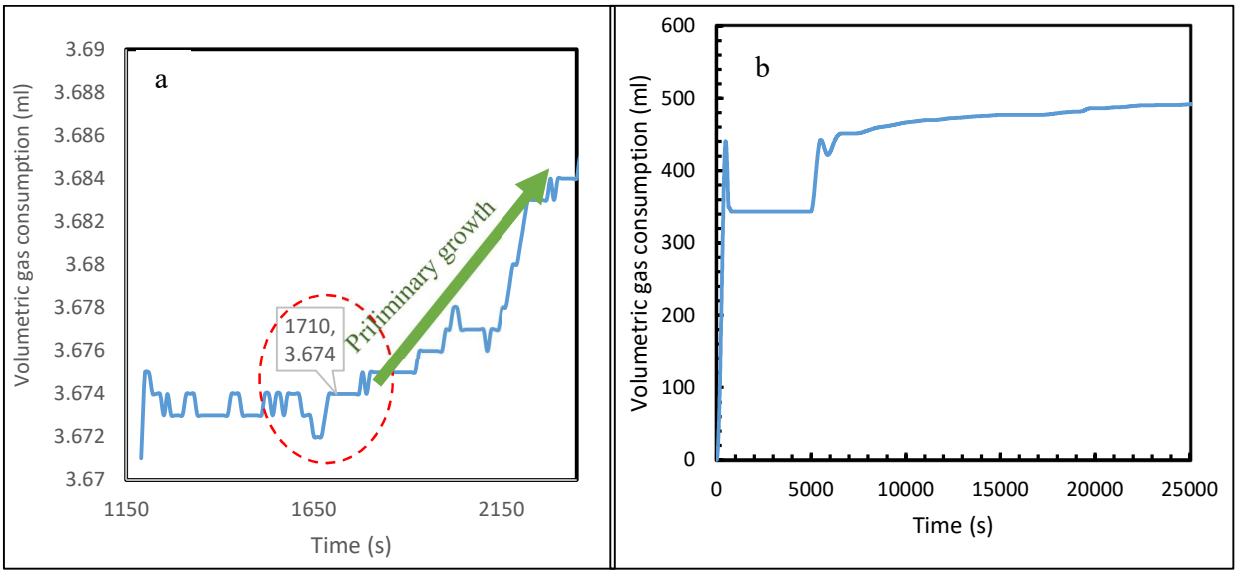

Figure 3.19. The volumetric consumptions of gases CH_4(a) and CO_2(b) during hydrate formation. Due to the exponential hydrate formation in case of CO_2, induction time was more visible in the case of CH_4.

3.4.4. Hydrate volume fraction at theoretical induction time

Figures 3.20 and 3.21 show the volume fractions of hydrate nucleation at the point of induction time calculated by the equation 3.24. For CO_2 nucleation, at pressures as low as 9-10MPa, the process achieved 100% conversion of water into hydrate, showing the rapidity of hydrate formation in case of CO_2 as guest gas supporting the experimental observations made in the section 3.4.3.

As observed from the induction times, CH_4 hydrate formation, required more pressure to reach the hydrate volume fraction to 100%. Amongst all the cases, the excessive hydrate formation was suggested by the case in for both CO_2 and CH_4 guest gases. Even though, a sharp rise in the total volume fraction was observed at lower pressure conditions in the case of CO_2 guest gas, similar to the profiles observed in the hydrate nucleation rates, an early depression in the total volumetric hydrate fraction at relatively lower operational temperatures were observed.

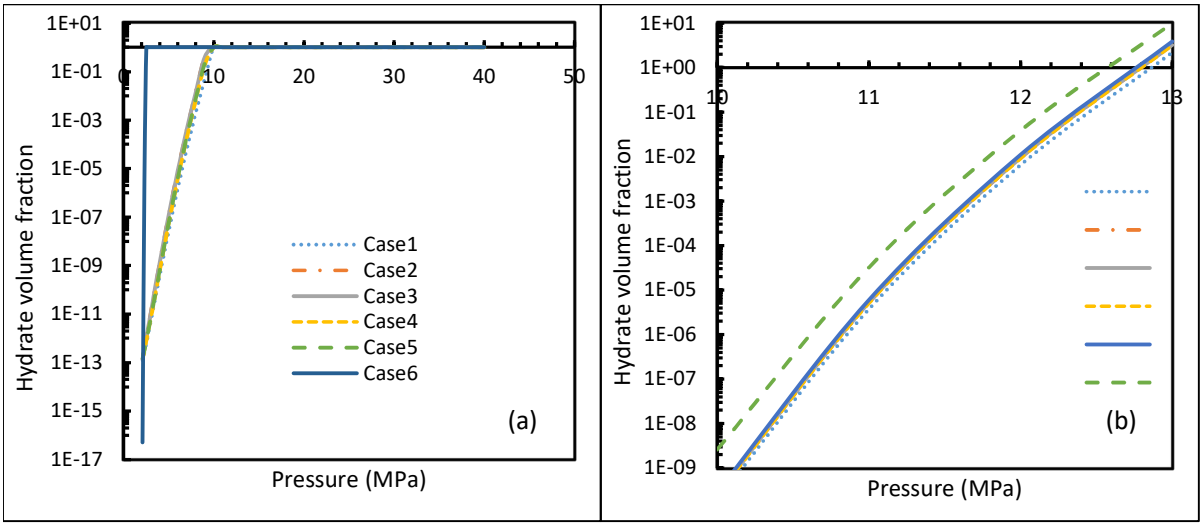

Figure 3.20. The case-wise CO_2 (a) and CH_4 (b) hydrate volume fraction profiles at the theoretical induction time under isothermal conditions with operational temperature 273.2K. These figures denote the rapid hydrate formation kinetics under sufficient pressure conditions adequate to show 100% water to hydrate conversion by the Kashchiev's induction time. In addition, an intense readiness of CO_2 towards hydrate formation at lower pressure conditions could be observed.

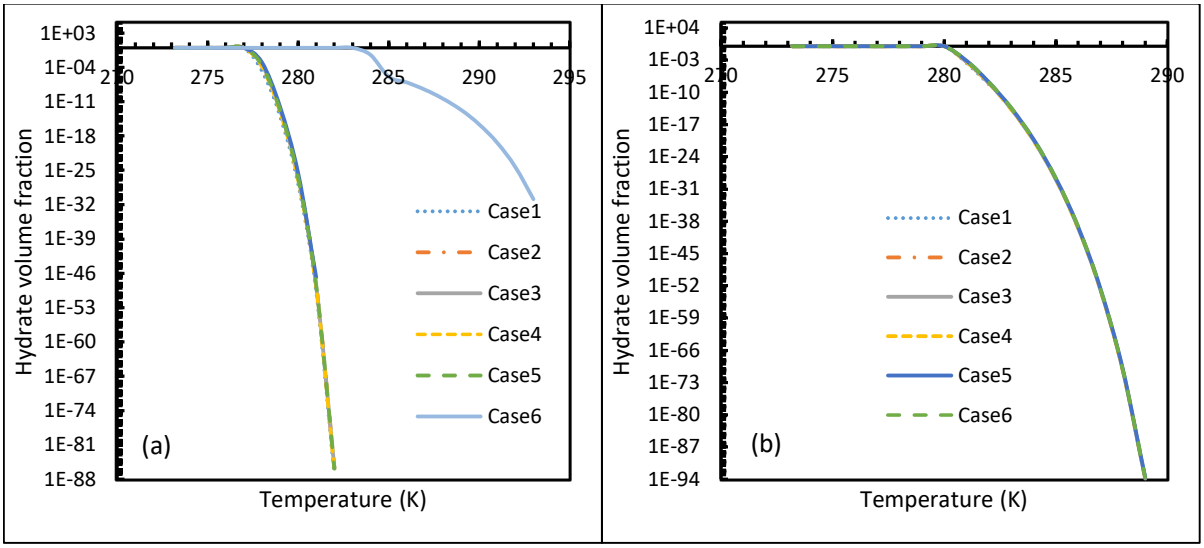

Figure 3.21. The case-wise CO_2 (a) and CH_4 (b) hydrate volume fraction profiles at the theoretical induction time under isothermal conditions with operational pressure 30MPa. From the figures it can be seen that a relatively lower hydrate volume fractions for CO_2 were seen compared to CH_4 at lower temperatures, which was contradicted by case 6 where a point of non-differentiability was seen.

However, case 6 showed a later depletion in the CO_2 hydrate volume fractions when compared to CH_4 as guest gas, which was against to the experimental observations, limiting the practicability of the case 6.

3.5. Summary

For the systems of CH_4 and CO_2 guest gases, their respective hydrate nucleation parameters such as rate of hydrate nucleation, hydrate volume fraction and induction times were analyzed for a range of hydrate favorable pressure and temperature conditions. For the calculation of dissolved gas concentrations and the fugacity for CO_2 and CH_4, various existing mathematical models were considered. By varying one correlation at time, a total of six cases were considered through which the intermediate parameters were calculated so that these parameters could be used to calculate the parameters of nucleation. From this comparative analysis, its been concluded that the researcher should be more cautious while utilizing either empirical or semi-empirical models to calculate the desired parameters as well as their modified versions to calculate intermediate parameters due to the concerns towards accuracy.

Between CO_2 and CH_4 as hydrate formers, higher deviations were found incase of CO_2 when compared to CH_4, which was because of the high tendencies of hydrate formation and hence high sensitivities towards hydrate forming conditions. Due to this reason, while calculating the parameters of CO_2 hydrate nucleation, the correlations or models are supposed to be more accurate to minimize the error. From the modification of the existing models, parameters such as volumetric volume fraction as well as theoretical induction time have been derived and their deviations with respect to the pressure and temperature conditions were presented in this chapter. Experiments were carried out to compare the theoretical induction time from this chapter with the experimental observations, which agreed well. Amongst all the cases, case 5 and 6 were observed to be more reliable in producing practicable values of induction time over the rest of the cases. However, case 5 has been observed to be more practicable when

considered both the rate of nucleation and the induction time. This suggests the researchers to calculate fugacity from both the theoretical as well as semi-empirical means to analyze the process of nucleation by using the method of Kashchiev and Firoozabadi.

As the required operational pressure decreases with the decrease in the operational temperatures, in order to decrease the cost of compression, it is important to choose the lower temperature conditions. Hence, while calculating the parameters of nucleation including the induction times, temperature near freezing point has been chosen, for which, the optimum operational pressure was found to be near 3.2MPa (Figure 3.15a). However, for the experimental analysis, a temperature of 274.15K has been used instead of 273.2K. Hence, an operational pressure of 3.5MPa has been chosen to assure the least induction times as well as CO_2 in the gaseous form.

Chapter 4

Hydrate formation for desalination

4.1. Introduction

As described in the chapter 2 there have been numerous studies carried out examining the performance of hydrate formation for various applications with experimental conditions suited to the chemical compositions of both the gas and the liquid. Additionally, the influence of various kinetic and thermodynamic additives as well as the physical interventions were analysed. Even though hydrate-based carbon capture and desalination techniques were understood to be relatively economical, these processes have not been established as industrial applications for the following barriers:

- Thermodynamic barrier that addresses the temperature raise in the hydrate formation system during the formation of hydrates because of the exothermic nature of the formation process.
- Physical barrier that addresses the difficulty of gas dissolution into water after the formation of hydrates across the gas-liquid interface.
- Requirement of high compression to deliver high pressure to carry out the hydrate formation process.
- Unavailability of reactor design to continuously produce and deliver hydrates.
- Low yields of final hydrate production

Additionally, the purity of CO_2 recovered in a single stage hydrate formation process from a post combustion gas mixture was less than 60% with a high-pressure requirement at low operational temperatures in the absence of an efficient thermodynamic additives. However, the recovery of CO_2 was directly proportional to the yield of hydrate formation with the exception

of hydrates being formed under the influence of other hydrate forming substrates such as thermodynamic additives (van Denderen, et al., 2009; Li, et al., 2010; Babu, et al., 2015).

As mentioned in the section 2.5.2 of the chapter 2, the involvement of the thermodynamic additives would result in hydrates which upon dissociation would require further distillation process to produce fresh water. Hence, the experiments conducted in this chapter did not involve thermodynamic additives. Alternatively, there have been numerous studies conducted to improve hydrate formation kinetics with the addition of various surfactants. They would not participate in hydrate formation directly but support the transfer of gas to the hydrate formation cite. Hence, the study considered the addition of various surfactants as kinetic additives. Even though, numerous studies tried to find the most effective surfactant towards improving the kinetics of hydrate formation, the governing factors behind the effectiveness of surfactant along with the proper reasoning have not been effectively established. In this chapter, an attempt was made to check the effect of heterogeneity of the solution. Hence, four surfactants have taken in the order of their solubility to check if heterogeneity of the solution has any effects on hydrate formation. Moreover, the surfactants were chosen in such a way, the study covers an analysis on surfactants with various carbon chain lengths as well as the charges on the hydrophobic end.

The combination of being one of the main contributors of global warming, its abundance in industrial gaseous emissions, and its high tendency towards hydrate formation under relatively low temperature and pressure conditions compared to other gases such as CH_4, N_2, H_2 or O_2 carbon sequestration through hydrate formation was well researched. This is the reason for opting CO_2 as the main guest gas for hydrate formation in this desalination studies. Even though, the main intended outcome of this chapter being the study of hydrate formation kinetics such as induction time and hydrate yield, the hydrate barriers and their influence upon the final hydrate yield were also analysed. Hence, instead of pure hydrate forming gas, a mixture of CO_2 and CH_4 were taken while the concentration of CH_4 was kept low. All the hydrate formation

experiments under quiescent conditions were conducted for two days, where volumetric gas consumption was taken as the measure towards the extent of hydrate formation in this study. Extrapolating the experiments, a cross comparison was made to check the effectiveness of stirring in improving the hydrate formation yield and the kinetics, stirring was included in the later experiments. The results were mainly discussed with respect to the effect of salt, CH_4, surfactant, from the perspective of kinetic and thermodynamic barriers towards hydrate formation.

4.2. Experimental procedure

4.2.1. Materials

These hydrate formation experiments were carried out to study the CO_2 hydrate formation kinetics in sea water in the presence of gaseous impurity CH_4 at low concentrations. The mixture of CH_4 and CO_2 is naturally found in crude oil and natural gas ores and CH_4 can actively participate in hydrate formation compared to N_2, H_2 and O_2 (van Denderen, et al., 2009). This active participation would highlight the influence of gaseous impurities towards hydrate formation. Hence along with the experiments in the presence of pure CO_2 as guest gas, a CO_2 + CH_4 gas mixture was prepared which is shown in table 4.1. Salt water was prepared in the configuration of sea water as explained in the study done by Nessim et. al., (2015) (Nessim, et al., 2015). Instead of considering all the minor salts, only three major salts contributing to the sea water salinity were considered.

While the molality of CO_2 was taken higher than required addressing the minor contributors of salinity. The saline water contribution is shown in table 4.1. Whereas the addition of salts and gaseous impurities were expected to provide barriers towards hydrate formation, to improve its kinetics 100 ppm of surfactants were added to the liquid phase. The material properties of these compositions are shown in table 4.2.

Table 4.1. Gas and saline mixture compositions

Component	Composition (mol%)	Mixture
CO_2	95.085±0.045	Gas
CH_4	4.915±0.045	Gas
NaCl	0.87±0.015	Saline
Na_2SO_4	0.056±0.001	Saline
$MgCl_2$	0.018±0.004	Saline

Table 4.2. Materials used in the experiments

Component	Supplier	Purity
NaCl	Sigma-Aldrich	99.5% (Mass%)
Na_2SO_4	BDH laboratory supplies, UK	99.0% (Mass%)
$MgCl_2.6H_2O$	Fisher Scientific, UK	99.5% (Mass%)
CO_2	Air products plc, UK	99.995% (Vol%)
SDS	Sigma-Aldrich	99.0% (Mass%)
CH_4	BOC, Edinburgh	99.995% (Vol%)
N_2	Air products plc, UK	99.995% (Vol%)
`Tween 20	Sigma-Aldrich	97% (Vol%)
Tween 80	Sigma-Aldrich	98% (Vol%)
CTAB	Sigma-Aldrich	98% (Mass%)

4.2.2 Operational Conditions

The operational conditions for these experiments were taken from the conclusions of the chapter 3, where the most optimum conditions with the least induction times were observed at approximately 3.2MPa under near freezing conditions. For the fact that the hydrate formation

is favoured by high operational pressure and low operational temperature conditions the system would require either high compressions or refrigeration (Tajima, et al., 2004). In order to reduce the cost of compression a temperature just above freezing point was chosen, which is 274K. As a further support, hydrate equilibrium pressures were calculated to ensure hydrate formation under the considered operational conditions. To check the hydrate equilibrium conditions in the presence of CO_2 and CH_4, the model proposed by Chapoy et. al., (2014) was used to generate the predictions which are presented in the figure 4.1 (Chapoy, et al., 2014).

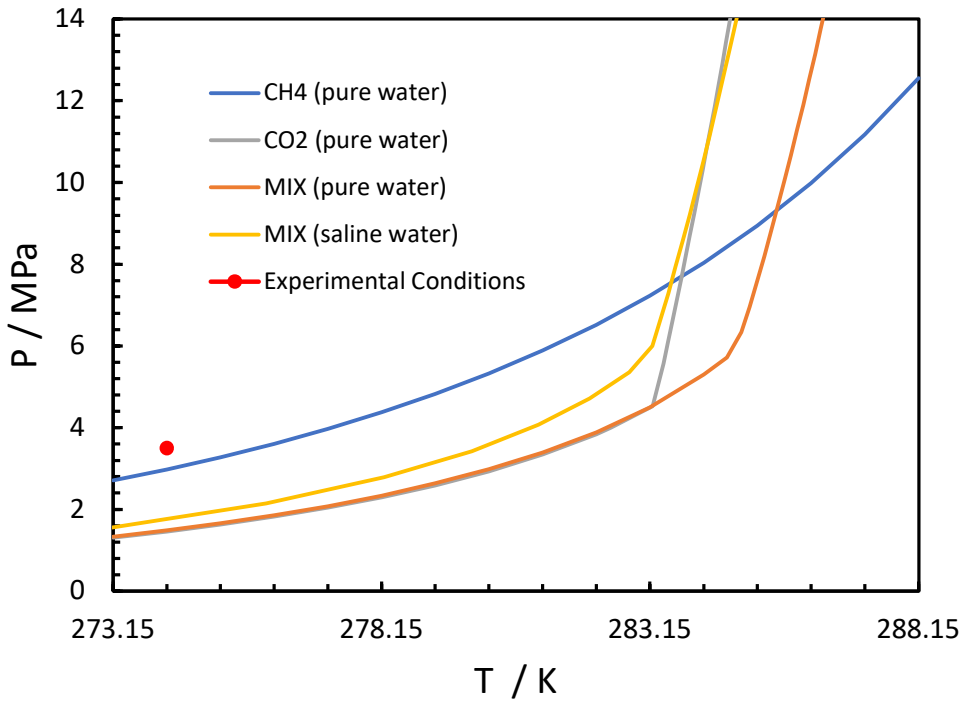

Figure 4.1. Hydrate equilibrium pressure data with temperature

However, as explained in the chapter 2 provision of equilibrium pressure under the given experimental temperature would not result in hydrate formation and hence the experimental pressure was chosen to be well above the hydrate equilibrium pressure in order to create driving force for the hydrate formation. Fakharian et. al., (2017) through his studies on CO_2 hydrate formation under various operational pressure conditions observed an unstable CO_2 hydrate formation at 5.5 MPa, while a stable CO_2 hydrate formation was observed at 3.5 MPa. It is also

important to understand that the Methane hydrate formation should not occur under the given hydrate formation conditions if at all Carbon sequestration was also aimed. Under the given temperature conditions (274.15K) with saline water having salinity of 3.5 weight percent. The CH_4 hydrate equilibrium pressure was 3.3 MPa while for CO_2 it is 1.6 MPa (Kashchiev & Firoozabadi, 2002; Fakharian, et al., 2017). As the experimental pressure for hydrate formation was 3.5MPa, which was comparable to CH_4 equilibrium pressure it is highly unlikely for the CH_4 hydrates to form. For these experiments, two reactors were chosen depending upon the requirement of physical interference: rocking cell reactor for quiescent conditions and stirred tank reactor to introduce stirring into the system.

Table 4.3. List of experiments conducted in this study

Exp.no.	System	Physical configuration	Experimental setup
1	CO_2+Distilled water	Quiescent	Rocking cell
2	CO_2+Saline water	Quiescent	Rocking cell
3	CO_2+CH_4+Saline water	Quiescent	Rocking cell
4	CO_2+CH_4+Saline water+SDS	Quiescent	Rocking cell
5	CO_2+CH_4+Saline water+Tween 20	Quiescent	Rocking cell
6	CO_2+CH_4+Saline water+Tween 80	Quiescent	Rocking cell
7	CO_2+CH_4+Saline water+DTAC	Quiescent	Rocking cell
8	CO_2+CH_4+Saline water+SDS	Stirring	Stirred tank
9	CO_2+N_2+Saline water+SDS	Stirring	Stirred tank

For reference, one can check the figure 2.2. Similar to the experimental procedure explained in the section 3.3, before commencing the hydrate formation experiments by providing the system with the required operational pressure and temperature conditions, the system was maintained

at higher temperatures (286.15K) to ensure full gas saturation into the liquid. Once the volumetric gas consumption reached to an asymptotic value, the temperature was lowered to 274.15K and the volumetric gas consumption in the data acquisition system was set to zero. Once the experiment was completed, the formed hydrate from the reactor was collected and subjected to the water activity measurements. These water activity measurements were done at 298.15K. The water activity data with respect to the concentration of salt in it was taken from USFDA (2012).

4.3. Results and discussions

The hydrate formation kinetics starting from the speed till the yield as well as the probable influencing factors have been discussed in this section. As stated in the section 4.2.2. the gas consumption was set to zero before lowering the temperature from 286.15K to 274.15K (operational conditions) and hence, the volumetric gas consumption occurred after lowering the temperature were the results of the following reasons:

1. As seen in the chapter 3, the extent of CO_2 dissolution would be higher at lower temperatures, which would contribute to the gas dissolution value at lower temperatures.
2. As the gas reaches to the operational temperature it contracts to accommodate more gas in the reactor, contributing to further gas dissolution. However, due to the negligible heat transfer coefficient of the gas, as well as higher inflow rates of gas at room temperature, under faster kinetics of hydrate formation, this was ignored.
3. Accelerated gas consumption from the gas phase into the liquid phase during the formation of hydrates could accommodate considerably high volumes of gas, causing more gas inflow rates. According to the current study, this has been observed to be the primary reason that contributed to the highest extent of gas consumption.

4. Hydrate has been considered to be lower in density compared to water+gas. During the hydrate formation, high volumes of water and gas are contracted into hydrate, causing more empty space for the gas to occupy, contributing to more gas consumption.

These experiments have been carried out for two to three days depending upon the gas consumption rates, so that there could be an opportunity to understand the gas consumption values for longer durations. Especially, the systems operated under quiescent conditions were carried out and compared amongst each other with the data collected for two to three days. However, the stirring experiment was stopped before 34 hours, because of the stirring was stopped prematurely due to the excessive hydrate formation in the reactor. The system with CO_2+distilled water under quiescent conditions from the chapter 3, was taken to be the base case, with which the rest of the experiments were compared from the perspective of speed and yield of hydrate formation.

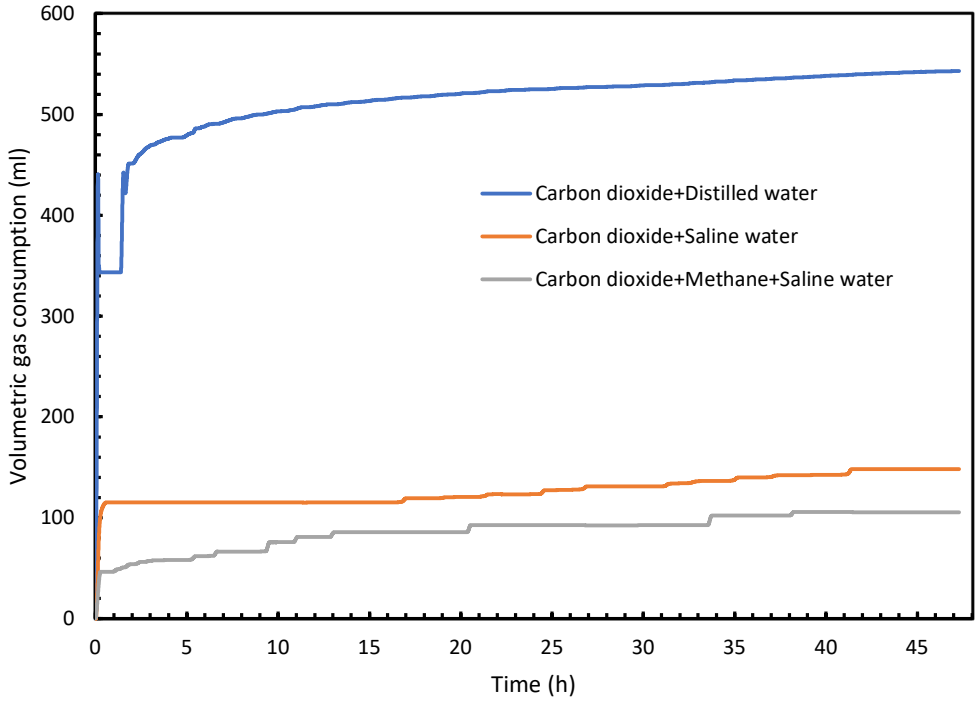

Figure 4.2. Effect of salt and CH_4 upon hydrate formation kinetics and yield

4.3.1. Effect of impurities in gas and liquid phases

Figure 4.2 shows how the presence of gaseous impurities like CH_4 and water pollutants such as electrolytes would affect the formation kinetics and yields of hydrate. For the base case, after lowering the temperatures from 285.15K to 274.15K, after 45 hours, a total of 542ml of volumetric gas consumption was observed, out of which 529ml gas consumption was contributed by hydrate formation alone. From the figure 4.2, the detrimental effect of salts upon the formation of hydrates. When replaced the distilled water with saline water with seawater configuration, a total of 148ml gas consumption was observed at the end of the second day, which was 73% less than the base case. In the next experiment, the inlet gas of pure CO_2 has been replaced by a gas mixture of 95%CO_2 +5mol% CH_4, at the end of the second day, a total volumetric gas consumption of 105ml was observed, which was 29% less than the previous experiment. With the addition of CH_4 to the inlet gas and the salt to the distilled water, the yield of hydrate formation has been plunged down 25% of its previous values from the base case.

4.3.2. Effect of surfactants

These observations signify the necessity of improving the hydrate formation kinetics as well as its yield through the available chemical and physical enhancers. The surfactants have been widely used to increase the hydrate formation kinetics as well as the final yield. As mentioned in the chapter 2, Surfactants are amphiphilic compounds consisting of a hydrophilic head and a hydrophobic tail and are mainly used to decrease the interfacial tension at various surfaces. As understood from the chapter 3, lowering the surface tension at the nucleation surface would lower the hydrate nucleation times as well as improve the kinetics of hydrate formation, which could be contributed by the surfactants. There have been numerous authors that worked upon assessing the effects of surfactants over the extent of hydrate formation by theorizing their mechanism in improving the hydrate formation process from various perspectives.

Authors such as Kalogerakis et al. (1993), Karaaslan and Parlaktuna (2000) and Kumar et al (2013), examined the efficiency of various surfactants depending upon the charge on their hydrophilic end, where they have observed that anionic surfactants such as SDS, STS and SHS have shown greater efficiency in improving hydrate formation kinetics. These were followed by non-ionic surfactants such as Tween 20 and Tween 80, while cationic surfactants such as CTAB and DTAC showed least efficiency. On the other hand, researchers such as Daimaru et al (2007) and Dicharry et al. (2016) tried to examine the effectiveness of the surfactants from another perspective where they tried to understand if there was any relationship between the carbon chain length of the surfactants and its effectiveness in improving the hydrate formation kinetics.

Table 4.4. Considered surfactants and their respective attributes, where the solubility values were taken from Pollard et al (2006).

S. No.	Surfactant	Carbon chain length	Charge on the hydrophilic end	Solubility in water (g/L)
1	SDS	12	Anionic	>588
2	Tween 20	12	Neutral	>671
3	Tween 80	18	Neutral	>1080
4	CTAB	16	Cationic	3.1

According to Daimaru et al. (2007), the hydrate formation was highly supported by the surfactant with the shortest carbon chain length, while Dicharry et al. (2016) concluded that the hydrate formation kinetics were strongly supported by the surfactant with the carbon chain length 12. Surfactants with shorter chain lengths were observed to have improved hydrate formation for a specific guest gas. Addressing these two perspectives, in this study, four

surfactants were taken addressing different ionic charges, different chain lengths and different extent of solubilities. The volumetric gas consumption values were collected and compared amongst each other to observe which attribute of the surfactant would play a pivotal role in promoting hydrate formation. Table 4.4. enlisted various attributes of the surfactants considered in this study. The solubility was added to the observations as it represents the heterogeneity in the liquid phase. As it was understood from the chapter 3, higher the heterogeneity, higher could be the kinetics of hydrate formation. In order to check the effect of heterogeneity in the liquid, the solubilities of these surfactants have been collected to check if the hydrate kinetics in the presence of these surfactants would be in the order of insolubility. From the table 4.4, the order of insolubility of these surfactants have been observed to be CTAB > SDS > Tween 20 > Tween 80. The figure 4.3 represents the profiles of gas consumption during hydrate formation for 45 hours.

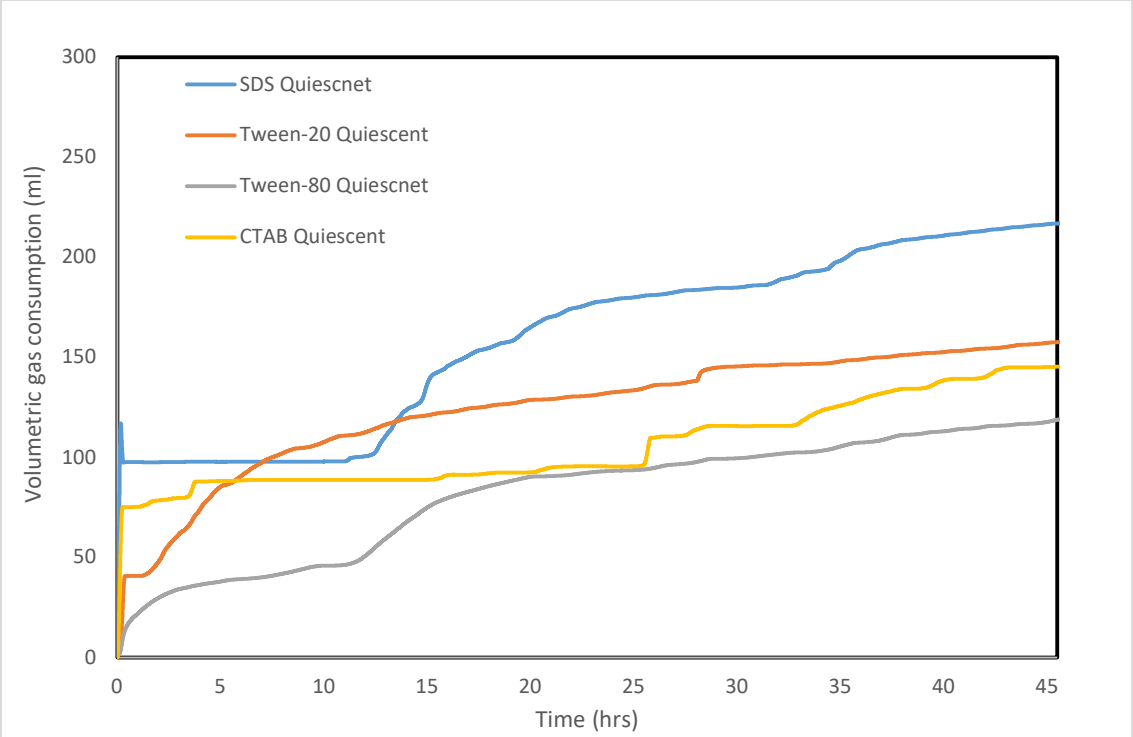

Figure 4.3. Volumetric gas consumptions during hydrate formation experiments in the presence of surfactants.

As seen from the figure 4.3, the hydrate formation yield has been observed to be at its highest in the presence of 100ppm SDS with the total volumetric gas consumption of 217ml at the end of 45th hours. This was followed by Tween 20 with 157ml of gas consumption and then CTAB with the volumetric gas consumption 145ml. The least elevation of hydrate formation yield has been observed to be 118ml, in the presence of Tween 80. When compared these values with the system having no surfactant conditions, the elevation in hydrate formation yield at the end of 45 hours were observed to be in the order of SDS > Tween 20 > CTAB > Tween 80, with the percentage elevations 106.67, 49.5%, 38.1% and 12.4% respectively.

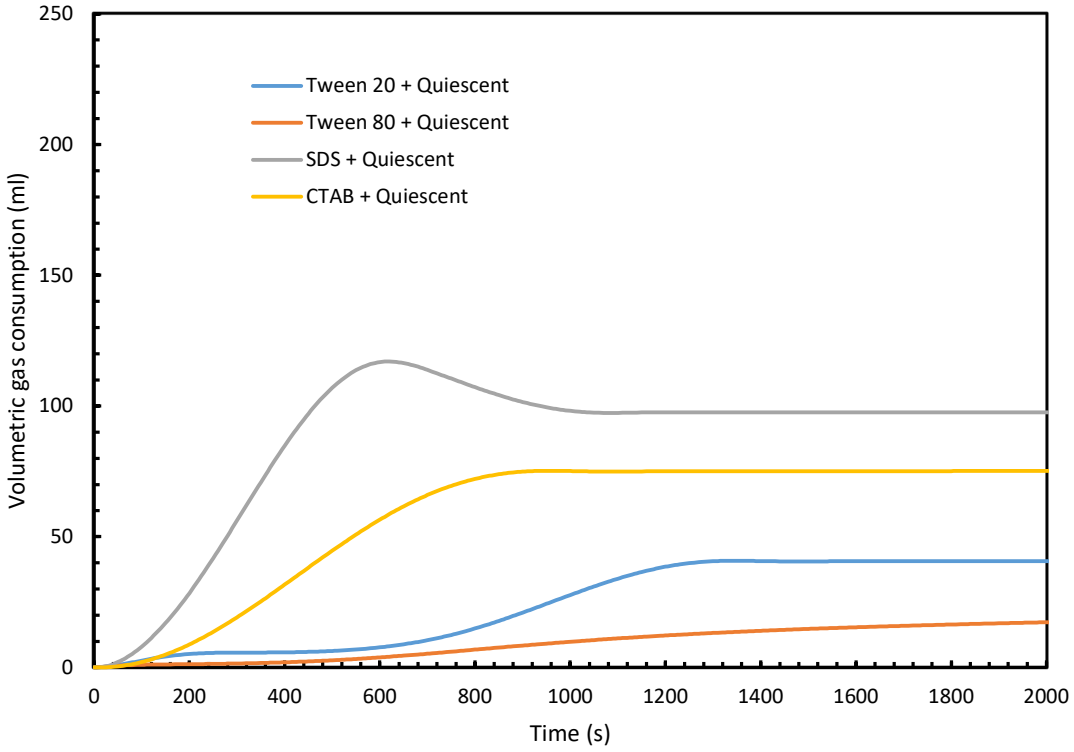

Figure 4.4. Initial volumetric gas consumption profiles in the presence of surfactants showing the local maxima within the first 2000 seconds of commencing the hydrate formation experiments.

The elevations produced in the presence of surfactants did not particularly followed any order of surfactant charges, the carbon chain length or their respective solubilities. When compared the volumetric gas consumptions contributed solely by hydrate formation, the values are as follows: 209.7ml for SDS; 150.6ml for Tween 20; 138.7ml for CTAB and 112.1ml for Tween 80. Thereafter, the initial hydrate formation kinetics were observed. For such reason, the hydrate formation yields for the first 500s were compared amongst the cases with all the surfactants. The figure 4.4 represents the volumetric gas consumptions during hydrate formation for the first 2000s in the presence of surfactants.

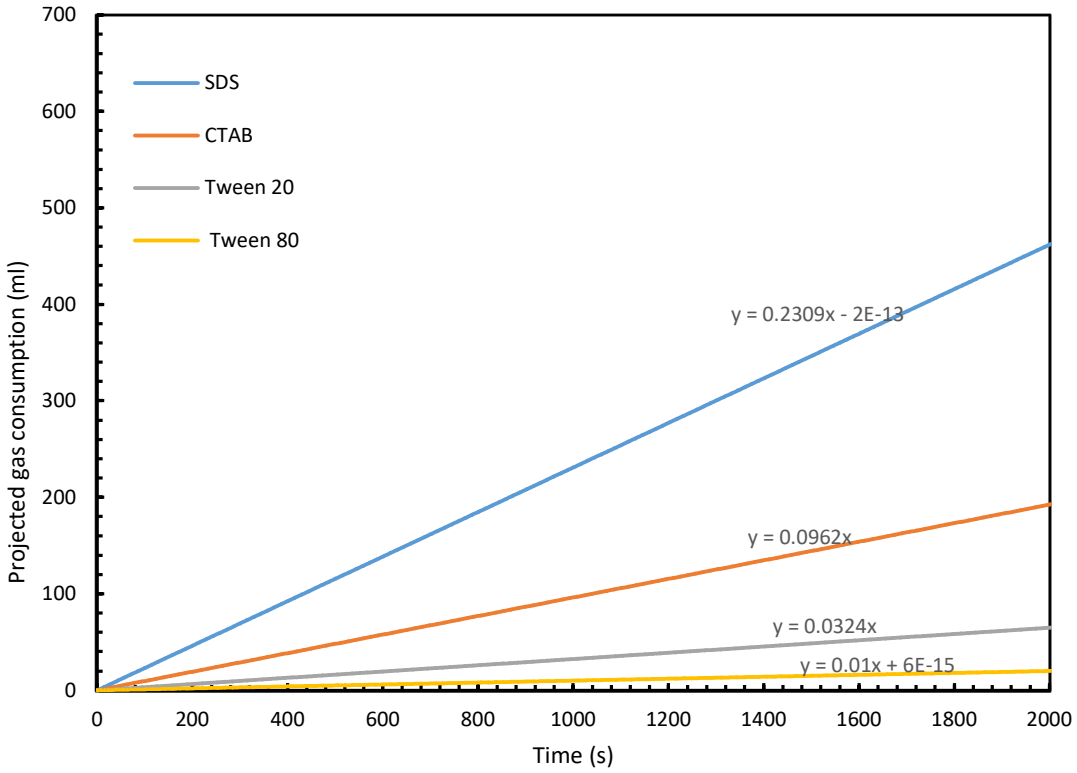

Figure 4.5. Projected gas consumptions for the first 2000 seconds as directed by the linear trendlines pertaining to the initial gas consumption profiles in the presence of surfactants.

As it can be seen from the figure 4.4, the rate of hydrate formations was considerably higher in the presence of SDS, which reached its highest point by 600s. In addition, the yields of hydrate

formations at the local maxima within the first 2000 secs were as follows: 117ml at 600s for SDS; 75.29ml at 960s for CTAB; 40.806ml at 1330s for Tween 20; 17.304ml at 2000s for Tween 80. From these results two main observations were made: the order of surfactants in their effectivity to improve hydrate formation kinetics were different at the initial phase when compared to the overall yields of hydrate formation after 45 hours.

To analyse further, trendlines were added representing the rates of hydrate formations until the volumetric consumptions reached local maxima within the first 2000s of the experiment. These profiles were provided in the figure 4.5. As it can be seen from the figure 4.5, if the hydrate formation kinetics were continued in the same rate till 2000 seconds as if they were before reaching the local maxima.

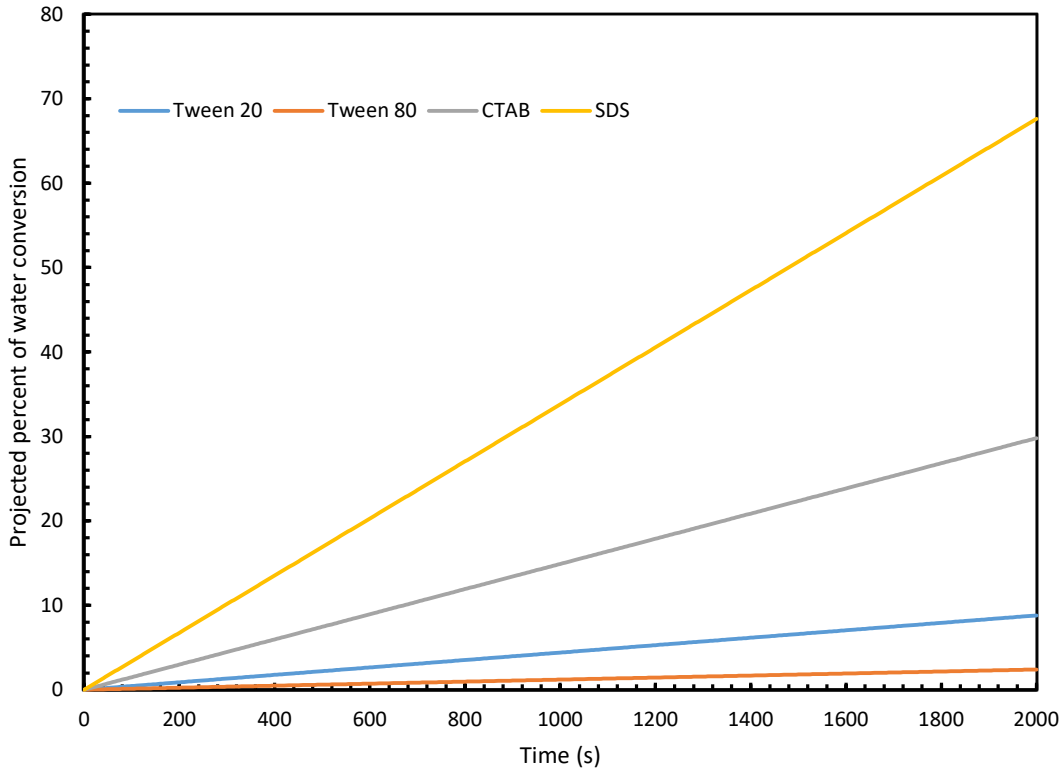

Figure 4.6. Projected percentage of water conversion with time under the influence of various surfactants in the quiescent conditions.

Specifically, in the case of SDS, the volumetric gas consumption could reach up to 460ml, which would be less than half (192.4ml) in case of CTAB, while Tween 20 and Tween 80 could reach the yields 64.8ml and 20ml respectively.

Considering the sI type of hydrate where the water to gas ratio in hydrate would be 5.75:1, the percent change of water into hydrate with respect to time has been calculated (McMullan & Jeffrey, 1965). These profiles were given in the figure 4.6. In the case of SDS, for by the end of 2000s, approximately 68% water could convert into hydrate, while the second most effective surfactant CTAB could convert less than 30% water into hydrate after 2000s.

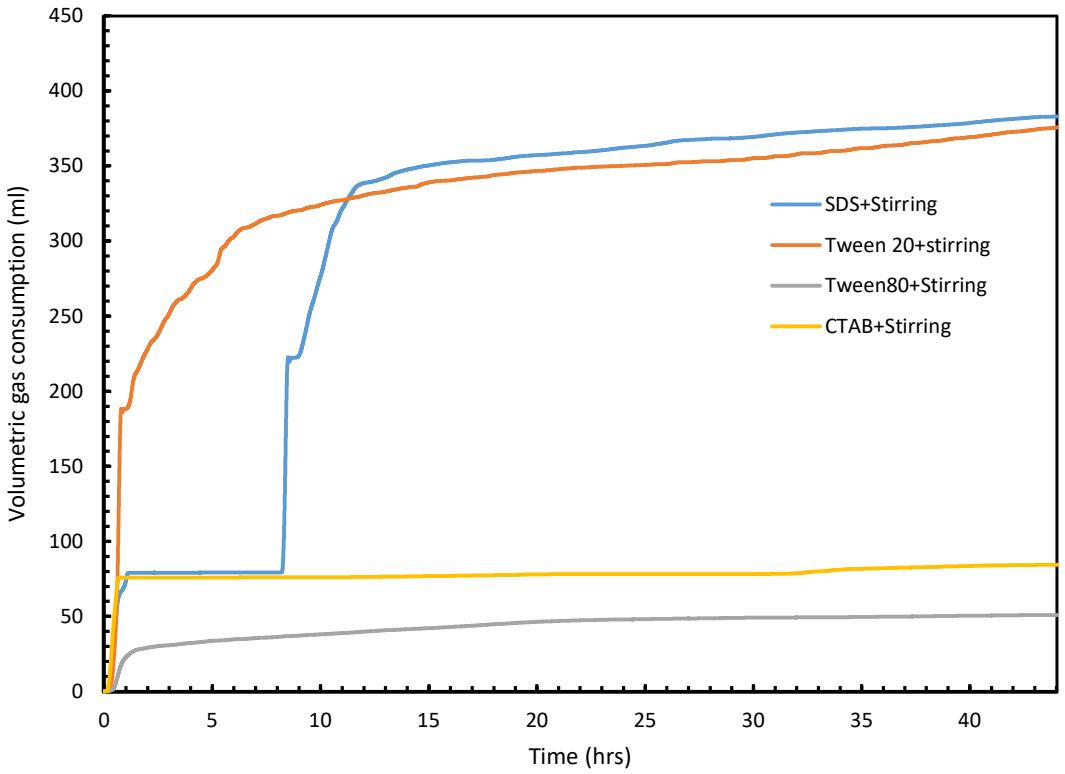

Figure 4.7. Gas consumptions during hydrate formation in the presence of surfactants with stirring.

The same experiments under similar chemical compositions were repeated by introducing stirring with a speed of 360 rpm into the system. The volumetric gas consumption values have

been reproduced through these experiments and presented in the figure 4.7. As it can be seen from the figure 4.9, after approximately 45 hours, the volumetric gas consumption values have been observed to be 383ml in case of SDS, while this value has been 376ml in case of Tween 20. Far below these values, recorded were the gas consumption values pertaining to the cases CTAB and Tween 80, where the consumptions were observed to be 84ml and 51ml respectively.

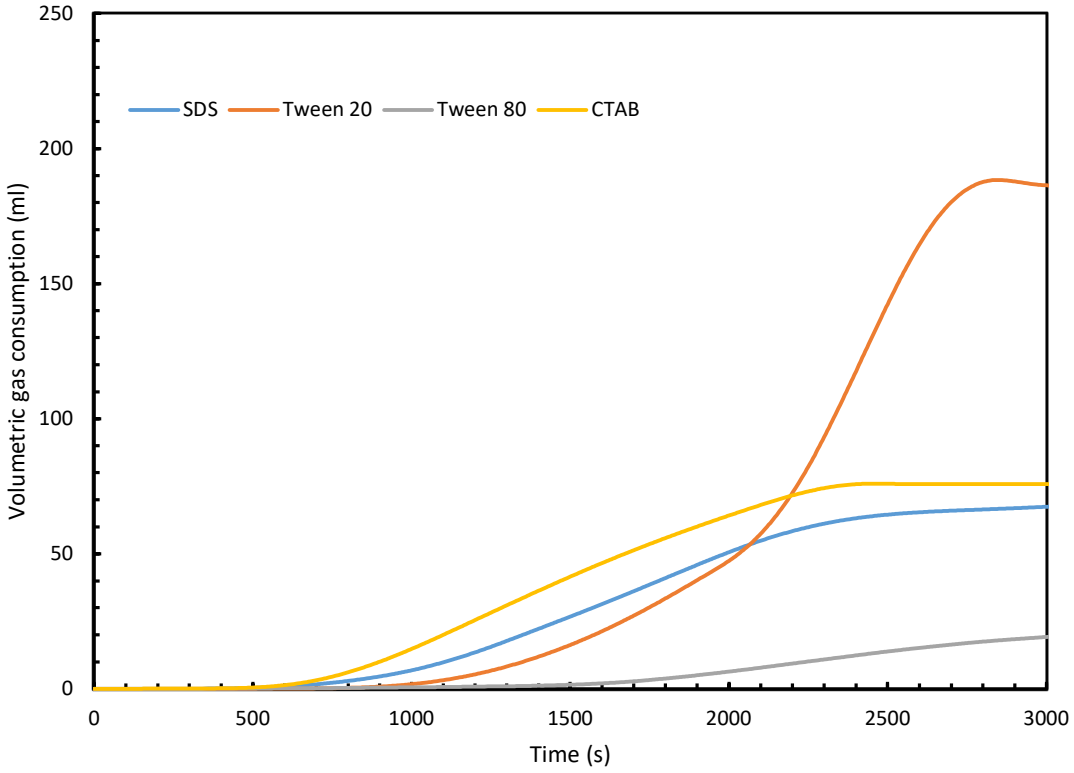

Figure 4.8. Initial volumetric gas consumption profiles during hydrate formation in the presence of surfactants in the stirred systems

When compared these values with the systems having no surfactant, the introduction of stirring with the surfactants have elevated gas consumption values in case of SDS and Tween 20, while in case of CTAB and Tween 80, the hydrate formation kinetics have been observed to be suppressed. Especially in case of Tween 20, with stirring, the performance of the surfactant has

been enhanced by 140%, where in case of SDS, this performance enhancement was observed to be 77%. Even though, the stirring has improved the hydrate formation kinetics in case of SDS and Tween 20, a time phase that lasted for approximately seven hours, was recognised in the gas consumption profiles, where no gas consumption was observed. Figure 4.8 shows the initial gas consumption profiles of these hydrate formation experiments under the influence of various surfactants in the stirred tank reactor. Similar to the unstirred conditions, the initial volumetric gas consumptions were slower in case of non-ionic surfactants. However, three major differences have been observed in between the unstirred and stirred systems: 1. The induction times were observed to be higher in case of stirred systems, despite the overall yield has been considerably improved through stirring; 2. SDS has seemed to have performed the best in improving the initial kinetics of the hydrate formation in the unstirred quiescent systems as observed through the gas consumption profiles. However, in the stirred systems, CTAB has given a better output than SDS in the first 2000s, which was, later, taken over by Tween 20. By the end of 3000s, the stirred system with Tween 20 has experienced a gas consumption of 186ml while the local maximum within 3000s was 188.32ml. In case of CTAB, the gas consumption was 75.84ml at the end of 3000s, while the local maximum was 75.89ml.

For SDS and Tween 80, the local maxima were found at 3000s with the values 67.48 and 19.31 respectively. The modified version of trendlines representing the extrapolated (or projected) volumetric gas consumption under the assumption of continuous hydrate growth, similar to the figure 4.5 has been presented in the figure 4.9 addressing the stirred systems. While calculating these projections, the time delay contributed by the induction time has been ignored by eliminating the x-intercept from the trendline equations. However, as it was seen from the figure 4.8, the order in which the induction times were observed to be as follows: Tween 80 > Tween 20 > SDS > CTAB. Even though, from the perspective of initial volumetric gas consumption representing the initial hydrate formation, SDS was not observed to be as

effective as either CTAB or Tween 20 in the stirred vessels, it was, however, proven its effectiveness from the perspective of overall yield after 45 hours as well as improving the initial kinetics in the unstirred (quiescent) reactors.

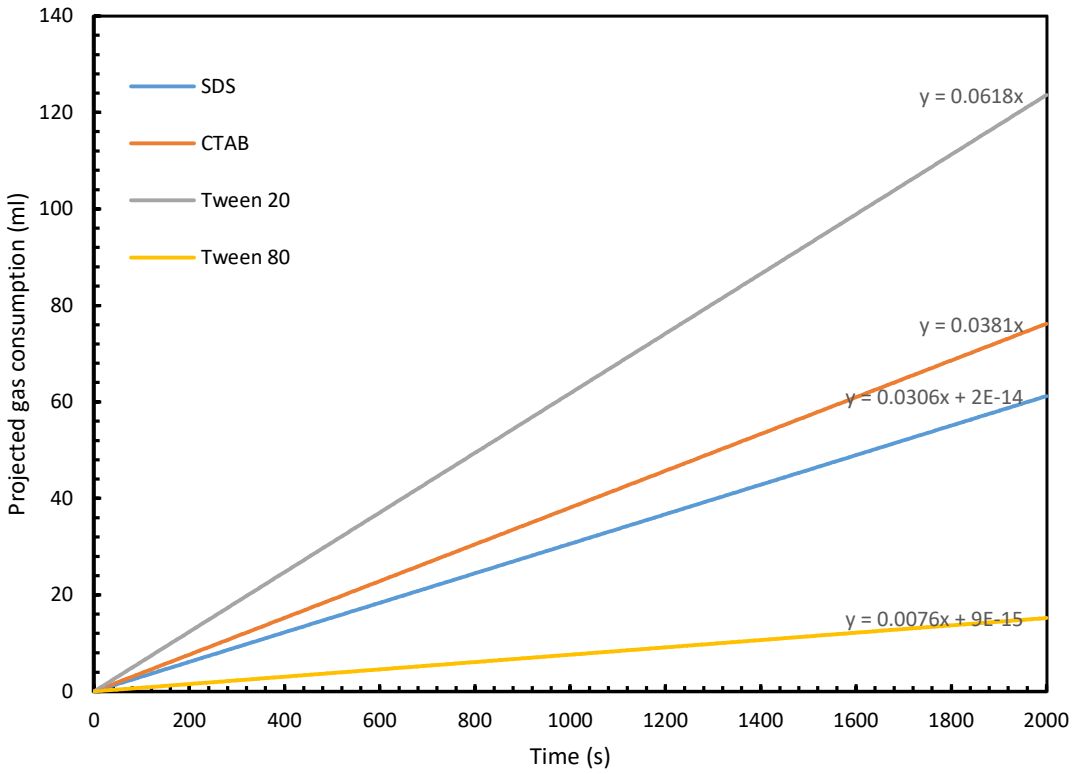

Figure 4.9. Projected gas consumptions for the first 2000 seconds as directed by the linear trendlines pertaining to the initial gas consumption profiles in the presence of surfactants in stirred reactors.

Supporting these observations, in the literature, the effect of SDS has been claimed to have enhanced hydrate formation kinetics by lowering the interfacial tension within the liquid phase and improving the diffusion rates of gas to the hydrate formation sites (Kumar, et al., 2013). In support of such observations, when 100ppm of SDS was added to the system, the volumetric gas consumption was increased to 2.28 times the gas consumption observed in the system without surfactant. The figure 4.10 depicts the hydrate yields in terms of volumetric gas

consumption showing the effect of adding SDS to the system along with the influence of stirring over the hydrate formation yield. By the end of 45th hour, this raise in the volumetric gas consumption was equivalent to 34% of the extent of gas consumption lost due to the addition of salt and CH_4 into the system. In order to analyse the reasons behind the trends, various factors either in the form of barriers or promotors are needed to be understood and extensively analysed.

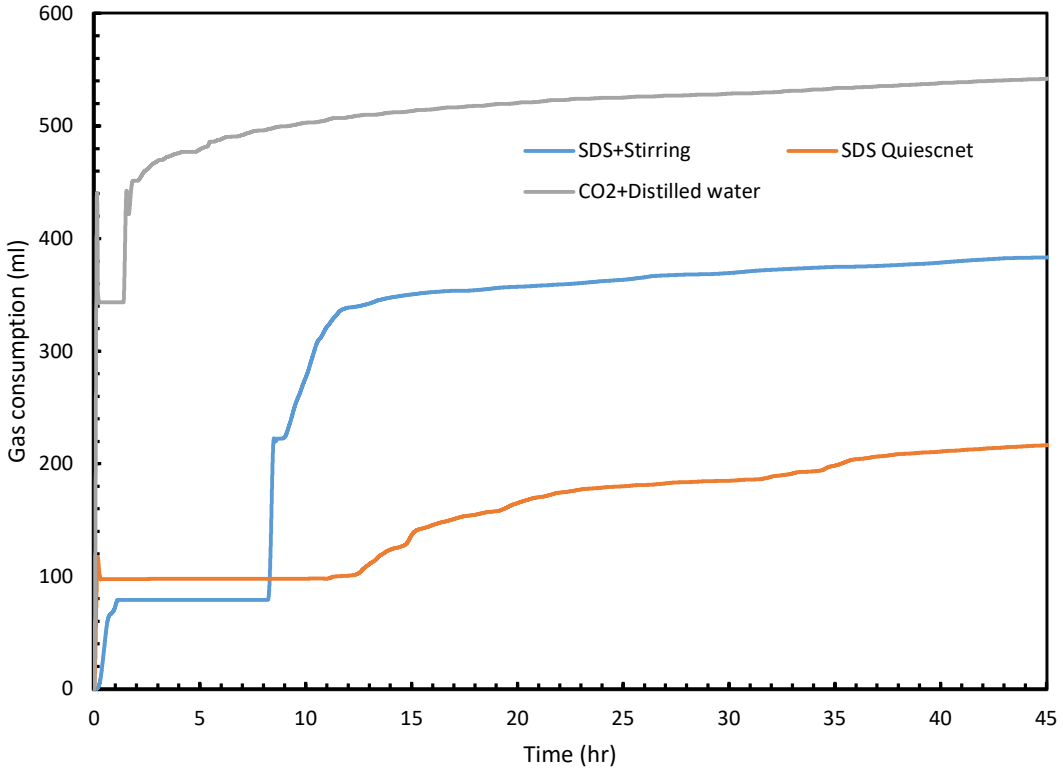

Figure 4.10. Comparison of volumetric gas consumption in the systems involving SDS with and without stirring with the base case of CO_2 + distilled water.

4.3.3. Barriers towards hydrate formation

There can be two barriers that could discourage hydrate formation from the start of the experiment: 1. Physical barrier; 2. Thermodynamic barrier. Thermodynamic barrier would be further distributed into two factors: heat generation and heat accumulation. Physical barrier

would be the resistance offered by the existing hydrate barrier at the gas-liquid interface restricting further gas to dissolve into the liquid, exhausting the hydrate forming sites in the liquids off the dissolved guest gas. During the experiments conducted by Long and Sloan (1996) and Takeya et al (2000) using CO_2 and CH_4 as guest gases, they observed the hydrate propagation occurred either alongside the gas-liquid interface or the reactor wall depending upon the effectiveness and solubility of the hydrate forming gas. In case of a low soluble gas such as CH_4, the hydrate propagation was mainly occurred alongside the gas liquid interface due to the availability of more dissolved gas at the gas liquid interface. However, in case of CO_2, which was considerably more soluble hydrate forming gas, the hydrate propagation occurred mainly at the wall, which was considerably lesser in temperature (in quiescent systems). The current experiments were conducted having the guest gas dominated by more CO_2 (95%) and less CH_4 (5%). Hence, in these experiments, the hydrate formation was observed to have mainly occurred alongside the reactor walls, which was observed by the shape of the collected hydrate from the reactor. This eliminated the probability of resistance offered by the existing hydrate layer at the gas-liquid interface.

As the hydrate formation process is exothermic in nature, the heat is generated during the hydrate growth step. The extent of heat generated would be dependent upon the kinetics of hydrate formation. As the hydrate formation is highly sensitive towards the temperature of the system (as seen from the chapter 3), the heat generation could be the potential barrier towards hydrate formation. When the heat generates, if the heat is distributed throughout the system, the hindrance offered could be distributed. When it is not distributed and instead, accumulated as it happens in the quiescent systems, a considerable dissociation of hydrates is found. This could lead to the drop in volumetric gas consumption as well as the hydrate dormant phases where no further gas consumption could be observed until the temperature drops to the operational temperature through external cooling. These phases of dormancy could still be

observed when the generated heat is excessive that it could result in higher temperatures of the system even after the heat distribution. For the guest gas mixture being dominated by high soluble CO_2 gas and the experimental observation states that the hydrate was observed to have formed alongside the reactor wall, it could be concluded that the major resistance towards hydrate formation occurred because of the thermodynamic barriers rather physical barriers as observed by Takeya el at (2000). Supporting this statement, during the current experiments, as mentioned in the section 4.3.2, a phase of dormancy was found in the case of SDS with and without stirring. Especially during the hydrate formation in the system in stirred reactor, an overall temperature raise of 4°C was observed that resulted into a dormancy of seven hours which followed a drop in gas consumption value. However, when the temperature dropped through an external cooling to an appropriate temperature, the gas up taking reoccurred improving hydrate yield, which was 2.31 times to the yield found in the quiescent system as shown in the figure 4.10.

4.3.4. Gas consumption towards hydrate formation

As it was mentioned at the introduction of the section 4.3, the overall gas consumption into the liquid during hydrate formation is not a mere quantitative representation of extent of hydrate formation. This is because staring from the volumetric gas contraction during the temperature drop till volumetric contraction of hydrate+liquid phase during the high dense hydrate formation four major factors contribute to the overall gas consumption. Due to considerably low thermal conductivity of gas, the contraction of gas under external cooling has been ignored in this study.

Before initiating the hydrate experiments, the systems were provided with adequate time at temperatures higher than hydrate equilibrium temptress for the gas-liquid systems to reach equilibrium conditions. However, due to the tendency of more gas dissolution at lower temperature conditions, when temperature dropped to 1°C, further gas dissolution into the

liquid would occur, which could contribute to the value of volumetric gas consumption. In order to calculate the excess volumetric gas consumption into the liquid has been calculated from the model developed by Duan and Sun (2003), which was also considered in the chapter 3. However, this model has been modified to fit the system of gas mixture, for which the fugacity of the gas mixture has been incorporated into the model, which was calculated from the process proposed by Ricaurte et al (2012). The excess gas volume dissolved into the liquid during the temperature drop from 284.15K to 274.15K have been calculated to be as follows: 0.392ml for the system of CH_4+CO_2 and for the system with pure CO_2 into saline water, it was 0.386ml. For the system with pure CO_2 and distilled water, the excess gas dissolution value was 0.389ml. When compared to the gas dissolution values representing overall hydrate formation yields, these values have been negligible.

To evaluate the contribution of water contracting into hydrate during the formation of hydrate to the overall volumetric gas consumption value, an iterative process has been chosen The density of water and hydrate were chosen to be 1.03g/cc and 1.10g/cc respectively (Aya, et al., 1997; Serway & Jewett, 2018). A water to gas ratio of 5.75:1 has been taken representing an sI hydrate formation in case of CO_2 ash guest gas, which was used to calculate the number of moles of water converted into hydrate during the formation hydrate, similar to the section 4.3.2 (McMullan & Jeffrey, 1965; Yoshioki, 2012). At first, the residual gas consumption was calculated by subtracting the gas consumption values contributed by excess dissolution under lowered temperature conditions.

The resultant values were considered for the iterative process to calculate the contribution of water contracting into hydrate towards hydrate to the overall volumetric gas consumption. By assuming the total residual gas consumption was used in the formation of hydrates, total volume of water and hydrates were calculated. To derive the new residual volumes, the excess volumes were subtracted from the previous residual volume. The excess volume values were

narrowed down to approximately 0.002ml after two iteration. Hence, the residual volumes produced after two iterations were considered to be the volumetric gas consumption contributed by solely hydrate formation, the values of which are given in the table 4.5.

Table 4.5. Volumetric gas consumptions contributed by solely hydrate formation after 34 hours.

Experiment number	Experiment	Volume of gas used for hydrate(ml)
1	CO_2+Distilled water	529.123
2	CO_2+Saline water	136.632
3	CO_2+CH_4+Saline water	94.380
4	CO_2+CH_4+Saline water+SDS	202.367
5	CO_2+CH_4+Saline water+SDS+stirring	367.862
6	CO_2+N_2+Saline water+SDS +stirring	273.51 (after 21 hours)

The values provided in the table 4.4, provide the extent of gas consumption values contributed by solely the hydrate formation at the end of 34 hours. The values given in table 4 show the extent of hydrate formation at the end of the 34-hour periods of the experiments except for the experiment involving N_2. These values represent the efficiency of chemical additives and physical interventions such as the addition of impurities to the gas mixture (CH_4), salt to the distilled water, surfactant to the saline water and stirring to the quiescent systems. By the time the experiments were conducted for 34 hours, the adding salt to the distilled water has contributed to a reduction of 80% in hydrate formation. The replacement of pure CO_2 with the

gas mixture of 95% CO_2 and 5% CH_4 has further reduced the volumetric gas consumption by 43%. The addition of 100ppm SDS into the saline water, in the presence of inlet gas mixture containing CO_2 and CH_4, the overall yield of hydrate formation has been improved by 25%. When introduced stirring to the quiescent surfactant system, this overall recovery of volumetric gas consumption lost during the addition of salt and CH_4 to the system was recovered by 57%. This was 2.3 times higher to the quiescent surfactant system.

4.3.5. Initial kinetics of hydrate formation

Similar to the analysis done in the section 4.3.2, the initial hydrate formation kinetics were cross compared to understand how various changes in the hydrate formation system such as addition of salt, addition of CH_4, addition of surfactant (SDS) and the addition of stirring would affect the speed of hydrate formation at the initial stages. While the overall hydrate formation kinetics observed for longer periods could inform regarding the final yield of hydrate, the information regarding the speed of hydrate formation and induction time could only be done through the analysis of hydrate formation at the initial stages.

Even though, the section 4.3.4 explains the advantage of introducing the stirring into the quiescent system for the conversion of water into hydrate and improving the overall yield of hydrate formation, the analysis of initial kinetics would conclude on the effectiveness of stirring otherwise. While from the chapter 3, it could be concluded that the heterogeneous hydrate formation was the most effective and faster hydrate formation process, the stirring was seen to have reduced the heterogeneous hydrate growth process. It can be understood from the gas consumption profiles deduced from the experiments few seconds after reducing the temperature to 274.15K.

The figure 4.11 shows the gas consumption values of various experiments depicting the effects of various changes in the system within the first 500 seconds. From the figure 4.11, the

exponential increase in the gas uptake immediately after the reduction of temperature from 286.15K to 274.15K was observed in the quiescent conditions. Whereas this exponential increase in the gas consumption was absent in the stirred system. At 480 seconds, the base case with pure CO_2 and distilled water reached its local maximum of 440ml of gas consumption, which had been the end of initial exponential hydrate formation. After reaching the local maximum, due to the increase in the temperature within the system, the system experienced in the loss of gas consumption values. This is the reason why the first 500 seconds were chosen so as to calibrate all the systems with respect to the base case.

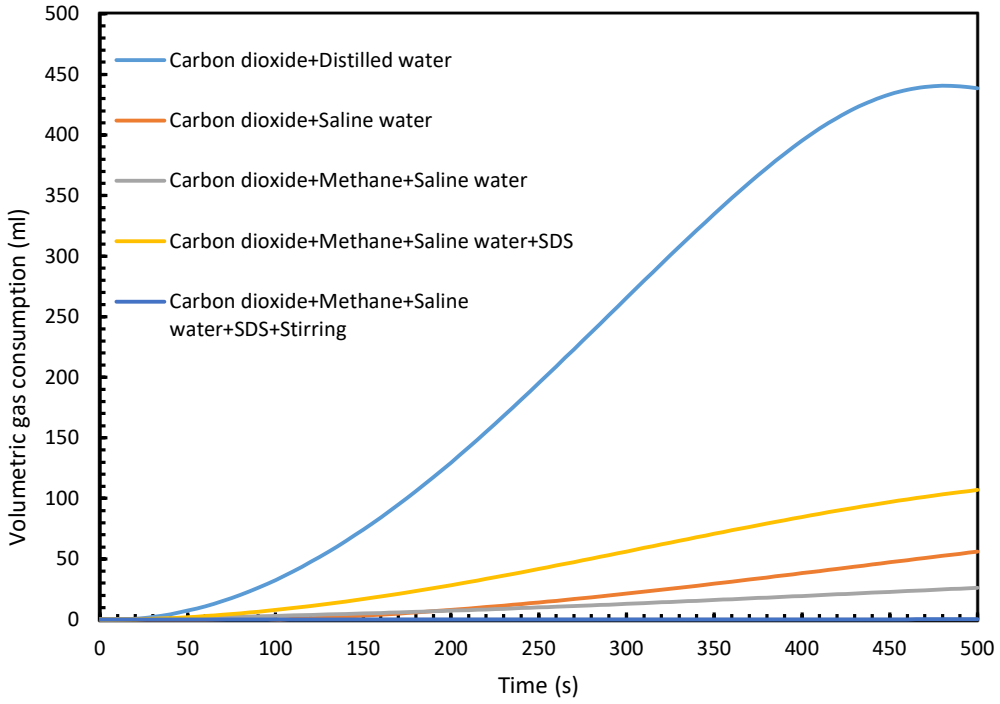

Figure 4.11. Volumetric gas consumptions observed amongst the experiments within the first 500s of commencing the experiments.

The other cases along with the case with the system containing both CH_4 and salt in the quiescent showed faster hydrate formation kinetics compared to the system with stirring. The slower hydrate formation might have been caused by the attrition of grown hydrate nuclei due

to the turbulence created by the stirring and also due to the detachment of hydrate nuclei from the reactor wall, which was the most favourable location for hydrate formation by providing heterogeneity as well as lower temperatures to support the hydrate growth.

4.3.6. Comparison between CH_4 and N_2 as gas impurity

Experiment with CO_2 + CH_4 + stirring was repeated by substituting CH_4 with N_2 to examine the effect of a lesser soluble gas as impurity in hydrate formation process (Kolev, 2011). This experiment was conducted for 21 hours to obtain the values of volumetric gas consumption along with the temperature fluctuations. These volumetric gas consumption profiles were compared with the system having CH_4 as an impurity. There have been studies such as Ahmad and Gersen (2014) that observed the addition of impurities such as N_2 and CH_4 have considerably reduced the CO_2 dissolution into the liquid, depriving the solution off the hydrate former (Ahmad & Gersen, 2014). In addition, it was observed that in the presence of more soluble gases such as CO_2, the solubility of less soluble gases into water increases (Li, et al., 2018). The increased concentration of less hydrate forming gases in the liquid could decelerate the overall hydrate formation kinetics by interfering in the hydrate formation process.

As seen from the figure 4.12, smoother and more exponential hydrate formation profiles were found in case of hydrate formation in the presence of N_2 as compared to CH_4 as impurity. It means that the hydrate formation kinetics were considerably faster in the systems with N_2 compared to CH_4. However, the yield hydrate formation at the end of 21 hours was considerably lesser in the system with N_2 than CH_4. This might be because of the earlier stoppage of stirring in the system with N_2.

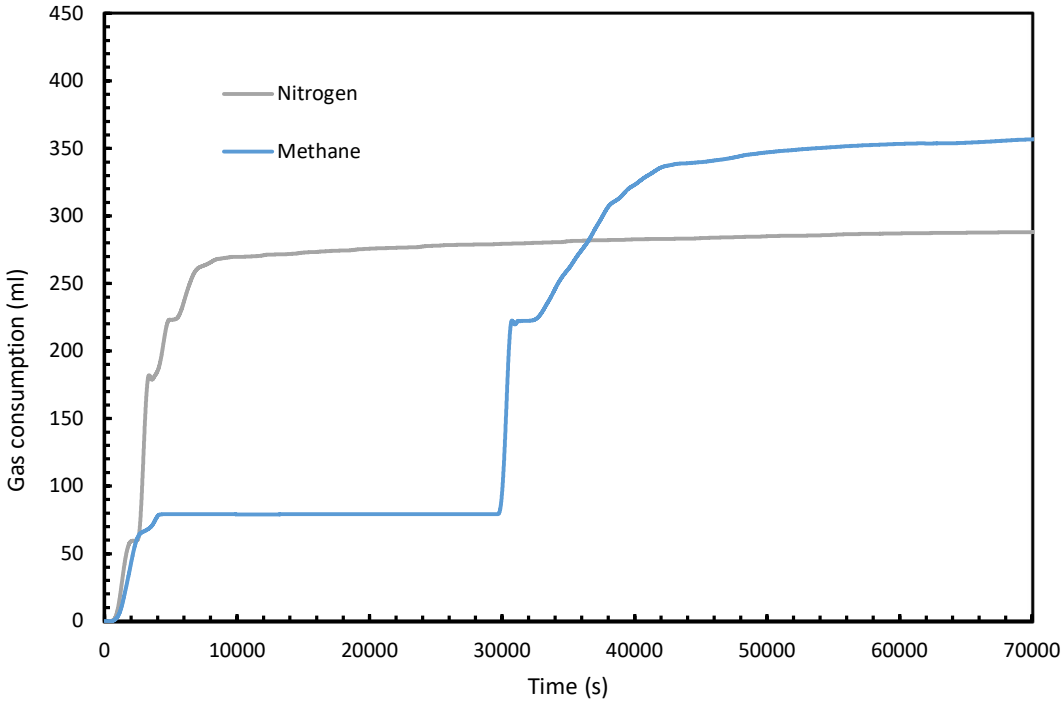

Figure 4.12. Comparison of CO_2 gas consumption in the presence of 5mol% N_2 and 5mol% CH_4 during hydrate formation.

Even for having lesser overall gas consumption at the end of 21 hours, for the system with N_2, it took only 6500 seconds to reach a gas consumption of 250ml, where for the system with CH_4, it took over 34000 seconds to reach the same value of gas consumption. This suggests the faster hydrate formation kinetics within the system having N_2 as gaseous impurity. For the lack of temperature probe immersed in the hydrate forming solution, the temperature fluctuations within the reactor during the hydrate formation were not captured accurately, while these values were recorded with utmost accuracy in case of stirred systems.

Figures 4.13 and 4.14 show the gas consumption profiles compared against the temperature fluctuations with time in the systems CH_4 and N_2 as impurities respectively. As seen from these figures, the temperature fluctuations were higher at the times of exponential hydrate growths.

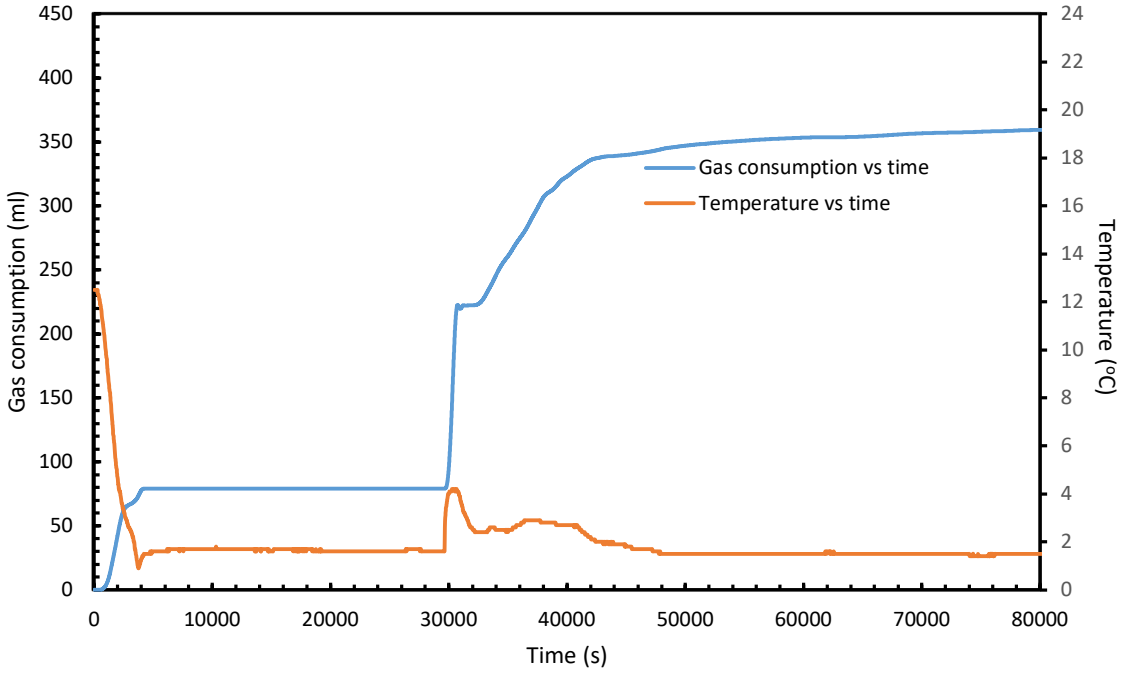

Figure 4.13. Gas consumption in the stirred system with CO_2+CH_4 gas mixture compared against the temperature fluctuations

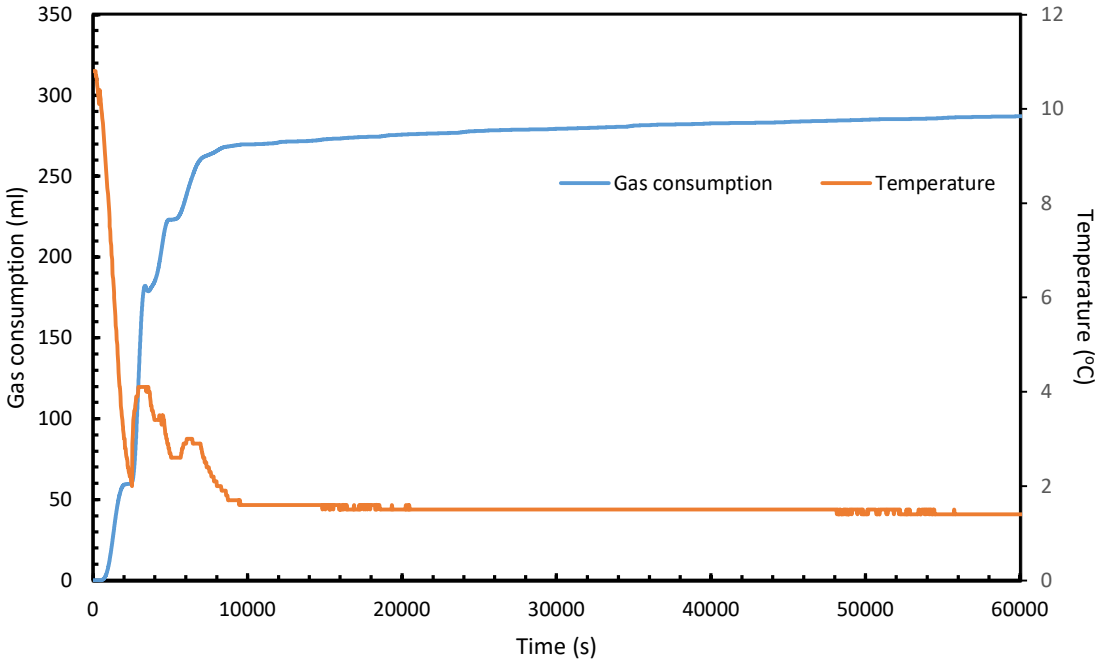

Figure 4.14. Gas consumption in the stirred system with CO_2+N_2 gas mixture compared against the temperature fluctuations

Additionally, the dissociation of hydrates as depicted by the drop in the gas consumption values were higher when the temperature reached its highest values. This suggests that the systems with heat absorbers, or the systems with continuous hydrate removal would be more compatible for a continuous hydrate growth (Yang, et al., 2011; Fan, et al., 2012). While most of the hydrate formation cells were the batch reactors, the reactor designed by Park et al (2011) which uses a dual piston system that enabled continuous production of hydrate pellets.

4.3.7. Water conversion into hydrate and desalination capacity

Considering the sI structure of CO_2 hydrates, the total percentage of water conversion into hydrate has been calculated. The results have been given in the table 4.6. As it was explained in the section 4.3.1 and also 4.3.4, the highest hydrate formation yields were observed in the base case. In accordance with these observations, the higher water conversion into hydrates were given by the base case with 57.75% water converted into hydrate. The lowest water conversion was shown by the system with CO_2+CH_4 gas mixture containing saline water operated under quiescent conditions, with the total conversion of 6.67%. Amongst the saline water systems, the highest water to hydrate conversion was recorded by the stirred system with added SDS into it with the total conversion value 35%. In the case of CO_2+N_2 system, this conversion was calculated to be 32%.

During the hydrate formation, while water converts into hydrate, the dissolved salts would lose the hydrogen bonds and hence the chemical affinity between the salt and water molecules would be lost. However, due to the porous structure of hydrates, the residual salt would be resided in the pores of the water, the quantity of which would be considerably less compared to brine. As seen from the experimental observations, the saline removal capacities did not follow any particular order. However, they have all fell into a bracket of 70% to 77%. These results were in agreement with the literature where the extents of salt removal were fell within

the bracket of 60%-85% for a single stage hydrate desalination process (Corak, et al., 2011; Park, et al., 2011; Kang, et al., 2014).

Table 4.6. Percentage of water conversion into hydrates as well as the salt removal capacities

Experiment number	Experiment	Molar percentage of water conversion	Desalination capacity
1	CO_2+Distilled water	57.75	N/A
2	CO_2+Saline water	11.64	72.2%
3	CO_2+CH_4+Saline water	6.67	76.7%
4	CO_2+CH_4+Saline water+SDS	19.36	74.75%
5	CO_2+CH_4+Saline water+SDS	35.96	71.8%
6	CO_2+N_2+Saline water+SDS	31.80	72.5%

4.4. Summary

The experiments were conducted to understand the hydrate formation kinetics including the speed as well as the total yield including various hydrate supporting as well as inhibiting conditions. A total of eight experiments were conducted with the first experiment being the basic including the hydrate forming gas (CO_2) and distilled water in the system. During the next two experiments, impurities such as salt and CH_4 were added to water and guest gas respectively, in order to study the kinetics and yield under the inhibiting conditions. The next set of experiments were addressed the efficiency of various promotors such as surfactants and the stirring from the perspective of speed of hydrate formation and the yield.

The hydrate formation was detected by the temporal volumetric gas consumption into liquid. As seen from the experimental observations, the addition of salts had a great impact over the hydrate formation, discouraging it where the overall yield was fallen below 70% of the pure

water condition. In addition, the sensitivity of hydrate formation over the purity of guest gas has also been examined, where 5% reduction in the purity of the guest gas has been resulted in a further 29% drop in the volumetric gas consumption. However, this loss in the volumetric gas consumption could be recovered by the addition of very low amounts of surfactants to the system. The addition of 100ppm of SDS to the saline and 95% CO_2 system resulted in 25% recovery in gas consumption, In the presence of stirring the recovery was approximately 57%.

Amongst the surfactants, from the perspective of overall yield, SDS has been observed to be the most effective surfactant in both the stirred as well as unstirred systems. However, from the perspective of initial hydrate formation kinetics, for unstirred quiescent conditions, SDS was observed to be the most effective with a high margin from the second effective surfactant (CTAB). The quiescent system with SDS as kinetic additive has been the most effective in terms of the initial hydrate formation kinetics in the entire set of experiments. Hence, this system has been considered to be used in the chapter 6, where the water production ratio of HBD-MSF hybrid would be examined. Compared to the unstirred systems, the stirred systems were observed to be less effective in improving the initial kinetics. They have fallen behind the quiescent system both in terms of less induction times as well as hydrate formation rates. Amongst the surfactants, however, Tween 20 has been observed to be the most effective amongst the stirred systems in terms of improving the hydrate formation kinetics, even though the observed induction times were high in this case.

From the experimental observations, as it was seen from the shape of the hydrate recovered from the reactor, it was understood that the physical barrier was absent. This is because of the absence of hydrate formation at the interface of gas and liquid. However, a considerable reduction in the gas consumption values were observed after the exponential growth of volumetric gas consumption curves representing accelerated hydrate formation. When compared these profiles with the profiles of temperature fluctuations, the times at which loss

in the volumetric gas consumptions occurred were coincided with the time at which the temperatures rose. Hence, it was concluded that the thermodynamic barriers were more important to be addressed in order to keep the hydrate formation kinetics constant. Even though, the hydrate yields were improved in the stirred systems, as observed in the surfactant calibration experiments, the stirring resulted in high induction rates and slower initial hydrate formation kinetics. From the perspective of salt removal capacity, all the hydrate formation experiments produced values in between 71-77% with no defined order of the experimental traits.

Chapter 5

Hydrate formation for carbon capture

5.1. Introduction

5.1.1. Requirement of carbon capture

The capture, separation and storage of CO_2 from industrial gaseous emissions is attracting profound research interest due to increased concerns about climate change. It is now considered essential, especially given the recent erratic global weather patterns against a background of increased fossil fuel consumption by industry (Bobicki, et al., 2012). According to the U.S. Energy Information Administration, carbon emissions from all fossil fuel sources totalled 5154 million metric tons in 2019 alone. When discussed the carbon emission through thermal desalination columns, the carbon footprint of MSF process was found out to be 2.988kg per cubic meter of water production, where the majority of the carbon emission was contributed by the brine heating process (Liu, et al., 2015). When extrapolated these values to a 16 stage Al Khobar II MSF desalination plant with a distillate production rate of approximately $0.26m^3/s$, the carbon emission would be 0.078kg/s, which could lead to a monthly emission of approximately 200 tons (Helal, et al., 1986; Rosso, et al., 1997).

5.1.2. Mechanism of gas absorption through amines

Most carbon capture technologies focus on absorption, while less attention has been paid to adsorption and membrane technologies (Bhown & Freeman, 2011). The chemisorption of CO_2 is generally carried out by solvents containing mixtures of aqueous amine solutions. Typical chemisorption reactions with mono-, di- and triamines are shown as follows (Sartori & Savage, 1983; Blauwhoff, et al., 1984):

With monoamines:

$$CO_2 + RNH_2 \leftrightarrow RNH_2{}^+COO^- \ (Zwitterion) \quad (1)$$

$$RNH_2 + RNH_2{}^+COO^- \leftrightarrow RNH^+COO^-(Carbamate) + RNH_3{}^+ \quad (2)$$

With diamines:

$$CO_2 + RR'NH_2 \leftrightarrow RR'NH^+COO^- \ (Zwitterion) \quad (3)$$

$$RR'NH^+COO^- + RR'NH_2 \leftrightarrow RR'NCOO^- \ (Carbamate) + RR'NH_2^+ \quad (4)$$

With Tertiary amines

$$CO_2 + RR'R''N \leftrightarrow HCO_3^- + RR'R''NH^+(Zwitterion) \quad (5)$$

As shown in equations 1-5, tertiary amines, like mono- and diamines, lack the ability to form carbamates due to the unavailability of replaceable hydrogen atoms. However, for high-equilibrium carbon loading capacity (1.0 mol of CO_2 per mol of amine) and with lower regeneration energy requirements, tertiary amines are a good choice for inclusion in absorption mixtures. Triisopropanolamine (TIPA) and Triethanolamine (TEA) were amongst the most researched tertiary alkanolamines addressing carbon capture and storage through absorption. At 313K and 36.27 KPa pressure, in the presence of 2mol/l of TEA the carbon loading was obtained to be 0.345 mol of CO_2/mol of amine. Under the similar conditions, the similar carbon loading was observed in the studies of Chauhan et al. (2003) with the introduction of 1.5 mol/l of TIPA instead of 2 mol/l of TEA. On the other side, the efficient carbon capture technology should also provide effective amine regeneration capabilities as well, in which TEA was observed to be more efficient (Baltar, et al., 2020). For the application of carbon capture through hydrate formation, it is important to investigate if the amines either encourage or discourage hydrate formation in the solutions, which has been investigated in the presence of TEA and TIPA.

Since the hydrate formation process is highly sensitive to the gas concentration in the inlet gas stream as well as the water activity, the use of post-combustion gas mixtures for hydrate formation requires a high driving force. In order to reduce the energy levels required for hydrate-based carbon capture (HBCC) processes, either kinetic and/or thermodynamic additives are added to the system. Amongst the various available thermodynamic promoters, THF is the most thoroughly explored additive due to its drastic reduction of operational energy requirements (Dashti, et al., 2015). Most of the studies on hydrate formation in the presence of thermodynamic additives focus upon changes in hydrate equilibrium conditions, carbon capture efficiency and microscopic hydrate structural analysis. However, HBCC efficiency still needs to be examined from the perspective of the extent of gas consumption during hydrate formation and also to improve the selectivity of a specific gas. A comparison of these trends in different pressure conditions in terms of yield and induction time can provide fuller knowledge of the relationship between hydrate formation and gas capture, especially in the presence of THF. A similar study has been reported by Linga et al. (2007b), but hydrate formation at low THF concentrations and in low pressure conditions may be intermittent and observation over extended periods may be required. In addition, it has been observed that the inclusion of kinetic additives such as Sodium Dodecyl Sulphate (SDS) along with THF has a positive effect on both hydrate formation and carbon capture (Tang, et al., 2013; Thoutam, et al., 2019b). The current study focuses on the usage of tertiary alkanolamines in SDS aqueous solutions in HBCC in terms of hydrate formation with a post-combustion gas mixture and selective carbon separation, with and without the presence of THF.

5.1.3. Proposed HBCC-MSF system

In this case, the HBCC system considered have planned to be operated on full recycle mode. In the figure 5.9, the HBCC block may not be necessarily a single HBCC column but a system of HBCC systems operating together. The post-combustion gas mixture emitting from (or due

to) the brine heater will be sent to the operating HBCC section, meanwhile the substitute HBCC system will be in the hydrate dissociation more, where the hydrate slurry will be sent to the hydrate dissociation column, then the water from gas will be separated. The gas will be sent to the gas storage system, whereas the entire hydrate forming solution will be recycled into the HBCC columns, ensuring 100% recycling and no wastage and disposal of the hydrate forming solution. However, during the hydrate formation process using amines in the system, it is possible that the system may face amine degradation. As the study considered significantly lower concentrations of amines along with the system being operated under lower temperature conditions compared to an independent amine-based gas absorption system, the degradation was ignored.

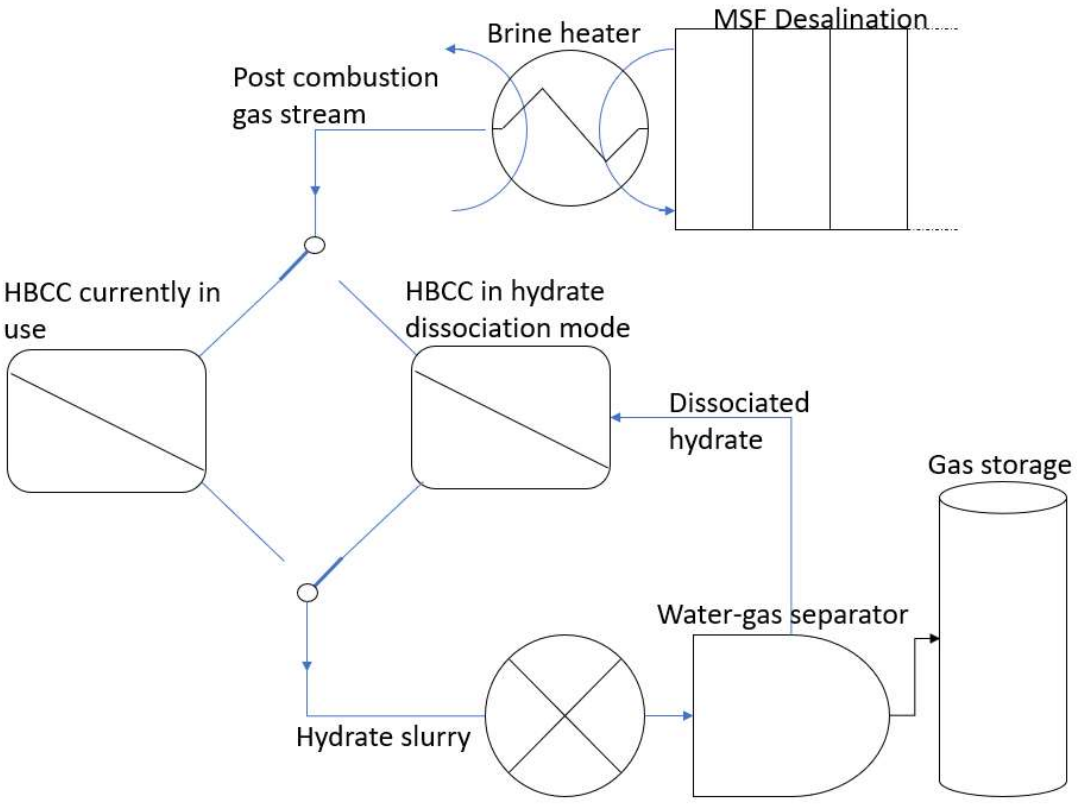

Figure 5.1. The HBCC-MSF system with HBCC being operated in 100% recycle mode.

5.2. Materials and methods .

The experiments were conducted to check gas consumption during the hydrate formation process when the system was provided with the post-combustion gas mixture 85% N_2 + 15% CO_2. The gas mixture was prepared gravimetrically taking CO_2 and N_2 with purity levels of 99.995% each. A list of chemical additives and gases used for the control of gas hydrate formation along with the suppliers is presented in Table 5.1.

Table 5.1. Materials used in the hydrate-based carbon capture experiments

Component	Supplier	Purity
Triisopropanolamine	Sigma-Aldrich	95.0% (mass%)
Triethanolamine	Sigma-Aldrich	99.0% (mass%)
Tetrahydrofuran	Sigma-Aldrich	99.0% (mass%)
CO_2	Air Products plc, UK	99.995% (vol%)
SDS	Sigma-Aldrich	99.0% (mass%)
N_2	BOC, Edinburgh	99.995% (vol%)

Three sets of tests were conducted to check the efficiency of tertiary amines (tertiary alkanolamines) in capturing CO_2 during hydrate formation as shown in Table 5.2. As mentioned in the introduction, tertiary amines encourage selective carbon dissolution from a gas mixture into aqueous solution. In addition, the dissolved CO_2 in the presence of tertiary amines, would be free from strong chemical bonds, allowing it to actively occupy hydrate cages at hydrate formation sites.

Table 5.2. Experimental design used to investigate the impact of composition on CO_2 capture

Set no	Expected Outcomes	Experiment No.	Operational pressure (MPa)	Experimental composition in aqueous solution			
				SDS (ppm)	TEA (wt%)	TIPA (wt%)	THF (mol%)
1	Hydrate formation yield and carbon capture efficiency under quiescent conditions	1	10	100	0	0	0
		2	10	100	1	0	0
		3	10	100	0	1	0
2	Hydrate formation yield and carbon capture efficiency under accelerated hydrate formation conditions	4	3.5	100	0	1	3
		5	3.5	100	0	0.5	3
		6	3.5	100	0	0	3
3	Hydrate formation yield and carbon capture efficiency under lower operational pressures	7	1.5	100	0	0.5	3

The experiments in set 1 aimed to observe the gas consumption process in the presence of the two tertiary amines Triethanolamine (TEA) and Triisopropanolamine (TIPA) compared with the quiescent system with a chemical composition of 100ppm SDS in distilled water. The addition of SDS was done to ensure a soft diffusion of CO_2 within the aqueous solution. The solution with a chemical composition that resulted in the lowest hydrate yield with the minimal hindrance of hydrate formation was then eliminated from consideration in the next set of experiments. For this test set, a pressure of 10 MPa was selected to ensure hydrate formation under quiescent conditions and especially to maintain the system at a pressure well above the hydrate equilibrium pressures as mentioned in the literature (Kang, et al., 2001; Linga, et al., 2007c).

5.3. Experimental set-up and data acquisition

Since high pressure and low temperature conditions generally favour hydrate formation, the operational temperature was chosen to be just above the freezing point (Thoutam, et al., 2019b). Due to the unavailability of data for systems with tertiary alkanolamines, operational conditions were chosen with respect to the quiescent conditions. For the THF-free systems, a quiescent system operating at 10 MPa and 274.15 K was chosen. These thermodynamic conditions are similar to those chosen by Linga et al. (2007b). Values of gas consumption in the first set of experiments were compared so that the most favourable amine would be chosen for the next set of experiments.

Various studies have presented data for the calculation of equilibrium conditions for hydrate-water and gas mixtures (Kang & Lee, 2000; Kang, et al., 2001; Linga, et al., 2007a). In the study by Kang et al. (2001), the hydrate equilibrium pressure for a similar gas composition at 277 K was 2 MPa. In this study, the operational pressure was chosen to be 3.5 MPa at 274.15 K so as to provide the driving force for hydrate formation well above equilibrium conditions.

In the third set of experiments, the operational pressure was reduced to 1.5 MPa to check the effect of less accelerated THF hydrate formation upon gas consumption.

The experiments were conducted under both isothermal and isobaric conditions, where the hydrate formation detection and assessment parameter used was volumetric gas consumption.

For these studies the jacketed type of stirred tank reactor with an internal volume of 525ml as shown in the figure 2.2c was used. Similar to the desalination experiments explained in the section 4.2.2, the gas dissolution was achieved at higher temperature conditions (286.15K), before adjusting the reactor temperatures to the operational temperature conditions (274.15K) and the volumetric gas consumption value in the data acquisition system was set to zero. During both dissolution and hydrate formation, a stirring speed of 360 rpm was chosen. When gas consumption reached an asymptotic value, the temperature of the system was set at 274.15 K to initialize the hydrate formation experiment. The experiments were then stopped either when the gas volume consumption reached a long-term quasi-steady state or after a time period of 24 hours.

Volumetric gas consumption, temperature and pressures were recorded and analysed to identify and assess hydrate formation. In this study, a total of seven experiments were conducted as listed in table 5.1. Four contributory factors affecting volumetric gas consumption during hydrate formation were considered in this study: 1. gas contraction due to temperature drop; 2. further gas dissolution into the aqueous phase at lower temperature; 3. gas consumed into hydrate during hydrate formation; and 4. excess gas phase volume due to the contraction of aqueous phase into hydrate phase. The overall gas consumption data was used to calculate the gas consumption into hydrate by subtracting the volume contributed by the other factors. The time at which the gas consumption became continuous was recorded as the induction time of that concerned hydrate formation experiment.

At the end of the hydrate formation experiments, the resulting gas mixtures were collected, and their compositions were quantitively assessed using Variant CP-3800 gas chromatography apparatus.

5.4. Results and Discussion

The main drawback of HBCC is the requirement for high pressure (Linga, et al., 2007b). To address this issue, the thermodynamic additive THF was added to aqueous solution. Linga et al (2007) observed the acceleration of hydrate formation without resulting in considerable gas loading into the hydrate phase in the presence of thermodynamic additives (Linga, et al., 2007c). A trial was conducted to extrapolate these results to extended time periods and also to check if the selectivity is affected by the addition of tertiary amines to the aqueous phase. As in previous research (Thoutam et al., 2019), the experiments in this study were designed to consider the factors affecting gas consumption. A detailed comparative analysis of the experimental data has been conducted to determine the influence of the four aforementioned factors on volumetric gas consumption. This has been applied in the quiescent hydrate formation experiments in sets 1, 2 and 3. However, in the experiments with THF, hydrate formation can only be detected from the volumetric gas consumption but not quantitively verified through mathematical correlations. However, in order to calculate gas consumption into the liquid and hydrate phases, a total value of water to hydrate conversion of 55% was taken for experiments 4, 5 and 7, while a conversion of 70% was taken for experiment 6. To verify these values, hydrates from experiments 6 and 7 were weighed, and the results show that 108 g and 77.89 g of hydrate respectively were found out of 150 g of solution. The volumes of gas consumption results from the experiments after three and 20 hours were compared in order to evaluate their efficiency in capturing CO_2.

5.4.1. Test set 1

The first set of tests was carried out without any thermodynamic additive at a pressure of 10 MPa and a temperature pf 274.15 K (Table 5.2). The experimental results for this set of experiments were analysed in terms of the yield of hydrate formation so as to eliminate the least favoured amine for hydrate formation. This set included three experiments, where one system was quiescent while the other two had 1wt% TEA and 1wt% TIPA respectively.

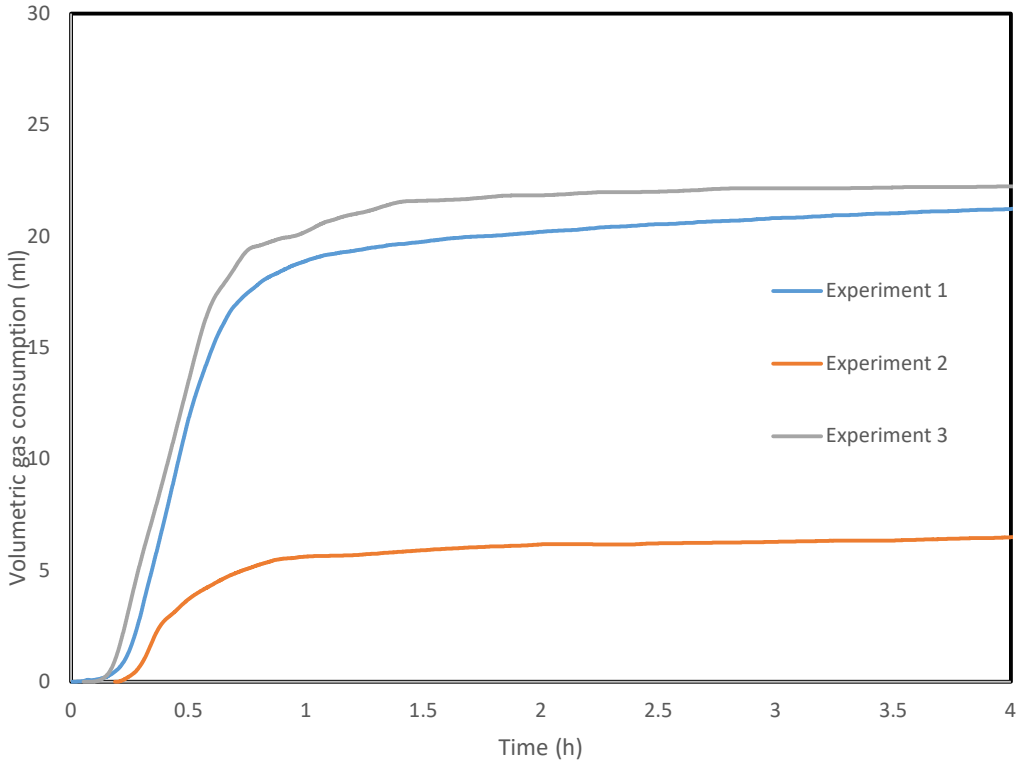

Figure 5.2. Initial volumetric gas consumption (ml) for the first set of experiments

Figure 5.2 shows the volumetric gas consumption for the first four hours of the systems during the experiment. In the Figure, an induction time can be seen before the formation of hydrates, unlike our previous study (Thoutam et al., 2019b). This could be due to the contribution of N_2 at higher concentrations (85% v/v) in the gaseous mixture. In the previous hydrate formation experiments at lower N_2 concentrations (5% v/v), no observable induction was noted whereas

here the induction time was approximately 6 mins (Thoutam, et al., 2019a). Figure 5.2 shows that the highest gas consumption was recorded for the system with 1wt% TIPA, while consumption was lowest in the system with TEA. This might be because of the suppressed initial hydrate formation in the presence of TEA. Figures 5.2 and 5.3 show the volumetric gas consumption of the systems in experiments 1, 2 and 3 in the first test set for two different time periods of three hours and 20 hours respectively. In addition to the lower overall hydrate yield, the system with TEA exhibited lower volumetric gas consumption, which at the end of 20 hours was observed to be less than 12 ml. This value was less than the excess volume of 20.8 ml created by contraction of the gas mixture when the temperature was lowered from 285.15 K to 274.15 K. This indicates that the gas mixture in the reactor has not attained the required operational temperature even after 20 hours, while the aqueous phase has. In comparing gas consumption levels, accelerated consumption can be seen in experiment 3 in the presence of TIPA, but the overall rate compared to experiment 1 was lower over time. As with SDS, TIPA is not participating in hydrate formation, and the elevated concentrations of the amine may have inhibited further hydrate formation after a threshold concentration at these operational conditions. However, it took more than 10 hours for the quiescent system to exhibit the same amount of volumetric gas consumption as the system with TIPA, which might be undesirable for continuous carbon removal at industrial level. Even after 20 hours, the difference between the levels of volumetric gas consumption for the TIPA and quiescent systems was not considerable.

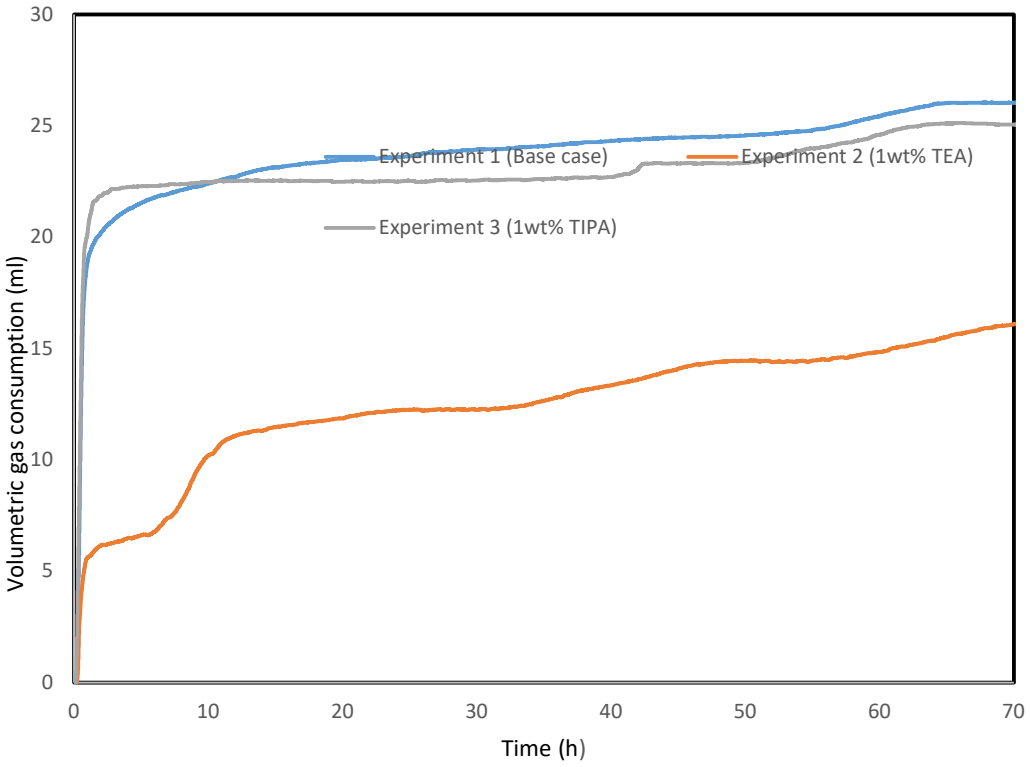

Figure 5.3. Volumetric gas consumption (ml) for a time period of 25 hours during the first set of experiments

For an improved analysis, volumetric gas consumption into the hydrate reactor has been converted into the moles. However, from the perspective of hydrate formation mechanism, the experimental set 1 followed and entirely different path to the rest of the experiments, which was considered. In the experimental set, the hydrate formation was driven by the hydrate formation gas (primarily CO_2), while it was THF in the rest of the experiments. Hence, the volume of gas over the liquid within the reactor was calculated through an iterative process considering the hydrate density that was growing with the consumption of gas into it. The molar volume of the gas composition (85% N_2 and 15% CO_2) was calculated using the following equation derived by Peng-Robinson EOS (Elnabawy, et al., 2013).

$$P = \frac{RT}{V - b_m} - \frac{a_m}{V^2 + 2Vb_m - b_m^2} \quad (5.1)$$

Where P is the pressure, V is the molar volume of the gas mixture, R is the gas constant, a_m is the attraction parameter and b_m is the repulsion parameter.

$$a_m = \sum_{i=1}^{2} \sum_{j=1}^{2} x_i x_j (1 - k_{ij}) \sqrt{a_i a_j} \quad (5.2)$$

Where x_i and x_j are the mole fractions of the gases CO_2 and N_2 respectively, while k_{ij} is the binary interaction parameter. Kij has been taken from the study conducted by Fandino et al (2015) (Fandino, et al., 2015)

$$b_m = \sum_{i=1}^{2} z_i b_i \quad (5.3)$$

The total number of moles of gas consumption into the hydrate reactor was calculated using the equation 5.4.

$$N = \frac{V_{T,t} - V_{excess,t}}{V} \quad (5.4)$$

Where $V_{T,t}$ is the total volume of gas supplied into the hydrate reactor at any time t, $V_{excess,t}$ is the excess volume created by the formation of hydrate, which was calculated by the equation 5.5.

$$V_{excess} = \frac{\varepsilon' N V_W \rho_w}{\rho_h} \quad (5.5)$$

Where $\boldsymbol{\varepsilon}'$ is the ratio of water molecules per gas molecule in a hydrate nucleus, V_w is the molar volume of water, $\boldsymbol{\rho}_w$ is the density of water and $\boldsymbol{\rho}_h$ is the density of hydrate.

However, for the experimental set 2 and 3, the excess volume contributed by hydrate formation was ignored because the hydrate formation was assumed to have occurred before the gas

consumption into the hydrate reactor. This is because the hydrate formation was not driven by the gas as the hydrate former was THF in the system (Kumar, et al., 2016; Li, et al., 2019).

While converting the volumetric gas consumptions into the molar gas consumptions during hydrate formation process two contributing factors affecting gas consumption were neglected: the excess gas consumption into the reactor due to the contraction of the gas and the excess gas dissolved into water when the temperature was lowered from 285.15 K to 274.15 K.

Table 5.3. Molar gas consumptions and induction times for experimental set 1 at three hours and 20 hours

Experiment No.	Induction time (min)	Moles of gas consumption	
		At three hours	At 20 hours
1	5.833	0.0862	0.0974
2	12.16	0.0250	0.0485
3	6.83	0.0918	0.0932

This can be attributed to the high concentrations of N_2 gas in the gas mixture and also its solubility being less sensitive to fluctuations in temperature. Values of molar gas consumption into the aqueous+hydrate phase after considering these adjustments are provided in table 5.3. The induction times reported by Li et al (2009) showed a value of 19 min corresponding to the hydrate formation in the N_2/CO_2 system, which were higher to the current experimental conditions (Li, 2009) (Tang, et al., 2013). However, the study did not consider the addition of SDS into the system. A considerable depression in induction times were observed in the study of Tang et al (2013). However, the minimum induction time was still higher than the value obtained in this study. The difference might have obtained due to the following reasons:

- Difference in the method of identifying the induction time
- Stochasticity associated with the hydrate induction time under conditions of lower driving force.

Supporting these arguments, the uncertainty in the induction times under the similar chemical compositions was further discussed in the study of Linga et al. (2007), where the authors observed their induction times as low as 4 mins (Linga, et al., 2007c). From the induction times reported in the table 5.3, it was evident that the addition of amine has discouraged the hydrate formation. However, the de-escalation of hydrate formation was considerably higher by the addition of TEA. The repetition of experiment 1 has yielded upon an induction time value of 12.5min, confirming the previous observations. Even from the perspective of total hydrate yield, its addition has considerably reduced hydrate formation. The TEA in the system in resulted in 71% less gas capture after three hours compared to the quiescent system (experiment 1), while the corresponding value was 50% after 20 hours.

However, the system with 1wt% TIPA in experiment 3 showed an elevated gas loading 7% higher than the quiescent system after 3 hours. This demonstrates the effectiveness of TIPA as a promoter for carbon capture into hydrate. However, the gas loading increased more rapidly over time in the quiescent system than in the 1wt% TIPA system, so that the recorded gas loading was 4% higher in capturing CO_2 in the aqueous/hydrate phase. Even though this difference is not substantial, the higher yield in the quiescent system further supports the argument that hydrate formation might have been hindered due to the elevated TIPA concentrations in the residual aqueous solution. At the end of the first set of experiments, TEA was eliminated from further examination, while concentrations of 3 mol% of THF along with 1wt% of TIPA in the aqueous surfactant solution were considered for experiment 4.

5.4.2. Test set 2

The second set of tests (Table 5.2) examined the volumetric gas consumption with respect to varying concentrations of TIPA in the presence of 3 mol% THF in the solution in experiments 4, 5 and 6. In these experiments, the concentrations of TIPA were varied between 0 and 1wt% in the THF+SDS aqueous solutions. These experiments were conducted at 3.5 MPa and 274.15 K. By comparing the results for volumetric gas consumptions in Figure 5.4 with those in Figure 5.2, as well as the comparison between the table 5.3 and table 5.4, a shift can be observed in the induction time to a relatively lower value in the second set Similar to the observations made my Linga et al (2007).

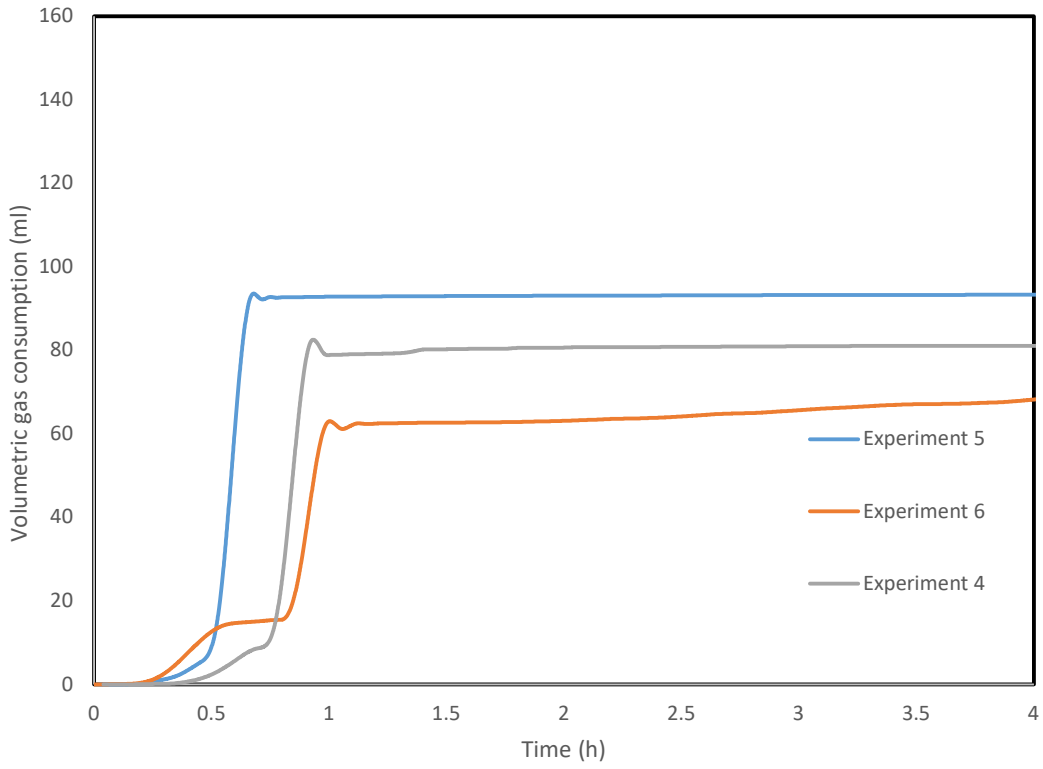

Figure 5.4. Initial volumetric gas consumption against time for experiments 4, 5 and 6.

Similar to the observations made in the test set 1, the addition of TIPA was seen to be delaying the induction time by a few minutes. Even though the difference is not huge when compared

to the overall period of experimentation, it seems that the addition of 3mol% THF is inadequate in initiating hydrate formation at 3.5 MPa as quickly as in the quiescent systems at 10 MPa. During hydrate formation in the presence of THF and in the gaseous mixture of CO_2 and N_2, two types of competition were observed (Dashti, et al., 2015), firstly between CO_2 and THF in occupying the larger cages of hydrate, and also between dissolved N_2 and CO_2 for both small and large cages of hydrate. However, due to the lower solubility of N_2 and also its lower affinity to form hydrates at low pressure conditions, the concentration of N_2 found in the hydrate would be negligible. For elevated gaseous consumption during the hydrate formation process with THF, readily available dissolved gas would be needed. Initial values of volumetric gas consumption for experiments 4, 5 and 6 are shown in figure 5.4. The results show that the quiescent system in experiment 6 recorded the lowest initial consumption of 66ml after three hours. This might have been due to the unavailability of dissolved CO_2 in the system at the time of hydrate formation with THF. In experiment 4 with 1wt% TIPA in 3mol% THF, a relatively higher initial gas consumption of 81ml was found after three hours. The highest volumetric gas consumption of 93.2ml after three hours was recorded for experiment 5 where 0.5wt% of TIPA was used. This might be attributed to the lower resistance to hydrate formation offered by lower concentrations of TIPA, at the same time as adequate concentrations of dissolved CO_2 are present in the aqueous phase due to the presence of TIPA in the system. The conclusions drawn concerning the efficiency of gas consumption differ when the experiments were carried out for longer. Figure 5.5 shows the profiles of gas consumption for experiments 4, 5 and 6 for a period of 20 hours. At 20 hours, the system with no amine in experiment 6) showed elevated gas consumption as a result of the elimination of the resistance towards hydrate formation caused by the presence of amines. The profile of gas consumption for experiment 6 crossed that for experiment 4 with 1wt% TIPA after eight hours, while it took

approximately 14 hours to achieve the gas consumption levels shown by experiment 5 with 0.5wt% TIPA.

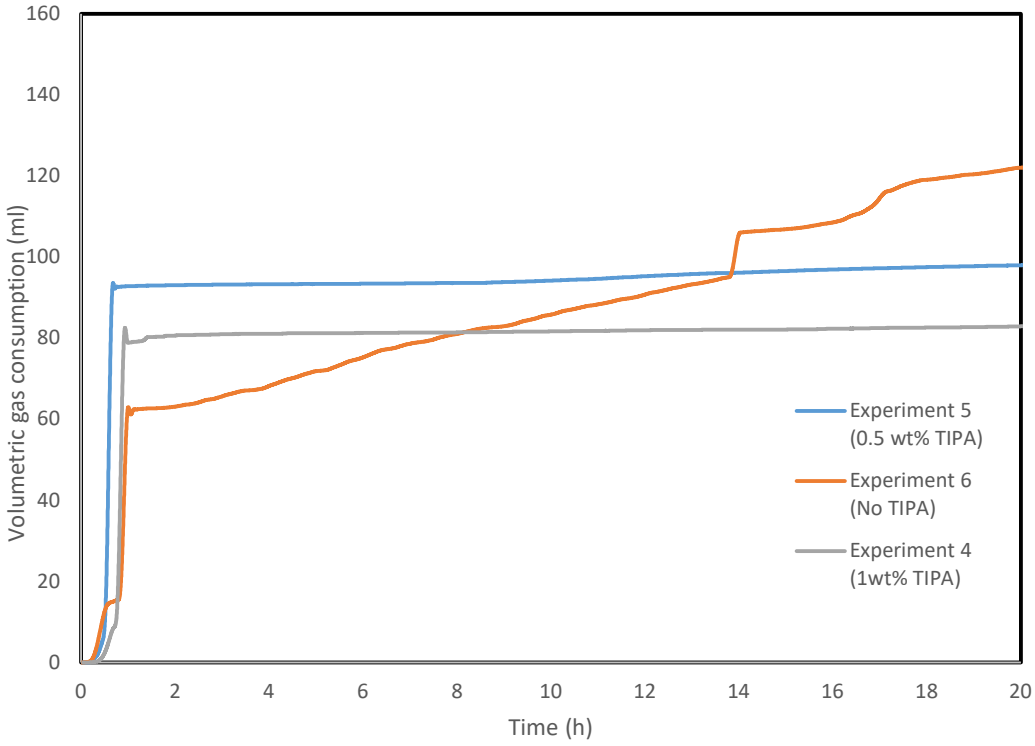

Figure 5.5. Volumetric gas consumption profiles in experiments in test set 2 for an extended period.

While converting the volumetric gas consumption values into molar gas, along with the gas consumption contributing factors 1 and 2, the factor 4 has also been neglected for the following reasons: 1. The hydrate formation in the presence of THF was exponential and faster when compared to the quiescent state; 2. It's contribution to the molar gas consumption value would be lesser as the density difference between hydrate and water would be less than 10% (Aya et al., 1997). This means, all the observed gas consumption during the hydrate formation experiments was considered to have been consumed into hydrates. The values of molar gas consumption for the experiments in test set 2 are given in table 5.4.

Table 5.4. Molar gas consumption values and induction times for test set 2 after three hours and 20 hours

Experiment No.	Induction time (min)	Moles of gas consumption	
		After three hours	After 20 hours
4	7.83	0.1097	0.1125
5	5.67	0.1280	0.1350
6	4	0.0830	0.1667

The table shows that the inclusion of 3mol% THF in the system with 1wt% of TIPA in experiment 4 led to a gas loading 20% higher than in the system without THF used in experiment 3 after three hours. This value was further improved to 21% after 20 hours. Meanwhile the molar gas loading in the quiescent system in experiment 1 was 16% higher after 20 hours. This suggests a better carbon capture in the system with 3mol% THF +1wt% TIPA at 3.5 MPa compared to the quiescent system at 10 MPa in terms of both economy and efficiency. Reducing the TIPA concentration to 0.5wt% improved the molar gas consumption into the aqueous+hydrate phase by 17% after three hours, while this increased to 20% after 20 hours. When compared the molar gas consumption values of the 0.5wt% TIPA+THF system with the system containing no amine in experiment 6, the former system recorded 54% higher gas capture after three hours, suggesting that 0.5wt% TIPA in the system gives better performance. On the other hand, the gas consumption after 20 hours shown by the 0.5wt% TIPA+THF system was 19% less than in the system with no maine (experiment 6), indicating lowered hydrate formation after a threshold of TIPA concentration in the residual liquid after a certain point of time during the experiment.

5.4.3. Test set 3

In order to obtain higher volumetric gas loadings in the presence of a thermodynamic additive (THF), the hydrate formation yield should be sufficient to avail the small unoccupied voids for CO_2 to occupy. Also, the hydrate formation rate should not be faster than the diffusion rate of CO_2 from water to the site of hydrate formation. Lower rates of hydrate formation imply the presence of less CO_2 in the system, whereas higher rates imply more empty voids and hence less CO_2 in the hydrate. And whereas the presence of amine reduces the hydrate formation yield and therefore limits gas capturability, accelerated hydrate formation could be a second limitation. To reduce the speed of hydrate formation with THF, experiment 5 was repeated in experiment 7 but this time at a lower operational pressure of 1.5 MPa.

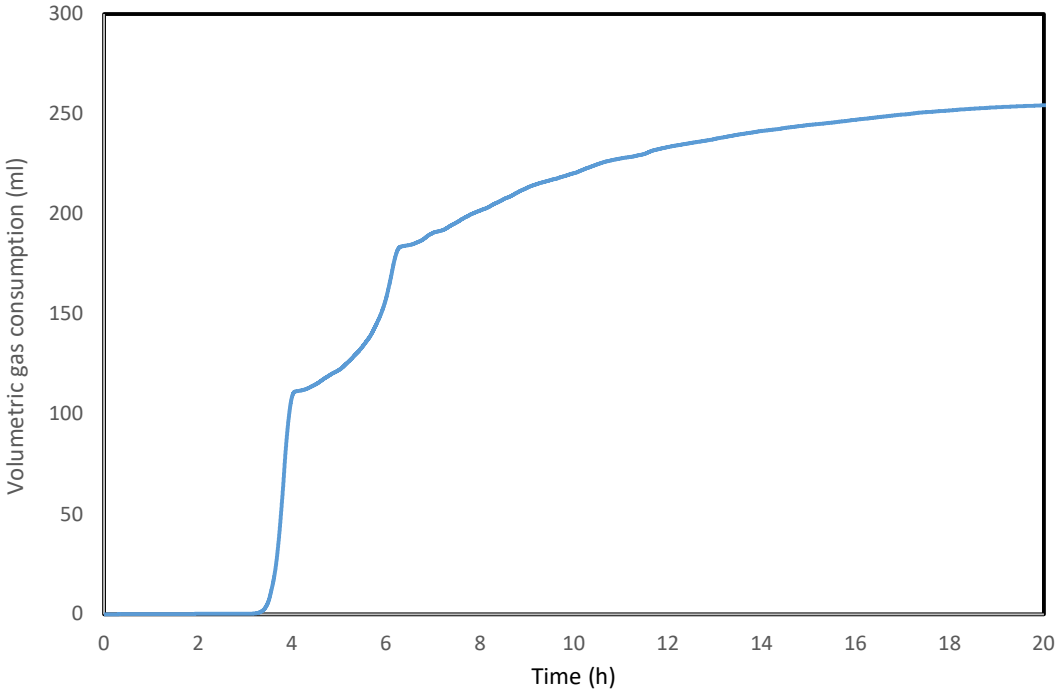

Figure 5.6. Volumetric gas consumption profile for experiment 7

The profile of volumetric gas consumption for experiment 7 is presented in figure 5.6. In accordance with our expectations, no substantial hydrate formation as indicated by an exponential increase in gas consumption, was observed until 3 hours and 3 minutes. This

induction time was considerably higher compared to that in experiment 5 (with 0.5wt% TIPA+THF at 3.5MPa), which was approximately 20 minutes. This system contained an aqueous phase configuration similar to that in experiment 5. Even though the induction time was more than three hours, the volumetric gas consumption achieved after 20 hours was more than 250 ml. However, this value cannot be compared with the results of the experiments in set 2 unless converted to molar values due to the difference in operational pressure.

Similar to testing set 2, while calculating molar gas consumption into hydrate, all the other contributing factors (1, 2 and 4) have been neglected for the same reasons explained in the section 4.2. The molar gas consumptions of this set are mentioned in the table 5.5.

Table 5.5. Molar gas consumptions for the experimental set 3 at three hours and 20 hours

Experiment no	Induction time (min)	Moles of gas consumption	
		At three hours	At 20 hours
7	185.1667	0.0002	0.1547

The molar gas loading in the aqueous+hydrate system was approximately 15% higher than the value observed in experiment 5. Hence, it is advised that researchers need to understand the difference between the rate and yield of THF hydrate formation when designing a hydrate-based gas capture system, especially when competition among its components to occupy hydrate voids is involved.

The initial gas consumption values observed to be negligible compared to the expected gas consumption due to the gas contraction in the reactor creating excess volume as the temperatures were lowered from 285.15K to 274.15K. This indicates that the gas mixture above the aqueous solution did not reach the operational temperature during hydrate formation. This

observation is supported by the negligible thermal conductivity of air compared to water (Lemmon & Jacobsen, 2004). To ensure the repeatability of these experiments, experiments 6 and 7 were repeated and similar results were obtained, hence confirming the reliability of these profiles.

5.4.4. Selective separation of CO_2

At the end of each experiment, the residual gaseous mixture was collected and subjected to chromatographic analysis to determine its chemical composition in order to gain an overall idea of the selectivity of hydrate formation. However, as these experiments were conducted for different time periods, the comparisons concerning the CO_2 selectivity of the systems used have limitations. The results for the composition of gases extracted from the experiments along with their times of extraction are listed in table 5.6.

The three main factors which govern the selective separation of CO_2 from a gaseous mixture are the dissolution of CO_2 in the aqueous mixture and the yield and speed of hydrate formation. Despite long periods of time allowed for dissolution, the first set of experiments conducted without thermodynamic additives resulted in lower selectivity than the rest. While being shorter in duration, experiment 2 showed slightly higher CO_2 selectivity, confirming our previous observations. Among the systems with THF at a pressure of 3.5 MPa, the system without amine showed better CO_2 selectivity. However, this might have been due to the extensive hydrate formation associated with the longer period in the experiments. However, a comparable level of CO_2 selectivity was achieved with the addition of 0.5wt% TIPA in experiment 6 after a shorter duration. In addition to supporting the idea of tertiary amine addition towards higher selectivity, from the second set of experiments, CO_2 selectivity towards hydrate formation was observed to be proportional to the experimentation time. However, amongst all the systems tested, the analysis of gas collected from the experiment 7 conducted at the lowest operational pressure showed that this system achieved the highest selectivity within the shortest time.

Table 5.6. Extracted gas compositions in the residual gaseous mixture along with their respective extraction times

Experiment No.	N_2 concentration (mol%)	CO_2 concentration (mol%)	Time of extraction (s)	Percent of CO_2 removed from the gas into hydrate
1	88.77	11.23	423100	25.13%
2	89.11	10.89	445340	27.4%
3	89.55	10.45	257130	30.33%
4	93.41	6.59	155150	56.07%
5	93.19	6.81	250640	54.6%
6	93.31	6.69	75990	55.4%
7	94.03	5.97	75000	60.2%

5.4.5. Carbon removal capacity from MSF desalination plant

From the table 5.6, it can be concluded that a single stage HBCC system has a capacity of removing 50-60% of CO2 from the post combustion gas stream into the hydrate. Which means, after subjecting to the HBCC systems, the effluent gas steams from the MSF would be 50-60% lesser in the carbon content. Agashichev and El-Nashar (2005) in their techno economic evaluation of the hybrid desalination column mentioned the specific carbon emissions of MSF desalination plants with respect to the amount of water output when the plant operated by various power sources such as gas turbine, auxiliary boiler and heat recovery steam generator. When considered an MSF being operated using a gas turbine with a loading of 0.6, the specific

carbon emission of the plant would be 13.75kg of CO_2/m^3 of distilled water. For a desalination plant such as Al Khobar II MSF desalination plant, as mentioned in the studies Helal et al (1986) and Ross et al (1997), the carbon emission of the plant would be 3.575kg of CO_2/s. However, the effluent gases generally consist of a post combustion gas mixture, where only 15% of the total gas mixture would be CO_2 while the rest (as taken in this chapter), would be filled with N_2. Hence, the total volumetric flowrate of the effluent gas from the MSF would be 1355.634ml/s. When converted this value into mol of carbon emission per mol of seawater input, considering the seawater input for the same MSF column mentioned in Rosso et al (1997), which was 1578kg/s, the resulting value would be $2.38x10^{-5}$mol CO_2/seawater intake. In order to compare this value with the hydrate-based carbon capture system, the most optimistic conditions similar to the chapter 4 (figure 4.11), were assumed based on the experimental observations.

As seen from the figure 5.5, the best system with the highest initial gas uptake kinetics were observed in the system consisting of 0.5mol% TIPA+3wt%THF and operated at 3.5MPa. The most optimistic conditions for this system would be the condition with no induction time delay and no thermodynamic barrier hindering further hydrate formation after reaching to local maximum at 45 mins (or 0.74 hours as seen from the figure 5.5). A trend line has been created mimicking the exponential gas uptake recorded in the figure 5.5 pertaining to the system with the aforementioned chemical composition. Figure 5.7 shows the trendline along with the projected gas uptake values if the system had no thermodynamic barrier (which could be created by continuously removing the hydrate from the system).

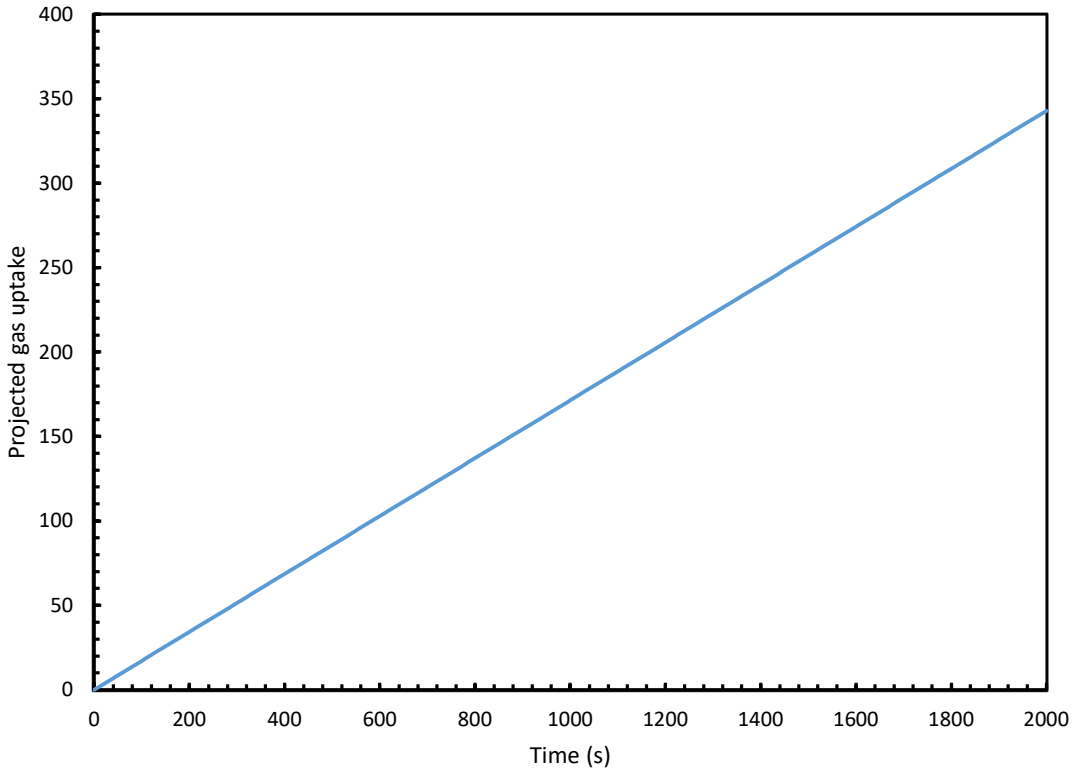

Figure 5.7. Projected gas uptake for the system with 0.5mol% TIPA+3wt%THF under the most optimistic conditions.

From the figure 5.7, the considered system has a capacity of uptaking over 340ml of gas into the liquid+hydrate phase. This value will not provide with any conclusion as this is an absolute value related to the amount of water taken in the system. In these experiments 150ml of water has been taken, whereas the amount of CO_2 emitted from MSF has a seawater intake of over $1.5x10^6$ml of water. These gas uptake values were further converted into the molar gas uptake per mole of available water. So that the water requirement for the HBCC in comparison with the water requirement of the considered MSF could be done. The figure 5.8 depicts the mols of gas intake occurs in the considered system under the optimistic conditions per mole of water intake.

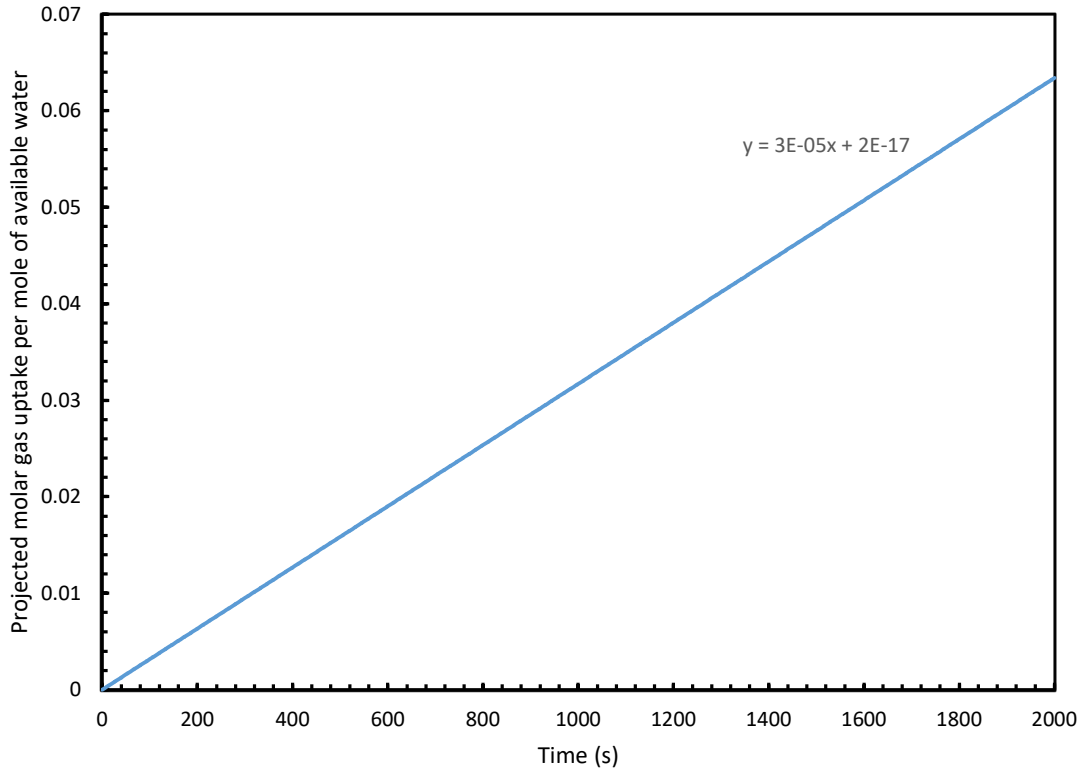

Figure 5.8. Projected molar gas uptake per mole of available water in the considered hydrate-based carbon capture (HBCC) system.

From the figure 5.8, it can be seen that the molar gaseous uptake per mol of water could reach up to 0.063 after 2000 seconds. From the trendline equation, the molar rate of gas uptake per mole of water could be observed to be $3x10^{-5}$. Comparing this value with the molar post combustion gas emission per mole of seawater intake, which was $2.58x10^{-5}$, a continuous system would take lesser water than the MSF seawater intake to capture the same amount of post combustion gases emitted from the MSF desalination column. However, in reality, irrespective of the amount of emissions from the MSF, it is impossible for any HBCC system to absorb all the emission into hydrate as the HBCC was designed to consume a CO_2 dominant gas mixture int hydrate while leaving N_2 dominant gas mixture in the gas phase. As the mole fraction of CO_2 in the post combustion gas mixture would be approximately 15%, the gas intake into the hydrate in the HBCC from the MSF emissions would be less than 15%. It means, the

water intake required for the HBCC system would be less than 15% of the seawater intake into the MSF desalination column, when HBCC is operated under the most optimistic conditions. Moreover, this HBCC, does not require as considerable amounts of seawater intakes as MSF, as 100% recycling of dissociated hydrate could be sent back to the HBCC system to be used for gas capture again (Figure 5.1).

Apart from the compatibility issues, another issue that could arise during the process of carbon capture through HBCC would be more carbon emission during the hydrate formation process through work done by the pump operating at high pressure conditions. Considering the pump and the reactor were placed on the same elevation, the power consumption by the pump was calculated from the equation 5.6 (Da Rosa, 2009)

$$P_{Pump} = \frac{Q\Delta P}{\eta} \tag{5.6}$$

Where, P_{Pump} is the power consumed by the pump (kW), Q is the volumetric flow rate of gas (m^3/s), ΔP is the pressure drop across the pump (kPa), and η is the efficiency of the pump, which would be 0.75 for the QUIZIX high-pressure syringe pump (Q6000-10K model).

In order to calculate the total carbon emission by hydrate formation process, especially during the supply of power to the pump, two hydrate formation configuration systems were taken where both the systems consist of 0.5 mol% TIPA and 3wt% THF. However, the first system would be operated at 3.5MPa while the second system would be operated at 1.5MPa. By using the equation 5.7, the total power consumption by the pump for the system 1 would be 6.32KW.

Agashichev and El-Nashar (2005) et al, have also mentioned the carbon emission rate with respect to the power consumption by gas turbines. If considered the power required for running the pump for hydrate system was run by gas turbines with a loading of 0.6, which had a specific carbon emission of 0.18kg/kWh of energy consumption. Which means, for the system 1, the specific carbon emission by the pump would be 0.000316kg/s. When converted it into the total

post-combustion gas mixture's volume flow rate, the value would be 0.0312ml/s. This means, the post combustion gas volume emission rate of the hydrate-based carbon capture system would be 0.0312ml/s that has a capacity of cleaning 1355.634ml/s of gas, which was highly negligible. In case of the system 2, which operated at a pressure of 1.5MPa, the post combustion gas volumetric emission would be 0.0134. This value is even more negligible to the emission rates of MSF. Hence, the process of HBCC is greener as well as compatible to the MSF process when operated under the most optimistic conditions.

5.5. Summary

The study was aimed at understanding the improvement in the efficiency of carbon capture technology through hydrate formation when combined it with chemisorption through tertiary amines. The hydrate formation kinetics and the carbon selectivity in the presence of amines and THF were examined. By observing the induction time and the hydrate yield, the characteristic of THF and TIPA towards the formation of hydrates was analysed. However, the sensitivity of hydrate formation resulted in the depression of its kinetics to the availability of tertiary amines in the system was found to be a major limitation. It was more serious in the presence of THF rather than TIPA. Hence, TIPA was used in a further investigation in the presence of THF. The availability of CO_2 in the liquid phase is crucial in the selective separation of CO_2 during the formation of hydrate in the presence of THF, as its capture occurs mainly through the occupation of large and small cavities in the hydrate, competing with both THF and N_2. From the analysis of volumetric gas consumption, a gradual resistance to hydrate formation was clearly observed in the presence of tertiary amines in the system. Furthermore, increased gas consumption was observed when the concentration of TIPA in the system was reduced. The results also suggest that the addition of TIPA in amounts as small as 0.5 wt% in the presence of THF could improve initial gas loading compared to amine-free systems.

To further improve CO_2 selectivity from the gas mixture, the operational pressure was lowered to 1.5MPa from 3.5MPa. The induction time of the system before hydrate formation began now extended to over three hours. However, once hydrate formation started, overall gas consumption significantly improved even with the same composition as at 3.5MPa. Evidenced from the residual CO_2 gas concentration, hydrate formation at 1.5 MPa (Experiment 7) showed higher CO_2 selectivity than other system with the same chemical composition within a lesser time period. It implied that lower hydrate formation kinetics could improve CO_2 selectivity into hydrate. The higher selectivity of CO_2 observed in the chromatogram of the experiment with 0.5wt% TIPA compared to the experiment with no TIPA showed that the yield of hydrate formation also has a role in selective separation. Amongst all the compositions, the highest amount of CO_2 separation from the gas stream into the hydrate was seen in the 0.5wt% TIPA operated at 1.5MPa. However, this system was not considered to be the most effective system due to the lower initial hydrate formation kinetics. Hence, the most effective HBCC system was observed to be the system with the same chemical composition but operated at 3.5MPa.

Using these experimental observations, the aforementioned most effective chemical composition and the operational conditions were chosen for the HBCC system so that its performance could be compared to the requirement of Al Khobar II MSF desalination plant. Apart from the efficiency of selectively separating CO_2 from the post-combustion gas stream, the molar gas loading per molar water available in the system were compatible to the molar gas emission per molar seawater inlet of the MSF desalination column. Which denotes less water requirement along with more water recyclable capacity for HBCC with respect to MSF. From the perspective of carbon emission during the hydrate formation due to the fuel consumption for the pump work, the emissions of hydrate formation were found to be negligible when compared to the emissions of MSF, making HBCC more desirable.

Chapter 6

HBD-MSF Hybrid

6.1. Introduction

The current chapter deals with the comparative analysis of the efficiency of the hybrid in the combination of Hydrate based desalination (HBD) and MSF and was discussed in terms of performance ratio as well as production ratio. There have been various issues questioning the longevity and the performance of MSF, amongst which, scale formation and fouling were considered to be the most challenging. Scale formation through the precipitation of salts from the saline water under heightened temperatures is a universal issue for all the major desalination processes around the globe. Especially in thermal desalination processes such as MSF and Multi-effect desalination (MED), operating at higher temperatures, this issue was even higher. Amongst all the parts of these desalination systems, the condenser tubes have been regarded to be most vulnerable to failure through the issues such as corrosion and scale formation. Approximately 80% of the outages occurring in these desalination processes were due to the failure of condenser systems, where 90% of them occur in the condenser tubes. Hence, condenser failure in thermal desalination processes is by default considered as the tube failure (El Din & Mohammed, 1998; El-Dahshan, 2001). As explained in the chapter 2, this study addressed the fouling issues occur in MSF as they are the most installed thermal desalination systems in the world.

Depending upon the pH requirement of scale formation, the scales are often classified as alkaline and non-alkaline scales. When the pH of the system increases, the bicarbonates in the system would convert into carbonate, causing carbonate supersaturation resulting in alkaline scale formation (Glade & Al-Rawajfeh, 2008). An illustration of how pH could trigger the scale

formation by creating carbonate supersaturation has been shown in the figure 6.1. Hence, controlling the scale formation would be important to suppress alkaline scale formation. The trigger behind the formation of alkaline scale is the lower solubilities of salts as well as accelerated decomposition of bicarbonates under heightened solution temperatures. The most common composition of alkaline scale consists of $CaCO_3$ and $Mg(OH)_2$. Calcium Carbonate based scale formation has been understood to be the most common type of scale that occurs at temperatures as low as 45°C, whereas Magnesium hydroxide based scale formation occurs at temperatures above 75°C which is most common for the MSF desalination systems operate at top brine temperatures above 108°C (El Din & Mohammed, 1989; El Din & Mohammed, 1994; El Din, et al., 2005).

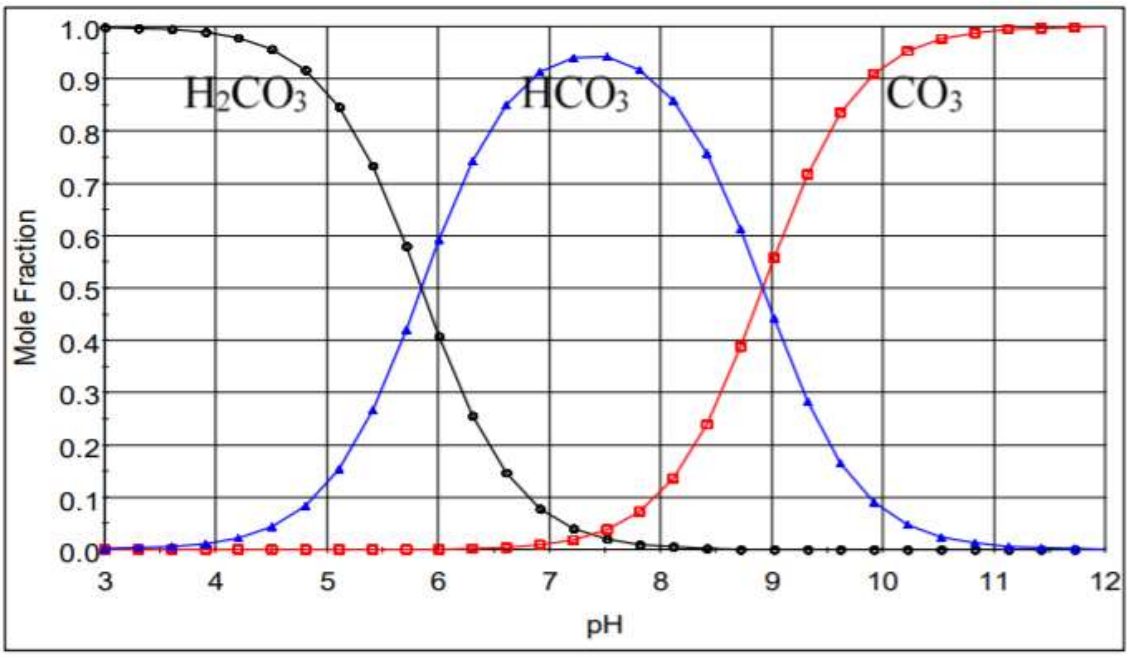

Figure 6.1. The CO_2, bicarbonate and carbonate mole fractions with respect to the solution's pH at operational temperature 298.15K and salinity 35g/l (Glade & Al-Rawajfeh, 2008)

Amongst the non-alkaline scales, $CaSO_4$ scale has been found to be the most common one. Similar to $Mg(OH)_2$, $CaSO_4$ would require temperatures as high as 75°C to form. As explained by Al-Sofi (1999), the precipitation of $CaSO_4$ in any form in MSF plants was observed to have

occurred only when the plant is operated at TBT more than 120ºC. Unlike alkaline scales, $CaSO_4$ would be the result of reaction of the pre-existing components in the saline water and independent of pH of the solution (Al-Sofi, 1999; Shams El Din, et al., 2005; Wildebrand, et al., 2007). In fact, as stated by Shams El Din et al (2005), for an MSF system operated with a TBT (Top brine Temperature) 112ºC, the first three stages were completely covered with $Mg(OH)_2$ scale while the later stage were dominated by $CaSO_4$, with an increasing quantities of $CaCO_3$ with stages. As the current study has been focussed on how pre-treated water from hydrate based desalination process could improve the Multi-stage flash, the system was considered to be operating at temperatures lower than 90ºC top brine temperature and hence, only $CaCO_3$ scale formation was considered. However, in order to give an overall idea, the basic mechanism of $Mg(OH)_2$ as well as $CaSO_4$ were also superficially explained.

Adding knowledge to the ongoing research on improving the performance of MSF, the current chapter analyses the performance of the combination of HBD-MSF hybrid, through a comparative analysis of rate of scale formation, mass deposition, distillate production, performance ratio and production ratio with MSF by means of mathematical modelling designed in Simulink software. For that purpose, two basic steady state MSF models were created representing once-through and brine-recycle. These models were created using the configurations presented in the modelling studies of Rosso et al (1997) and Ali and Kairouani (2014) (Rosso, et al., 1997; Ali & Kairouani, 2014)

6.2. MSF modelling

The following assumptions were considered while modelling the MSF desalination column, which has been illustrated in the figure 6.2:

1. The heat losses are negligible apart from the condenser tubes.
2. The distillate produced from the MSF desalination is free of salt.

3. Negligible heat of mixing
4. The salinity changes in the coolant flowing in the condenser tubes is negligible
5. The entrainment of mist within by the flashed vapour is negligible.

The entire set of modelling equations are a collection of mass and heat transfer equations, which is given as follows:

6.2.1. Equations within the stages

Mass, salt, and energy balance within the flash chamber are given in the equations 6.1, 6.2 and 6.3 respectively:

$$B_{i-1} = B_i + D_i \tag{6.1}$$

$$X_{bi-1}B_{i-1} = X_{bi}B_i \tag{6.2}$$

$$D_i\lambda_{vi} = B_{i-1}C_{pbi-1}(T_{bi-1} - T_{bi}) \tag{6.3}$$

Where B, D, X and the subscript 'i' represents the brine flowrate (kg/s), distillate flowrate (kg/s), salt concentration (g/kg) and the stage number. The vapour temperature above the demister does not stay constant as the vapour loses a fraction of heat while passing through demisters, the correlation for which has been provided by Rosso et al (1997).

$$T_{di} = T_{vi} - \frac{\exp(1.885-0.02063T_{vi})}{1.8} \tag{6.4}$$

Where T_{di} is the temperature of vapour after passing through the demisters while T_{vi} is the temperature of vapour before it. The temperature of vapour before passing through the demisters would be equal to the brine temperature (T_{bi}) leaving the stage. The pressure (mmHg) of each stage has been calculated from the Antoine Equation, which is given in the equation 6.5 (Boublik, et al., 1984)

$$log_{10}P = A - \frac{B}{(T+C)} \tag{6.5}$$

Where the temperature T is in Celsius, and the A, B and C values are 8.07131; 1730.63 and 133.426.

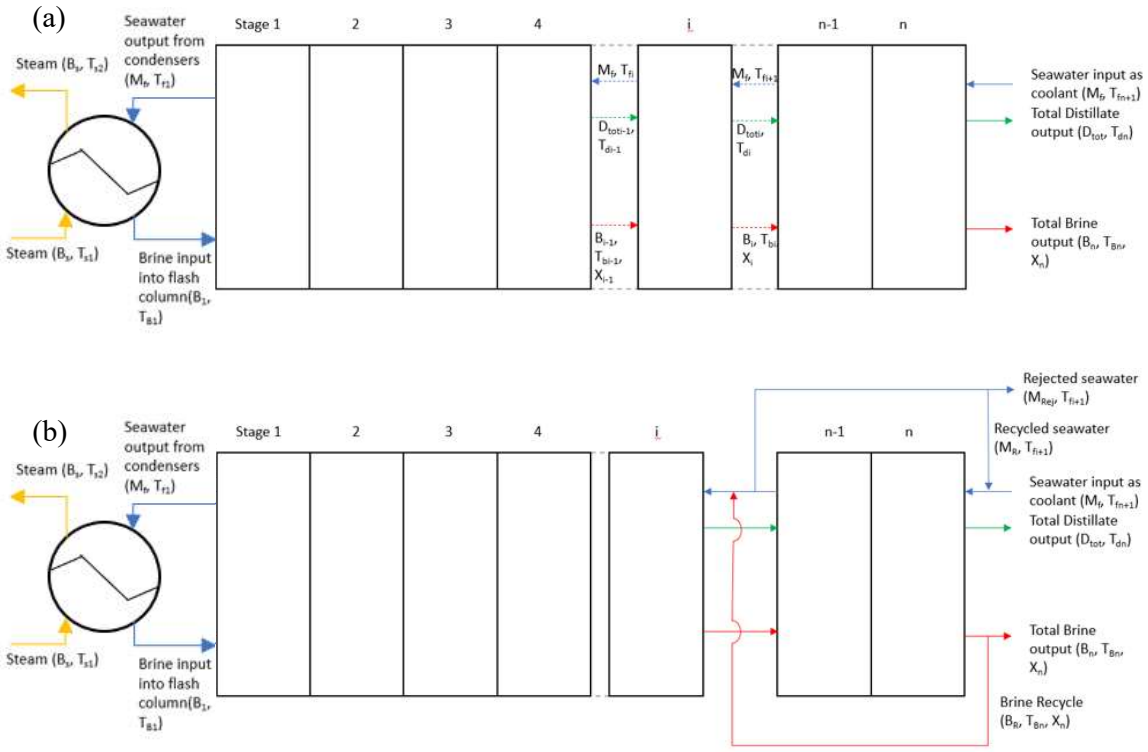

Figure 6.2. The configurations of MSF-OT (a) and MSF-BR (b)

6.2.2. Equations within the condensers

The heat transfer in between the coolant within the condenser and the vapour in the heat recovery section is given in the equation 6.6:

$$(M_R + M_f)C_{pfi}(T_{fi} - T_{fi+1}) = U_{ci}A_c(LMTD)_{ci} \qquad 6.6$$

Where M_R and M_f are the flowrates (Kg/s) of recycled brine and intake seawater, T_f is the temperature of the coolant, U is the overall heat transfer coefficient, A is the heat transfer area and LMTD is the Log mean temperature difference. The values of LMTD were calculated from the equation 6.7:

$$(LMTD)_{ci} = (T_{fj} - T_{fj+1})/ln\left(\left[\frac{T_{dj}-T_{fj+1}}{T_{dj}-T_{fj}}\right]\right) \qquad 6.7$$

The equation 6.8 was derived to calculate the value of T_f, which was obtained by solving the equations 6.6 and 6.7.

$$T_{fi} = T_{di} - \left(T_{di-}T_{fi+1}\right)e^{-\left(\frac{U_c A_c}{\left(M_R+M_f\right)c_{pfj}}\right)} \quad 6.8$$

The overall heat transfer coefficient equation was taken from the MSF modelling work carried out by Alasfour and Abdulrahim (2009) is given in the equation 6.9 (Alasfour & Abdulrahim, 2009).

$$\frac{1}{U_{ci}} = \left(\frac{d_o}{d_i}\right)\frac{1}{h_{in\,i}} + \left(\frac{d_o}{d_i}\right)r_{fi} + \left(\frac{d_o}{2k_{tube}}\right)ln\left(\frac{d_o}{d_i}\right) + \frac{1}{h_{out\,i}} + r_{fo} \quad 6.9$$

Where d_o and d_i are the outer and inner diameters of the condenser tube, k_{tube} is the thermal conductivity of the tube, h_{in} and h_{out} are the inside and outside heat transfer coefficients, and r_{fi} and r_{fo} are the heat transfer resistances on the inside and the out sides of the condenser tube. The calculation methodology for the heat transfer resistance has been discussed in the section 6.3.

The parameter $h_{in\ i}$ can be calculated by using Dittus-Boelter equation (El-Dessouky & Bingulac, 1996; El-Dessouky & Ettouney, 2002) which is provided in the equation 6.10

$$h_{in\,i} = \frac{(3293.5 + T_{fi+1}\left(84.24 - 0.1714T_{fi+1}\right) - X_{if}(8.471 + 0.1161X_{if} + 0.2716Tf_{i+1})}{\left(\frac{d_i}{0.017272}\right)^{0.2}(0.656Vel)^{0.8}\left(\frac{d_i}{d_0}\right)} \quad 6.10$$

Where Vel is the velocity of the coolant stream flowing inside the condenser tubes. The medium of heat transfer coefficient on the outside of the tubes ($h_{out\ i}$) is mainly caused by the availability of noncondensable gases (NCG). In order to keep the model simple, the contribution of noncondensable gases towards heat transfer coefficient has been ignored in this study.

The overall energy balance around the condensers in the heat rejection section can be calculated from the equation 6.13

$$D_i\lambda_{ci} + C_{pdi-}\ (T_{di-1} - T_{dj}) \sum_{k=1}^{j-1} D_{\mathrm{k}} = (M_{cw} + M_f)C_{pfi}(T_{fi} - T_{fi+1}) \qquad 6.13$$

Where the subscript k represents any stage number that is less than the i^{th} stage. Similar to the equation 6.6, the heat transfer equation for the condenser tubes in the heat rejection could be written as shown in the equation 6.12

$$\left(M_{CR} + M_f\right)C_{pfi}\left(T_{fi} - T_{fi+1}\right) = U_{ci}A_c(LMTD)_{ci} \qquad 6.12$$

Where M_{CR} is the recirculated coolant mass flowrate. The temperature of the effluent stream from the coolant from the stage i in the heat rejection section could be calculated from the equation 6.13

$$T_{fi} = T_{di} - \left(T_{di-}T_{fi+1}\right)e^{-\left(\frac{U_CA_C}{\left(M_{CR}+M_f\right)C_{pfj}}\right)} \qquad 6.13$$

Energy balance equation around the condensation chamber of the heat rejection section is given in the equation 6.14

$$D_i\lambda_{ci} + C_{pdi-1}(T_{di-1} - T_{dj}) \sum_{k=1}^{j-1} D_{\mathrm{k}} = (M_{CR} + M_f)C_{pfi}(T_{fi} - T_{fi+1}) \qquad 6.14$$

6.2.3. Equations within the brine heater and mixers

The energy balance equation around the brine heater is given by the equation 6.15

$$M_s\lambda_s = (M_R + M_f)C_p(T_{bo} - T_{f1}) \qquad 6.15$$

The energy balance equation around the recycled brine and the seawater input (considering j number of stages in the heat rejection section) is given in the equation 6.16.

$$\left(M_R + M_f\right)C_{pfn-j}T_{fn-j} = M_RC_{Pb}T_{bn} + M_fC_{pfn-j}T_{fn-j} \qquad 6.16$$

The energy balance equation around the recycled coolant and the seawater input (considering j number of stages in the heat rejection section) in the stage n is given in the equation 6.17.

$$\left(M_{CR} + M_f\right)C_{pfn}T_{fn} = M_{CR}C_{Pbn} \quad T_{bn-j} + M_f C_{p,ambient}T_{f,ambient} \tag{6.17}$$

6.2.4. Generic equations

The seawater specific heat at constant (in kJ/kg^{o}C) pressure was calculated through the equation 6.18.

$$C_P = A_{Cp} + B_{Cp}T + C_{Cp}T^2 + D_{Cp}T^3)X10^{-3} \tag{6.18}$$

Where A_{cp}, B_{cp}, C_{cp} and D_{cp} are dependent upon the water salinity and was calculated from the equations 6.19, 6.20, 6.21 and 6.22 respectively.

$$A_{Cp} = 4206.8 - 6.6197X + 1.228x10^{-2}\,X^2 \tag{6.19}$$

$$B_{Cp} = -1.1262 + 5.4178x10^{-2}X + 2.2719x10^{-4}\,X^2 \tag{6.20}$$

$$C_{Cp} = 1.2026\,x10^{-2} - 5.3566x10^{-4}X + 1.8909x10^{-4}\,X^2 \tag{6.21}$$

$$D_{Cp} = 6.8777\,x10^{-7} - 1.517x10^{-6}X + 4.4268x10^{-9}\,X^2 \tag{6.22}$$

The dynamic viscosity (kg/m.s) of seawater could be calculated from the equations 6.23 – 6.27

$$\mu = \mu_w\mu_R x10^{-3} \tag{6.23}$$

$$Ln\,(\mu_w) = -3.79418 + \frac{604.129}{(139.18+T)} \tag{6.24}$$

$$\mu_R = 1 + A_{\mu R}X + B_{\mu R}X^2 \tag{6.25}$$

$$A_{\mu R} = 1.474\,x\,10^{-3} + 1.5\,x\,10^{-5}T - 3.927\,x\,10^{-8}T^2 \tag{6.26}$$

$$B_{\mu R} = 1.0734\,x\,10^{-5} - 8.5\,x\,10^{-8}T + 2.23\,x\,10^{-10}T^2 \tag{6.26}$$

The temperature dependent latent heat of vaporization is given in the equation 6.28.

$$\lambda = 2051.89714 - 2.407064037\,T + 1.192217\,x\,10^{-3}T^2 \qquad 6.28$$

Based on these equations, two MSF desalination models were created representing both MSF-OT and MSF-BR models and were run to generate results such as the brine and distillate flowrates. They were compared to the model results by Rosso et al., 1997 to validate the current model before introducing scale formation to the model.

6.3. Mechanism of scale formation

As the entering sea-water temperature rises, various chemical reactions occur, which were mentioned by various authors. The reacting ions such as Ca^{+2}, Mg^{+2}, OH^-, CO_3^{-2} and HCO_3^- would be diffused from the bulk liquid to the heat transfer surface under the scale forming conditions triggering a series of reactions before the production of scale forming substrates ($CaCO_3$, $Mg(OH)_2$ and $CaSO_4$) and its deposition onto the surface. The foremost reaction, addressing the figure 6.1, would be the generation of carbonates and CO_2 from bicarbonates as shown in the equation 6.28.

$$2HCO_3^- \rightleftharpoons CO_2 \uparrow + CO_3^{-2} + H_2O \qquad 6.29$$

However, according to Mubarak (1998) and El Din et al (2002), the reaction 6.29, occurs in two steps as mentioned in the equations 6.30 and 6.31, rather than in one step (Mubarak, 1998; El Din, et al., 2002). The first step consists of liberation of CO_2 from the dissociation of bicarbonates which is followed by acid neutralization producing carbonates:

$$HCO_3^- \rightleftharpoons CO_2 \uparrow + OH^- \qquad 6.30$$

$$OH^- + HCO_3^- \rightarrow CO_3^{-2} + H_2O \qquad 6.31$$

In addition to the reactions mentioned in the equations 6.30 and 6.31, a parallel bicarbonate dissociation into carbonate and CO_2 step was also mentioned in various studies, which are as shown in the equations 6.32 and 6.33 (Olderøy, et al., 2009; Segev, et al., 2012). Eventhough,

the equation 6.32 was recognised as acidification reaction in seawater to discourage the decomposition of bicarbonate (Patel & Finan, 1999; El Din, et al., 2002).

$$HCO_3^- \rightleftharpoons CO_3^{-2} + H^+ \quad 6.32$$

$$H^+ + HCO_3^{-2} \rightleftharpoons CO_2 \uparrow + H_2O \quad 6.33$$

The generated carbonate ions would react with calcium ions to produce Calcium Carbonate, which would deposit when its solubility is lowered under the operational conditions.

$$Ca^{+2} + CO_3^{-2} \rightarrow CaCO_3 \downarrow \quad 6.34$$

When combined equations 6.30, 6.31 with 6.32, the resultant equation shows the precipitation of $CaCO_3$ causing scale formation.

$$2HCO_3^- + Ca^{+2} \rightarrow CaCO_3 \downarrow + CO_2 \uparrow + H_2O \quad 6.35$$

Under the higher temperature conditions, the reaction 6.31 would reverse into the formation of bicarbonate ions and hydroxyl ions from carbonates. These hydroxyl ions would react with Magnesium ions to form Magnesium hydroxide, which would start forming scales once its solubility limit is reached. The entire process has been shown in the equations 6.36 and 6.37.

$$CO_3^{-2} + H_2O \rightarrow HCO_3^- + OH^- \quad 6.36$$

$$2OH^- + Mg^{+2} \rightarrow Mg(OH)_2 \downarrow \quad 6.37$$

According to Mubarak (1998), the formation of carbonate from the dissociation of bicarbonate is faster when compared to its reverse reaction. However, given the substrate is formed, the precipitation of $Mg(OH)_2$ is thermodynamically more spontaneous than the deposition of $CaCO_3$. Contrary to the alkaline scale formation, non-alkaline scale formation is straight forward, for example Calcium ions would react with Sulphate ions to form Calcium sulphate

($CaSO_4$) which precipitates when solubility limit is exceeded under the given operational conditions.

$$SO_4^{-2} + Ca^{+2} \rightarrow CaSO_4 \downarrow \quad 6.38$$

When the scale formation starts occurring, due to the change in roughness of the surface with the progression of scale formation, other substrates start agglomerating over the scale, causing irregularities in the fouling layer's structure (Slesarenko, et al., 2003).

6.4. Model for scale formation

During the modelling of scale formation, the following assumptions were considered.

- Lumped distribution of scale formation along the condenser tubes was considered.
- Pressure drop in between the inlet and outlets of the tubes was neglected.
- The velocity fluctuation due to the narrowing of the tube cross-sectional area with the scale formation was neglected.
- The heat flux along the walls of tube bundles was neglected.
- All the ions are transported from the bulk to the heat transfer wall.

6.4.1. Calculation of scale deposition rate

The net scale formation would be the resultant of both the deposition of scale formation substances under the suitable operational conditions as well as the removal of scale resulted by the turbulence associated with the velocity of the stream. The final scale deposition was be calculated from the equation 6.39.

$$\frac{dm_f}{dt} = m_d - m_r \quad 6.39$$

Where m_f is net scale deposition, while m_d and m_r are the progressive deposition rate and mass removal rates respectively.

Figure 6.3 illustrates the mass deposition process through ions diffusion and/or surface reaction rates. As shown in the figure, the diffusion of ions from the bulk to the heat transfer surface (condenser tube surface) is considered to be the first step of progressive scale formation and it is calculated from the equation 6.40.

$$\frac{dm_d}{dt} = k_D\,(C_{b-}\,C_i) \qquad 6.40$$

Where k_D is the coefficient of mass transfer, C_b is the ion concentration in the bulk stream while C_i is the ion concentration at the liquid-solid boundary layer.

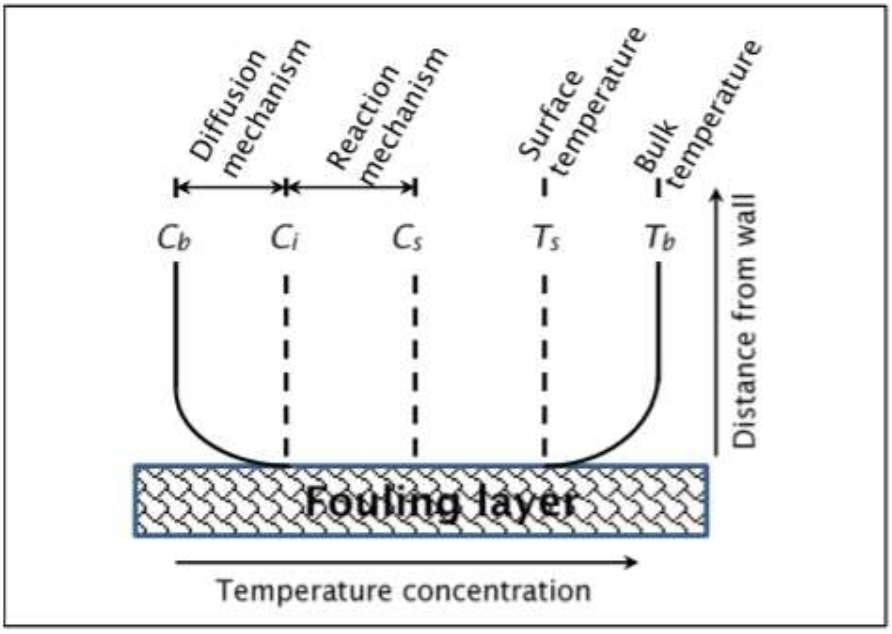

Figure 6.3. The profiles of ion concentrations and temperatures near the condenser tube surface (Hasson, et al., 1968).

The second step represents the deposition, where the accumulation of these transported species occur by means of the concentration difference driving force, which has been shown in the equation 6.13.

$$\frac{dm_d}{dt} = k_r(C_i - C_s)^n \quad 6.41$$

Where the constant of reaction rate has been represented by k_r, saturation concentration was represented by C_s while n is the order of reaction. When it comes to the $CaCO_3$ scale formation, due to the involvement of Ca^{+2} and CO_3^{-2} ions, the order of reaction was considered to be a second order reaction (Brahim, et al., 2003). As it is difficult to calculate the ion concentration at the heat exchanger surface, as mentioned in the assumptions in the current section, all the ions are transported from the bulk to the heat exchanger surface, which makes the reaction step to be the controller of the scale formation process. Evidently, the scale formation process is controlled by diffusion step only under lower stream velocities, while under higher velocities, it is the reaction step that governs the kinetics of scale formation (Helalizadeh, et al., 2000; Fahiminia, et al., 2007). Especially, Najibi, et al. (1997) assumed the control of diffusion over the scale formation under velocities less than 0.9m/s based on the experimental observations on activation energy by Andritsos (1996) (Andritsos, 1996; Najibi, et al., 1997). The reaction step's control over the $CaCO_3$ scale formation was observed and confirmed by Augustin and Bohnet (1995) and Paakkonen et al (2012) respectively (Augustin & Bohnet, 1995; Pääkkönen, et al., 2012). Under the consideration of controlled mechanism for scale formation, the equation 6.40 could be used to calculate the rate of scale formation taking appropriate conditions as well as the ion concentrations into account. As described by Hasson et al. (1978), the concentration driving force that has to be used in the equation 6.40, has been defined as the difference between the concentration of calcium and carbonate ions and the solubility product of $CaCO_3$ (Hasson, 1978). When $CaCO_3$ formation reaction order was assumed to be a second order reaction following the finding of Hasson et al (1968), the equation 6.40 would evolve into the equation 6.42.

$$\frac{dm_d}{dt} = k_r([Ca][CO_3] - k_{sp})^2 \quad 6.42$$

By adjusting the equations 6.40 and 6.41, Bohnet (1987) derived an equation to calculate the rate of scale deposition in the case of $CaSO_4$ that would consider the contribution of both the diffusion as well as reaction, besides eliminating the unknown parameter interfacial ion concentration C_i (Bohnet, 1987). Using the method proposed by Bohnet (1987), Helalizadeh et al (2005) and Paakkonen et al (2015) calculated the rate of $CaCO_3$ precipitation through the equation 6.43 (Helalizadeh, et al., 2005; Pääkkönen, et al., 2015). As the current study takes a modified version of the equation 6.44, it has to be understood that this study acknowledges the contribution of both diffusion as well as the reaction into the calculation of scale formation.

$$\frac{dm_d}{dt} = \beta\left[\frac{1}{2}\left(\frac{\beta}{k_r}\right) + (c_b - c_s) - \sqrt{\frac{1}{4}\left(\frac{\beta}{k_r}\right)^2 + \left(\frac{\beta}{k_r}\right)(c_b - c_s)}\right] \quad 6.43$$

Where β is the mass transfer coefficient, which could be calculated from the equation 6.44.

$$\beta = \frac{0.034 Re^{0.875} Sc^{0.33} D}{D_h} \quad 6.44$$

Where Re is Reynolds number, Sc is Schmidt number, D is coefficient of diffusion, and D_h is the hydraulic diameter of the tube. The coefficient of diffusion values for the systems containing calcium and carbonate could be taken from the work done by Segev et al (Segev, et al., 2012). The equations 6.45 and 6.46 presents the means to calculate Reynolds number and Schmidt number.

$$Re = \frac{\rho_w v D_h}{\mu_w'} \quad 6.45$$

$$Sc = \frac{\mu_w}{\rho_w D} \quad 6.46$$

Where μ_w and $\boldsymbol{\rho}_w$ are the viscosity and density of water. Bu considering the suggestion given by Paakkonen et al (2015), flow velocity is added to the equation 6.41. After applying Arrheneus expansion for the reaction rate coefficient, the resulting equation would be the equation 6.46. The reaction rate coefficient and the activation energy values

were taken from the experimental evaluation studies upon $CaCO_3$ scale formation conducted by Bohnet (Bohnet, 1987).

$$\frac{dm_d}{dt} = k'_r(C_i - C_s)^n \frac{\mu_w}{\rho_w V^2} = (k'_0 e^{\frac{-E_a}{RT_s}})(C_i - C_s)^2 \frac{\mu_w}{\rho_w V^2} \quad 6.47$$

Where V represents the friction velocity and can be calculated from the equation 6.48

$$V = \sqrt{f\frac{v^2}{2}} \quad 6.48$$

Even though, calcite has the lower solubility in water, it is aragonite that contributes more to the scale formation. When conducted X-ray analysis, Helalizadeh et al. found that over 99% of the $CaCO_3$ scale formation was contributed by Aragonite (Helalizadeh, et al., 2000). Plummer and Busenberg derived a temperature dependent equation to calculate the solubility product of Aragonite (Plummer & Busenberg, 1982). However, considering the fluctuations of temperature, pressure and salinity in water, a more advanced version of solubility product equation was derived by Al-Anezi and Hilal, where the activity coefficient of water was considered (Al-Anezi & Hilal, 2007), which is provided as the equation 6.49.

$$K_{sp} = \frac{K_{sp}^0}{\gamma_{Ca}\gamma_{CO_3}} \quad 6.49$$

Where γ is the component's activity coefficient. K_{sp} and Ts are in molar units and in kelvin respectively. While Plummer and Busenberg's equation could be used to calculate K_{sp}^0 value, which is given as equation 6.50 (Plummer & Busenberg, 1982).

$$Log(K_{sp}^0) = \left[-171.9773 - 0.077993T_s + \frac{2903.293}{T_s} + 71.595\log(T_s)\right] \quad 6.50$$

WATEQ-Debye-Huckel's equation has been used to calculate the activity coefficient of an ion 'a', which has been given as the equation 6.51 (Al-Anezi & Hilal, 2007).

$$Log(\gamma_a) = -A_{DH} Z_a^2 \frac{\sqrt{I}}{1+B_{DH} a_a \sqrt{I}} + b_a I \quad 6.51$$

Where A_{DH} is Debye-Huckel parameter, z is the ionic charge, B is the temperature dependent variable, a_a, b_a are the parameters specific to ion 'a' and the ionic strength has been represented by I. To calculate I, the equation 6.52 could be used.

$$I = 0.5 \sum z_i^2 m_i \quad 6.52$$

6.4.2 Calculation of scale removal rate

Along with the mass deposition of scale formation components, reducing the tube cross sectional area blocking the flow as well as decreasing the heat transfer rates, the velocity of the liquid flowing inside the tubes create shear stress upon the scale. Under the high turbulence in the tube, this shear stress would lead to the removal of scale deposits. Bohnet developed an equation (6.53) to calculate the scale removal rate considering that the rate is proportional to the shear stress of the flow, while it is inversely proportional to the layer's shear strength (Bohnet, 1987).

$$\frac{dm_r}{dt} = k_{rem} \frac{\tau_f}{\sigma_f} \boldsymbol{\rho_f} \left(\frac{\mu_w g}{\rho_w}\right)^{0.33} \quad 6.53$$

Where the removal rate constant is represented by krem,, while τ_f, ρ_f and σ_f are the surface shear stress, density and the shear strengths of the fouling layer, while g represents the gravitational acceleration. The equation (6.54) to calculate the shear strength was also provided by Bohenet (Bohnet, 1987).

$$\sigma_f = K. \frac{P_f}{N x_f (1+\delta \Delta T) d_p} \quad 6.54$$

The equation 6.55 is the result of substituting the equation 6.54 into the equation 6.53.

$$\frac{dm_r}{dt} = \frac{k_{rem}}{k} \frac{N x_f (1+\delta \Delta T) d_p T_f}{\sigma_f} \boldsymbol{\rho_f} \left(\frac{\mu_w g}{\rho_w}\right)^{0.33} \quad 6.55$$

In order to calculate the term (k. Pf/ krem. N), Kraus made a suggestion (equation 6.56), which has been applied by Brahim et al in their scale formation calculations (Krause, 1993; Brahim, et al., 2003).

$$\frac{k\ P}{k_{rem}N} = 83.2\ v^{0.54} \tag{6.56}$$

When the equation 6.56 is substituted in the equation 6.55, it results into the equation 6.57.

$$\frac{dm_r}{dt} = \frac{x_f(1+\delta\Delta T)d_p\ T_f}{83.2\ v^{0.54}}\boldsymbol{\rho_f}\left(\frac{\mu_w g}{\rho_w}\right)^{0.33} \tag{6.57}$$

6.4.3 Calculation of fouling resistance

The rate of mass deposition of the scale forming substances in the equation 6.39 can be written as the product of rate of change in the fouling layer thickness (x_f) and the density of the fouling layer as shown in the equation 6.58.

$$\frac{dm_f}{dt} = \rho_f \frac{dx_f}{dt} \tag{6.58}$$

Whereas this rate of change in the fouling layer thickness, combined with the conductivity of the fouling layer is used to calculate the rate of change in the thermal resistance as shown in the equation 6.59.

$$\frac{dR_f}{dt} = \frac{1}{\lambda_f}\frac{dx_f}{dt} \tag{6.59}$$

A definitive integration of the equation 6.58 from the time t = 0 to t would lead to the following equation 6.60 (considering the conductivity of the fouling layer is independent of fouling layer's thickness and time and is when the lumped distribution of the scale formation along the tube surface is taken into account)

$$\int_{t=0}^{t} dR_f = \frac{1}{\lambda_f}\int_{t=0}^{t} dx_f \tag{6.60}$$

Considering zero resistance and zero scale formation at the time t=0, the equation 6.59 will transform into the following equation (6.61).

$$R_f = \frac{x_f}{\lambda_f} \tag{6.61}$$

Substituting equation 6.58 into equation 6.61 considering zero deposition and zero removal of the scale formation substance on the heat transfer surface at the time t = 0 with some adjustments including integration would produce the equation 6.62.

$$R_f = \frac{\rho_f}{\lambda_f}(m_d - m_r) \tag{6.62}$$

The current work considered the approach proposed by Zhang et al (2015) to calculate the density of the fouling layer. They considered the fouling layer to be porous with the porosity 'w', which in this study was considered to be 50%. The density equation is presented in the equation 6.63.

$$\rho_f = w\rho_{water} + (1 - w)\rho_{solid} \tag{6.63}$$

For calculating the ther mal conductivity of the fouling layer, the study considered the approach proposed by Brahim et al (2003). As the fouling layer is immersed in the water medium, as well as it was considered to be a porous medium with the porosity w, the total value of the thermal conductivity has been considered to be as shown in the equation 6.64.

$$\lambda_f = \frac{\lambda_{f,1} + \lambda_{f,2}}{2} \tag{6.64}$$

Where λ_{f1} and λ_{f2} were calculated from the equations 6.65 and 6.66

$$\lambda_{f,1} = w\lambda_{water} + (1 - w)\lambda_{solid} \tag{6.65}$$

$$\frac{1}{\lambda_{f,2}} = \frac{w}{\lambda_{water}} + \frac{(1-w)}{\lambda_{solid}} \tag{6.66}$$

The equation 6.62 has been implemented in various studies under various operational conditions of the heat transfer process that resulted in different shapes for the rate of scale deposition. One of the most unconventional profiles that were to be cited in the literature was the curve in the shape of 'S' for the scale deposition (Mwaba, et al., 2006). Even though, the rate of fouling depends upon various factors such as temperature and concentration of salt (or ions) as well as pH of the solution, the S shape was found out to be the result of considering nucleation, which is also dependent upon the velocity and the concentration of ions (Najibi, et al., 1997). However, the experimental observations done by Hamed and Al-Otaibi (2010) did not result in an S shaped scale formation kinetics, where as the curve was almost a straight curve with negligible nucleation times. One can argue that the higher velocity conditions might have suppressed the shape into an almost straight profile of scale formation kinetics. In support of the observations done by Hamed and Al-Otaibi (2010), the experimental observations of Brahim et al (2003) and Zhang et al (2015) resulted into the similar curves while their velocities were approximately 0.2m/s (Brahim, et al., 2003; Zhang, et al., 2015). Even though, they considered the removal rates, their rate did not have a major effect on the fouling curve's shape. However, even though there has been numerous disambiguation regarding the fouling curves, it is imperative that the fouling process varies with the configuration of MSF as well as the chemical composition of seawater intake along with the operational conditions. The final effect of scale formation can not be understood until the comparative analysis on the extents of heat exchanges before and after the scale formation in the condenser tubes. Hence, the equation 6.62 was substituted in the equation 6.9, to calculate the overall heat transfer coefficient, which was further utilised to calculate the rate of distillate production from the equation 6.13 and then the performance ratio (PR) of the MSF column by using the equation 6.67.

$$PR = \frac{\sum_{i=1}^{n} D_i}{M_s} = \frac{D_{tot}}{M_s} \qquad 6.67$$

6.5. Results and Discussions

6.5.1. MSF Steady state model and validation

In order to calibrate the effectiveness of the hybrid desalination, initially two MSF desalination designs were created with one representing one through (MSF-OT), while the second representing brine recycle model (MSF-BR) (Table 6.1).

Table 6.1. The overall configuration of the MSF columns

S.No.	Parameter	Value
1.	No. of Columns for OT	16
	In the case of BR model	
	a. Heat rejection section	06
	b. Heat recovery section	13
2.	Total sea water intake for OT	3340 kg/s
	In the case of BR model	
	a. Total seawater intake	1562 kg/s
	b. Cooling brine recycle	1578 kg/s
	c. Reject cooling brine	203 kg/s
3.	Brine temperature into the flash column	89°C
4.	Superheated steam temperature	111°C
5.	Intake seawater salinity	35000ppm
6.	Intake seawater temperature	37.7°C

As the current study focusses upon the comparative analysis of the hybrid and the MSF processes from the perspective of scale formation and overall productivity of the desalinated water, the MSF desalination system created had an adequate accuracy with respect to the study objectives. The configuration of the MSF-OT and BR desalination columns have been taken from Russo et al (1997) and Ali and Kairouani, 2014, which have been as shown in the table 1.The results such as the brine temperature, coolant temperature and the distillate profiles produced by this study were also compared with the results produced by Russo et al. (1997). These comparisons were shown in the figures 6.4, 6.5 and 6.6.

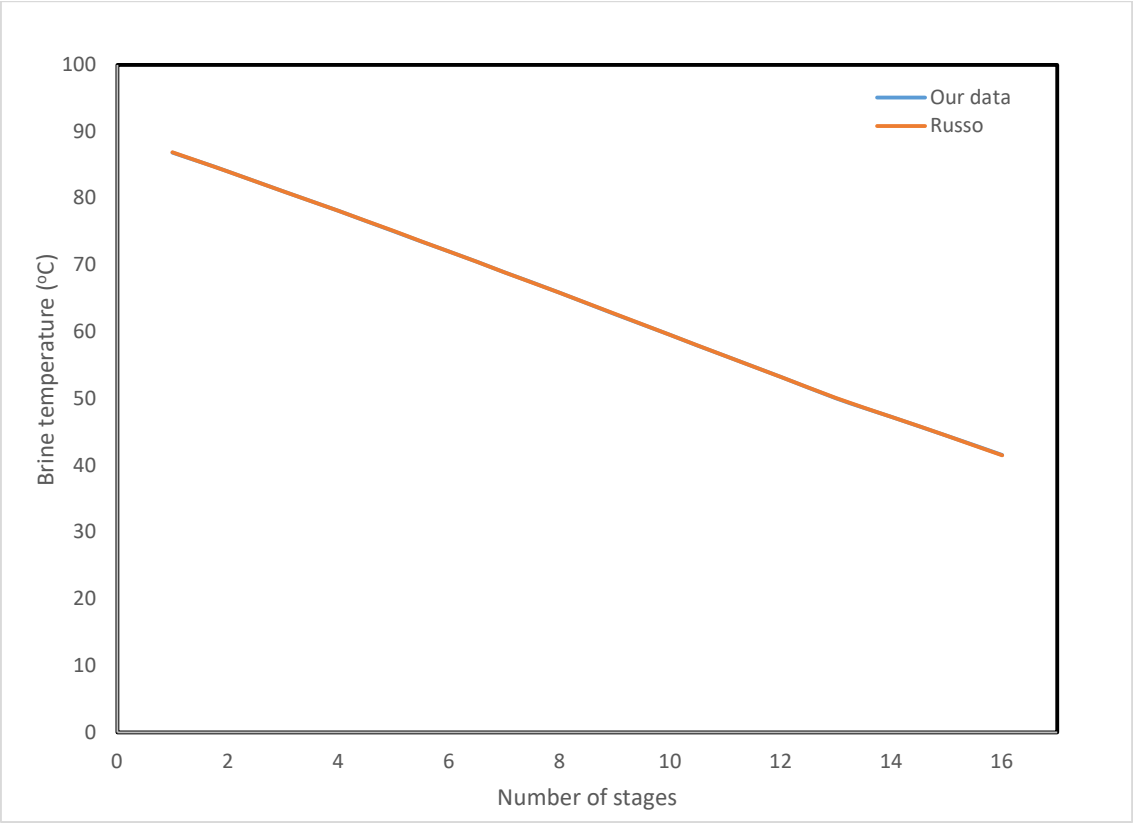

Figure 6.4. The comparison of stagewise brine temperatures from this study with the temperature profiles produced by Russo et al (1997).

The brine temperature profiles of Russo et al (1997) and the current study had a mutual agreement where the maximum deviation between these two studies were found to be 0.1%.

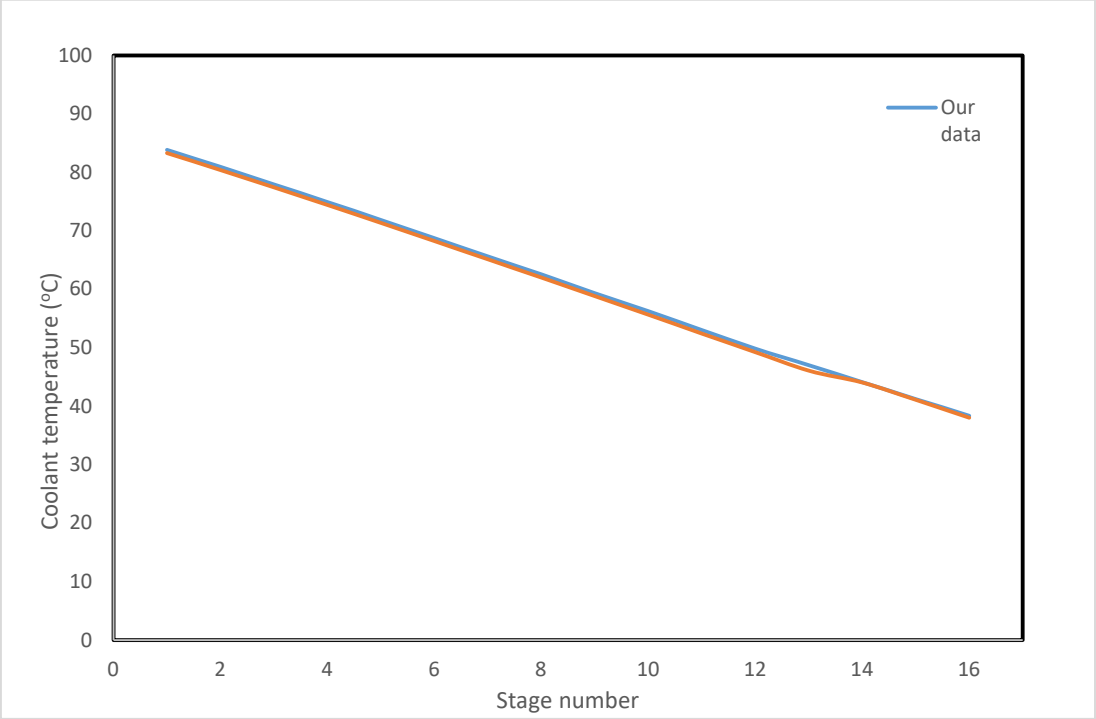

Figure 6.5. Comparison of coolant temperature profiles between the current study and Russo et al. (1997)

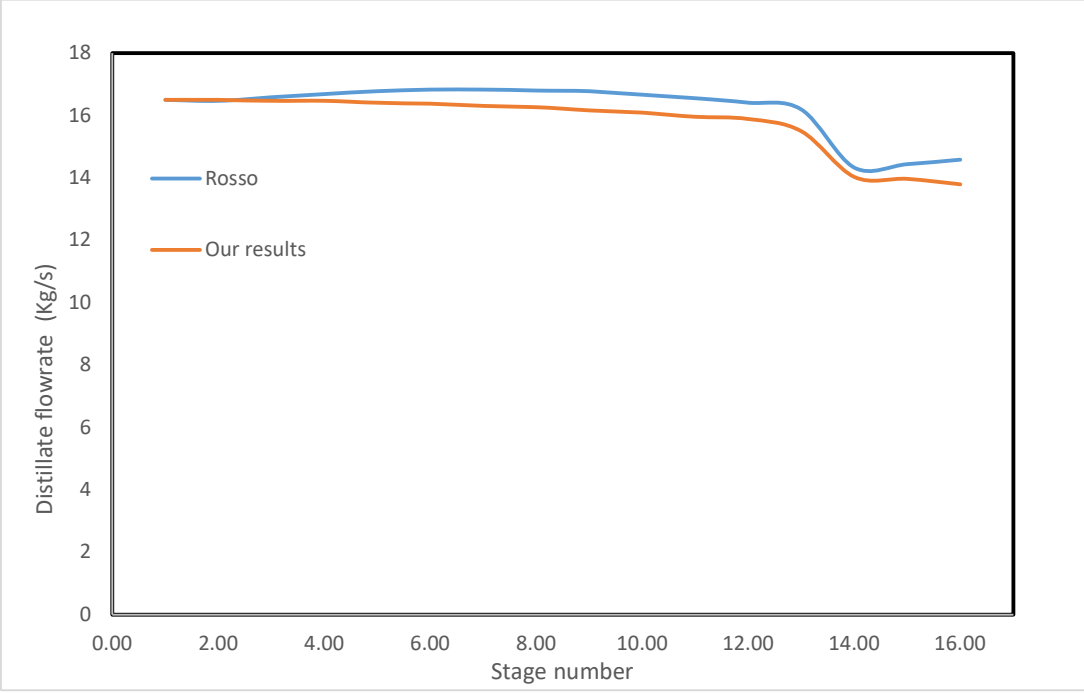

Figure 6.6. Comparison of distillate profiles calculated from this study with Russo et al (1997)

The maximum deviation this study derived from Russo et al (1997) in case of coolant temperature was found to be 2.08%, whereas the maximum deviation this study resulted in from the perspective of distillate production was found to be 4.5% (<5%). The current study did not consider the contribution of non-equilibrium allowance while calculating the temperature of the vapour, which might have contributed to the deviations in both the distillate production rate as well as the coolant temperature profiles. From these results, one can understand that the model produced in Simulink is agreeable with the modelling data produced by Russo et al (1997), calibrating the current model. In addition, the performance of the current model has been measured in terms of performance ratio and production ratio. Performance ratio was calculated using the equation 6.67, while the production ratio (PDR) has been taken as the ratio between the seawater intake and the distillate output as shown in the equation 6.68.

$$PDR = \frac{D_{tot}}{M_f} \tag{6.68}$$

For the case of MSF-OT, the performance ratio of the system has been calculated to be 9.446, while the production ratio of the system was 0.076. The lower production rates were the attributes of having absolutely no brine recycle, where the total water wastage in the form of brine would be higher in MSF-OT model. These values could be further explained by the cross comparison of MSF-OT with the BR model. Even though there were no heat rejection and heat recovery sections in the MSF-OT model, the heat transfer area of the last three stages, which would have represented the heat rejection section were kept equal to the heat transfer area of the heat rejection section in MSF-BR. In the brine recycle mode, the recycled brine flowrate and the seawater intake were chosen in such a way that it would not affect the initial temperature of the inlet coolant water into the condenser tubes of the stage 16 (Table 1). The same amount of rejected seawater from the coolant section after the heat rejection section was substituted from the brine in the stage 16 (figure 2b), where the inlet coolant temperature

decreased to a lower value, increasing the distillate flow rate. Hence, the final Performance ratio was slightly increased to 9.671, where the total production of the brine was resulted to be 258.1kg/s, against the distillate production of MSF-OT 252.1kg/s. However, the production ratio of the system has been considerably improved to a value double to the MSF-OT column (0.1652).

6.5.2. Scale formation

As explained in the section 6.4, the current study uses the scale deposition method proposed in the studies of Pääkkönen, et al. (2015) through the equation 6.43. The removal of scale from the heat transfer area was calculated from the equation (6.56) proposed by Bohnet (1987) and modefied by Brahim et al. (2003), whereas the net rate of scale formation was calculated from the equation 6.39. As explained in the section 6.4.3, the fouling rate profiles will result in different shapes under different conditions. As explained in the section 6.3, the contributing factors for scale formation are pH, temerpature, ion concentration and pressure.

However, in this study, the reasons such as temperture and the saline concentration were considered. As it was understoof by various researchers, the scale formation in the first stage has been explained extensively while the scale formation in the rest of the stages were mentioned when required a comparative analysis. For example, the figure 6.7 shows the overall scale formation in all the 16 stages of MSF-OT, while the figure 6.8 shows shows the same in MSF-BR. From these figures (6.7 and 6.8), it could be seen that the scale formation for MSF-OT and MSF-BR have been very different from eachother. As the stage number increases, the bracket in which the magnitude of scale formation recorded decreased while the initial scale formation varied from $1.88 \times 10^{-6} kg/m^2.s$ till $1.48 \times 10^{-6} kg/m^2.s$. In the MSF-BR, desalination column, for the heat recovery section, from the stage 1 till 13, the initial scale formation ranged from $2.28 \times 10^{-6} kg/m^2.s$ till $1.89 \times 10^{-6} kg/m^2$,whereas in the heat rejection section, these numbers varied from $1.55 \times 10^{-6} kg/m^2.s$ to $1.48 \times 10^{-6} kg/m^2.s$, from the stages 14 to 16 respectively.

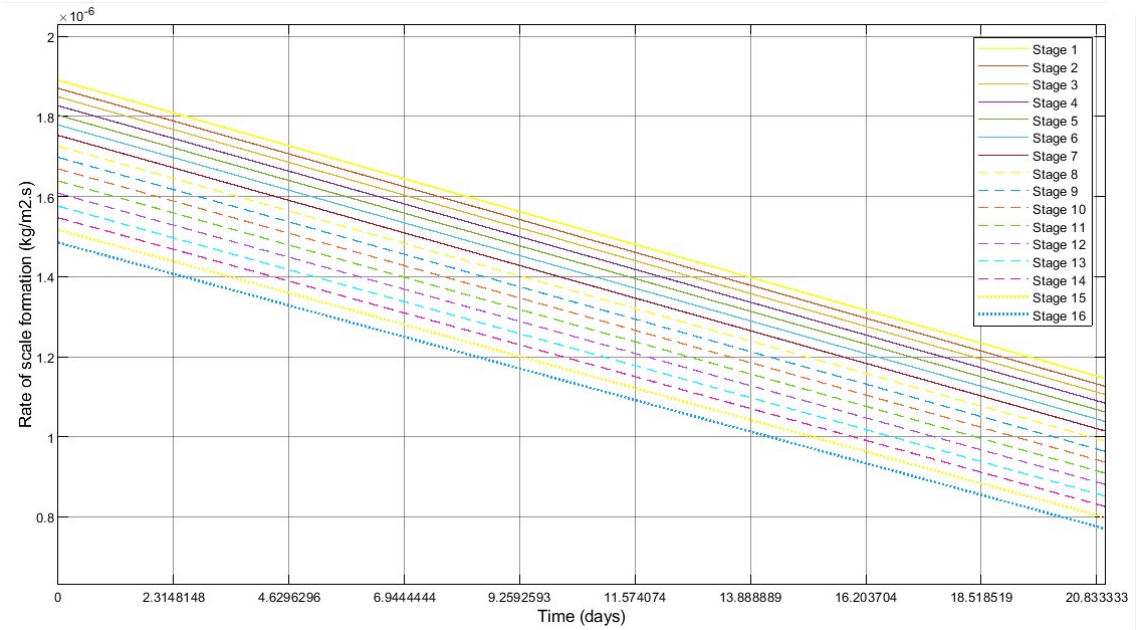

Figure 6.7. The rates of scale formation profiles amongst the stages in MSF-OT as derived from the Simulink model

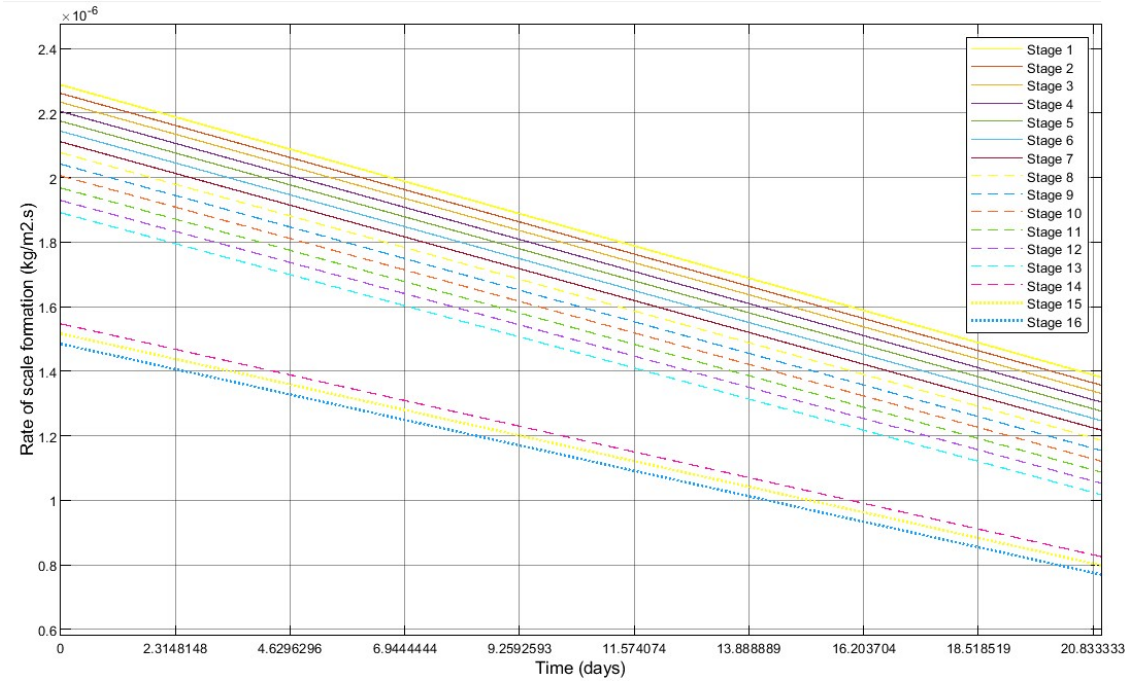

Figure 6.8. The rates of scale formation profiles amongst the stages in MSF-BR as derived from the Simulink model.

One of the main concerns of the scale formation plots would be their profile shapes. Even though, there have been many authors that explained the profiles of these rates were almost a straight line (Hamed & Al-Otaibi, 2010), there have been some other authors, produced these profiles almost asymptotic (Alsadaie, 2017). However, it is important to understand that there is no universally accepted observation over the profiles of scale formation as their profiles are highly dependent upon the configuration of the MSF. Evidently, even in the scale formation curves produced by Alsadaie, (2017), under the lower temperature (top brine temperature or TBT) conditions, the curvature of these profiles decreased, which can be seen from the figure 6.9. However, the extent of scale formations were observed to be comparably higher on this study as the current study did not considered the elevated scale removal rates due to the narrowing of the tubes. Still the scale formation results produced from this study were comparable to the results by Alsadaie.

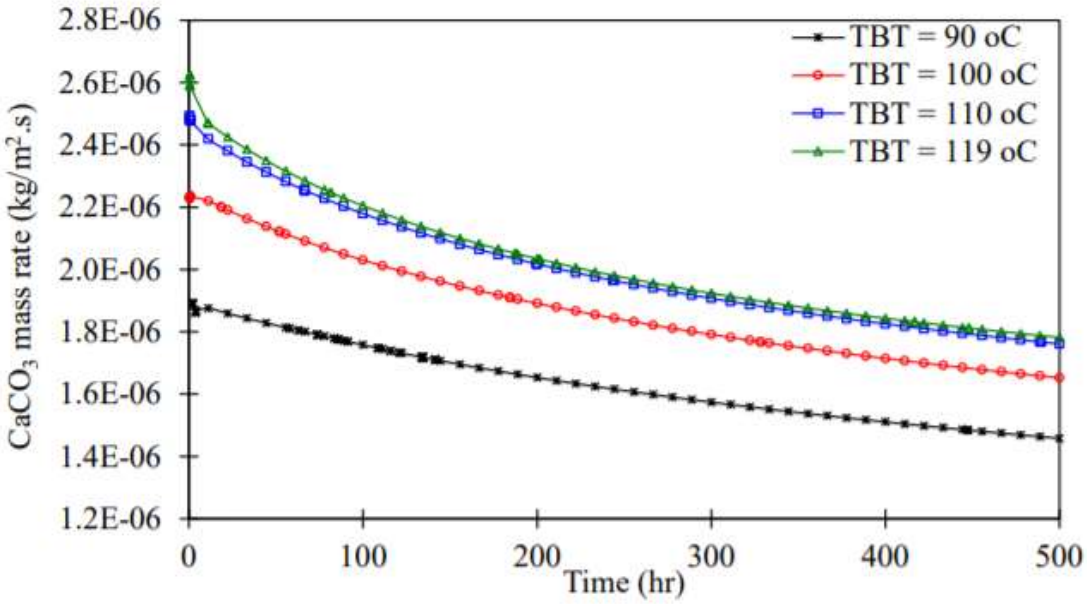

Figure 6.9. The scale deposition rates produced by Alsadaie (2017) under different TBTs of MSF

From the perspective of scale formation, as it is highly sensitive towards the salt concentration, one of the major differences between MSF-OT and MSF-BR is the heightened salt concentrations due to the mixing of brine into the heat recovery section. The effect of salt concentration over the scale formation has been clearly seen from the figure 6.8. In addition, the effect of temperature over the scale formation rates has also been observed from the figures 6.7 and 6.8, where the rates were declined down from the lower stages to the higher stages. It was also seen that the temporal rates of scale formation rates were observed to be decreasing in all the stages. This lowering was contributed by the increase in the removal rates (not contributed by the narrowing of the tubes) where the rate of removal in the first stage of the MSF-OT is presented in the figure 6.10.

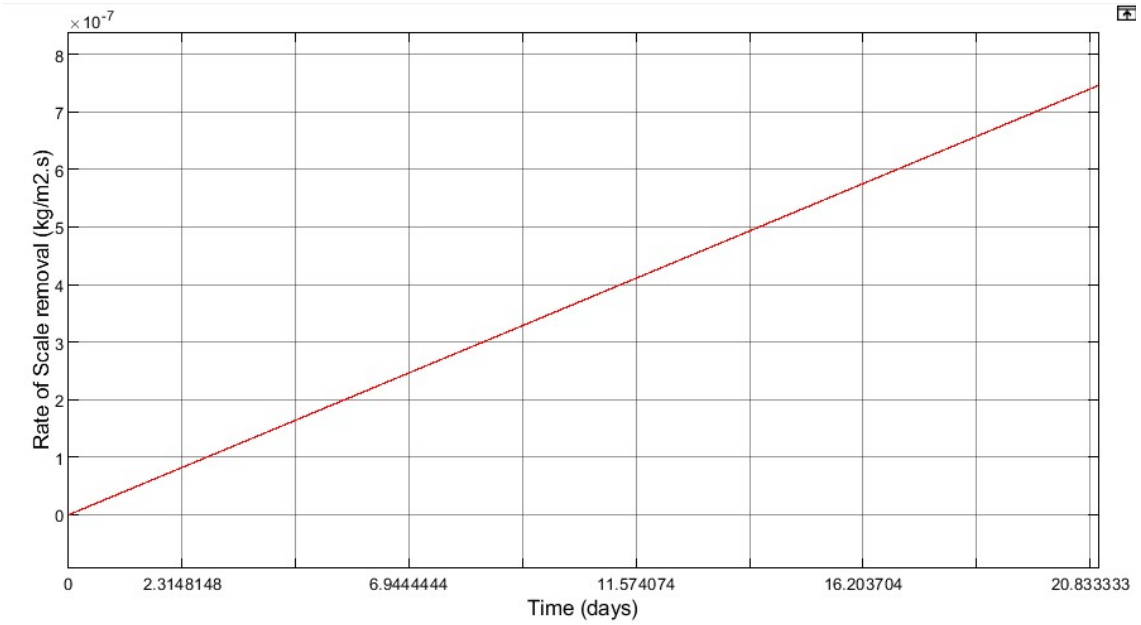

Figure 6.10. The temporal scale removal rate in the stage 1 of MSF-OT

The rates of scale formations were used to calculate the extent of aragonite ($CaCO_3$) depositions on the heat transfer surface in the condenser tubes. Similar to the observations done by the studies of Shams El Din et al. (2005), the Aragonite depositions were found in all the

stages of the MSF (both in OT and BR columns) (Shams El Din, et al., 2005; Zhao, et al., 2018).

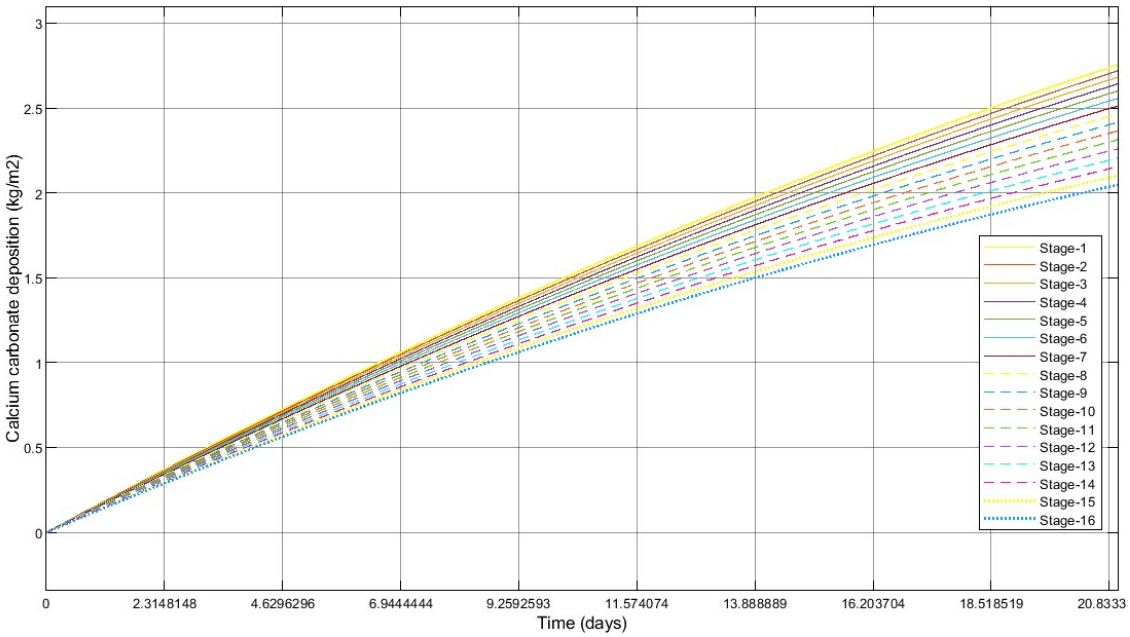

Figure 6.11. Profiles of stagewise Aragonite deposition on the heat transfer surface MSF-OT desalination column

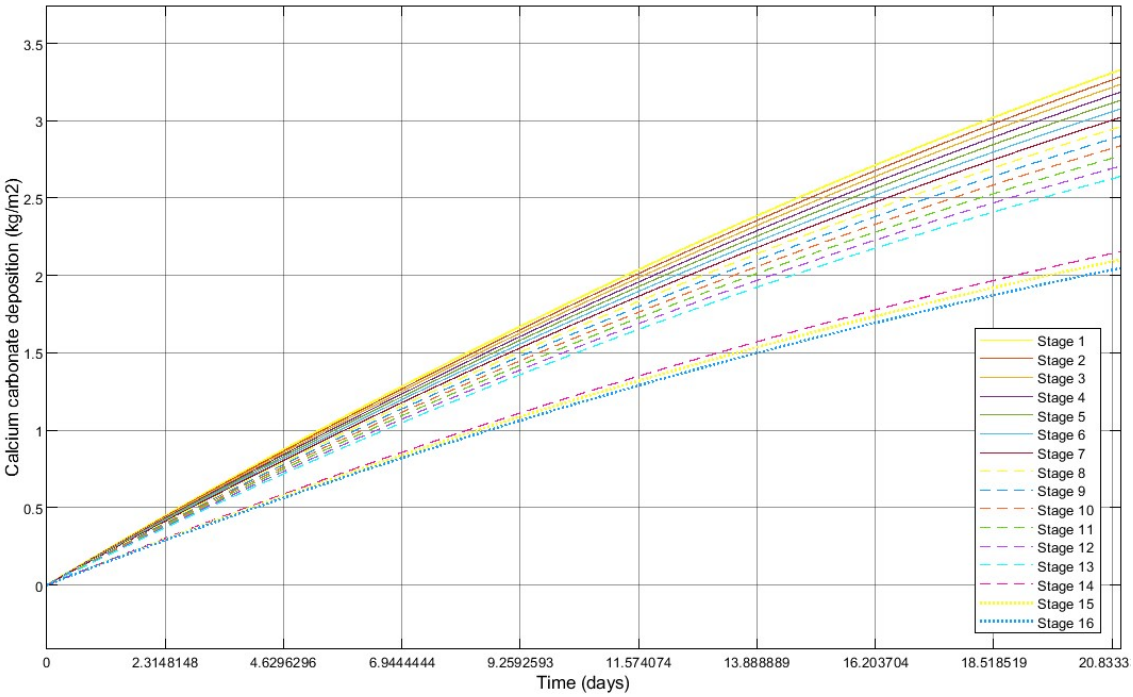

Figure 6.12. Profiles of stagewise Aragonite deposition on the heat transfer surface MSF-BR desalination column

In both the figures (6.11 and 6.12), the profiles of $CaCO_3$ scale deposition in the condensers have followed damped incremental curves, where the highest depositions were seen in the stage 1, while the stage 16 resulted in the least scale formation, similar to the rate of deposition profiles shown in 6.7. Similar to the observations done in the figure 6.8, there has been a visible hiatus in the argonite temporal deposition curves in MSF-BR desalination column, where the gap was found in between the heat rejection section and the heat recovery section.

Even though, these depositions were observed to be considerably high for the tubes with the internal diameter 0.0220m (while the external diameter 0.0244). However, it has to be understood that these disposition values were calculated for all the 4300 tubes in both the heat recovery as well as heat rejection sections. For example, after 21 days (500 hours as taken by Asadaie and Mujtaba (2017)), in the first column of MSF-BR the total scale formed was found to be 3.195kg/m^2, while distributing this value amongst all the tubes in the condenser unit, the final value per each tube would be as low as 0.743g/m^2. However, this amount of deposition would be adequate to considerably lessen the heat transfer rate and lowering the overall efficiency of the condensers.

These aragonite deposition values were further used into calculating the thermal resistance provided by the scale, which was further substituted into the equation 6.9 to calculate the overall heat transfer coefficient. Even though, there have been reported various opinions from the researchers depending upon the flow velocity and the fouling resistance relationship, majority of the researchers believe that the increase in the flow velocity would result in decrease in the fouling resistance (Helalizadeh, et al., 2005; Pääkkönen, et al., 2015). When mentioned the lower velocities, it was inferred that the velocities supporting the dominance of diffusion over the reaction upon the mass deposition. As mentioned in the section 6.4, generally these velocities were as low as 0.2m/s (Hamed & Al-Otaibi, 2010), whereas the velocities

above 1.5m/s represent the marginal influence of reaction step into governing the fouling resistance (Brahim, et al., 2003; Zhang, et al., 2015).

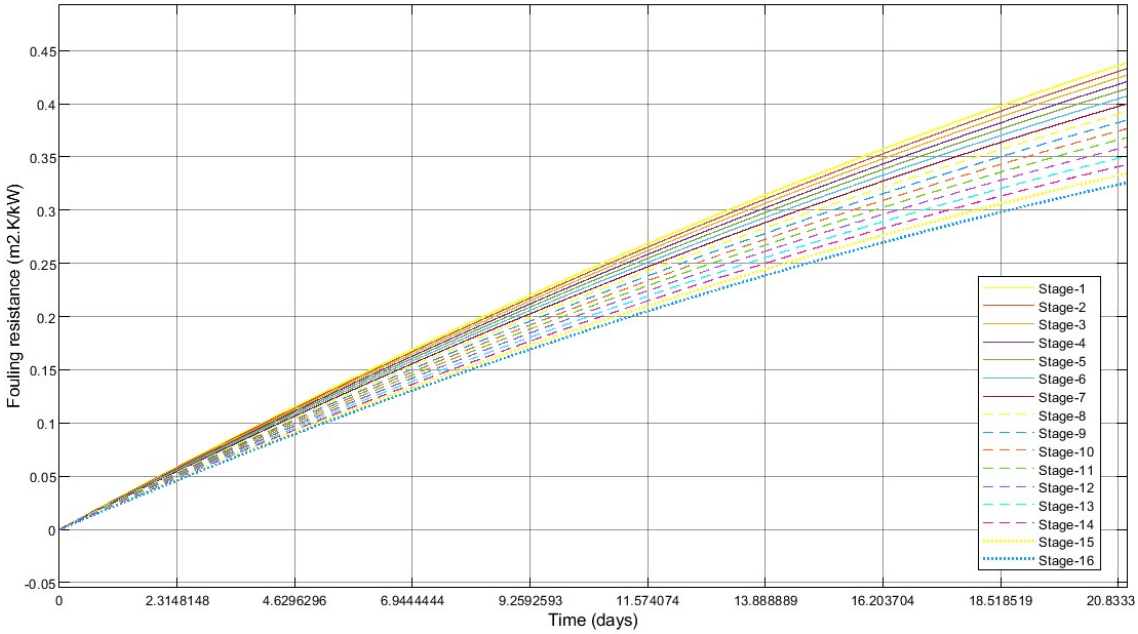

Figure 6.13. Stagewise fouling resistances from the formation of aragonite scales in MSF-OT

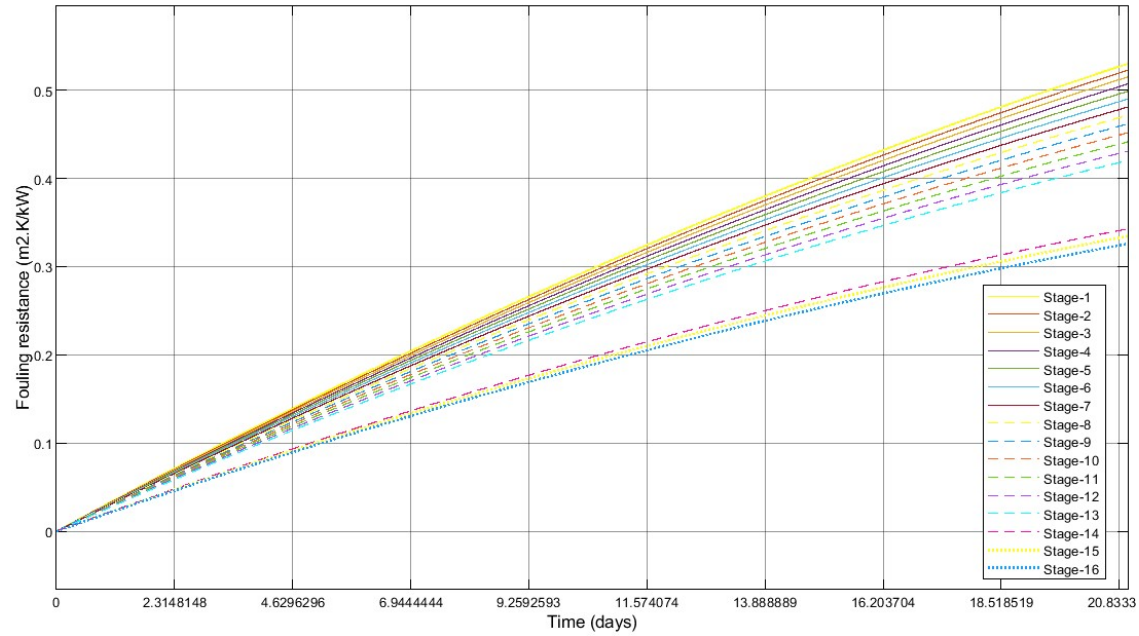

Figure 6.14. Stagewise fouling resistances from the formation of aragonite scales in MSF-BR

Hence, the current model considered both the diffusion as well as reaction into calculating the mass depositions and then fouling resistances. The stagewise thermal resistance by scale formation (fouling resistance) profiles found in various stages of MSF-OT and MSF-BR have been shown in the figures 6.13 and 6.14. In order to calculate the thermal resistances provided by fouling, the density as well as thermal conductivity of these materials were needed. As the systems were operated under low TBT conditions, considering pure aragonite scale formation, these values were taken from NIOSH (2007) and Horai (1971) respectively. While calculating these values, the fouling layer was assumed to be porous as mentioned in the section 6.4.3, where its porosity was considered to be 10% with voids filled with water.

From the figure 6.13 and 6.14, the shapes of the fouling resistance profiles were found to be similar to the profiles of the mass depositions of Aragonite. In case of MSF-OT, the fouling resistances after 21 days were resulted in a range of 0.35 to 0.44 m^2K/kW, whereas these values varied from 0.35 to 0.53 m^2K/kW in case of MSF-BR. The higher fouling resistances recorded in the first stages of MSF-BR compared to the first stages of MSF-OT were the result of higher salinity in the coolant water flowing in the condensers. However, in the last three stages, the fouling resistances recorded in the MSF-BR were similar to the values obtained from MSF-OT.

They are the result of low When compared these results with the fouling resistance profiles of Alsadaie (2017), the profiles from this study were found to be in accordance with their study. However, the fouling resistances calculated from this study were comparatively lesser than the fouling resistances from Alsadaie (2017) for two reasons: 1. The current study considered only the scale formation from Aragonite while the $Mg(OH)_2$ scale formation was ignored due to the low TBT operational conditions of the considered MSF desalination columns and 2. Low TBT resulting in low temperatures of the coolant water flowing in condensers. In addition, design factors such as coolant flow rate and number of tubes in the condenser could contribute to the

velocity of the stream in the condenser tubes, which could contribute to the scale deposition and the fouling resistance. As reported by Alsadaie, the flow velocities varied in between 1.8 to 2.2m/s, while the flow velocity calculated in the current study varied in between 1.6 to 1.7m/s, which confirms the design conditions of Alsadaie were comparable to the current study. From these observations, the fouling resistances calculated from this study have been found to be satisfactory.

Using the fouling resistance values, along with the other design and operational parameters of the MSF-OT and MSF-BR columns, the overall heat transfer coefficient was calculated. There have been numerous studies found in literature relating the heat transfer with the scale formation, where the heat transfer rate was observed to have decreased to a value up to 80% due to the formation of scales (Watkinson & Martinez, 1975; Veenman, 1977; Hawaidi & Mujtaba, 2010; Alsadaie & Mujtaba, 2017; Al-Saleh & Khan, 1994).

However, the experimental studies conducted by Watkinson and Martinez (1975) experimental analysis on heat transfer coefficient in the presence of $CaCO_3$ scale formation resulted into over 54% loss in heat transfer coefficient value. Their design conditions were 1.57m/s velocity of the fluid, which was comparable to the current study. The stagewise heat-transfer coefficient profiles were presented in the figures 6.15 and 6.16. From these figures, it can be seen that two sets of heat transfer profiles were found in both MSF-OT and MSF-BR. This was because the design parameters for both the desalination columns such as the inner and outer diameters of the tubes and the number of tubes in the first 13 stages and in the later three stages were taken similar for the mutual comparability. From the figures 6.15 and 6.16, it can also be seen that the overall heat transfer coefficients were lower in the first stages and then increased as the stage number increased. With time, these heat transfer coefficients declined, whereas by the end of 21 days, these values were found to be almost 55% lower to the initial value found.

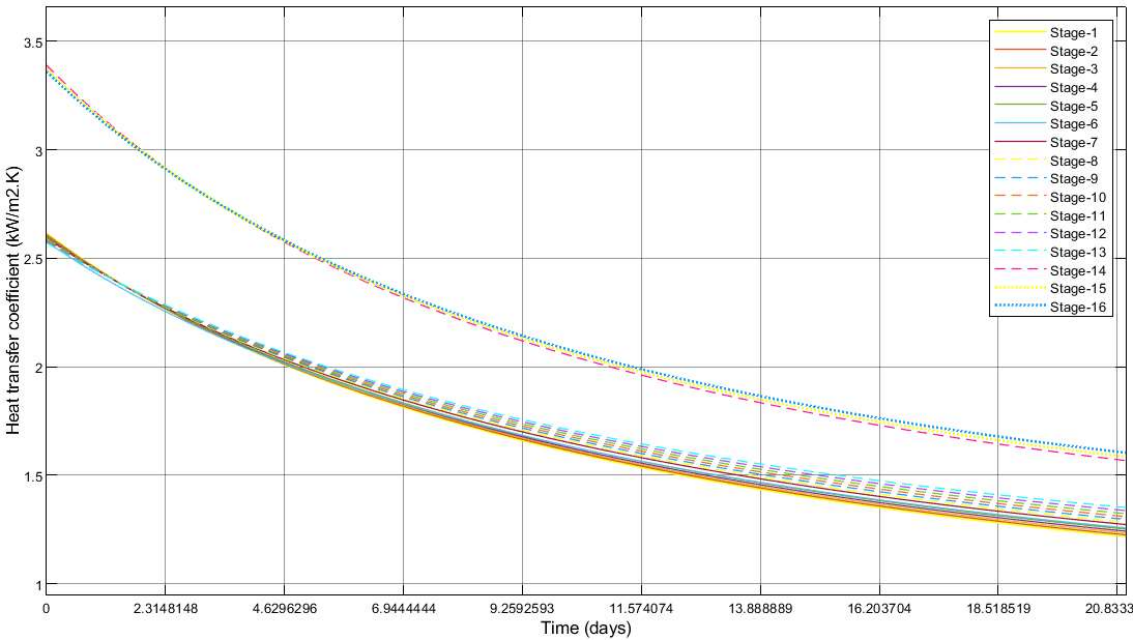

6.15. Stagewise heat transfer coefficients for MSF-OT desalination column

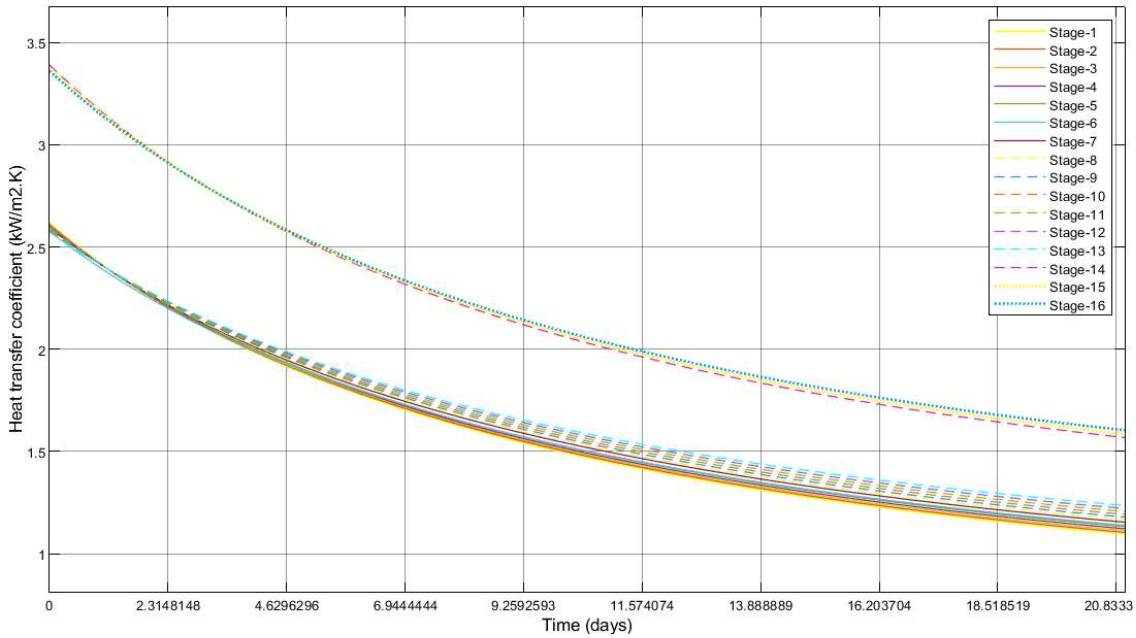

6.16. Stagewise heat transfer coefficients for MSF-BR desalination column

When compared the rate of change in the heat transfer coefficients amongst the stages, the rate was found to be higher in the initial stages when compared to the later stages, which was been a result of coolant water temperatures in the condenser tubes. Similar to the mass deposition

and fouling resistances, there has been a significant gap has been found in the profiles of heat transfer coefficient as seen from the figure 6.16. Even in these profiles, at the end of 21 days, the heat transfer coefficient has been plunged by 60% similar to the observations of Watkinson and Martinez (1975).

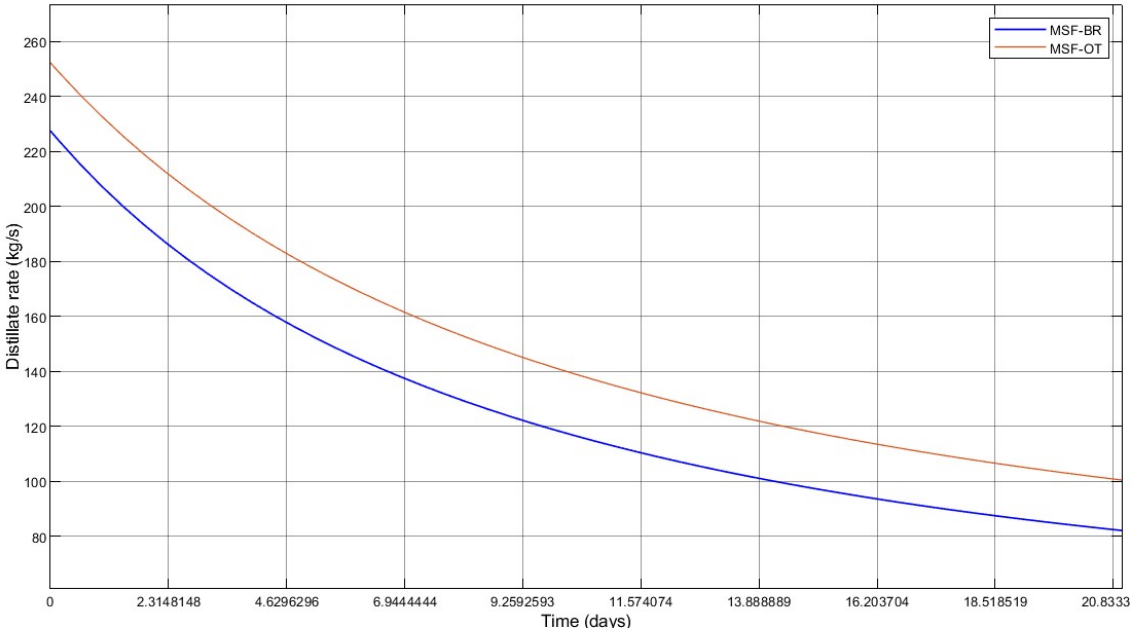

6.17. Distillate production rates calculated from both MSF-OT and MSF-BR

From these results, the distillate productions rates were calculated. The overall distillate production rates under the influence of scale formation as well as the performance ratios of MSF OT and MSF BR are given in the figures 6.17 and 6.18. As seen from the figure 6.17, the initial and final distillate production rates were higher in MSF-OT model, while at the end of 21 days, both the rates were plunged down to the production values that were approximately 60% lesser than the initial values. The lesser distillate production rates were caused by both the higher salinity in the heat recovery section of MSF-BR, as well as higher inlet water temperatures into the condenser section.

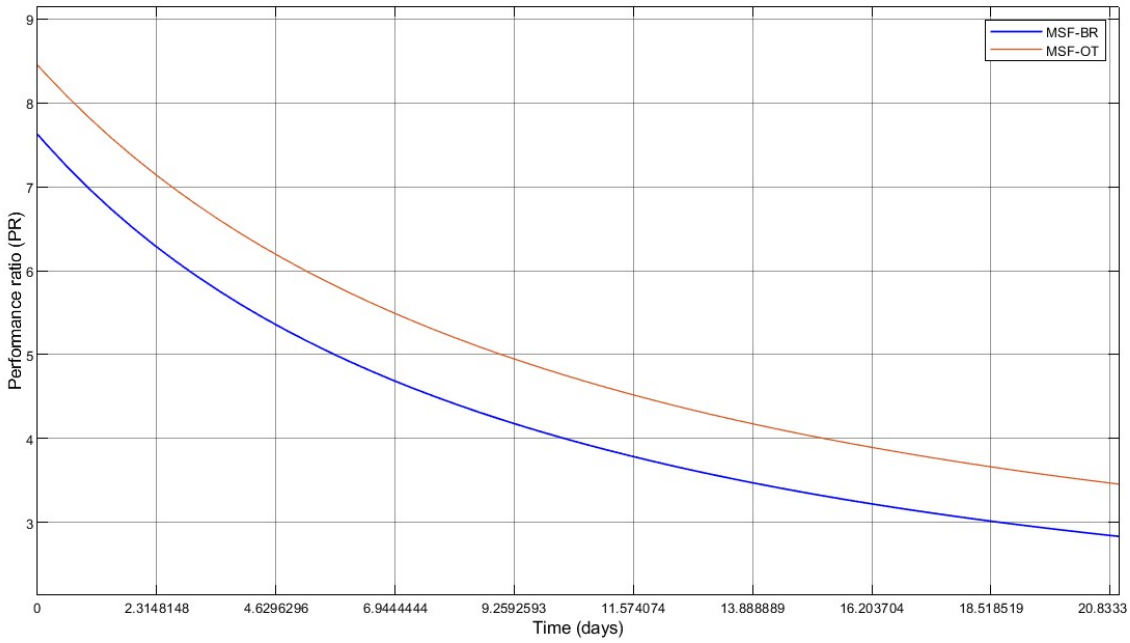

6.18. Performance ratios of MSF-OT and MSF-BR from the current study

In the case of MSF-BR, the total plunge in the distillate production rates after 21 days was observed to be approximately 63%, whereas on the case of MSF-OT, this plunge was observed to be 59%. From the perspective of performance ratio, the initial PRs of MSF-OT and MSF-BR were 8.4 and 7.6 respectively, while after 21 days, their respective PRs were found to be 3.5 and 2.9 respectively. This explains the extent of loss Multi-stage columns experience due to the formation of scales, despite the conditions of low TBT.

6.5.3. Introduction of HBD into MSF

Contrary to the conventional MSF distillation columns, where the partially treated seawater with no biological impurities, entering the coolant section, the seawater is partially desalinated through hydrate-based desalination. The inlet water of MSF after partially desalinated would consists of lesser amounts of salts, contributing to lesser scale formation. At the same time, lesser inlet temperatures of the coolant, which would require more coolant recycle (M_R), changing the production ratio. The hydrate formation experiments explained in the chapter 4, gives the overall idea of 1. Hydrate formation conditions or the inlet temperatures of water

from hydrate counterparts into MSF coolant section; 2. The yield of hydrate or rate of flowrate of hydrate counter part into MSF coolant section. As CO_2 hydrate being highly sensitive to temperature and pressure conditions, its dissociation would be more probable while transporting hydrate from the hydrate reactor to the MSF column. Hence, it has been assumed that by the time hydrate slug flows to coolant water inlet at the heat rejection section, the entire hydrate would have been dissociated, while the inlet water temperature would be constant as the hydrate formation conditions (in this case 274.15K). To analyse the performance of hybrid, the following configuration was taken for the hydrate formation process:

- The hydrate would form in the unstirred vessel where the temporal collection of hydrate would occur. This could serve as the process of het removal as well as a method to make the hydrate formation process continuous.
- The liquid phase would consist of saline water with seawater configuration along with 100ppm of SDS
- The gas would be 95% of CO_2 with 5% impurities (probably the gas as soluble and as hydrate forming/hindering as CH_4).

The hydrate formation kinetics, yield and the extrapolated profiles of water to hydrate conversion when eliminated the thermodynamic barrier were analysed in the chapter 4 (in the section 4.3.2). From the perspective of desalination, the hydrate formation would represent the overall performance of MSF by reducing the scale formation as well as the lower temperature of dissociated hydrate would lower the freshwater intake to maintain the same amount of distillate. Initially the performance ratios of the hybrids have been evaluated, which have been compared with their respective MSF alone counterparts.

When compared the overall distillate production between MSF-OT and Hybrid, even the initial total distillate production values of Hybrid -OT were higher than the initial total distillate water

production from MSF-OT, this was because of the lower inlet water temperature. For the MSF-OT, the inlet water temperature was considered to be 311.55K as directed by Ali and Kairouani (2014). However, as referred from the chapter 4, the hydrate forming temperature was 274.15K. As the total hydrate dissociation, which was an endothermic process, was considered, the resultant dissociated hydrate water was considered to be at a constant temperature of 274.15K until it reaches the MSF inlet. Due to these lower temperature conditions of the inlet water, the initial distillate production rate was resulted to be 311kg/s while this value was 252kg/s incase of MSF-OT. After 21 days, this value was plunged to 100kg/s incase of MSF-OT, whereas in case of Hybrid-OT, the distillate production rate was plunged to 246kg/s, which was 2.46 times higher than the MSF-OT distillate production rate. The profiles of temporal distillate production rates representing 21 days of operation were given in the figure 6.19.

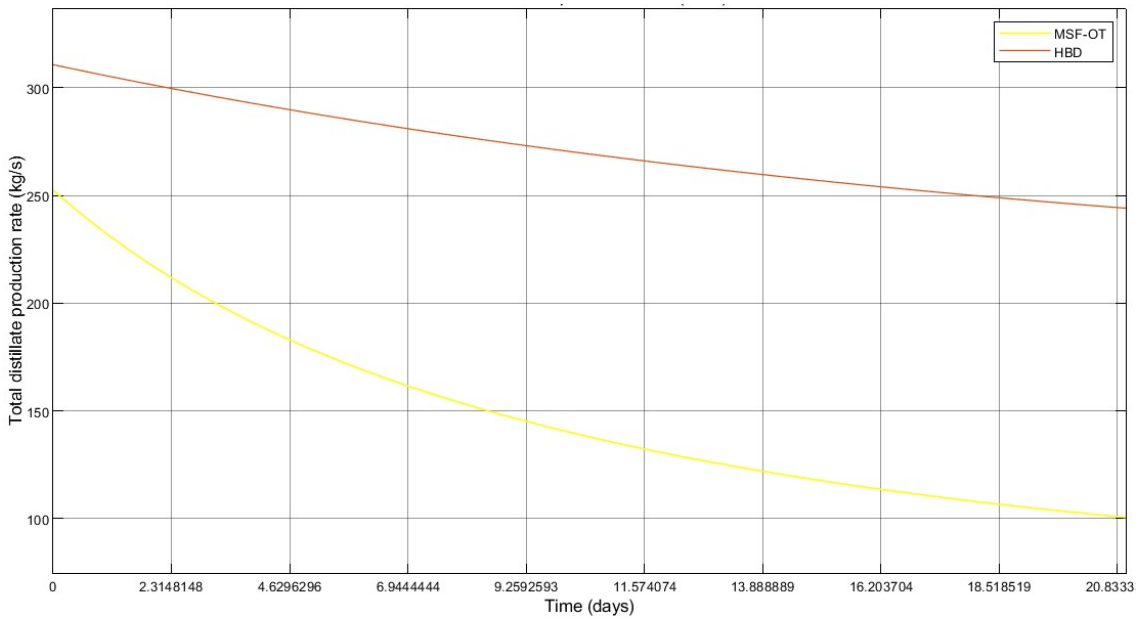

Figure 6.19. Total distillate production rates for the first 21 days of operation in case of MSF-OT and Hybrid-OT desalination systems.

The performance ratios of MSF-OT and Hybrid-OT have been plotted in the figure 6.20. As it can be seen from this figure, Hybrid-OT showed a considerably better performance than MSF-OT both at the initial stages and after 21 days. Due to the higher initial distillate production rates in Hybrid-OT system, its initial performance ratio was calculated to be 8.8, which was higher when compared to MSF-OT, which had the initial performance ratio of 7.2. It means, the effect of inlet water temperature from the dissociated hydrate had improved the initial performance ratio by 1.22 times. Because of the scale formation, under lower heat transfer rates occurred in the condensers, after 21 days the performance ratio has been found to have plunged to a value of 2.96 in case of MSF-OT system. From the chapter 4, for the configuration considered in this chapter, the percent salt removal was observed to be 74.5%. Hence, the salinity of inlet water in case of Hybrid-OT system was 8.925mg/g, against 35mg/g of salt in the inlet stream of MSF-OT.

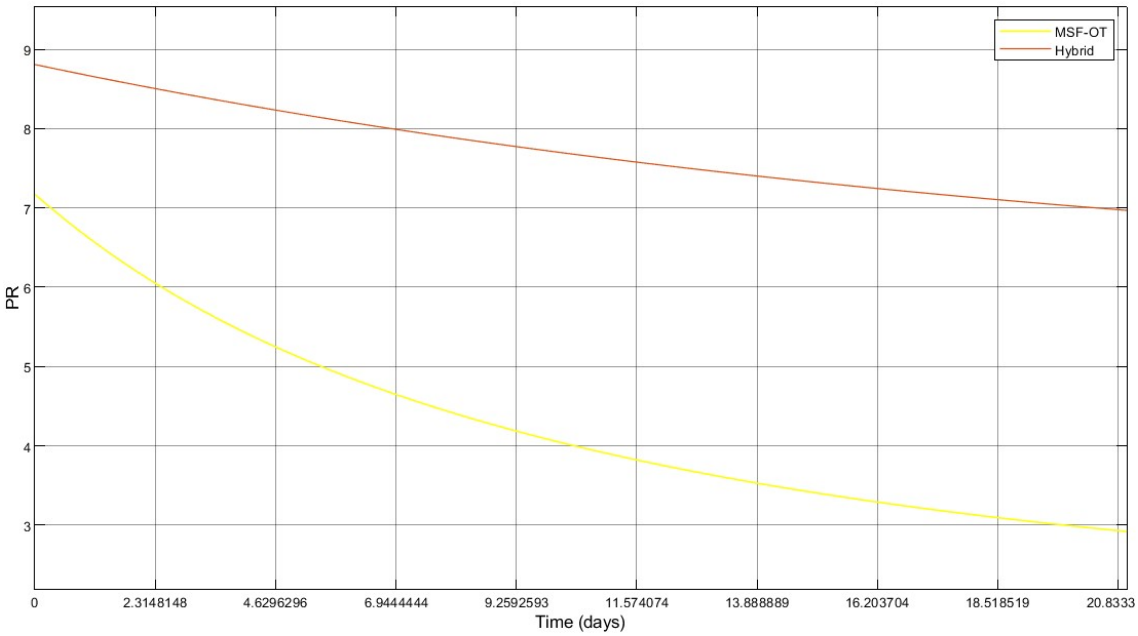

Figure 6.20. Profiles of temporal performance ratio (PR) fluctuations for the first 21 days of operation in case of MSF-OT and Hybrid-OT desalination systems.

Due to the less salinity values obtained through hydrate-based desalination process, the final PR of the MSF counterpart of the Hybrid-OT system was calculated to be 7.025. This value was 2.37 times higher than the final PR of MSF-OT system.

The operation of HBD in MSF-BR was different from MSF-OT. In case of MSF-OT, the entire coolant water inlet of the Hybrid-OT was provided by the dissociated hydrate. However, in case of Hybrid-BR, the ratio of brine recycle and the dissociated hydrate intake were maintained in such a way that the inlet coolant temperature was maintained at 317.25K temperature as directed by Rosso et al (1997). This temperature was calculated considering the ratio of Brine recycle with total brine flowrate in the condensers (recycle ratio) as given in Rosso et al (1997), along with the consideration of seawater temperature 311.55K as taken in case of MSF-OT. The initial brine recycle ration was 0.503, where as the brine recycle ratio in the Hybrid was calculated to be 0.936. This means, the requirement of excess water input from the outside of MSF was 7.75 times lesser in case of Hybrid-BR, when compared to MSF-BR.

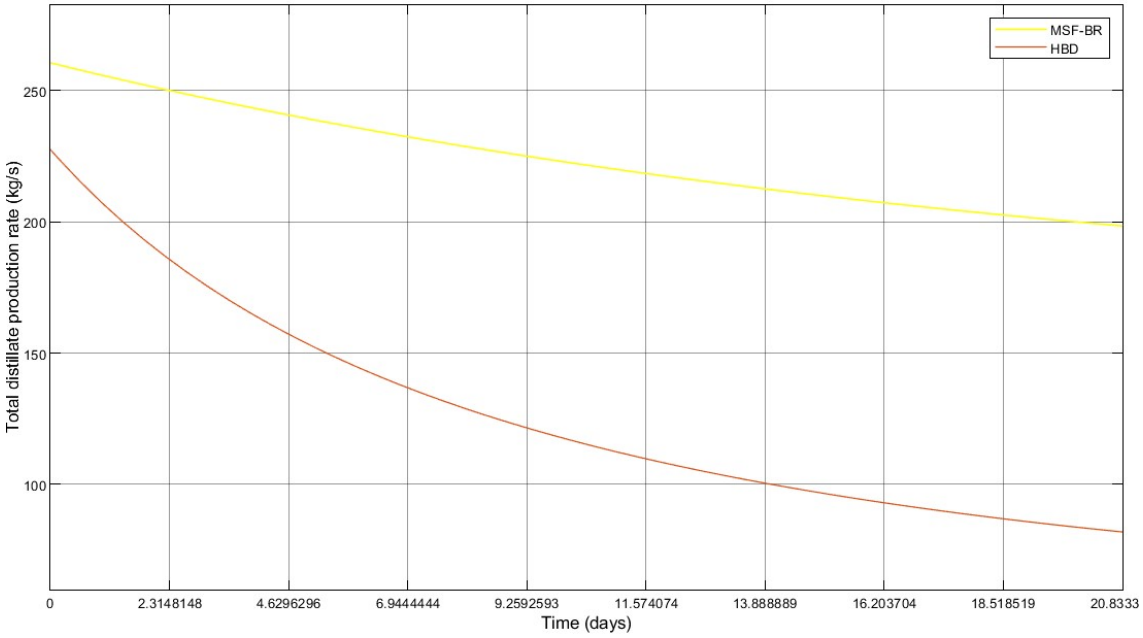

Figure 6.21. Total distillate production rates for the first 21 days of operation in case of MSF-BR and Hybrid-BR desalination systems.

When compared the overall distillate production values of Hybrid-BR with MSF-BR, similar to the comparison between MSF-OT and Hybrid-OT, the Hybrid-BR initial production rates were considerably higher, which was 1.14 times higher to the production rates of MSF-BR. This was due to the low salinity of the inlet water. At the end of 21 days, the production rate of distillate was plunged down to 84.07kg/s in case of MSF-BR. This was a decrement of approximately 63% from the initial production rates. However, due to the lower salinity contributing to low scale formation and higher heat transfer rates in the condensers, the final production rates were calculated to be 200.3kg/s. This decrement in production was equivalent to approximately 23% reduction in the initial value.

A similar trend was observed in case of the performance ratio when compared the PR of Hybrid-BR with MSF-BR models, the profiles of which were shown in the figure 6.22.

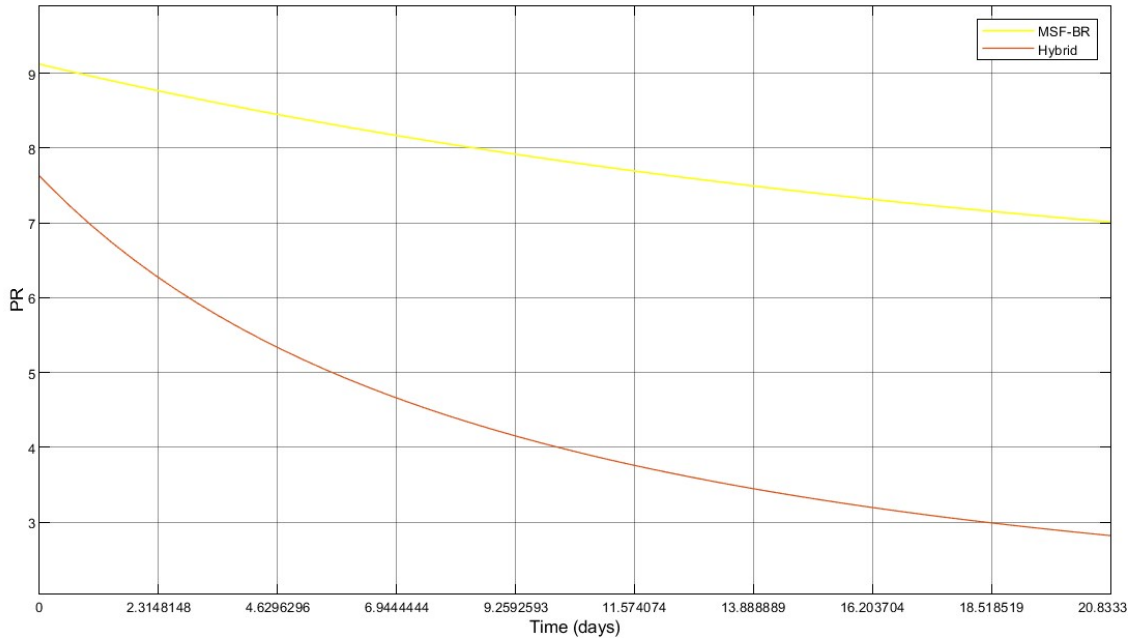

Figure 6.22. Profiles of temporal performance ratio (PR) fluctuations for the first 21 days of operation in case of MSF-BR and Hybrid-BR desalination systems.

In case of MSF-BR, the initial PR was observed to be 7.75, whereas in case of Hybrid-BR, this value was 1.17 time higher than MSF-BR (9.10). The initial value of PR was mainly affected

by the requirement of more steam due to the higher outlet temperatures of coolant stream from the stage 1 of MSF-BR. Due to the higher salinity of inlet water, which was further increased by the recycled brine from the last stage of the flash chamber, the PR of the MSF-BR was fallen down by 62.6% after 21 days of the operation. However, this plunge was calculated to be 22% in case of Hybrid. When compared the final PRs of MSF-BR and Hybrid-BR, the Hybrid-BR recorded a PR of 7.08, which was 2.44 times higher than the final PR value of MSF-BR.

Alongside with the performance ratio, production ratio is also calculated for any desalination system to analyse the water wastage. The production ratio (PDR) is the ratio of the produced distillate from the MSF desalination column to the inlet seawater from the outside of MSF desalination column. As there was no brine recycling, MSF-OT and Hybrid-OT will the entire water flowing in the condensers as the denominator for the production ratio and hence the production ratio would be a relatively smaller quantity compared to BR models.

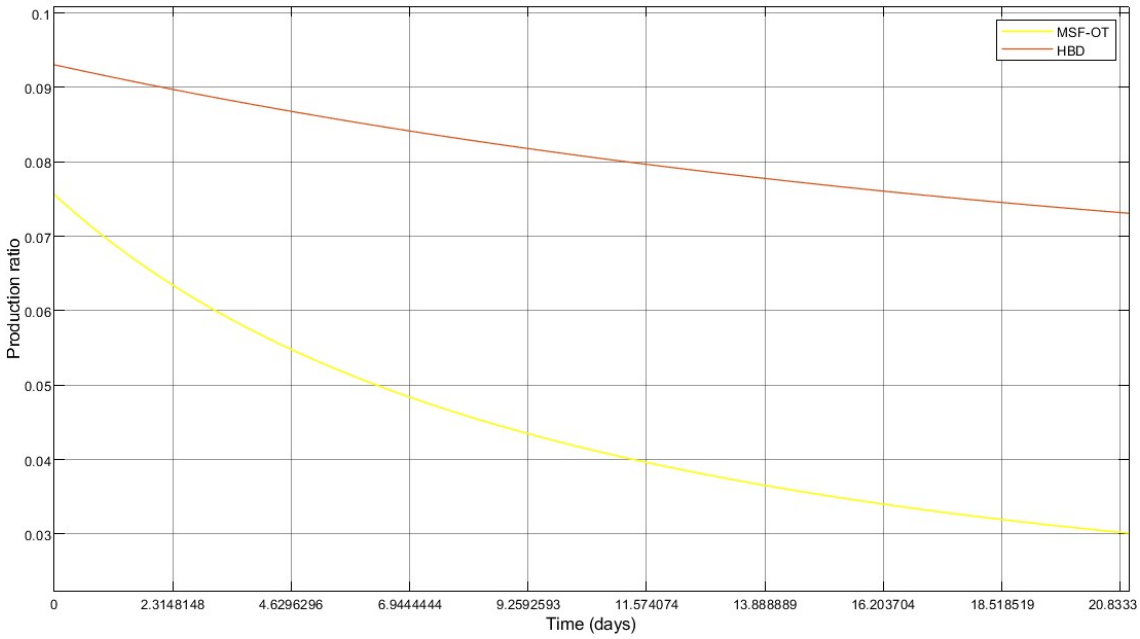

Figure 6.23. Profiles of temporal production ratio (PDR) fluctuations for the first 21 days of operation in case of MSF-OT and Hybrid-OT desalination systems.

Even though, the denominator was same for both Hybrid-OT and MSF-OT systems, due to the variable rates of distillate productions the production ratios of these systems were turned out to be different from each other. As seen from the figure 6.19, total distillate production rates were higher in the Hybrid-OT system when compared to MSF-OT system, which led to the higher production rates of Hybrid-OT, both at the initial and final phases of the period 21 days. Figures 6.23 and 6.24 shows the profiles of temporal production rates of MSF-OT and Hybrid-OT; and MSF-BR and Hybrid-BR systems, respectively. As seen from these figures, the production ratios of BR systems were considerably higher than the OT systems due to the brine recycle. From the figure 6.24, a profoundly higher production rations were seen in case of Hybrid-BR when compared to MSF-BR. This was because of higher rates of brine recycle to attain the same inlet temperature of water into the condenser tubes pertaining to the energy rejection system of MSF-BR counterpart.

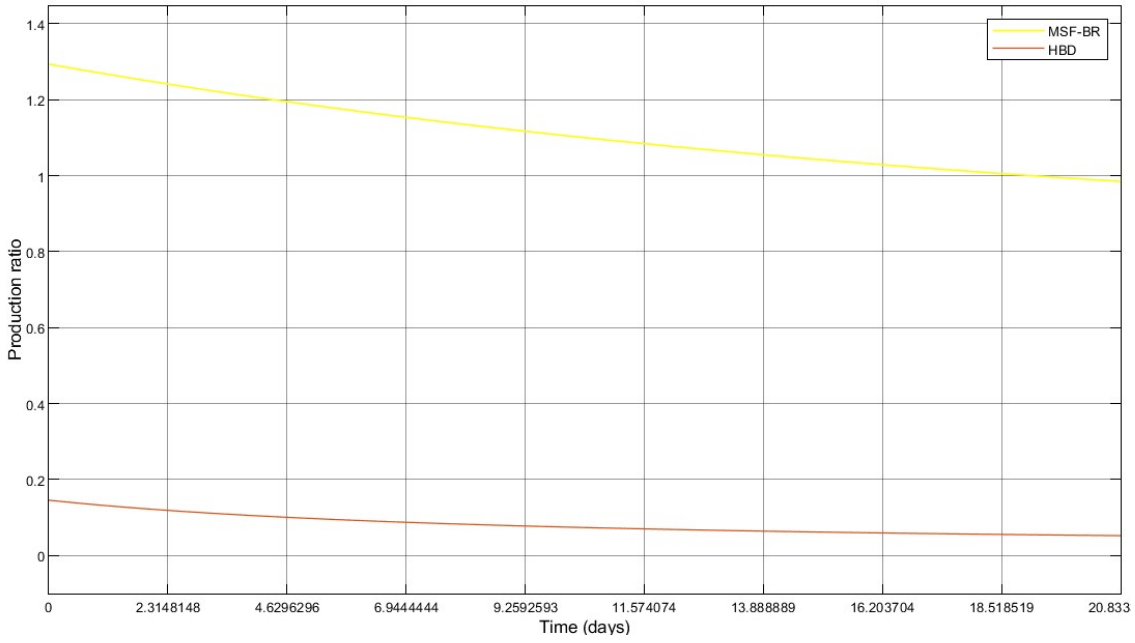

Figure 6.24. Profiles of temporal production ratio (PDR) fluctuations for the first 21 days of operation in case of MSF-BR and Hybrid-BR desalination systems.

Even though, these performance and production ratios of the considered systems show the effectiveness of Hydrate based desalination precursor into improving the performance of MSF. However, these values do not completely provide an overall view of the efficiency of the Hybrid system. This is because these values were calculated from the perspective of MSF and not from the perspective of the entire Hybrid column. In order to calculate the production ratio of the entire Hybrid column, one has to attain the information of rate of pre-treated water production from Hybrid with respect to the rate of inlet seawater provided to the same desalination column. To analyse this, as mentioned in the introduction of this section (6.5.3), the system with the aforementioned chemical configurations were taken. The projected rates of hydrate formation yields were already calculated in the chapter 4, which is provided in the figure 6.25.

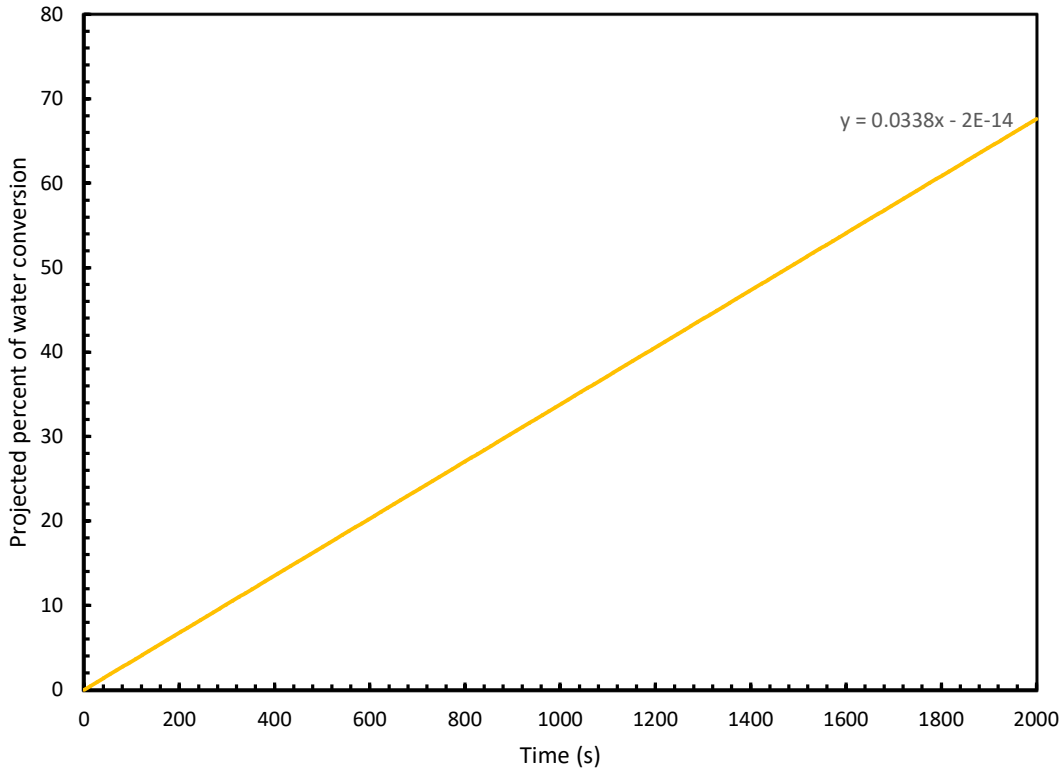

Figure 6.25. The projected percentage of water conversion (molar conversion) into hydrate with time in the considered hydrate formation system.

From the figure 6.25, in the considered hydrate formation system, the projected water conversion shows an approximate conversion of 67.3% water converted into hydrate in 2000s. It means the rate of water converted into hydrate was calculated to be 0.03365 percent per second or 0.0003365 fraction per second. The MSF-OT requires an inlet pre-treated water of 3340kg/s. When calculated the total amount of seawater required to produce 3340kg/s from the hydrate-based desalination process that has a conversion rate of 0.0003365 fraction per second, the value would be 9925706kg/s. In order to produce water 201.45kg/s of water as demanded by MSF-BR, the inlet sea water rate should be 598656 kg/s, which would be highly impracticable for a medium range desalination process. Moreover, the considered system could produce these conversion rates when operated under ideal conditions where the continuous removal of hydrate along with the heat from the reactor is possible. Considering the total seawater input to the hydrate formation unit, the production ratios were calculated again and compared with their respective MSF-OT and MSF-BR systems.

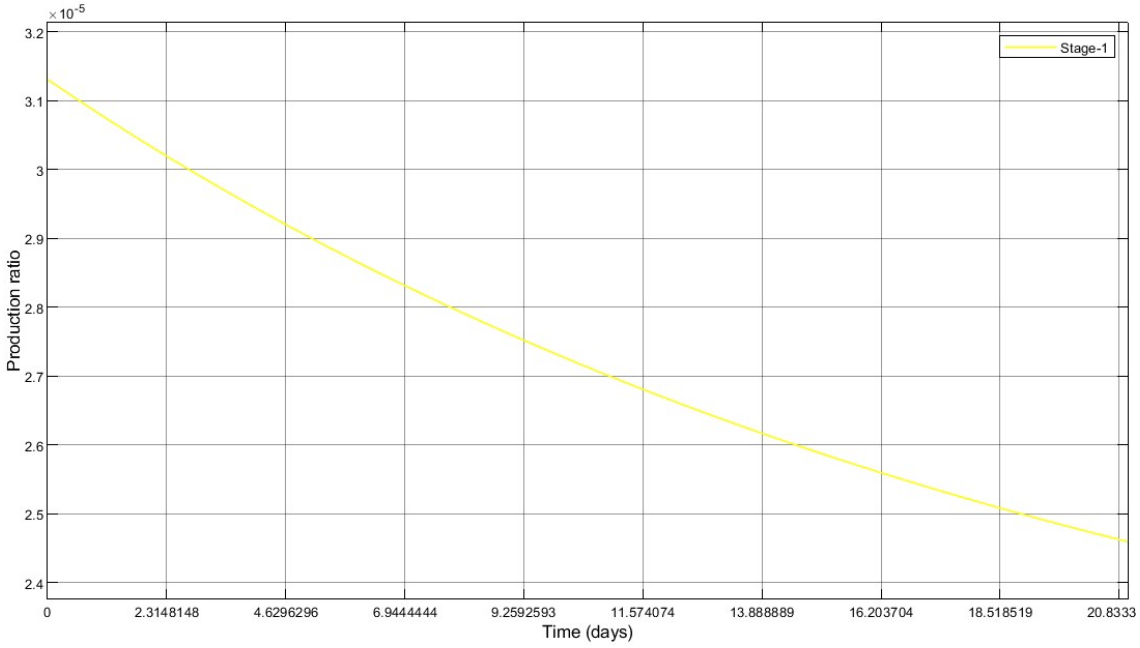

Figure 6.26. The overall production ratio of Hybrid-OT system

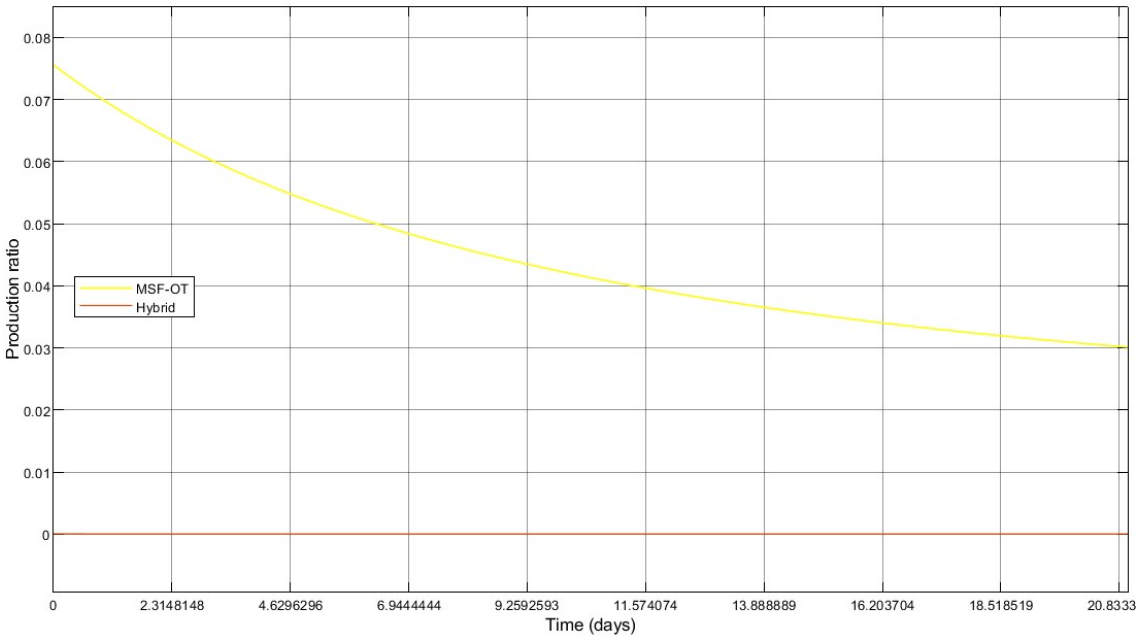

Figure 6.27. The comparison of overall production ratio of Hybrid-OT system with MSF-OT system

As it can be seen from the figure 6.26, the production ratio of Hybrid-OT was in terms of 10^{-5}, which was almost 1000 times less than the production ratios observed in the MSF-OT system (Figure 6.27).

Similar to the Hybrid-OT and MSF-OT systems, the production ratios of Hybrid-BR as well as MSF-BR systems were produced, presented and compared in the figures 6.28 and 6.29. From the figure 6.28, the production ratios of Hybrid were turned out to be in terms of 10^{-4}, which were ten times higher than the production rations of Hybrid-OT system. However, the production ratios of MSF-BR were also comparatively higher than MSF-OT, in comparison with MSF-BR, this improvement in the production rates seen in Hybrid-BR system had no significance (figure 6.29).

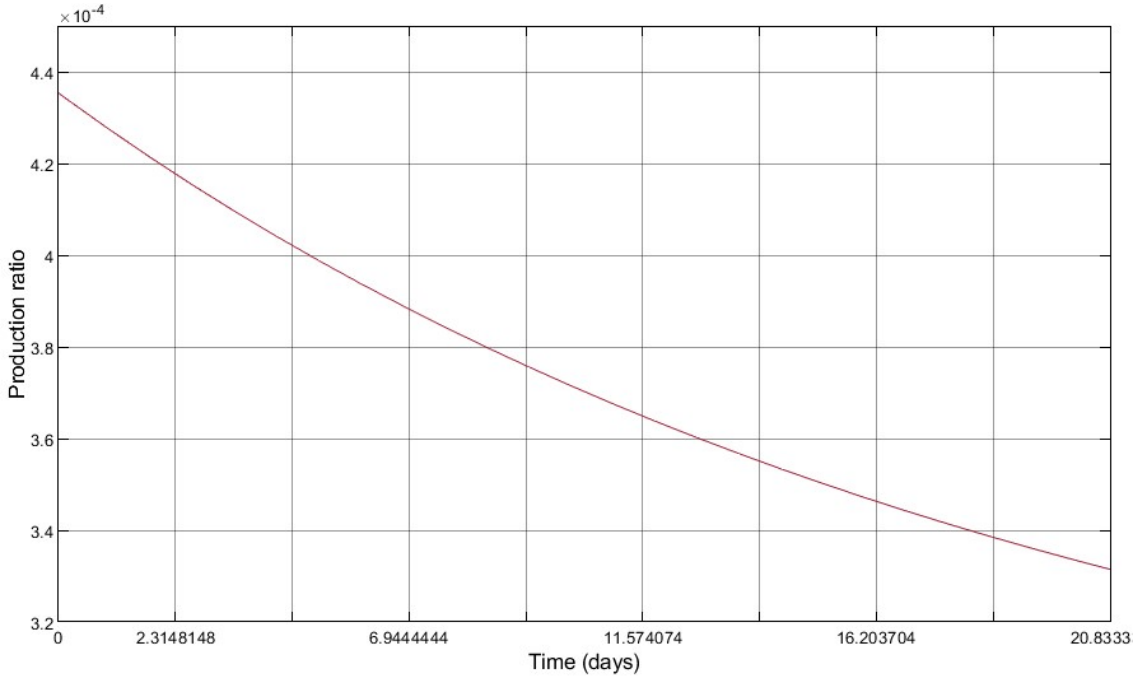

Figure 6.28. The overall production ratio of Hybrid-BR system.

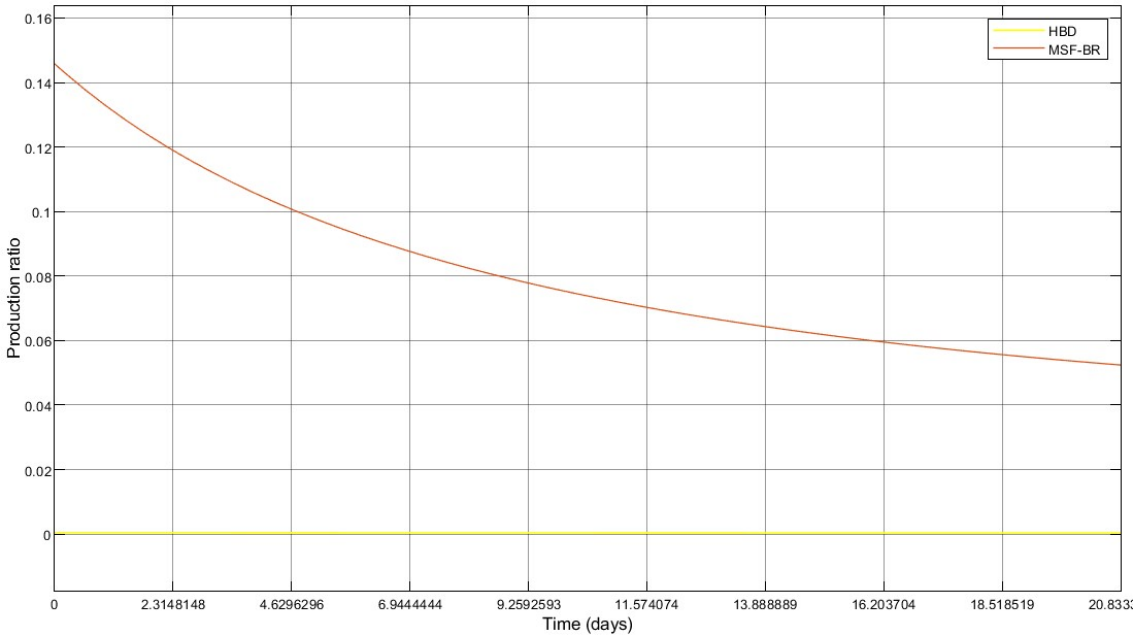

Figure 6.29. The comparison of overall production ratios of MSF-BR and Hybrid-BR models.

6.6. Summary

To calibrate the effectiveness of HBD as precursor to the MSF desalination process, two MSF models were created representing Once Through and Brine Recycle configurations as guided by Rosso et al (1997) and Ali and Kairouani (2014) in Simulink software. They have been validated from the perspective of stagewise distillate production, stagewise brine temperature and stagewise coolant temperatures. These values produced from these models were observed to be in good agreement with the literature data, despite neglecting the nonequilibrium allowance.

To calculate the scale formation the method proposed by Pääkkönen, et al. (2015) was considered. Through this, the deposition rates of $CaCO_3$, scale thinkness, fouling resistance and overall heat transfer coefficient were calculated. Links amongst these parameters were analysed and their contribution in depressing the overall distillate production rates were examined. All these evaluations were done from the perspective of water salinity and stream temepratures.

Thereafter, the performance ratio and the production ratios of the considered MSF-BR and MSF-OT were calculated with time and they have been compared against the PR and PDRs of HBD-OT and HBD-BR systems. From the perspecitve of improving the performance of MSF, the pretreatment of seawater by HBD had considerably desirable influences on the system. Due to the lower temperature and salinity of the outflux from the HBD system, the overall PR and PDR has seen to be higher even after 21 days when compared to MSF alone systems.

Howeever, when compared the production ratios of the entire hybrid systems, by taking the sea-water intake of hydrate The On a concluding note, due to the quality of output water in terms of salinity and temperature, the pre-treatment process through HBD has improved the performance of MSF by lowering the scale formation rates considerably along with improving the overall production rates of distillate from MSF. However, when compared the values of

total production rates considering the total sea-water input to the HBD system with the MSF alone systems, the production rates obtained from the hybrid systems were profoundly negligible. Even though the hydrate formation rates were taken from the projected values of the fastest hydrate formation system, the rates of hydrate production were not adequate to the requirement of MSF process. It suggests the requirement of improving the hydrate formation kinetics either through the additives or by changing the hydrate forming conditions. Instead of improving the hydrate forming kinetics, the hydrate forming system could be built nearby the seashores or inside the sea, where plentiful water supply could be provided. Or else, various other HBD-MSF configurations have to be examined to check the practicability of HBD-MSF-hybrid system.

Chapter 7

Conclusions and Recommendations

7.1. Conclusions

The nucleation parameters calculated from various models shown higher deviations under the unfavourable conditions of hydrate formation such as lower pressure and higher temperature conditions predominantly. Coincidentally, higher deviations in induction times were found under hydrate unfavourable conditions which was comparable to the stochasticity in induction times. As explained by Ribeiro and Lage (2008), the induction times were more stochastic under higher temperature and lower pressure conditions. At near freezing conditions, the pressure of 3.2MPa was observed to be more optimum ensuring lowest induction times.

Amongst the experimental observations, it was found that the addition of impurities to either the gas and liquid systems had detrimental effects over the overall rates and yields of hydrate formation. Approximately 70% decline in overall hydrate yield was observed when used seawater instead of distilled water for hydrate formation. When introduced CH_4 equivalent to 5vol% of the total gas volumetric flow rate, the hydrate formation was further lowered by 29%. An improvement of 25% hydrate formation yield was observed when added 100ppm of SDS, which was improved to 55% when introduced stirring to it. The effect of thermodynamic barrier upon the rates of hydrate formation was observed from the experiments by cross comparing the temperature fluctuations with the volumetric gas consumption profiles. Even though, stirring resulted in higher yields after 45hours, the overall rates of hydrate formation were higher in case of quiescent systems. This might have been caused by higher heterogeneity provided by stagnant water for accelerated hydrate formation in the initial stages.

Amongst the experiments conducted towards gas capture, a system with TIPA was observed to have supporting the hydrate formation, while TEA depressed its yield. When added THF, the required pressure for hydrate formation was lowered extensively. The operational conditions were lowered to 3.5MPa in the presence of THF. Contradicting the observations made by Lee et al. (2010) the addition of THF did not depress the extent of CO_2 separation as observed in the table 5.6, especially when added amine to the system. Approximately 50-60% of CO_2 could be separated from the post combustion gas mixture under the most optimum conditions. The practicability of the HBCC-MSF was also found to be higher due to the lower emissions of CO_2 during hydrate formation and the requirement of water during hydrate formation in 100% recycle mode.

From the perspective of HBD-MSF hybrid, two MSF configurations were created in Simulink representing Once through (OT) and Brine recycle (BR) models. As it was observed from the chapter 6, the introduction of HBD precursor has lowered the scale formation and improved the distillate production rates. Even the initial distillate production rates were found to be higher in HBD-MSF systems than individual MSF systems, due to the lower temperatures of hybrid effluent streams. At start of the 21days period, the ratio between distillate production rate by the hybrid to the same by the MSF-OT were observed to be 1.21, which was increased to 2.36 by the end of 21days. In case of BR models, this ratio was found out to be 1.17 at the start of the 21 days period, which increased to 2.44 by the end of 21 days. Even the MSF- performance ratios and production rations were higher accordingly to the distillate productions rates in the hybrid systems. However, the sea-water intake of hydrate desalination was observed to be profoundly higher compared to individual MSF desalination columns. While the inlet seawater flow rates of MSF-BR were 3340kg/s, where the required water flow rates of Hybrid were calculated to be 9925706kg/s. Hence, the production ratios of the hybrid systems were almost negligible compared to individual MSF systems. This makes the hybrid of HBD-MSF not

practicable under the considered HBD configurations with the rates of hydrate formation unless a solution is found for this excessive water requirement or lower hydrate formation rates.

7.2. Recommendations

Apart from the nucleation models proposed by Kashchiev and Firoozabadi, there have not been many nucleation models that could estimate the rates of nucleation without the support of experimental data. Even though, Kashchiev and Firoozabadi's nucleation model was efficient in calculating various aspects of nucleation, its applicability to a wide range of pressure and temperature conditions were questioned by various authors (Reibero and Lage; 2008; Khurana et al., 2017). Especially, under the unfavourable conditions of hydrate formation, the values produced by Kashchiev's nucleation model were observed to be more sensitive. Hence, a robust hydrate nucleation model is required to help the future researchers in choosing the optimum hydrate forming conditions for various purposes without spending more time on experimentation.

From the perspective of hydrate growth, as mentioned in the chapter 6, the initial rates of hydrate formation were seemed to be encouraging in the quiescent systems. Still they have not been adequate enough to satisfy the water requirement of pre-treated water production without consuming enormous amounts of water. Even though various methods were available in improving the overall hydrate yield, as mentioned by Babu et al. (2018) most of these methods associated with various issues related to either the separation of hydrates physically, or elimination of additives chemically. This is main reason, which directed the current study, not to utilise porous media, nano particles, foams, or chemical additives such as THF, TBAB and Propane to enhance hydrate kinetics for the application of desalination. This suggests the requirement of either improving non-toxic additive effective enough to enhance hydrate

formation kinetics adequately or to improve design apparatus or methods to separate hydrates from rest of the medium or to separate toxic substances economically.

The current study investigated the combination of HBD, and MSF connected through the basic configuration where the output of the HBD will be sent to the heat rejection section of MSF. The study also considered only two configurations of MSF (BR and OT). However, there have been numerous studies that proposed various configurations of proposed to improve the overall performance of MSF. By changing number of stages and flow patterns various authors proposed various configurations of MSF that were claimed to be promising in providing better performance as well as compatible for high water output desalination plants (Mussati, et al., 2003; Mussati, et al., 2006). Including hydrate precursor to improve their performance through an optimal configuration of HBD and MSF could become a potential futuristic research idea.

One of the main findings of the chapter 6 was that the HBD was effective in addressing the issues of MSF, while it required enormous amounts of saline water, HBD was concluded to be impractical. However, designing a undersea HBD plant could effectively address this problem.

Even though, the HBCC was seen to be promising for the application of carbon capture from the post-combustion gases emitted from MSF, three issues should be addressed before it could be practically applied to the mainstream industrial carbon capture: 1. Continuous removal of heat from the system so that the hydrate formation kinetics would not be discouraged after reaching certain yield; 2. A compatible apparatus that enables continuous removal of hydrates from the reactor for the design of a continuous HBCC process; 3. Effective additives/operational conditions/physical interventions that could further suppress the induction time economically. Or else, an optimum configuration in the combination of HBCC and MSF along with other commercial carbon capture processes can be examined.

7.3. Future works

The current study has analysed the practicability of hydrate formation to be used for carbon capture and desalination from the perspective of addressing the challenges of MSF. However, the work considered two separate chemical and physical compositions of hydrate formation systems addressing these purposes individually. The future work consists of developing a single module of a continuous hydrate formation reactor with the choice of the most suitable chemical composition along with the operational conditions for both the purposes. This module would also be able to produce desalinated water with accelerated water to hydrate conversion capabilities. This work mostly consists of using propane as a thermodynamic additive, which could support hydrate formation under lower pressure conditions with higher water to hydrate conversion capabilities. Propane was considered as thermodynamic additive because it can be easily removed from both CO_2 and water through a simple distillation process. The study will consist of both experimental as well as mathematical analysis to understand the kinetics of hydrate formation under various concentrations of propane under a range of pressure and temperature conditions followed by optimization. If the process is turned out to be practicable from the perspective of higher carbon capture capacities as well as higher production ratios of the desalination hybrid, an economic analysis of this Hydrate (HBD & HBCC)-MSF hybrid will be evaluated.

References

Adeyemo, A. et al., 2010. Capture of carbon dioxide from flue or fuel gas mixtures by clathrate crystallization in a silica gel column. *International Journal of Greenhouse Gas Control,* 4(3), pp. 478-485.

Ahmad, M. & Gersen, S., 2014. Water solubility in CO2 mixtures: Experimental and modelling investigation. *Energy Procedia,* Volume 63, pp. 2402-2411.

Al-Ahmad, M. & Aleem, F. A., 1994. Scale formation and fouling problems and their predicted reflection on the performance of desalination plants in Saudi Arabia.. *Desalination,* Volume 96, pp. 409-419.

Al-Anezi, K. & Hilal, N., 2007. Scale formation in desalination plants: effect of carbon dioxide solubility. *Desalination,* Volume 204, pp. 385-402.

Alasfour, F. N. & Abdulrahim, H. K., 2009. Rigorous steady state modeling of MSF-BR desalination system. *Desalination and Water treatment,* Volume 1, pp. 259-276.

Al-Badawi, A. et al., 1995. *Operation and analysis of Jeddah-1, Phase-II plant, Proc..* Abu Dhabi, IDA World Congress.

Aliev, A., Yusifov, R., Kuliev, A. & Yusifov, Y., 2008. Method of gas hydrate formation for evaluation of water desalination. *Russian Journal of Applied Chemistry,* 81(4), pp. 588-591.

Ali, M. & Kairouani, L., 2014. Solving equations describing the steady-state model of MSF desalination process using Solver Optimization Tool of MATLAB software. *Desalination and Water Treatment,* 52(40-42), pp. 7473-7483.

Ali, S., Kazi, I. & Rahman, F., 2015. Synthesis and evaluation of phosphate-free antiscalants to control CaSO4· 2H2O scale formation in reverse osmosis desalination plants. *Desalination,* Volume 357, pp. 36-44..

Alsadaie, S. M., 2017. *Design and Operation of Multistage Flash (MSF) Desalination: Advanced Control Strategies and Impact of Fouling (PhD Thesis)..* Bradford: University of Bradford.

Alsadaie, S. & Mujtaba, I., 2017. Dynamic modelling of Heat Exchanger fouling in multistage flash (MSF) desalination. *Desalination,* Volume 409, pp. 47-65.

Al-Saleh, S. & Khan, A., 1994. Evaluation of Belgard EV 2000 as antiscalant control additive in MSF plants. *Desalination,* 97(1), pp. 87-96..

Al-Sofi, M. A. K., 1999. Fouling phenomena in multi stage flash (MSF) distillers. *Desalination,* Volume 126, pp. 61-76.

Amjad, Z. & Zuhl, R., 2007. *Effect of heat treatment on the performance of deposit control polymers as calcium carbonate inhibitors..* Nashville, CORROSION/2007.

Anderson, F. & Prausnitz, J. 1., 1986. Inhibition of gas hydrates by methanol.. *A.I.Ch.E Journal,* Volume 32, pp. 1321-1333.

Anderson, R., Llamedo, M., Tohidi, B. & Burgass, R., 2003. Experimental measurement of methane and carbon dioxide clathrate hydrate equilibria in mesoporous silica. *Journal of Physical Chemistry B,* 107(15), pp. 3507-3514.

Andritsos, N., 1996. Calcium carbonate deposit formation under isothermal conditions. *Canadian journal of chemical engineering,* Volume 74, pp. 911-919.

Anklam, M. & Firoozabadi, A., 2004. Driving Force and Composition for Multicomponent Gas Hydrate Nucleation from Supersaturated Aqueous Solutions. *Journal of Chemical Physics,* 121(23), pp. 11867-11875.

Augustin, W. & Bohnet, M., 1995. Influence of the ratio of free hydrogen ions on crystallization fouling.. *Chemical Engineering and Processing: Process Intensification,* Volume 34, pp. 79-85.

Aya, I., Yamane, K. & Nariai, H., 1997. Solubility of CO2 and density of CO2 hydrate at 30 MPa. *Energy,* 22(2), pp. 263-271.

Babu, P., Chin, W., Kumar, R. & Linga, P., 2014. Systematic evaluation of tetra-n-butyl ammonium bromide (TBAB) for carbon dioxide capture employing the clathrate process. *Industrial & Engineering Chemistry Research,* 53(12), pp. 4878-4887.

Babu, P., Kumar, R. & Linga, P., 2013a. Pre-combustion capture of carbon dioxide in a fixed bed reactor using the clathrate hydrate process. *Energy,* 50(1), pp. 364-373.

Babu, P., Kumar, R. & Linga, P., 2013b. Medium pressure hydrate based gas separation (HBGS) process for pre-combustion capture of carbon dioxide employing a novel fixed bed reactor. *International Journal of Greenhouse Gas Control,* Volume 17, pp. 206-214.

Babu, P., Linga, P., Kumar, R. & Englezos, P., 2015. A review of the hydrate-based gas separation (HBGS) process for carbon dioxide pre-combustion capture. *Energy,* Volume 85, pp. 261-279.

Babu, P. et al., 2018. A Review of Clathrate Hydrate Based Desalination to Strengthen Energy–Water Nexus. *ACS Sustainable Chemistry & Engineering ,* 6(7), pp. 8093-8107.

Babu, P. et al., 2013. Hydrate phase equilibrium of ternary gas mixtures containing carbon dioxide, hydrogen and propane. *The Journal of Chemical Thermodynamics,* Volume 61, pp. 58-63..

Ballard, A. & Sloan, E. 2., 2002. The next generation of hydrate prediction: an overview. *Journal of Supermolecular Chemistry,* Volume 2, pp. 385-392.

Barrer, R. & Edge, A., 1967. Gas hydrates containing argon krypton and xenon: kinetics, and energetics of formation and equilibria.. *Proceedings of the Royal Society of London A,* Volume 300, p. 1–24.

Barrer, R. & Ruzicka, J., 1962. Non-stoichiometric clathrate compounds of water. Part 4: kinetics of formation of clathrate phases. *Transactions of the Faraday Society,* Volume 58, p. 2262–2271..

Becker, R. & Dö ring, W., 1935. Kinetische behandlung der keimbildung in ü bersattigten da¨ mpfen. *Annals of Physics,* 416(8), pp. 719-752.

Belandria, V. et al., 2012b. Phase equilibrium measurements for semi-clathrate hydrates of the (CO2+ N2+ tetra-n-butylammonium bromide) aqueous solution systems: Part 2.. *Fluid phase equilibria,* Volume 322, pp. 105-112.

Belandria, V., Mohammadi, A. & Richon, D., 2012a. Compositional analysis of the gas phase for the CO2+ N2+ tetra-n-butylammonium bromide aqueous solution systems under hydrate stability conditions. *Chemical engineering science,* Volume 84, pp. 40-47.

Bergeron, S. & Servio, P., 2009. CO2 and CH4 mole fraction measurements during hydrate growth in a semi-batch stirred tank reactor and its significance to kinetic modeling. *Fluid phase equilibria,* 276(2), pp. 150-155.

Blanco C, L. & Smith, N., 1978. The high-pressure volubility of methane in aqueous calcium chloride and aqueous tetraethylammonium bromide. Partial molar properties of dissolved methane and nitrogen in relation to water structure. *Journal of Physical Chemistry,* 82(2), pp. 186-191.

Boels, L., Keesman, K. & Witkamp, G., 2012. Adsorption of phosphonate antiscalant from reverse osmosis membrane concentrate onto granular ferric hydroxide. *Environmental science & technology,* 46(17), pp. 9638-9645.

Bohnet, M., 1987. Fouling of heat transfer surfaces.. *Chemical engineering & technology,* Volume 10, pp. 113-125.

Boublik, T., Fried, V. & Hala, E., 1984. *The vapour pressures of pure substances,* United states: OSTI.

Brahim, F., Augustin, W. & Bohnet, M., 2003. Numerical simulation of the fouling process.. *International Journal of Thermal Sciences,* Volume 42, pp. 323-334.

Buchanan, P. et al., 2005. Search for memory effects in methane hydrate: structure of water before hydrate formation and after hydrate decomposition. *Journal of Chemical Physics,* Volume 123, pp. 1645071-1645077.

Cai, J. et al., 2018. Raman spectroscopic studies on carbon dioxide separation from fuel gas via clathrate hydrate in the presence of tetrahydrofuran. *Applied energy,* Volume 214, pp. 92-102.

Carter, B., Wang, W., Adams, D. & Cooper, A., 2009. Gas storage in “dry water” and “dry gel” clathrates. *Langmuir,* 26(5), pp. 3186-3193.

Chapoy, A., Burgass, R., Tohidi, B. & Alsiyabi, I., 2014. Hydrate and phase behavior modeling in CO2-rich pipelines. *Journal of Chemical & Engineering Data,* 60(2), pp. 447-453.

Chari, V. D., Prasad, P. S. R. & Murthy, S. R., 2015. Hollow silica: A novel material for methane storage. *Oil and Gas Science and Technology,* 70(6), pp. 1125-1132.

Chari, V. D., Raju, B., Prasad, P. S. R. & Rao, D. N., 2013. Methane hydrates in spherical silica matrix: Optimization of capillary water.. *Energy and Fuels ,* Volume 27, pp. 3679- 3684.

Chari, V. D., Sharma, D. V. S. G. K., Prasad, P. S. R. & Murthy, S. R., 2013a. Methane hydrates formation and dissociation in nano silica suspension.. *Journal of Natural Gas Science and Engineering,* Volume 11, pp. 7-11.

Chatti, I., Delahaye, A., Fournaison, L. & Petitet, J., 2005. Benefits and drawbacks of clathrate hydrates: a review of their areas of interest.. *Energy conversion and management,* 46(9), pp. 1333-1343.

Chen, B. et al., 2020. Effect of a weak electric field on THF hydrate formation: Induction time and morphology. *Journal of Petroleum Science and Engineering,* Volume 194, p. 107486.

Chen, Y., Baygents, J. & Farrell, J., 2017. Removing phosphonate antiscalants from membrane concentrate solutions using granular ferric hydroxide. *Journal of Water Process Engineering,* Volume 19, pp. 18-25.

Daimaru, T., Yamasaki, A. & Yanagisawa, Y., 2007. Effect of surfactant carbon chain length on hydrate formation kinetics. *Journal of Petroleum Science and Engineering,* 56(1), pp. 89-96.

Daraboina, N., Ripmeester, J. & Englezos, P., 2013. The impact of SO2 on post combustion carbon dioxide capture in bed of silica sand through hydrate formation. *International Journal of Greenhouse Gas Control,* Volume 15, pp. 97-103.

Darwish, M. et al., 2016. Viability of integrating forward osmosis (FO) as pretreatment for existing MSF desalting unit.. *Desalination and Water Treatment,* 57(31), pp. 14336-14346.

Dashti, H. Y. L. Z. &. L. X. (. .. J. o. N. G. S. a. E. 2. 1., 2015. Recent advances in gas hydrate based CO2 capture. *Journal of Natural Gas Science and Engineering,* Volume 23, p. 195.

de Chazournes, L., 1998. *Kyoto protocol to the united nations framework convention on climate change. UN's Audiovisual Library of International Law.* [Online] Available at: http://untreaty. un. org/cod/avl/ha/kpccc/kpccc. html [Accessed 22 10 2020].

Denbigh, K., 1981. *The principles of chemical equilibrium: with applications in chemistry and chemical engineering..* Cambridge: Cambridge University Press..

Duan, Z. & Mao, S., 2006a. A thermodynamic model for calculating methane solubility, density and gas phase composition of methane-bearing aqueous fluids from 273 to 523 K and from 1 to 2000 bar. *Geochimica et Cosmochimica Acta,* 70(13), pp. 3369-3386.

Duan, Z., Møller, N., Greenberg, J. & J.H., W., 1992. An equation of state for the CH4-CO2-H2O system: II. Mixtures from 50 to 1000°C and 0 to 1000 bar. *Geochimica et Cosmochimica Acta,* 56(4), pp. 1451-1460..

Duan, Z. & Sun, R., 2003. An improved model calculating CO2 solubility in pure water and aqueous NaCl solutions from 273 to 533 K and from 0 to 2000 bar. *Chemical Geology,* 193(3), pp. 257-271.

Duan, Z., Sun, R., Zhu, C. & Chou, I., 2006b. An improved model for the calculation of CO2 solubility in aqueous solutions containing Na+, K+, Ca2+, Mg2+, Cl−, and SO42−. *Marine Chemistry,* 98(2), pp. 131-139.

Duc, N. C. F. a. H. J., 2007. CO2 capture by hydrate crystallization–A potential solution for gas emission of steelmaking industry. *Energy Conversion and Management,* 48(4), pp. 1313-1322.

Duc, N., Chauvy, F. & Herri, J., 2007. CO2 capture by hydrate crystallization–A potential solution for gas emission of steelmaking industry.. *Energy Conversion and Managemen,* 48(4), pp. 1313-1322.

Dyer, S. & Graham, G., 2002. The effect of temperature and pressure on oilfield scale formation. *Journal of Petroleum Science and Engineering,* 35(1), pp. 95-107.

El Din, A., El-Dahshan, M. & Mohammed, R., 2005. Scale formation in flash chambers of high-temperature MSF distillers. *Desaliantion,* 177(1-3), pp. 241-258.

El Din, A. & Mohammed, R., 1994. Brine and scale chemistry in MSF distillers. *Desalination,* 99(1), pp. 73-111.

El Din, A. & Mohammed, R., 1998. Contribution to the problem of vapour-side corrosion of copper-nickel tubes in MSF distillers. *Desaliantion,* 115(2), pp. 135-144.

El Din, A. M. S., El-Dahshan, M. E. & Mohammed, R. A., 2002. Inhibition of the thermal decomposition of HCO 3− A novel approach to the problem of alkaline scale formation in seawater desalination plants. *Desalination,* Volume 142, pp. 151-159..

El Din, A. M. S. & Mohammed, R. A., 1989. The problem of alkaline scale formation from a study on Arabian Gulf water. *Desalination,* Volume 71, pp. 313-324.

El-Dahshan, M., 2001. Corrosion and scaling problems present in some desalination plants in Abu Dhabi. *Desalination,* 138(1), pp. 371-377..

El-Dessouky, H. & Bingulac, S., 1996. Solving equations simulating the steady-state behavior of the multi-stage flash desalination process,. *Desalination,* Volume 107, pp. 171-193.

El-Dessouky, H. T. & Ettouney, H. M., 2002. *Fundamentals of salt water desalination.* Amsterdam, Elsevier Science..

Elliot, M., 1969. The present state of scale control in sea water evaporators. *Desalination,* 6(1), pp. 87-104..

El-Sayed, E., Ebrahim, S., Al-Saffar, A. & Abdel-Jawad, M., 1998. Pilot study of MSFRO hybrid systems. *Desalination,* 120(1), pp. 121-128..

Englezos, P., 1993. Clathrate hydrates. *Industrial and Engineering Chemistry Research,* Volume 32, pp. 1251-1274.

Englezos, P., Kalogerakis, N., Dholabhai, P. & Bishnoi, P., 1987. Kinetics of formation of methane and ethane gas hydrates.. *Chemical Engineering Science,* Volume 42, p. 2647–2658.

Eslamimanesh, A. et al., 2012. Application of gas hydrate formation in separation processes: A review of experimental studies. *The Journal of Chemical Thermodynamics,* Volume 46, pp. 62-71.

Fahiminia, F., Watkinson, A. P. & Epstein, N., 2007. Early events in the precipitation fouling of calcium sulphate dihydrate under sensible heating conditions.2007. *The Canadian Journal of Chemical Engineering,* Volume 85, pp. 679-691.

Fakharian, H., Ganji, H. & Naderifar, A., 2017. Saline produced water treatment using gas hydrates. *Journal of environmental chemical engineering,* 5(5), pp. 4269-42735.

Falabella, B., 1975. *A study of natural gas hydrates, Ph.D. Thesis.* Massachusetts: University of Massachusetts..

Fan, S. et al., 2012. Kinetics and thermal analysis of methane hydrate formation in aluminum foam.. *Chemical Engineering Science ,* Volume 82, pp. 185-193.

Fan, S. et al., 2012. Kinetics and thermal analysis of methane hydrate formation in aluminum foam. *Chemical engineering science,* Volume 82, pp. 185-193.

Feiner, M., Beggel, S., Jaeger, N. & Geist, J., 2015. Increased RO concentrate toxicity following application of antiscalants—acute toxicity tests with the amphipods Gammarus pulex and Gammarus roeseli. *Environmental Pollution,* Volume 197, pp. 309-312.

Fosbøl, P. v. S. N. G. A. T. K. a. K. G., 2017. *Methods and Modelling for Post-combustion CO2 Capture. Process Systems and Materials for CO2 Capture: Modelling, Design, Control and Integration.* Hoboken, New Jerey: John Wiley & Sons, Inc..

Ganji, H., Manteghian, M. & Zadeh, K., 2006. A kinetic study on tetrahydrofuran hydrate crystallization.. *Journal of Chemical Engineering of Japan,* Volume 39, pp. 401-408.

Gayet, P. et al., 2005. Experimental determination of methane hydrate dissociation curve up to 55 MPa by using a small amount of surfactant as hydrate promoter.. *Chemical engineering science,* 60(21), pp. 5751-5758.

Gayet, P. et al., 2005. Experimental determination of methane hydrate dissociation curve up to 55 MPa by using a small amount of surfactant as hydrate promoter. *Chemical Engineering Science,* Volume 60, pp. 5751-5758.

Ghani, S. & Al-Deffeeri, N., 2010. Impacts of different antiscalant dosing rates and their thermal performance in Multi Stage Flash (MSF) distiller in Kuwait. *Desalination,* 250(1), pp. 463-472..

Gholinezhad, J., Chapoy, A. & Tohidi, B., 2011. Separation and capture of carbon dioxide from CO2/H2 syngas mixture using semi-clathrate hydrates.. *chemical engineering research and design,* 89(9), pp. 1747-1751.

Giavarini, C., Maccioni, F. & Santarelli, M., 2003. Formation kinetics of propane hydrates. *Industrial and Engineering Chemistry Research,* Volume 42, p. 1517–1521.

Giavarini, C., Maccioni, F. & Santarelli, M., 2003. Formation kinetics of propane hydrates. *Industrial & engineering chemistry research,* 42(7), pp. 1517-1521.

Glade, H. & Al-Rawajfeh, A. E., 2008. Modeling of CO2 release and the carbonate system in multiple-effect distillers.. *Desalination,* Volume 222, pp. 605-625.

Hamed, O., 2005. Overview of hybrid desalination systems—current status and future prospects. *Desalination,* 186(1-3), pp. 207-214.

Hamed, O. A. & Al-Otaibi, H. A., 2010. Prospects of operation of MSF desalination plants at high TBT and low antiscalant dosing rate.. *Desalination,* Volume 256, pp. 181- 189..

Hammerschmidt, E., 1934. Formation of gas hydrates in natural gas transmission lines.. *Industrial and Engineering Chemistry,* pp. 851-855.

Hand, J., Katz, D. & Verma, V., 1974. *Review of gas hydrates with implication for ocean sediments.* Boston, Springer, pp. 179-194.

Han, X., Wang, S., X., C. & Liu, F., 2002. Surfactant Accelerates Gas Hydrate Formation. *4th International Conference on Natural Gas Hydrates; Yokohama, Japan,* Volume 63, p. 1039.

Harvey, A., 1996. Semiempirical correlation for Henry's Constants over Large Temperature Ranges. *AICHE Journal,* 42(5), p. 1491.

Hashemi, S., Macchi, A., Bergeron, S. & Servio, P., 2006. Prediction of methane and carbon dioxide solubility in water in the presence of hydrate. *Fluid Phase Equilibria,* 246(1), pp. 131-136.

Hasson, D., 1999. *Progress in precipitation fouling research—a review.* Pascoli, Italy, Understanding heat exchanger fouling and its mitigation, pp. 67-90.

Hasson, D. et al., 1968. Mechanism of calcium carbonate scale deposition on heat-transfer surfaces. *Industrial & Engineering Chemistry Fundamentals,* Volume 7, pp. 59-65.

Hasson, D. S. H. &. B. M., 1978. *Prediction of Calcium Carbonate Scaling Rates..* Las Palmas, Gran Canaria, Spain, International symposium on freshwater from the sea, pp. 193-199.

Hasson, D., Shemer, H. & Sher, A., 2011. State of the art of friendly "green" scale control inhibitors: a review article. *Industrial & Engineering Chemistry Research,* 50(12), pp. 7601-7607.

Hawaidi, E. & Mujtaba, I., 2010. Simulation and optimization of MSF desalination process for fixed freshwater demand: Impact of brine heater fouling. *Chemical Engineering Journal,* 165(2), pp. 545-553.

Helal, A., El-Nashar, A., Al-Katheeri, E. & Al-Malek, S., 2004. Optimal design of hybrid RO/MSF desalination plants Part II: Results and discussion.. *Desalination,* 160(1), pp. 13-27.

Helal, A., Medani, M., Soliman, M. & Flower, J., 1986. A tridiagonal matrix model for multistage flash desalination plants. *Computers & chemical engineering,* 10(4), pp. 327-342.

Helalizadeh, A., Müller-Steinhagen, H. & Jamialahmadi, M., 2000. Mixed salt crystallisation fouling. *Chemical Engineering and Processing: Process Intensificatio,* Volume 39, pp. 29-43.

Helalizadeh, A., Müller-Steinhagen, H. & Jamialahmadi, M., 2000. Mixed salt crystallisation fouling.. *Chemical Engineering and Processing: Process Intensification,* Volume 39, pp. 29-43..

Helalizadeh, A., Müller-Steinhagen, H. & Jamialahmadi, M., 2005. Mathematical modelling of mixed salt precipitation during convective heat transfer and sub-cooled flow boiling.. *Chemical engineering science,* Volume 60, pp. 5078-5088.

Hendriks, E., Edmonds, B., Moorwood, R. & Szczepanski, R., 1996. Hydrate structure stability in simple and mixed hydrates. *Fluid phase equilibria,* 117(1), pp. 193-200.

Henry, W., 1803. Experiments on the Quantity of Gases Absorbed by Water, at Different Temperatures, and under Different Pressure. *Philosophical Transactions of the Royal Society of London,* Volume 93, pp. 269-276..

Hussain, S. et al., 2006. Study of the kinetics and morphology of gas hydrate formation. *Chemical Engineering and Technology.,* Volume 29, p. 937–943.

Islam, A. & Carlson, E., 2012. *Activity Coefficient Models for Calculations of Supercritical CO2 and H2O at High Temperatures and Pressures.* 36 ed. s.l.:GRC Transactions.

Japas, M. & Sengers, J., 1989. Gas solubility and Henry's law near the solvent's critical point. *AIChE Journal,* 35(5), pp. 705-713..

Javanmardi, J. & Moshfeghian, M., 2003. Energy consumption and economic evaluation of water desalination by hydrate phenomenon.. *Applied thermal engineering,* 23(7), pp. 845-857.

Kalin, M. & Polajnar, M., 2014. The wetting of steel, DLC coatings, ceramics and polymers with oils and water: The importance and correlations of surface energy, surface tension, contact angle and spreading. *Applied Surface Science,* Volume 293, pp. 97-108.

Kalogerakis, N., Jamaluddin, A., Dholabhai, P. & Bishnoi, P., 1993. *In Effect of Surfactants on Hydrate Formation Kinetics; SPE International Symposium on Oilfield Chemistry.* New Orleans, Luisiana, Society of Petroleum Engineers.

Kalogirou, S. A., 2014. Chapter 8 - Solar desaliantion systems . In: S. A. Kalogirou, ed. *Solar energy engineering* . s.l.:Academic press, pp. 431-479.

Kang, K. et al., 2014. Seawater desalination by gas hydrate process and removal characteristics of dissolved ions (Na+, K+, Mg2+, Ca2+, B3+, Cl−, SO42−). *Desalination,* Volume 353, pp. 84-90.

Kang, S. & Lee, H., 2000. Recovery of CO2 from flue gas using gas hydrate: thermodynamic verification through phase equilibrium measurements. *Environmental science & technology,* 34(20), pp. 4397-4400.

Kang, S. & Lee, H., 2000. Recovery of CO2 from flue gas using gas hydrate: thermodynamic verification through phase equilibrium measurements.. *Environmental science & technology,* 34(20), pp. 4397-4400..

Kang, S., Lee, H., Lee, C. & Sung, W., 2001. Hydrate phase equilibria of the guest mixtures containing CO2, N2 and tetrahydrofuran.. *Fluid Phase Equilibria,* 185(1), pp. 101-109.

Kang, S. P., Lee, J. & Seo, Y., 2013. Pre-combustion capture of CO2 by gas hydrate formation in silica gel pore structure.. *Chemical engineering journal,* Volume 218, pp. 126-132.

Kang, S. P. & Lee, J. W., 2010a. Formation characteristics of synthesized natural gas hydrates in meso- and macroporous silica gels. *Journal of Physical Chemistry B,* 114(20), pp. 6973-6978.

Kang, S. P. & Lee, J. W., 2010. Kinetic behaviors of CO2 hydrates in porous media and effect of kinetic promoter on the formation kinetics. *Chemical engineering science,* Volume 65, p. 1845.

Karaaslan, U. U. & Parlaktuna, M., 2000. Surfactants as hydrate promoters?. *Energy fuels,* 14(5), pp. 1103-1107.

Kashchiev, D., 2000. *Nucleation: Basic theory and applications.* Oxford: Butterworth-Heinemann..

Kashchiev, D. & Firoozabadi, A., 2002a. Driving force for crystallization of gas hydrates. *Journal of Crystal Growth,* Volume 241, p. 220.

Kashchiev, D. & Firoozabadi, A., 2002a. Driving force for crystallization of gas hydrates.. *Journal of Crystal Growth,* Volume 241, pp. 220-230.

Kashchiev, D. & Firoozabadi, A., 2002b. Nucleation of gas hydrates. *Journal of Crystal Growth,* Volume 243, pp. 476-489.

Kashchiev, D. & Firoozabadi, A., 2002. Driving force for crystallization of gas hydrates. *Journal of crystal growth,* 241(1), pp. 220-230.

Kashchiev, D. & Firoozabadi, A., 2003. Induction time in crystallization of gas hydrates. *Journal of crystal growth,* 250(3), pp. 499-515.

Kashchiev, D. & Firoozabadi, A., 2003. Induction time in crystallization of gas hydrates. *Journal of Crystal Growth,* Volume 250, p. 499.

Kazemeini, M., Freidoonian, F. & Fattahi, M., 2012. Developing a Mathematical Model for Hydrate Formation in a Spray Batch Reactor. *Advances in Materials Physics and Chemistry,* Volume 2, pp. 244-247..

Kazi, S. N., 2012. Fouling and Fouling Mitigation on Heat Exchanger Surfaces. In: J. Mitrovic, ed. *Heat Exchangers- Basic Design and Applications.* s.l.:Intechopen.

Khurana, M., Veluswamy, H., Daraboina, N. & Linga, P., 2019. Thermodynamic and kinetic modelling of mixed CH4-THF hydrate for methane storage application. *Chemical Engineering Journal,* Volume 370, pp. 760-771.

Khurana, M., Yin, Z. & Linga, P., 2017. A review of clathrate hydrate nucleation. *ACS Sustainable Chemistry & Engineering,* 5(12), pp. 11176-11203.

Kim, S. et al., 2011. Gas hydrate formation method to capture the carbon dioxide for pre-combustion process in IGCC plant.. *International journal of hydrogen energy,* 36(1), pp. 1115-1121.

King, M., Mubarak, A., Kim, J. & Bott, T., 1992. The mutual solubilities of water with supercritical and liquid carbon dioxides. *Journal of Supercritical Fluids,* 5(4), pp. 296-302.

Knox, W., Hess, M., Jones, G. & Smith, H., 1961. Chemical Engineering Progress. *The hydrate process,* Volume 57, pp. 66-71.

Kolev, N., 2011. *Solubility of O2, N2, H2 and CO2 in water. In: Multiphase Flow Dynamics.* 4 ed. Berlin, Heidelberg: Springer.

Kolev, N. I., 2011. *Solubility of O2, N2, H2 and CO2 in water. In: Multiphase Flow Dynamics.* Berlin, Heidelberg: Springer.

Krause, S., 1993. Fouling of heat transfer surfaces by crystallization and sedimentation. *International Chemical engineering,* 33(3).

Kumar, A., Bhattacharjee, G., Kulkarni, B. & Kumar, R., 2015. Role of surfactants in promoting gas hydrate formation. *Inductrial and engineering chemistry,* 54(49), p. 12217−12232..

Kumar, A., Sakpal, T., Linga, P. & Kumar, R., 2013. Influence of contact medium and surfactants on carbon dioxide clathrate hydrate kinetics.. *Fuel,* Volume 105, p. 671.

Kumar, A., Sakpal, T., Linga, P. & Kumar, R., 2013. nfluence of contact medium and surfactants on carbon dioxide clathrate hydrate kinetics. *Fuel,* Volume 105, pp. 664-671.

Kumar, R., Linga, P., Ripmeester, J. & Englezos, P., 2009. Two-stage clathrate hydrate/membrane process for precombustion capture of carbon dioxide and hydrogen. *Journal of environmental engineering,* 135(6), pp. 411-417.

Kumar, R., Wu, H. & Englezos, P., 2006. Incipient hydrate phase equilibrium for gas mixtures containing hydrogen, carbon dioxide and propane. *Fluid phase equilibria,* 244(2), pp. 161-171.

Lang & F., 2016. *Liquid phase characterization of multicomponent gas hydrate systems-Doctoral dissertation.* Montreal, Quebec: McGill University Libraries.

Lee, D., Lee, Y., Lee, S. & Seo, Y., 2016. Accurate measurement of phase equilibria and dissociation enthalpies of HFC-134a hydrates in the presence of NaCl for potential application in desalination. *Korean Journal of Chemical Engineering,* 33(4), pp. 1425-1430.

Lee, H. et al., 2010. Gas hydrate formation process for pre-combustion capture of carbon dioxide. *Energy,* 35(6), pp. 2729-2733.

Lee, J. & Englezos, P., 2006. Unusual kinetic inhibitor effects on gas hydrate formation. *Chemical Engineering Science,* Volume 61, p. 1368–1376.

Lee, J., Susilo, R. & Englezos, P., 2005a. Kinetics of structure H gas hydrate. *Energy & Fuels,* Volume 19, p. 1008–1015.

Lee, J., Susilo, R. & Englezos, P., 2005b. Methane–ethane and methane–propane hydrate formation and decomposition on water droplet. *Chemical Engineering Science,* Volume 60, p. 4203–4214.

Lee, J., Susilo, R. & Englezos, P., 2005. Methane–ethane and methane–propane hydrate formation and decomposition on water droplets. *Chemical Engineering Science,* Volume 60, p. 4203–4214.

Lee, S. et al., 2007. Methane hydrate equilibrium and formation kinetics in the presence of an anionic surfactant.. *Journal of Physical Chemistry C,* Volume 111, p. 4734–4739.

Li, J., Liang, D., Guo, K. & Wang, R., 2005. The influence of additives and metal rods on the nucleation and growth of gas hydrates. *Journal of Colloid and Interface Science,* Volume 283, p. 223–230.

Linga, P. a. C. M. 2. E. &. F. 3. p.-1., 2017. A review of reactor designs and materials employed for increasing the rate of gas hydrate formation.. *Energy and fuels,* 31(1), pp. 1-13.

Linga, P., Adeyemo, A. & Englezos, P., 2008. Medium-pressure clathrate hydrate/membrane hybrid process for postcombustion capture of carbon dioxide. *Environmental science & technology,* 42(1), pp. 315-320.

Linga, P. & Clarke, M., 2016. A review of reactor designs and materials employed for increasing the rate of gas hydrate formation. *Energy and Fuels,* 31(1), pp. 1-13.

Linga, P. & Clarke, M., 2016. A review of reactor designs and materials employed for increasing the rate of gas hydrate formation. *Energy & Fuels,* 31(1), pp. 1-13.

Linga, P. & Clarke, M. A., 2017. A review of reactor design and materials employed for increasing the rate of gas hydrate formation. *Energy fuels,* 31(1), p. 1.

Linga, P., Daraboina, N., Ripmeester, J. A. & Englezos, P., 2012. Enhanced rate of gas hydrate formation in a fixed bed column filled with sand compared to a stirred vessel.. *Chemical engineering science,* 68(1), pp. 617-623.

Linga, P. et al., 2009. Gas hydrate formation in a variable volume bed of silica sand particles.. *Energy and fuels,* 23(11), pp. 5496-5507.

Linga, P. et al., 2009. Gas hydrate formation in a variable volume bed of silica sand particles. *Energy & Fuels,* 23(11), pp. 5496-5507.

Linga, P. K. R. a. E. P. 2. .. 6. p., 2007. Gas hydrate formation from hydrogen/carbon dioxide and nitrogen/carbon dioxide gas mixtures. *Chemical engineering science,* 62(16), pp. 4268-4276.

Linga, P., Kumar, R. & Englezos, P., 2007. Gas hydrate formation from hydrogen/carbon dioxide and nitrogen/carbon dioxide gas mixtures. *Chemical Engineering Science,* Volume 62, p. 4268–4276..

Link, D., Ladner, E., Elsen, H. & Taylor, C., 2003. Formation and dissociation studies for optimizing the uptake of methane by methane hydrates. *Fluid Phase Equilibria,* Volume 1-10, p. 211.

Link, D., Ladner, E. P. & Elsen, H. A., 2003. Taylor, C. E. Formation and Dissociation Studies for Optimizing the Uptake of Methane by Methane Hydrates. *Fluid phase equilibria,* Volume 10, p. 211.

Lin, W. et al., 2004. Effect of surfactant on the formation and dissociation kinetic behaviour of methane hydrate. *Chemical Engineering Science,* Volume 59, p. 4449–4455.

Liu, B. et al., 2011. Heat transfer related to gas hydrate formation/dissociation. In: *Developments in Heat Transfe.* Beiging: P.R.China, pp. 477-502..

Liu, J., Chen, S., Wang, H. & Chen, X., 2015. Calculation of carbon footprints for water diversion and desalination projects. *Energy Procedia,* Volume 75, pp. 2483-2494.

Li, X., Xia, Z., Chen, Z. & Wu, H., 2011. Precombustion capture of carbon dioxide and hydrogen with a one-stage hydrate/membrane process in the presence of tetra-n-butylammonium bromide (TBAB). *Energy and Fuels,* 25(3), pp. 1302-1309..

Li, X., Xia, Z., Chen, Z. & Wu, H., 2011. Precombustion capture of carbon dioxide and hydrogen with a one-stage hydrate/membrane process in the presence of tetra-n-butylammonium bromide (TBAB). *Energy & Fuels,* 25(3), pp. 1302-1309.

Li, X. et al., 2010. Equilibrium hydrate formation conditions for the mixtures of CO2+ H2+ tetrabutyl ammonium bromide.. *Journal of Chemical & Engineering Data,* 55(6), pp. 2180-2184.

Li, X., Xu, C., Chen, Z. & Cai, J., 2012. Synergic effect of cyclopentane and tetra-n-butyl ammonium bromide on hydrate-based carbon dioxide separation from fuel gas mixture by measurements of gas uptake and X-ray diffraction patterns.. *international journal of hydrogen energy, 37(1), pp.,* 37(1), pp. 720-727.

Li, X., Xu, C., Chen, Z. & Wu, H., 2010. Tetra-n-butyl ammonium bromide semi-clathrate hydrate process for post-combustion capture of carbon dioxide in the presence of dodecyl trimethyl ammonium chloride. *Energy,* 35(9), pp. 3902-3908.

Li, Z., Wang, X., Xue, Q. & Liu, M., 2018. *Calculation for solubility of methane and carbon dioxide in water in presence of hydrate. In The 28th International Ocean and Polar Engineering Conference..* Sapporo, Japan, International Society of Offshore and Polar Engineers.

Li, Z. et al., 2017. Preferential enclathration of CO2 into tetra-n-butyl phosphonium bromide semiclathrate hydrate in moderate operating conditions: Application for CO2 capture from shale gas. *Applied energy,* Volume 199, pp. 370-381.

Long, J. & Sloan, E., 1996. Hydrates in the ocean and evidence for the location of hydrate formation. *International Journal of Thermophysics,* Volume 17, pp. 1-13.

Maini, B. & Bishnoi, R., 1981. Experimental investigation of hydrate formation behaviour of a natural gas bubble in a simulated deep sea environment.. *Chemical Engineering Science,* Volume 36, p. 183–189..

Mali, G., Chapoy, A. & Tohidi, B., 2018. Investigation into the effect of subcooling on the kinetics of hydrate formation.. *The Journal of Chemical Thermodynamics,* Volume 117, pp. 91-96.

MarketsandMarkets, 2020. *Antiscalants/Scale Inhibitors Market by Type (Phosphonates, Carboxylates/Acrylic, Sulfonates, and Others), Application (Power & Construction, Mining, Oil & Gas, Water & Wastewater Treatment, Food & Beverage) and by Region - Global Forecast to 2020.* [Online] Available at: https://www.marketsandmarkets.com/Market-Reports/scale-inhibitors-market-482.html [Accessed 09 November 2020].

Max, M. & Pellenbarg, R., 1999. *Desalination through methane hydrate.* U.S., Patent No. 5,873,262.

McCallum, S. D., Reistenberg, D. E., Zatsepina, O. Y. & Phelps, T. J., 2007. Effect of pressure vessel size on the formation of gas hydrates.. *Journal of Petroleum Science and Engineering,,* Volume 57, p. 54.

McMullan, R. & Jeffrey, G., 1965. Polyhedral clathrate hydrates. IX. Structure of ethylene oxide hydrate. *The Journal of Chemical Physics,,* 42(8), pp. 2725-2732..

Michels, A. G. J. a. B. A. 1. ,. P. 3. p., 1936. The influence of pressure on the solubility of gases. *Physica,* 3(8), pp. 797-808.

Mohammadi, A., Eslamimanesh, A. & Richon, D., 2013. Semi-clathrate hydrate phase equilibrium measurements for the CO2+ H2/CH4+ tetra-n-butylammonium bromide aqueous solution system. *Chemical Engineering Science,* Volume 94, pp. 284-290.

Monfort, J. & Nzihou, A., 1993. Light-scattering kinetics study of cyclopropane hydrate growth.. *Journal of Crystal Growth,* Volume 128, p. 1182–1186..

Moudrakovski, I., Sanchez, A., Ratcliffe, C. & Ripmeester, J., 2001. Nucleation and growth of hydrates on ice surfaces: new insights from 129Xe NMR experiments with hyperpolarized xenon. *Journal of Physical Chemistry B,* Volume 105, p. 12338–12347.

Mubarak, A., 1998. A kinetic model for scale formation in MSF desalination plants. Effect of antiscalants. *Desalination,* Volume 120, pp. 33-39.

Müller-Steinhagen, H., Malayeri, M. & Watkinson, A., 2011. Heat exchanger fouling: mitigation and cleaning strategies. *Heat trnsfer engineering,* 32(3), pp. 189-196.

Mussati, S., Aguirre, P. & Scenna, N., 2003. Novel configuration for a multistage flash-mixer desalination system. *Industrial & engineering chemistry research,* 42(20), pp. 4828-4839..

Mussati, S., Aguirre, P. & Scenna, N., 2006. Superstructure of alternative configurations of the multistage flash desalination process. *Industrial & engineering chemistry research,* 45(21), pp. 7190-7203..

Mwaba, M. G., Golriz, M. R. & Gu, J., 2006. A semi-empirical correlation for crystallization fouling on heat exchange surfaces. *Applied Thermal Engineering,* Volume 26, pp. 440-447.

Nada, N., Yanaga, Y., Serizawa, S. & Tanaka, K., 1995. *Design features of the largest SWRO plant in the world — 33.8 MGD in Madina and Yanbu, Proc..* Abu Dhabi, IDA World Congress.

Najibi, S. H., Müller-Steinhagen, H. & Jamialahmadi, M., 1997. Calcium sulphate scale formation during subcooled flow boiling. *Chemical Engineering Science,* Volume 52, pp. 1265-1284.

Nambiar, A., Babu, P. & Linga, P., 2015. CO2 capture using the clathrate hydrate process employing cellulose foam as a porous media. Canadian. *Journal of Chemistry ,* 93(8), pp. 808-814.

Natarajan, V., 1993. *Thermodynamic and Nucleation Kinetics of Gas Hydrates. Ph. D. thesis.* Calgary: University of Calgery.

Natarajan, V., Bishnoi, P. & Kalogerakis, K., 1994. Induction phenomena in gas hydrate nucleation. *Chemical Engineering Science,* Volume 49, p. 2075–2087..

Nessim, R., Tadros, H., Taleb, A. & Moawad, M., 2015. Chemistry of the Egyptian Mediterranean coastal waters. *The Egyptian Journal of Aquatic Research,* 41(1), pp. 1-10.

Nishia, Y., Qianb, L., Higashimotob, M. & Abdelmoneimb, M., 2020. Linear programming determination of blend ratios for desalinated water produced by multistage flash and reverse osmosis in a hybrid plant.. *DESALINATION AND WATER TREATMENT,* Volume 181, pp. 40-46.

Nohra, M., Woo, T., Alavi, S. & Ripmeester, J., 2012. Molecular dynamics Gibbs free energy calculations for CO2 capture and storage in structure I clathrate hydrates in the presence of SO2, CH4, N2, and H2S impurities.. *The Journal of Chemical Thermodynamics,* 44(1), pp. 5-12.

Okutani, K., Kuwabara, Y. & Mori, Y. H., 2008. Surfactant effects on hydrate formation in an unstirred gas/liquid system: An experimental study using methane and sodium alkyl sulfates.. *Chemical engineering science,* Volume 63, p. 194.

Olderøy, M. Ø. et al., 2009. Growth and nucleation of calcium carbonate vaterite crystals in presence of alginate. *Crystal Growth & Design,* Volume 9, pp. 5176-5183.

Oshima, M. et al., 2010. Memory effect on semi-clathrate hydrate formation: A case study of tetragonal tetra-n-butyl ammonium bromide hydrate. *Chemical engineering science,* 65(20), pp. 5442-5446.

Pääkkönen, T. M. et al., 2012. Crystallization fouling of CaCO 3–analysis of experimental thermal resistance and its uncertainty. *International Journal of Heat and Mass Transfer,* Volume 55, pp. 6927-6937.

Pääkkönen, T. M. et al., 2015. Modeling CaCO3 crystallization fouling on a heat exchanger surface–Definition of fouling layer properties and model parameters.. *International journal of heat and mass transfer,* Volume 83, pp. 84-98.

Pangborn, J. & Barduhn, A., 1970. The kinetics of methyl bromide hydrate formation. *Desalination,* Volume 8, p. 35–68.

Parent, J. & Bishnoi, P., 1996. Investigation into the nucleation behaviour of methane gas hydrates. *Chemical Engineering Communications,* Volume 144, pp. 51-64.

Parent, J. & Bishnoi, P., 1996. Investigations into the nucleation behaviour of methane gas hydrates.. *Chemical Engineering Communications,* 144(1), pp. 51-64.

Park, K. et al., 2011. A new apparatus for seawater desalination by gas hydrate process and removal characteristics of dissolved minerals (Na+, Mg2+, Ca2+, K+, B3+). *Desalination,* 274(1), pp. 91-96.

Park, S. et al., 2013. Hydrate-based pre-combustion capture of carbon dioxide in the presence of a thermodynamic promoter and porous silica gels. *International Journal of Greenhouse Gas Contro,* Volume 14, pp. 193-199.

Parsazadeh, M. & Duan, X., 2016. Numerical study of a hybrid thermal insulation with phase change material for subsea pipelines. In ASME International Mechanical Engineering Congress and Exposition. *Proceedings of the ASME 2016 International Mechanical Engineering Congress and Exposition.,* Volume 8, p. V008T10A060.

Pasieka, J., Coulombe, S. & Servio, P., 2013. Investigating the effects of hydrophobic and hydrophilic multi-wall carbon nanotubes on methane hydrate growth kinetics. *Chemical Engineering Science,* Volume 104, pp. 998-1002.

Patel, S. & Finan, M. A., 1999. New antifoulants for deposit control in MSF and MED plants. *Desalination,* Volume 124, pp. 63-74.

Pervov, A., Andrianov, A., Chukhin, V. & Efremov, R., 2015. The development and evaluation of new biodegradable acrylic acid based antiscalants for reverse osmosis. *International Journal of Applied Engineering Research,* 10(5), pp. 3979-3986.

Plummer, L. N. & Busenberg, E., 1982. The solubilities of calcite, aragonite and vaterite in CO 2-H 2 O solutions between 0 and 90 C, and an evaluation of the aqueous model for the system CaCO 3-CO 2-H 2 O. *Geochimica et Cosmochimica Acta,* Volume 46, pp. 1011-1040.

Pogiatzis, T. et al., 2012. Identifying optimal cleaning cycles for heat exchangers subject to fouling and ageing.. *Applied energy,* 89(1), pp. 60-66.

Popov, K. et al., 2016. A comparative performance evaluation of some novel “green” and traditional antiscalants in calcium sulfate scaling.. *Advances in Materials Science and Engineering,* Volume 2016.

Prajitno, D., Maulana, A. & Syarif, D., 2016. *Effect of surface roughness on contact angle measurement of nanofluid on surface of stainless steel 304 by sessile drop method. In Journal of Physics: Conference Series.* s.l., IOP Publishing.

Prasad, P. S. R., 2015. Methane hydrate formation and dissociation in the presence of hollow silica.. *Journal of Chemical and Engineering Data,* 60(2), pp. 304-310.

Prasad, P. S. R. & Chari, V. D. .., 2015. Preservation of methane gas in the form of hydrates: Use of mixed hydrates.. *Journal of Natural Gas Science and Engineering,* Volume 25, pp. 10-14.

Prasad, P. S. R. & Sowjanya, Y., 2014. Dhanunjana Chari, V. Enhancement in methane storage capacity in gas hydrates formed in hollow silica. *Journal of Physical Chemistry C,* 118(15), pp. 7759-7764.

Raoult, F., 1887. Loi générale des tensions de vapeur des dissolvants. *Comptes rendus hebdomadaires des séances de l'Académie,* Volume 104, pp. 1430-1433.

Renon, H. & Prausnitz, J., 1968. Local compositions in thermodynamic excess functions for liquid mixtures. *AIChE journal,* 14(1), pp. 135-144.

Ribeiro Jr, C. & Lage, P., 2008. Modelling of hydrate formation kinetics: State-of-the-art and future directions. *Chemical Engineering Science,* 63(8), pp. 2007-2034.

Ribeiro, C. & Lage, P., 2008. Modelling of hydrate formation kinetics: State-of-the-art and future directions. *Chemical Engineering Science,* 63(8), pp. 2007-2034.

Ripmeester, J. & Alavi, S., 2016. Some current challenges in clathrate hydrate science: Nucleation, decomposition and the memory effect.. *Current Opinion in Solid State and Materials Science,* 20(6), pp. 344-351..

Robinson, D., Peng, D. & Chung, S., 1985. The development of the Peng-Robinson equation and its application to phase equilibrium in a system containing methanol. *Fluid Phase Equilibria,* 24(1), pp. 25-41.

Roosta, H., Khosharay, S. & Varaminian, F., 2013. Experimental study of methane hydrate formation kinetics with or without additives and modeling based on chemical affinity. *Energy conversion and management,* Volume 76, pp. 499-505.

Rosso, M., Beltramini, A., Mazzotti, M. & Morbidelli, M., 1997. Modeling multistage flash desalination plants. *Desalination,* 108(1-3), pp. 365-374.

Rosso, M., Beltramini, A., Mazzotti, M. & Morbidelli, M., 1997. Modeling multistage flash desalination plants. *Desalination,* 108(1), pp. 365-374.

Sa, J. et al., 2013. Hydrophobic amino acids as a new class of kinetic inhibitors for gas hydrate formation.. *Scientific reports,* Volume 3, p. 2428.

Sander & R., 2015. Compilation of Henry's law constants (version 4.0) for water as solvent. *Atmospheric Chemistry and Physics,* 15(8), pp. 4399-4981.

Schroeter, J., Kobayashi, R. & Hildebrand, M., 1983. Hydrate decomposition conditions in the system H2S–methane–propane.. *Industrial and Engineering Chemistry Fundamentals,* Volume 22, p. 361–364.

Sear, R., 2007. Nucleation: theory and applications to protein solutions and colloidal suspensions. *Journal of Physics: Condensed Matter,* 19(3), p. 033101.

Segev, R., Hasson, D. & Semiat, R., 2012. Rigorous modeling of the kinetics of calcium carbonate deposit formation. *AIChE Journal,* Volume 58, pp. 1222-1229.

Segev, R., Hasson, D. & Semiat, R., 2012. Rigorous modeling of the kinetics of calcium carbonate deposit formation.. *AIChE Journal,* Volume 58, pp. 1222-1229.

Seo, Y. et al., 2005. Efficient recovery of CO2 from flue gas by clathrate hydrate formation in porous silica gels. *Environmental science & technology,* 39(7), pp. 2315-2319.

Seo, Y. T. et al., 2005. Efficient recovery of CO2 from flue gas by clathrate hydrate formation in porous silica gels. *Environmental Science and Technology,* 39(7), pp. 2315-2319.

Servio, P. & Englezos, P., 2003. Morphology of methane and carbon dioxide hydrates formed from water droplets. *A.I.Ch.E. Journal,* Volume 49, p. 269–276.

Serway, R. & Jewett, J., 2018. *Physics for scientists and engineers with modern physics..* 1 ed. s.l.:Cengage learning.

Shams El Din, A. M., El-Dahshan, M. E. & Mohammed, R. A., 2005. Scale formation in flash chambers of high-temperature MSF distillers. *Desalination,* Volume 177, pp. 241-258.

Shi, W. et al., 2017. Design and synthesis of biodegradable antiscalant based on MD simulation of antiscale mechanism: A case of itaconic acid-epoxysuccinate copolymer. *Computational Materials Science,* Volume 136, pp. 118-125.

Skovborg, P., Ng, H., Rasmusseen, P. & Mohn, U., 1993. Measurements of induction times for the formation of methane and ethane gas hydrates. *Chemical Engineering Science,* Volume 48, p. 445–453.

Slesarenko, V. N., Dobrzansky, V. G. & Slesarenko, V. V., 2003. The account of heat exchange features when modelling scale formation at distillation plants. *Desalination,* Volume 152, pp. 229-236.

Sloan Jr, E. a. K. C. 2. .. .., 2007. *Clathrate hydrates of natural gases.* 3 ed. Newyork: CRC press.

Sloan Jr, E. & Koh, C., 2007. *Clathrate hydrates of natural gases.* 7 ed. s.l.:CRC Press.

Sloan, E., 2003. Clathrate hydrate measurements: microscopic, mesoscopic and macroscopic. *Journal of Chemical Thermodynamics,* Volume 35, pp. 41-53.

Sloan, E., 2005. A changing hydrate paradigm—from apprehension to avoidance to risk management. *Fluid Phase Equilibria,* Volume 228, pp. 67-74.

Sloan, E. D., 2003a. Fundamental principles and applications of natural gas hydrates. *Nature,* 426(6964), p. 353−363..

Sloan, E. & Fleyfel, F., 1991. Molecular mechanism for gas hydrate nucleation from ice. *A.I.Ch.E. Journal,* Volume 37, p. 1281–1292.

Sloan, E. et al., 1998. Quantifying hydrate formation and kinetic inhibition.. *Industrial & engineering chemistry research,* 37(8), pp. 3124-3132..

Song, L. et al., 2010. *ExxonMobil Research and Engineering Co, Mitigation of in-tube fouling in heat exchangers using controlled mechanical vibration..* U.S.A, Patent No. 7,836,941.

Steinhagen, R., Müller-Steinhagen, H. & Maani, K., 1993. Problems and costs due to heat exchanger fouling in New Zealand industries.. *Heat transfer engineering,* 14(1), pp. 19-30.

Su, F. et al., 2009. Reversible hydrogen storage in hydrogel clathrate hydrates. *Advanced materials,* 21(23), pp. 2382-2386.

Su, F., Bray, C. L., Tan, B. & Cooper, A. I., 2008. Rapid and reversible hydrogen storage in clathrate hydrates using emulsion-templated polymers. *Advanced Materials,* 20(14), pp. 2663-2666.

Suslick, K., 1998. *Kirk-Othmer Encyclopedia of Chemical Technology.* 26 ed. Newyork: John Wiley&Sons.

Tajima, H., Yamasaki, A. & Kiyono, F., 2004. Energy consumption estimation for greenhouse gas separation processes by clathrate hydrate formation. *Energy,* 29(11), pp. 1713-1729.

Takeya, S., Hori, A., Hondoh, T. & Uchida, T., 2000. Freezing-memory effect of water on nucleation of CO2 hydrate crystals.. *Journal of Physical Chemistry B ,* Volume 104, p. 4164–4168.

Tang, J. et al., 2013. Study on the influence of SDS and THF on hydrate-based gas separation performance. *Chemical Engineering Research and Design,* 91(9), pp. 1777-1782..

Thompson, S. et al., 1984. A molecular dynamics study of liquid drops.. *Journal of Chemical Physics,* 81(1), p. 530−542.

Thoutam, P., Rezaei Gomari, S., Ahmad, F. & Islam, M., 2019. Comparative Analysis of Hydrate Nucleation for Methane and Carbon Dioxide. *Molecules,* 24(6), p. 1055.

Torré, J. et al., 2011. CO2 capture by hydrate formation in quiescent conditions: in search of efficient kinetic additive. *Energy Procedia,* Volume 4, pp. 621-628.

van Denderen, M., Ineke, E. & Golombok, M., 2009. CO2 removal from contaminated natural gas mixtures by hydrate formation. *Industrial & Engineering Chemistry Research,* 48(12), pp. 5802-5807.

Veenman, A., 1977. Heat transfer in a multi-stage flash/fluidized bed evaporator (MSF/FBE). *Desalination,* 22(1), pp. 55-76.

Vera, J., Sayegh, S. & Ratcliff, G., 1977. A quasi lattice-local composition model for the excess Gibbs free energy of liquid mixtures. *Fluid Phase Equilibria,* 1(2), pp. 113-135.

Volmer, M. & Weber, A., 1926. Keimbildung in ü bersattigten Gebilden. *Zeitschrift fur Physikalische Chemie,* 119(1), p. 277−301.

Vysniauskas, A. & Bishnoi, P., 1983. Kinetic study of methane hydrate formation.. *Chemical Engineering Science,* Volume 38, p. 1061–1072.

Wang, H. et al., 2015. Performance of an environmentally friendly anti-scalant in CaSO4 scale inhibition. *Desalination and Water Treatment,* 53(1), pp. 8-14.

Wang, H., Zhou, Y., Yao, Q. & Sun, W., 2015.. Calcium sulfate precipitation studies with fluorescent-tagged scale inhibitor for cooling water systems. *Polymer Bulletin,* 72(9), p. 2171–2188.

Watkinson, A. & Martinez, O., 1975. Scaling of heat exchanger tubes by calcium carbonate.. *Journal of Heat transfer,* Volume 97, pp. 504-508.

Wiebe, R. & Gaddy, V., 1939. The solubility in water of carbon dioxide at 50, 75 and 100, at pressures to 700 atmosphere. *Journal of the American Chemical Society,* 61(2), pp. 315-318.

Wildebrand, C. et al., 2007. Effects of process parameters and anti-scalants on scale formation in horizontal tube falling film evaporators. *Desalination,* Volume 204, pp. 448-463.

Wilson, P. & Haymet, A., 2010. Hydrate formation and re-formation in nucleating THF/water mixtures show no evidence to support a “memory” effect. *Chemical engineering journal,* 161(1), pp. 146-150.

Xie, N., Liu, Z., Yang, S. & Tan, C., 2019. Energy Efficiency Analysis of Postcombustion Hydrate-Based CO2 Capture with Tetrahydrofuran and Tetra-n-butylammonium Bromide. *Industrial & Engineering Chemistry Research,* 59(2), pp. 802-813.

Xu, C. & Li, X., 2014. Research progress of hydrate-based CO2 separation and capture from gas mixtures. *Rsc Advances,* 4(35), pp. 18301-18316.

Yang, L. et al., 2011. Accelerated formation of methane hydrate in aluminum foam. *Industrial & Engineering Chemistry Research,* 50(20), pp. 11563-11569.

Yang, L. et al., 2011. Accelerated formation of methane hydrate in aluminum foam.. *Industrial and Engineering Chemistry Research,* 50(20), pp. 11563-11569.

Yang, M. et al., 2017. Hydrate-based CO2 capture from flue gas in constant pressure process with the presence of THF. *Energy Procedia,* Volume 142, pp. 3939-3943.

Yin, Z., Khurana, M., Tan, H. & Linga, P., 2018. A review of gas hydrate growth kinetic models. *Chemical Engineering Journal,,* Volume 342, pp. 9 - 29.

Yoshioki, S., 2012. Identification of a mechanism of transformation of clathrate hydrate structures I to II or H.. *Journal of Molecular Graphics and Modelling,* Volume 37, pp. 39-48.

Yoslim, J., Linga, P. & Englezos, P., 2010. Enhanced growth of methane propane clathrate hydrate crystals with sodium dodecylsulfate, sodium tetradecylsulfate, and sodium hexadecylsulfate surfactants. *Journal crystal growth,* Volume 313, p. 80.

Zhang, F., Xiao, J. & Chen, X. D., 2015. Towards predictive modeling of crystallization fouling: A pseudo-dynamic approach.. *Food and Bioproducts Processing,* Volume 93, pp. 188-196.

Zhang, J. & Lee, J., 2009. Enhanced kinetics of CO2 hydrate formation under static conditions. *Industrial & engineering chemistry research,* 48(13), pp. 5934-5942.

Zhang, J. S., Lee, S. & Lee, J. W., 2007. Kinetics of Methane Hydrate Formation from SDS Solution. *Industrial and engineering chemistry,* Volume 46, p. 6359.

Zhang, J., Yedlapalli, P. & Lee, J., 2009. Thermodynamic analysis of hydrate-based pre-combustion capture of CO2. *Chemical engineering science,* 64(22), pp. 4732-4736.

Zhao, J. et al., 2018. A review of heterogeneous nucleation of calcium carbonate and control strategies for scale formation in multi-stage flash (MSF) desalination plants. *Desalination,* Volume 442, pp. 75-88.

Zhao, Y. et al., 2016. Inhibition of calcium sulfate scale by poly (citric acid). *Desalination,* Volume 392, pp. 1-7.

Zheng, H. et al., 2017. Induction time of hydrate formation in water-in-oil emulsions. *Industrial & Engineering Chemistry Research,* 56(29), pp. 8330-8339..

Zhong, S. & Mucci, A., 1989. Calcite and aragonite precipitation from seawater solutions of various salinities: Precipitation rates and overgrowth compositions. *Chemical Geology,* Volume 78, pp. 283-299.

Zhong, Y. & Rogers, R., 2000. Surfactant effects on gas hydrate formation. *Chemical Engineering Science,* 55(19), pp. 4175-4187.

Zhong, Y. & Rogers, R. E., 2000. Surfactant Effects on Gas Hydrate Formation. *Chemical engineering science,* Volume 55, p. 4187.

Appendix A

Derivation of Nucleation rate

As mentioned by Kashchiev, the rate of nucleation is a function of equilibrium frequency of attachment (f*) and the equilibrium concentration of nuclei (C*) with the aqueous phase (Kashchiev, 2000).

$$J_s = zf^*C^* \quad \text{A1.01}$$

Where the equilibrium concentration of the nuclei is given by the following equation, considering C_0 as the concentration of nucleation sites under the hydrate-water equilibrium conditions and W is the work done by the system in forming a nucleus with the equilibrium crystal size.

$$C^* = C_0 e^{\left(\frac{W}{kT}\right)} \quad \text{A1.02}$$

The work done by the system for the formation of a unit stable hydrate crystal under the given operational conditions can be calculated by using the following equation.

$$W = \frac{8c^3 v_h^2 \sigma_{ef}^3}{27\,\Delta\mu^2} \quad \text{A1.03}$$

While the frequency of attachment and the frequency of attachment at the equilibrium (hydrate-water) conditions is given by the following equation, considering Δμ as the driving force for the hydrate formation.

$$f^* = {f_0}^* e^{\left(\frac{\Delta\mu}{kT}\right)} \quad \text{A1.04}$$

The driving force for the hydrate formation could be calculated by the following equation.

$$\Delta\mu = kT \ln\left(\frac{\emptyset P}{\emptyset_e P_e}\right) + (n_w v_w - v_h)(P - P_e) \quad \text{A1.05}$$

Combining these three equations, the equation for the rate of nucleation could be produced (equation 3.14).

$$J = z f_e^* C_0 e^{\frac{\Delta\mu}{kT}} e^{\frac{-W}{kT}} \quad \text{A1.06}$$

Considering the effect of sticking coefficient (ε), shape factor (c), volume of hydrate unit (v_h), and the concentration of dissolved gas at the water-hydrate equilibrium conditions (M_{i0}) the equilibrium frequency of attachment could be written as follows.

$$f_e^* = \varepsilon(4\pi c)^{\frac{1}{2}} v_h^{\frac{1}{3}} D M_{i0} n^{*\frac{1}{3}} \quad \text{A1.07}$$

Considering the equation for the equilibrium frequency of attachment into the rate of nucleation equation (3.14), the equation would transform into the following form (Refer to the equation 3.16).

$$J = z\left(\varepsilon(4\pi c)^{\frac{1}{2}} v_h^{\frac{1}{3}} D M_{i0} n^{*\frac{1}{3}}\right) C_0 e^{\frac{\Delta\mu}{kT}} e^{\frac{-W}{kT}} \quad \text{A1.08}$$

Appendix B

Adjustments done to the rate of nucleation equation.

The expanded version of the rate of hydrate nucleation equation has been addressed by the equation 3.16, which is written as follows.

$$J = z\left(\varepsilon(4\pi c)^{\frac{1}{2}} v_h^{\frac{1}{3}} D M_{i0} n^{*\frac{1}{3}}\right) C_0 e^{\frac{\Delta\mu}{kT}} e^{\frac{-W}{kT}} \qquad \text{A2.01}$$

The term M_{i0} represents the dissolved gas concentration at the hydrate equilibrium conditions, which is not dependent upon either pressure or the temperature. To measure the sensitivity of this equation towards various calculating methods for dissolved gas concentration and the fugacity, the term M_{i0} should be transformed into a pressure and temperature dependent term. For this requirement, it is important to find the expression that addresses the excessive gas dissolution under a different set of operational conditions. As it can be seen from the equation (3.16), the expression consisting of the driving force ($e^{\frac{\Delta\mu}{kT}}$) could be considered as the correction factor. Combining the exponential term with the equilibrium gas concentration, the following adjustments could be made.

$$J = z\left(\varepsilon(4\pi c)^{\frac{1}{2}} v_h^{\frac{1}{3}} D (M_{i0} e^{\frac{\Delta\mu}{kT}}) n^{*\frac{1}{3}}\right) C_0 e^{\frac{-W}{kT}} \qquad \text{A2.02}$$

$$J = z\left(\varepsilon(4\pi c)^{\frac{1}{2}} v_h^{\frac{1}{3}} D M_i n^{*\frac{1}{3}}\right) C_0 e^{\frac{-W}{kT}} \qquad \text{A2.03}$$

Where Mi represents the gas concentration in the aqueous phase under the operational conditions. This adjustment is valid because the gas concentration is driven by the same driving force which is influencing the rate of hydrate formation. To further evaluate the accuracy of this adjustment, the rates of hydrate formation values calculated from the equation 3.16 have

been compared against the adjusted rate of nucleation equation. This comparison was presented through an error (Δ) analysis by means of the following equation.

$$\Delta = \left(\frac{J_{adjusted} - J_{original}}{J_{original}}\right) X100 \qquad \text{A2.04}$$

Appendix C

The derivation of theoretical induction time

According to Sloan and Koh (Sloan Jr & Koh, 2007), the Gibb's free energy change (ΔG_{tot}) of the system forming hydrates from the solution of water and dissolved gas can be interpreted as the summation of surface excess free energy (ΔG_s) representing the solute molecules becoming a part of the hydrate crystal surface and volume excess free energy (ΔG_v) representing the solute molecules becoming a part of the volume of the hydrate crystal.

$$G_{tot} = (\Delta G_s + \Delta G_v) \quad \text{A3.01}$$

Where ΔG_v and ΔG_s could be calculated by the following equations, respectively.

$$\Delta G_s = 4\pi r^2 \sigma \quad \text{A3.02}$$

$$\Delta G_v = \frac{4}{3}\pi r^3 \Delta g_v \quad \text{A3.03}$$

The hydrate formation would become a spontaneous process when the Gibb's free energy of the system reaches to its maximum. Upon the differentiating the total Gibb's free energy equation with respect to the radius and equating it to zero, the following equation for the critical radius is obtained.

$$R_c = \frac{2\sigma}{(\Delta g)} \quad \text{A3.04}$$

Where the Gibb's free energy change per unit volume (Δg) is calculated from the following equation.

$$-\Delta g = \frac{kT}{v_h} \ln\left(\frac{\emptyset P}{\emptyset_e P_e}\right) + \frac{n_w v_w (P - P_e)}{v_h} \quad \text{A3.05}$$

As the hydrate formation process becomes spontaneous when the size of the hydrate nucleus becomes the critical radius, for the calculation of induction time, the extent of crystal growth equation proposed by Kashchiev and Firoozabadi was considered (Kashchiev & Firoozabadi, 2003). The following equation represents the progressive growth (R_G) of the hydrate crystal.

$$R_G(t) = \sqrt{\left(2\varepsilon v h D M_i \left(e^{\left(\frac{\Delta\mu}{kT}\right)} - 1\right) t\right)} \quad \text{A3.06}$$

By equating the extent of hydrate formation with the critical radius, the induction time equation is derived, which is as follows.

$$t_{ind} = \frac{\sigma^2}{2\varepsilon v_h \mathrm{D}(M_i - M_{i0})(\Delta \mathrm{g})^2} \quad \text{A3.07}$$

Appendix D

Scale formation

According to Alsadaie and Mujtaba (Alsadaie & Mujtaba, 2017), the overall deposition rate of the scale is the difference between the progressive mass deposition of the scale and the mass removal at any given point of time.

$$\frac{dm_f}{dt} = m_d - m_r \quad \text{A4.01}$$

The progressive mass deposition rate is calculated from the mass transfer rates of the scale forming reagents from the bulk to the heat-transfer area. Considering k_D to be the mass transfer coefficient, the progressive mass deposition rate could be calculated from the following equation.

$$\frac{dm_d}{dt} = k_D\,(C_{b-}\,C_i) \quad \text{A4.02}$$

The mass removal rate could be calculated from the following equation.

$$\frac{dm_d}{dt} = k_r(C_i - C_s)^n \quad \text{A4.03}$$

The progressive deposition of Calcite/Aragonite scale is influenced by two steps: the rate of Calcite/Aragonite formation or the reaction step and the rate of Calcite/Aragonite diffusion to the heat transfer area. Considering the higher stream velocities, the progressive deposition rates are limited by the reaction step and hence the rate of reaction would be the rate of progressive deposition of the Calcite scale (Helalizadeh, et al., 2000; Fahiminia, et al., 2007).

$$\frac{dm_d}{dt} = k_r([Ca][CO_3] - k_{sp})^2 \quad \text{A4.04}$$

However, for more accuracy, the study considered the approach proposed by Paakkonen (Pääkkönen, et al., 2015), where the rate of progressive deposition considered both diffusion and the reaction steps. The equation could be written as follows.

$$\frac{dm_d}{dt} = \beta\left[\frac{1}{2}\left(\frac{\beta}{k_r}\right) + (c_b - c_s) - \sqrt{\frac{1}{4}\left(\frac{\beta}{k_r}\right)^2 + \left(\frac{\beta}{k_r}\right)(c_b - c_s)}\right] \qquad \text{A4.05}$$

Where β is the mass transfer coefficient, which could be calculated from the following equation.

$$\beta = \frac{0.034 Re^{0.875} Sc^{0.33} D}{D_h} \qquad \text{A4.06}$$

The Reynolds number (Re) and the Schmidt number (Sc) could be calculated by the following equations.

$$Re = \frac{\rho_w v D_h}{\mu_w} \qquad \text{A4.07}$$

$$Sc = \frac{\mu_w}{\rho_w D} \qquad \text{A4.08}$$

By considering the flow velocity and the Arrheneus expansion for the reaction rate coefficient, the progressive rate of scale deposition could be transformed into the following equation (Helalizadeh, et al., 2005; Pääkkönen, et al., 2015).

$$\frac{dm_d}{dt} = k'_r (C_i - C_s)^n \frac{\mu_w}{\rho_w V^2} = \left(k'_0 e^{\frac{-E_a}{RT_s}}\right)(C_i - C_s)^2 \frac{\mu_w}{\rho_w V^2} \qquad \text{A4.09}$$

Where V represents the friction velocity and can be calculated from the equation 6.47

$$V = \sqrt{f\frac{v^2}{2}} \qquad \text{A4.10}$$

However, considering the fluctuations of temperature, pressure and salinity in water, an accurate version of solubility product equation was derived by Al-Anezi and Hilal, where the

activity coefficient of water was considered (Al-Anezi & Hilal, 2007), which is provided as follows.

$$K_{sp} = \frac{K_{sp}^0}{\gamma_{Ca}\gamma_{CO_3}} \quad \text{A4.11}$$

While Plummer and Busenberg's equation could be used to calculate K_{sp}^0 value, which is shown by the following equation (Plummer & Busenberg, 1982).

$$Log\left(K_{sp}^0\right) = \left[-171.9773 - 0.077993T_s + \frac{2903.293}{T_s} + 71.595\log(T_s)\right] \quad \text{A4.12}$$

WATEQ-Debye-Huckel's equation has been used to calculate the activity coefficient of an ion 'a', which has been given in the following equation (Al-Anezi & Hilal, 2007).

$$Log(\gamma_a) = -A_{DH}Z_a^2\frac{\sqrt{I}}{1+Ba_a\sqrt{I}} + b_aI \quad \text{A4.13}$$

$$I = 0.5\sum z_i^2 m_i \quad \text{A4.14}$$

The following scale removal rate equation was developed by Bohnet (Bohnet, 1987), where the equation was derived from the idea that the removal rate was proportional to the shear stress of the flow while inversely proportional to the layer's shear strength.

$$\frac{dm_r}{dt} = \frac{k_{rem}}{k}\frac{Nx_f(1+\delta\Delta T)d_p\,T_f}{\sigma_f}\rho_f\left(\frac{\mu_w g}{\rho_w}\right)^{0.33} \quad \text{A4.15}$$

To eliminate the rate constants (k and k_{rem}), Kraus made a suggestion, where the expression (k. Pf/ krem. N) could be replaced by $83.2v^{0.54}$ (Krause, 1993; Brahim, et al., 2003). After this adjustment, the Bohnet's rate of scale removal would transform into the following equation.

$$\frac{dm_r}{dt} = \frac{x_f(1+\delta\Delta T)d_p\,T_f}{83.2\,v^{0.54}}\rho_f\left(\frac{\mu_w g}{\rho_w}\right)^{0.33} \quad \text{A4.16}$$

The rate of mass deposition of the scale forming substance can be written as the product of rate of change in the fouling layer thickness (x_f) and the density of the fouling layer.

$$\frac{dm_f}{dt} = \rho_f \frac{dx_f}{dt} \quad \text{A4.17}$$

Whereas this rate of change in the fouling layer thickness, combined with the conductivity of the fouling layer is used to calculate the rate of change in the thermal resistance as shown in the following equation.

$$\frac{dR_f}{dt} = \frac{1}{\lambda_f}\frac{dx_f}{dt} \quad \text{A4.18}$$

Considering the conductivity of the fouling layer is independent of fouling layer's thickness and time, a definitive integral from time t=0 to t would lead the rate of change in thermal resistance to the following equation.

$$\int_{t=0}^{t} dR_f = \frac{1}{\lambda_f}\int_{t=0}^{t} dx_f \quad \text{A4.19}$$

Considering zero resistance and zero scale formation at the time t=0, the rate of change in the thermal resistance with respect to the thickness of the scale can be written as follows.

$$R_f = \frac{x_f}{\lambda_f} \quad \text{A4.20}$$

As the thickness of the layer could be written in terms of the mass deposition and the density of the scale, the thermal resistance change rate would transform into the following equation.

$$R_f = \frac{\rho_f}{\lambda_f}(m_d - m_r) \quad \text{A4.21}$$

According to Zhang et al (Zhang, et al., 2015) the density of the scale could be written as a function of porosity, density of the scaling substance and the density of water.

$$\rho_f = w\rho_{water} + (1-w)\rho_{solid} \quad \text{A4.22}$$

For the calculation of the thermal conductivity of the fouling layer, Brahim's approach was considered. (Brahim, et al., 2003).

$$\lambda_f = \frac{\lambda_{f,1}+\lambda_{f,2}}{2} \quad \text{A4.23}$$

$$\lambda_{f,1} = w\lambda_{water} + (1-w)\lambda_{solid} \quad \text{A4.24}$$

$$\frac{1}{\lambda_{f,2}} = \frac{w}{\lambda_{water}} + \frac{(1-w)}{\lambda_{solid}} \quad \text{A4.25}$$

Appendix E

Experimental validation of the derived induction time equation

From the mathematical models for hydrate nucleation and growth proposed by Kashchiev and Firoozabadi (2000, 2002a, 2002b, 2003) and Sloan and Koh (2007), a theoretical induction time for the hydrate formation was derived in this study. The equation for the induction time was provided in the chapter 3 (eq. 3.24), which is as follows:

$$t_{ind} = \frac{\sigma^2}{2\varepsilon v_h \mathrm{D}(M_i - M_{i0})(\Delta \mathrm{g})^2} \qquad \text{A5.01}$$

However, the induction time equation is valid for only homogeneous nucleation as the nucleation model by Kashchiev and Firoozabadi (2002a), was developed under the assumption of nucleation in the liquid bulk. However, the occurrence of homogeneous nucleation is impractical as the primary nucleation generally occurs at either gas-liquid-wall or gas-liquid interface. The occurrence of the surface or the heterogeneity of the nucleation was represented by the parameter superficial energy, which was represented by σ. The ratio between the homogeneous and heterogeneous nucleation was given by the following equation:

$$\frac{\sigma_{eff}}{\sigma} = \varphi \qquad \text{A5.02}$$

Where σ_{eff} is the superficial energy of the heterogeneous nucleation process and the factor φ has a value in between 0 and 1. The equation for this heterogeneity factor is given by the following equation. Considering cap-shaped clusters, the value of φ is calculated by the following equation (Kashchiev & Firoozabadi, 2002a)

$$\varphi = (0.25(2 + cos\theta)(1 - cos\theta)^2)^{\frac{1}{3}} \qquad \text{A5.03}$$

Combining the equations A5.02 and A5.03, the following equation could be obtained, which is a modified version of the equation 3.25.

$$\frac{\sigma_{eff}}{\sigma} = (0.25(2 + cos\theta)(1 - cos\theta)^2)^{\frac{1}{3}} \quad \text{A5.04}$$

When the equation A5.01 was modified into an equation for the heterogeneous nucleation, it will become the following equation:

$$t_{ind}^{h} = \frac{\sigma_{eff}^2}{2\varepsilon v_h \mathrm{D}(M_i - M_{i0})(\Delta g)^2} \quad \text{A5.05}$$

Where t^{h}_{ind} represents the heterogeneous induction time. By equating A5.05 with the equation A5.01, the following equation was obtained.

$$\frac{t_{ind}^{h}}{t_{ind}} = \frac{\sigma_{eff}^2}{\sigma^2} = (0.25(2 + cos\theta)(1 - cos\theta)^2)^{\frac{2}{3}} \quad \text{A5.06}$$

Considering the cosine function to be a random variable x, with adjustments, the equation A5.06 transformed into the following equation:

$$x^3 - 3x + 2 - \left(\frac{4t_{ind}^{h}}{t_{ind}}\right)^{\frac{3}{2}} = 0 \quad \text{A5.07}$$

For the validation, the induction time observed for the methane clathrate nucleation at 12MPa pressure and 274K was compared with the homogeneous induction time values calculated for the same methane clathrate nucleation under the same operational conditions. However, by considering various models to calculate the fugacity and dissolved gas concentration, various values of induction time were obtained. These induction times were presented in six cases. For the current calculation, the induction time value obtained in case 5 has been considered (t_{ind} = 6558.779s), whereas the experimentally obtained induction time was 1710s. By substituting these values, the equation A5.07 would transform into the following form:

$$x^3 - 3x + 1.065 = 0 \quad \text{A5.08}$$

Upon solving the equation A5.08, three roots would be obtained for cosϴ. They are -1.88789 1.5157, and 0.37219. Amongst these roots, as cosine function can not exceed the bounds [-1,1], the only feasible root would be 0.372. This value yields upon the angle 68.697^{o}, as shown in the table 3.3. As the experiments were conducted in a stainless-steel reactor, this contact angle would be practicable. Hence, the derived theoretical induction time equation is valid to apply for the practical applications.